Flow structure, mixing, flame stabilization and pollutant emissions from a coaxial dual swirl CH4/H2/air injector

Sylvain Marragou

To cite this version:

Sylvain Marragou. Flow structure, mixing, flame stabilization and pollutant emissions from a coaxial dual swirl CH4/H2/air injector. Other [cond-mat.other]. Institut National Polytechnique de Toulouse - INPT, 2023. English. NNT : 2023INPT0031 . tel-04169678

HAL Id: tel-04169678
https://theses.hal.science/tel-04169678v1

Submitted on 24 Jul 2023

THÈSE

En vue de l'obtention du

DOCTORAT DE L'UNIVERSITÉ DE TOULOUSE

Délivré par :

Institut National Polytechnique de Toulouse (Toulouse INP)

Discipline ou spécialité :

Energétique et transferts

Présentée et soutenue par :

M. SYLVAIN MARRAGOU

le mercredi 17 mai 2023

Titre :

Flow structure, mixing, flame stabilization and pollutant emissions from a coaxial dual swirl CH4/H2/air injector

---

Ecole doctorale :

Mécanique, Energétique, Génie civil, Procédés (MEGeP)

Unité de recherche :

Institut de Mécanique des Fluides de Toulouse (IMFT)

Directeurs de Thèse :

M. THIERRY SCHULLER

M. THIERRY POINSOT

Rapporteurs :

M. JAMES R. DAWSON, NORWEGIAN UNI OF SCE AND TECHN TRONDHEIM

MME SIMONE HOCHGREB, UNIVERSITE DE CAMBRIDGE

Membres du jury :

MME CHRISTINE ROUSSELLE, UNIVERSITE D'ORLEANS, Présidente

M. CHRISTOPHE VIGUIER, GROUPE SAFRAN, Invité

M. DANIEL DUROX, CENTRALESUPELEC GIF SUR YVETTE, Invité

M. THIERRY POINSOT, TOULOUSE INP, Membre

MI. THIERRY SCHULLER, UNIVERSITE PAUL SABATIER, Membre

Abstract

Developing hydrogen fueled burners that meet stringent conditions of aeroejet engine gas turbines is challenging. In this work, a dual swirl coaxial injector concept is investigated at atmospheric conditions. The structure of the flow, mixing, flame stabilization and pollutant emissions are scrutinized. This co-axial injector operates with hydrogen injected in a central tube and with air or a CH_4/air mixture in the annular channel. For a fixed swirl level in the annular channel, the swirl level in the hydrogen injector, the recess distance of hydrogen injection with respect to the chamber backplane and the hydrogen injection velocity are identified as the main parameters controlling flame stabilization. Conferring swirl to the hydrogen stream is identified as a necessary condition to lift H_2/air flames. A small recess distance considerably enhances the range of operating conditions for which the flame is lifted. Particle Image Velocimetry (PIV) measurements indicate that the swirled hydrogen central jet expands radially right at the injector outlet, cutting the low velocity zone in the wake of the injector lips, explaining the observed necessity of an inner swirl motion to lift the flame. Raman scattering is used to infer the gas concentration profiles at the burner outlet. Conferring swirl to the hydrogen stream greatly enhances mixing in the first millimeters right out of the central hydrogen injector. Augmenting the hydrogen injector recess distance favors partial premixing before combustion. The velocity ratio between the central and annular stream and the central jet angle are shown to drive mixing and a physical-based model is derived to scale a mixing progress parameter.
In reactive conditions, PIV shows that thermal expansion of the gas across the flame substantially increases the spreading angle of the swirled jet leading to lower recirculation velocities. When the flame is anchored, the presence of heat release right at the outlet of the central injector leads to a decrease of the diameter of the central recirculation zone at the outlet of the annular injector. Thermal boundary conditions along the combustion chamber, gas temperatures at several locations in the flow and pollutant emissions are also analyzed. NOx emissions decrease when the flame is lifted due to a better mixing consecutive to the increased distance between the hydrogen injection outlet and the flame. They drop with the global equivalence ratio and drop for increased thermal powers. A scaling law based on the adiabatic temperature and the residence time of burnt gases in the combustion chamber enables to collapse the data for lifted flames. Finally, a predictive model based on an edge flame displacement speed is developed to describe the physical mechanisms leading to flame re-anchoring. It considers that, for an initially lifted flame, if a zone with a flammable mixture and with velocities lower than the triple flame speed exists from the flame leading edge to the injector lips, the flame will re-anchor to the injector. With a limited set of experimental data taken in cold flow conditions, this model is able to predict the transition from lifted to anchored flames for all operating conditions. These experiments and models open the path to the optimization of hydrogen injectors in swirling flows.

Keywords: *Hydrogen, Methane, Swirl, Flame stabilization, NOx emissions, Mixing, Particle Image Velocimetry, Raman scattering, Modeling*

Résumé

Développer des brûleurs alimentés à l'hydrogène qui répondent aux conditions strictes des turbines à gaz équipant les moteurs d'avions à réaction est un défi. Dans ce travail, un concept d'injecteur coaxial à double swirl est étudié dans une chambre de combustion opérant à pression atmosphérique. La structure de l'écoulement, le mélange, la stabilisation de la flamme et les émissions polluantes sont étudiés. Cet injecteur coaxial fonctionne avec de l'hydrogène injecté dans un tube central et avec de l'air ou un mélange CH_4/air dans le canal annulaire. Pour un niveau de swirl fixé dans le canal annulaire, le niveau de swirl dans l'injecteur d'hydrogène, la distance de retrait de l'injecteur d'hydrogène par rapport au fond de chambre de combustion et la vitesse d'injection d'hydrogène sont les principaux paramètres contrôlant la stabilisation de flamme. Conférer un swirl à l'écoulement d'hydrogène est une condition nécessaire pour décrocher les flammes H_2/air des lèvres de l'injecteur. Une petite distance de retrait de l'injecteur d'hydrogène améliore considérablement l'intervalle des conditions de fonctionnement pour lesquelles la flamme est stabilisée aérodynamiquement. Les mesures de vitesse par Vélocimétrie par Image de Particules (PIV) indiquent que le jet central d'hydrogène swirlé se détend radialement dès sa sortie de l'injecteur, coupant la zone de faible vitesse dans le sillage des lèvres de l'injecteur, expliquant la nécessité du swirl interne pour détacher la flamme. La diffusion Raman est utilisée pour déduire les profils de concentration de gaz à la sortie du brûleur. Conférer un swirl à l'écoulement d'hydrogène améliore considérablement le mélange dès les premiers millimètres après la sortie de l'injecteur central d'hydrogène. L'augmentation de la distance de retrait de l'injecteur d'hydrogène favorise un prémélange partiel avant la combustion. Le rapport de vitesse entre les écoulements central et annulaire et l'angle du jet central contrôlent l'état du mélange. Un modèle d'ordre réduit est développé avec un paramètre de progression du mélange valide pour un grand nombre de conditions de fonctionnement.

Dans des conditions réactives, les mesures PIV montrent que la dilatation thermique du gaz à travers la flamme augmente considérablement l'angle d'expansion du jet swirlé conduisant à des vitesses de recirculation plus faibles. Lorsque la flamme est attachée aux lèvres de l'injecteur, la présence d'un dégagement de chaleur dès la sortie de l'injecteur central entraîne une diminution du diamètre de la zone centrale de recirculation en sortie de l'injecteur annulaire. Les conditions aux limites thermiques le long de la chambre de combustion, les températures des gaz en plusieurs points dans l'écoulement et les émissions de polluants sont également déterminées. Les émissions de NOx diminuent lorsque la flamme est détachée du fait d'un meilleur mélange consécutif à l'augmentation de la distance entre la sortie d'injection d'hydrogène et la flamme. Les émissions de NOx chutent avec la richesse globale et pour des puissances thermiques accrues. Une loi d'échelle basée sur la température adiabatique de flamme et le temps de séjour des gaz brûlés dans la chambre de combustion permet de réduire les données pour les flammes détachées. Enfin, un modèle prédictif basé sur une vitesse de déplacement de l'extrémité de la flamme est développé pour décrire les mécanismes physiques conduisant au réattachement de la flamme. Il considère que, pour une flamme initialement détachée, s'il existe une zone de mélange inflammable avec des vitesses inférieures à la vitesse de flamme triple, depuis l'extrémité de la flamme jusqu'aux lèvres de l'injecteur, la flamme se réattachera à l'injecteur. Avec un ensemble limité de données expérimentales acquises dans des conditions d'écoulement à froid, ce modèle est capable de prédire la transition de réattachement des flammes détachées pour toutes les conditions de fonctionnement explorés. Ces expériences et modèles ouvrent la voie à l'optimisation des injecteurs swirlés d'hydrogène pour les turbines à gaz.

Mots clés: *Hydrogène, Méthane, Swirl, Stabilisation de flamme, Emissions de NOx, Mélange, Vélocimétrie par Images de Particules, Diffusion Raman, Modélisation*

Acknowledgement

First of all, I would like to thank my thesis director Thierry Schuller and my co-supervisor Thierry Poinsot for welcoming me to IMFT. With Laurent Selle, they have accompanied me since my master's degree, helping me, training me and encouraging me without limits in an environment particularly conducive to the dynamism of scientific research, creativity and teamwork. I have just spent three unforgettable years during which I went from a simple student to a passionate young researcher. I also particularly thank Bernard Ferret for the passionate exchanges and his welcome at the IUT GMP in Toulouse.

My atypical career was made possible thanks to many people who are passionate about their profession. I must sincerely thank Yves Martin, Jean-Baptiste Blanc, Laurent Perris, Philippe Ventre, Sébastien Tanguy, Benoit Bédat and Thierry Schuller who believed in me and allowed me to get here.

I must thank all the members of the MIR research group for these three exceptional years within IMFT, and more particularly Gorkem Oztarlik, Jimmy Suarez, Tarik Yahou, Andrea Aniello, Pierre-Alexandre Masset, Antoine Gosset and Hervé Magnes.

During these three years at IMFT, I was supported by the laboratory staff. I would like to thank Rudy Soeparno, Sébastien Cazin, Moïse Marchal, Laurent Mouneix, Gilles Albert, Stefano Lun Kwong, André Rouch, Muriel Sabater, Karine Defretin and Célines Perles-Picotto.

Finally I have a thought for all my friends and especially my parents and my sister who have supported me unfailingly for many years.

Contents

Chapter 1

Introduction

> “*Product of optimism and knowledge is a constant.*”
>
> Lev Landau

Overview

1.1 Context

Since the discovery of fire, humanity's energy consumption has increased, with a dramatic acceleration in the consumption of fossil fuels at the beginning of the industrial era in Great Britain in the late 18th century [1]. The use of fossil fuels, such as coal, oil and natural gas, has led to the release of massive quantities of CO_2 into the atmosphere. This additional CO_2, which was previously trapped in the earth's subsoil, is now having a significant impact on the earth's climate through the greenhouse effect theorized by Fourier in 1827 [2]. The radiative properties of CO_2 and other gases released by human activities enhance the natural greenhouse effect, leading to an increase in global temperatures, as first investigated by Tyndall in 1859 [3]. Climate change has been studied for over 150 years as reviewed by Jain [4].

In 2017, 81% of the world's energy was produced from fossil fuels, according to the report of the International Energy Agency [5]. It is now clear that humanity needs to urgently decrease CO_2 emissions in order to limit the increase of the earth's mean temperature. The Paris climate agreements [6], signed by most countries, aim to limit the increase of the earth's temperature bellow 2°C above pre-industrial levels. To reach this goal, the world's energy consumption needs to be reduced, and fossil fuels need to be replaced with carbon-free and low-carbon technologies. Several solutions have been proposed to replace the energy currently produced by fossil fuels, including:

- Renewable energy sources such as solar, wind, hydraulic and geothermal power.
- Nuclear power, which generates electricity through the process of nuclear fission.
- Synthetic fuels, which are made from renewable plant materials.
- Carbon capture and storage (CCS) technologies, to capture carbon dioxide emitted from power plants powered by hydrocarbon fuels and store it.
- Enhancing the efficiency of current systems, such as improving building insulation.

All these solutions must be considered and used together in order to reach the goals of the Paris climate agreements [6]. This study focuses on the use of hydrogen as a fuel for gas turbines. Hydrogen is a synthetic carbon-free fuel that can be produced from nuclear and renewable energy sources, and it is one of the ways currently being investigated for the decarbonization of aviation [7] and electricity generation through power production gas turbines [8].

1.2 Gas turbine injector technologies

Gas turbines are combustion engines extensively used since the beginning of the 20th century. They are mostly used for propulsion of aircrafts and helicopters and for terrestrial power generation. They are also used to drive transportation of hydrocarbon fuels in pipelines, or for power generation units in military boats and as thrusters for missiles. Marginally, gas turbines also propel some locomotives, cars, motorcycles or jet-packs [9].

1.2.1 Aeronautical technologies

Aeronautical gas turbines are the most common turbines used in the world. This quick state of the art on aeronautical gas turbines focuses on fuel and air injection technologies used to power the engine. Gas turbines equip most of the civil and military aircrafts and helicopters and generally burn kerosene. Because kerosene is a liquid fuel, it needs to be atomized and mixed with air before combustion. Airblast and pressure-swirl atomizers are generally used for this purpose.

Figure 1.1 illustrates three different fuel injection technologies. The pre-filming type in Fig. 1.1.a consists in atomizing the liquid kerozen on a surface to create a liquid film, from which small droplets are torn from the liquid film by the airflow. In Fig. 1.1.b, a hybrid injector scheme with a central pressure-swirl atomizer and an external airblast atomizer is presented, and is denoted piloted airblast atomizer. Another technique is the plain fuel jet which is generally injected as a jet in the air shear cross-flow as in Fig. 1.1.c.

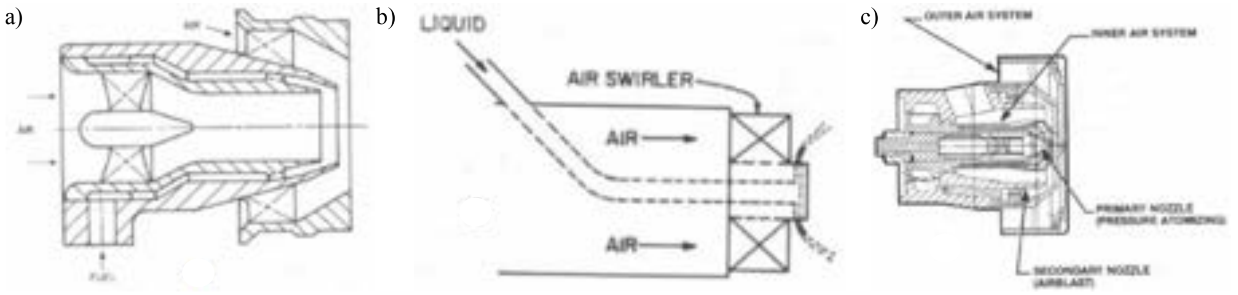

Figure 1.1 – Typical fuel atomizers in gas turbines. (a) Pre-filming, (b) piloted and (c) plain-jet airblast atomizers. Figure adapted from [10].

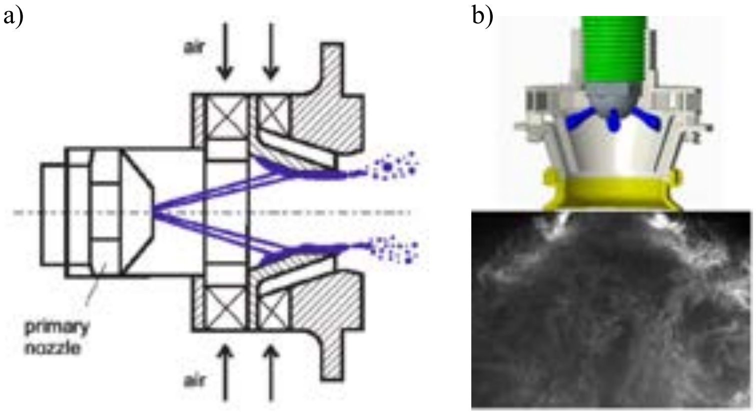

Figure 1.2 – Pre-filming atomizers: (a) Schematic reproduced from [11]. (b) Experimental visualization of the resulting spray reproduced from [12].

The most common airblast atomizer is the pre-filming type, further detailed in Fig. 1.2. In Fig. 1.2.a, the atomization mechanisms are described. The liquid fuel is atomized in a primary nozzle and impinges the external surface of the main air channel. A liquid film is created and small fuel droplets are torn from the liquid film in the shear layer between the primary and secondary air flow. These fuel droplets are then transported by the flow to the combustion zone. The resulting fuel droplets entering the combustion chamber are shown in Fig. 1.2.b.

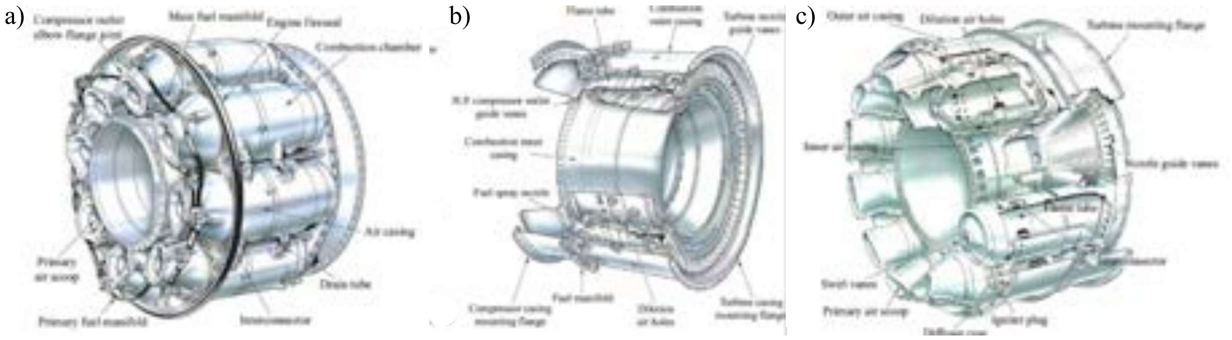

Figure 1.3 – Illustration of typical aeronautical combustion chambers (a) CAN, (b) annular and (c) CAN-annular combustion chamber. Figure adapted from [13].

Different combustion chamber architectures exist. Most of aeronautical turbines are annular, CAN and CAN-annular combustors, as illustrated in Fig. 1.3. In both cases, flames form a ring around the central shaft. A fraction of the inlet air flow is deviated from the injector to dilute burnt gases and reduce the temperature before the turbine first stage to lower NOx emissions. This work only focuses on a single sector of the combustion chamber, i.e. a single injector, which is a necessary step in the design of a new injection unit.

1.2.2 Power generation technologies

Gas turbines are also extensively used for generation of electricity. Initially mostly derived from aeronautical gas turbines, new technologies have been developed for cleaner combustion. Several power generation gas turbines burn natural gas instead of kerosene as in aeronautical gas turbines. As for aeronautical gas turbines, the combustion chamber can be a CAN, CAN-annular or annular technology (see Fig. 1.3). Several small-size turbines are also powered by a single burner.

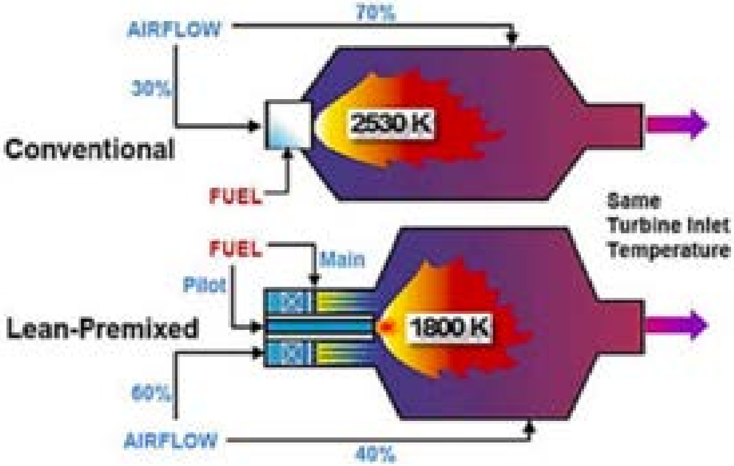

Figure 1.4 – Comparison of non-premixed and lean-premixed injection schemes. Figure reproduced from [14].
.

Figure 1.5 – Illustration of the CAN-annular General Electric 9F.03 gas turbine producing 265 MW electrical power.

In the last decades, several combustors operated with lean CH_4/air mixtures has been developed to increase efficiency and reduce pollutant emissions. The difference with conventional non-premixed systems is illustrated in Fig. 1.4. Due to lean premixed combustion, less air dilution is needed to reach the same combustion chamber exit temperature compared to non-premixed combustors. These systems are subject to thermo-acoustic instabilities but are able to produce very low NOx emissions with efficiencies higher than 60% [15]. These high efficiencies are achieved thanks to bulky and heavy systems which are difficult to adapt to aeronautical turbines. An illustration of the CAN-annular General Electric 9F.03 gas turbine is provided in Fig. 1.5. This gas turbine produces 265 MW electrical power.

1.2.3 Hydrogen gas turbine technologies

To decarbonize the industry, technologies of gas turbines are developed to burn free-carbon or low-carbon fuels. A historical development is the Tupolev Tu-155 shown in Fig. 1.6, a Russian aircraft burning hydrogen as fuel. The demonstrator engine Kuznetsov NK-89 is supplied with liquid hydrogen stored in additional fuel tanks installed inside the plane as shown in Fig. 1.6.b. This prototype was tested in flight in 1988, but was never commercialized. Nowadays, EU and France are pushing to adapt or develop new gas turbines burning carbon free fuels, as hydrogen or ammonia [16, 17]. Ammonia is easier to transport because it is a liquid fuel at conditions close to atmospheric conditions but ammonia flames have a low reactivity and produce unacceptable NOx emissions levels [18].

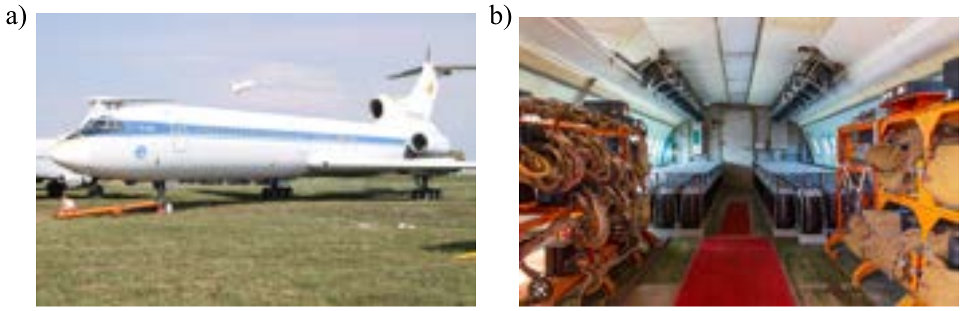

Figure 1.6 – (a) Picture of the prototype Tupolev Tu-155 equipped with the Kuznetsov NK-89 hydrogen gas turbines. (b) Additional cryogenic hydrogen tanks installed inside the cabin of the Tupolev Tu-155.

Since the end of the 20th century, new concepts of hydrogen fuelled aircrafts have been investigated by Airbus, Daimler-Chrysler and NASA, but so far they have not reached the state of a demonstrator as the Tupolev Tu-155. In the last decade, the concept of hydrogen fuelled gas turbines re-appeared initially for gas turbine power generation. New generations of power generation gas turbines are able to burn fuel blends with hydrogen up to a certain fraction which were reviewed in [19].

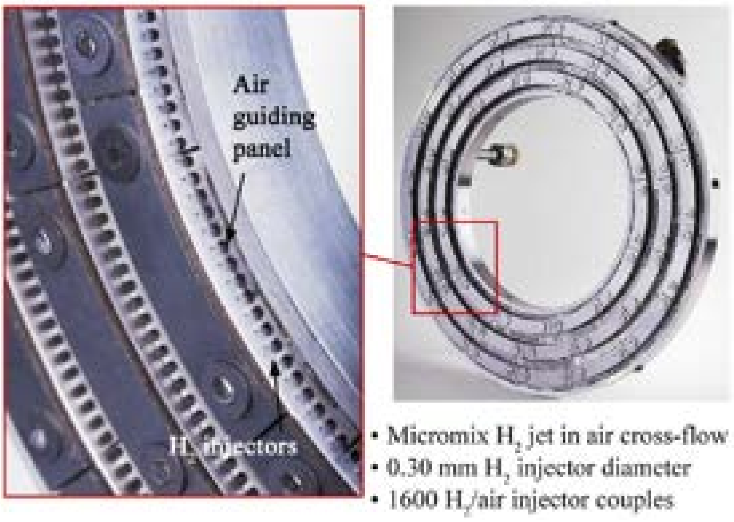

Figure 1.7 – Illustration of the Micromix prototype injector for gas turbine Honeywell/Garrett Auxiliary Power Unit APU GTCP36-300. Figure reproduced from [20].

These turbines are based on similar technologies as natural gas powered gas turbines. New concepts of injectors have also been developed in the last decades. The most advanced technology is the Micromix injector [21], which consists in injecting hydrogen perpendicular to the air stream as a jet-in-cross flow through several small holes as indicated Fig. 1.7. It has already been tested in small size gas turbines, but requires large modifications of the combustion chamber design of current gas turbines.

For aeronautic applications, GE, Safran and Rolls-Royce have recently started to develop aeronautical

Figure 1.8 – Adapted Rolls-Royce AE 2100-A regional aircraft engine for hydrogen combustion recently tested by Rolls Royce in collaboration with EasyJet [13].

gas turbines fuelled with pure hydrogen. A turboprop fueled by hydrogen shown in Fig. 1.8 was recently successfully tested by Rolls Royce in collaboration with EasyJet. The turbine is an adaptation for hydrogen combustion of the Rolls-Royce AE 2100-A regional aircraft engine.

1.3 Swirled flows

All injectors used in gas turbine combustors exploit the features of swirled flows. As consequence, investigations of swirled flows is an important topic in fluids mechanics. Imparting a swirl to the inlet flow, typically the air flow, allows to stabilize flames on a large range of operating conditions and leads to more compact flames [22]. This allows to enlarge the operability range of the systems and reduce the volume of the combustion chamber. The swirl number quantifies the angular momentum conferred to the rotating flow with respect to the axial momentum. In a cylindrical injection tube and neglecting the pressure effect, the swirl number S is defined by Gupta *et al.* [23] as:

$$S = \frac{G_\theta}{R_e G_z} = \frac{1}{R_e} \frac{\int_{R_i}^{R_e} u_\theta u_z r^2 dr}{\int_{R_i}^{R_e} u_z^2 r dr} \tag{1.1}$$

where R_i and R_e denote respectively the inner and outer radius of the injection tube, u_θ and u_z denote respectively the azimuthal and axial velocities at the outlet of the injection tube. The swirl number can be estimated analytically with certain assumptions on the shape of the azimuthal and axial velocity profiles [24]. Several swirler technologies have been developed [25].

Without swirl, it is difficult to stabilize turbulent flames away from the sidewalls when the thermal power increases. In the worth case, the flame blows-off when the characteristic time of the flow becomes too small compared to the chemical time [26]. The poor degree of mixing when the injection velocities are high [27] and the increase of flame size with the thermal power [28] are other common issues. These issues are considerably lowered when a swirl is imparted to the annular air channel. It increases the turbulence intensity due to the increase of the shear of the jet flow leading to a better mixing. It also leads to a reversal flow along the burner axis due to an adverse pressure gradient [25, 29]. These features are illustrated by the variation of the flame length presented in Fig. 1.9 reproduced from Chen *et al.* [22].

These observations are the result of the influence of the swirl on the flow structure. The sudden apparition of a large Central Recirculation Zone (CRZ) is clearly visible in Fig. 1.9.c for a swirl level $S = 0.25$, leading to a transition of the flame from a jet-like regime in Fig. 1.9.a to a swirled stabilized regime in Figs. 1.9.c to 1.9.e.

In a swirled flow, when the transverse pressure gradient created by the swirl motion becomes so high,

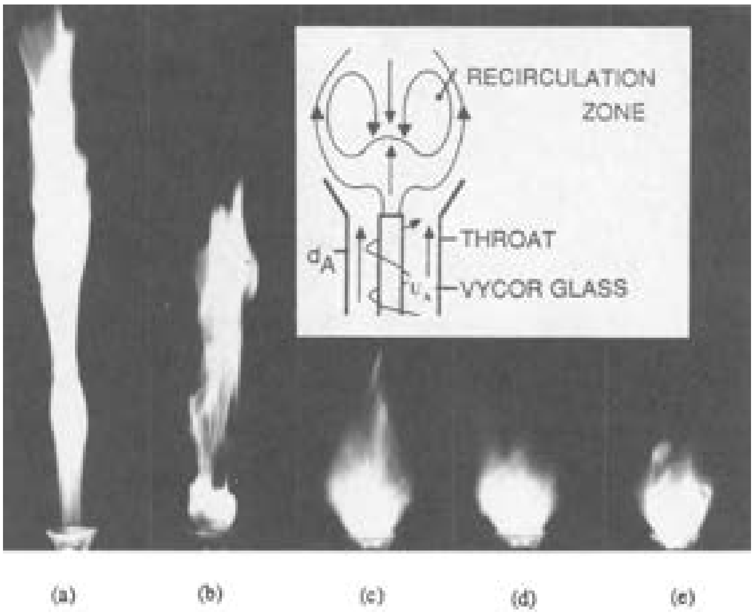

Figure 1.9 – Illustration of the effect of swirl on methane/air flame length. (a) $S = 0.0$ (no swirl). (b) $S = 0.2$. (c) $S = 0.25$. (d) $S = 0.5$. (e) $S = 1.1$. Figure reproduced from [22].

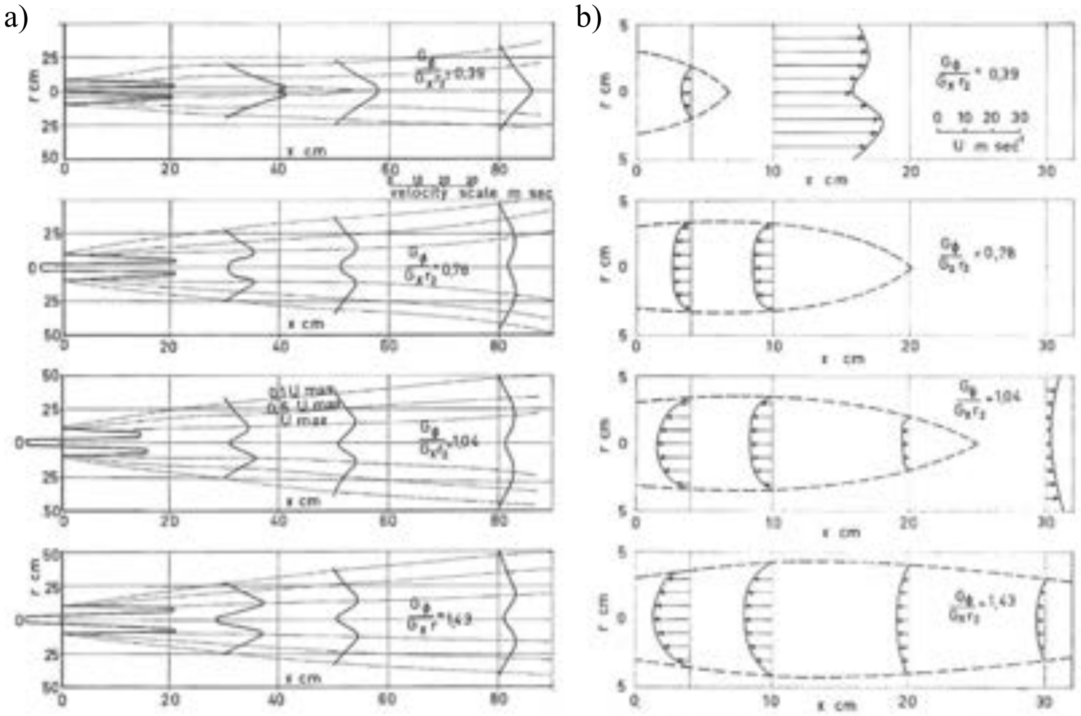

Figure 1.10 – Development of the Central Recirculation Zone (CRZ) increasing the swirl number. From top to bottom: $G_\theta/(G_x r) = 0.39$ to $G_\theta/(G_x r) = 1.43$. (a) Mean axial velocity profiles. (b) Central recirculation zone (CRZ) with mean recirculation velocity profiles. Figure reproduced from [30].

a vortex breakdown occurs and a CRZ is created [31]. The development of the CRZ is illustrated in Fig. 1.10. From top to bottom, the swirl number of the isothermal flow is increased from $G_\theta/(G_x r) = 0.39$ to $G_\theta/(G_x r) = 1.43$, where G_θ and G_x are respectively the angular and axial momentum of the flow and r the radius of the burner outlet. In the top row of Fig. 1.10, for $G_\theta/(G_x r) = 0.39$, a small CRZ appears at the outlet of the injector but disappears slightly further downstream. Increasing $G_\theta/(G_x r)$, the length and the intensity of the central recirculation zone increases.

Swirled flows are also often accompanied by helical hydrodynamic instabilities like the Precessing Vortex

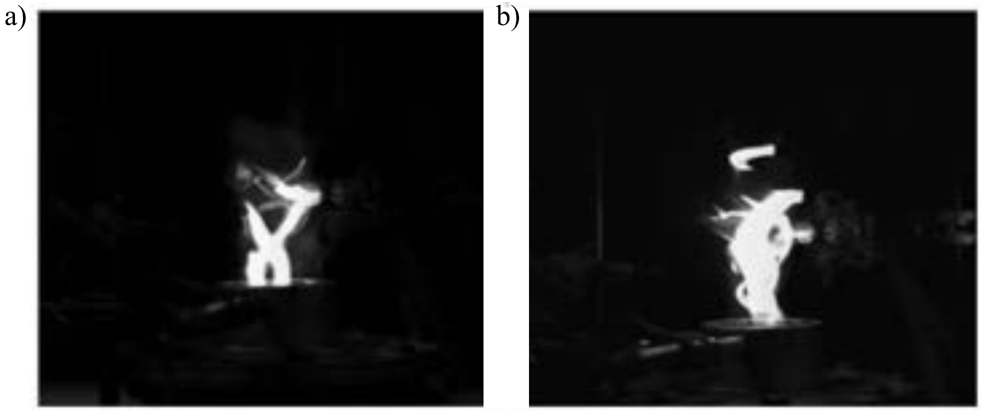

Figure 1.11 – Experimental visualization of double precessing vortex core (PVC) instabilities. (a) Pair of strong precessing vortex cores. (b) Bifurcation from stable flow to a double precessing vortex core. Figure adapted from [32].

Core (PVC) that as been extensively studied [33]. This hydrodynamic instability develops in the shear layer between the main flow and the central recirculation zone [23, 25, 33, 34]. It is a strong coherent helical structure that develops in the shear layer on the external side of the central recirculation zone [33]. Consequently, unsteady structure of the CRZ is in this case no longer axisymmetric. The structure of PVC has been studied experimentally [35–37], analytically [36, 38] and numerically [39, 40]. It can be a single or a double helical structure [41]. In Fig. 1.11, an experimental visualization of a double helical structure is shown. In Fig. 1.11.a, the PVC is installed, the transition is shown in Fig. 1.11.b.

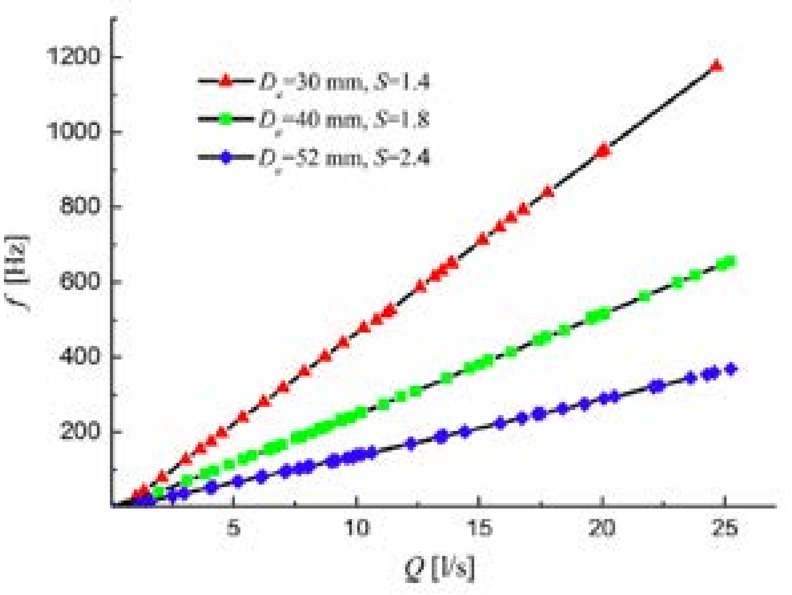

Figure 1.12 – Variation of the PVC frequency plotted against the volumetric flowrate for different swirl numbers and injector outlet diameters. Figure reproduced from [42].

This hydrodynamic instability has a strong impact on flame stabilization [43–45], mixing [43], flashback [46, 47] and also combustion instabilities [34, 48]. The frequency of the PVC is linearly related to the swirl number and the bulk velocity [42, 49] as shown in Fig. 1.12. But switching from non-reacting to reacting conditions leading to strong density gradients across the flame can suppress the PVC instability [38].

1.4 Hydrogen and methane/hydrogen flames

The transition to hydrogen combustion devices needs to adapt the burners to the singular properties of hydrogen flames. First, compared to classical hydrocarbon fuels, as natural gas or oil, the laminar and turbulent flame speeds of hydrogen flames are much higher [50]. The laminar burning velocity increases with the hydrogen content in CH_4/H_2/air flames in atmospheric conditions as shown in Fig. 1.13.a. The adiabatic flame temperature increases too with X_{H2}^f (Fig. 1.13.b) [50].

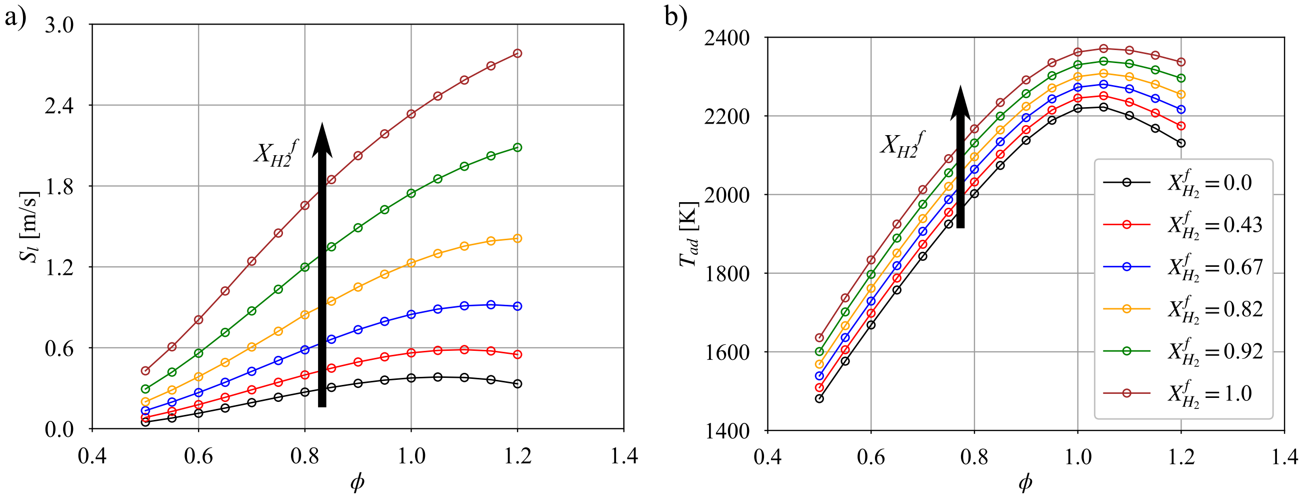

Figure 1.13 – (a) Laminar burning velocity of CH_4/H_2 blends for different H_2 contents plotted against the equivalence ratio ϕ. (b) Adiabatic flame temperature for different H_2 contents plotted against the equivalence ratio ϕ. The values are calculated with Cantera with the San Diego kinetic mechanism [51] for freely propagating premixed flames at $p = 1$ atm and $T = 300$ K.

This high reactivity leads to an increase propensity of hydrogen or hydrogen enriched flames to flashback in premixed burners [52–54]. Increasing the hydrogen content, the Markstein length of CH_4/H_2/air flames also globally decreases [50]. In real combustors, this increase of flame temperature substantially increases the thermal flux on the solid parts of the combustion devices.

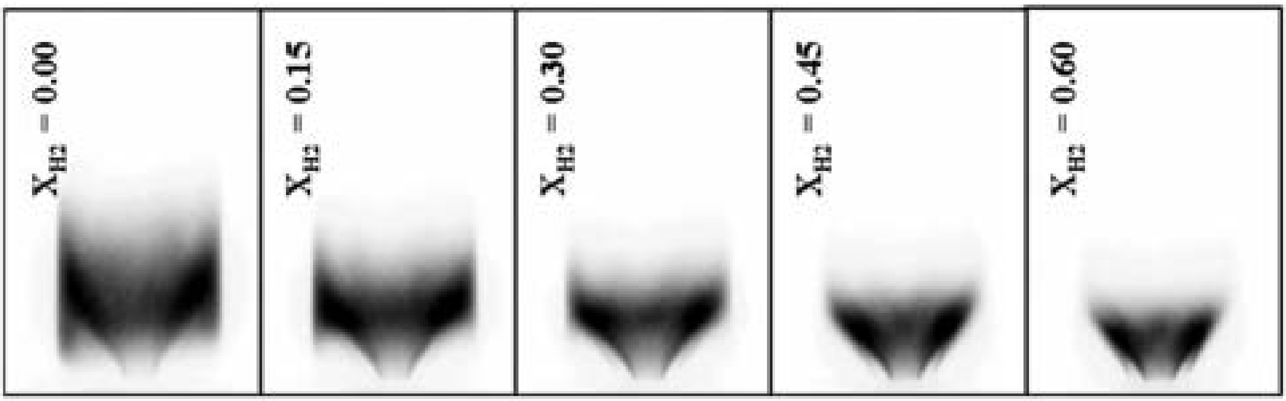

Figure 1.14 – CH* pictures of CH_4/H_2/air premixed flames increasing the hydrogen content in the mixture. The inlet reactants are preheated to $T = 473$ K, the bulk flow velocity is set to $u = 60$ m/s and the equivalence ratio to $\phi = 0.6$. Figure reproduced from Kim *et al.* [55].

These properties lead to increased flame surface densities [56], with more compact flames [55]. The effect of the increase of the flame speed and the flame surface density is particularly visible in premixed CH_4/H_2/air flames as shown in Fig. 1.14. Increasing the hydrogen content in the CH_4/H_2/air mixture leads, for a fixed equivalence ratio and bulk velocity, to a reduction of the flame height.

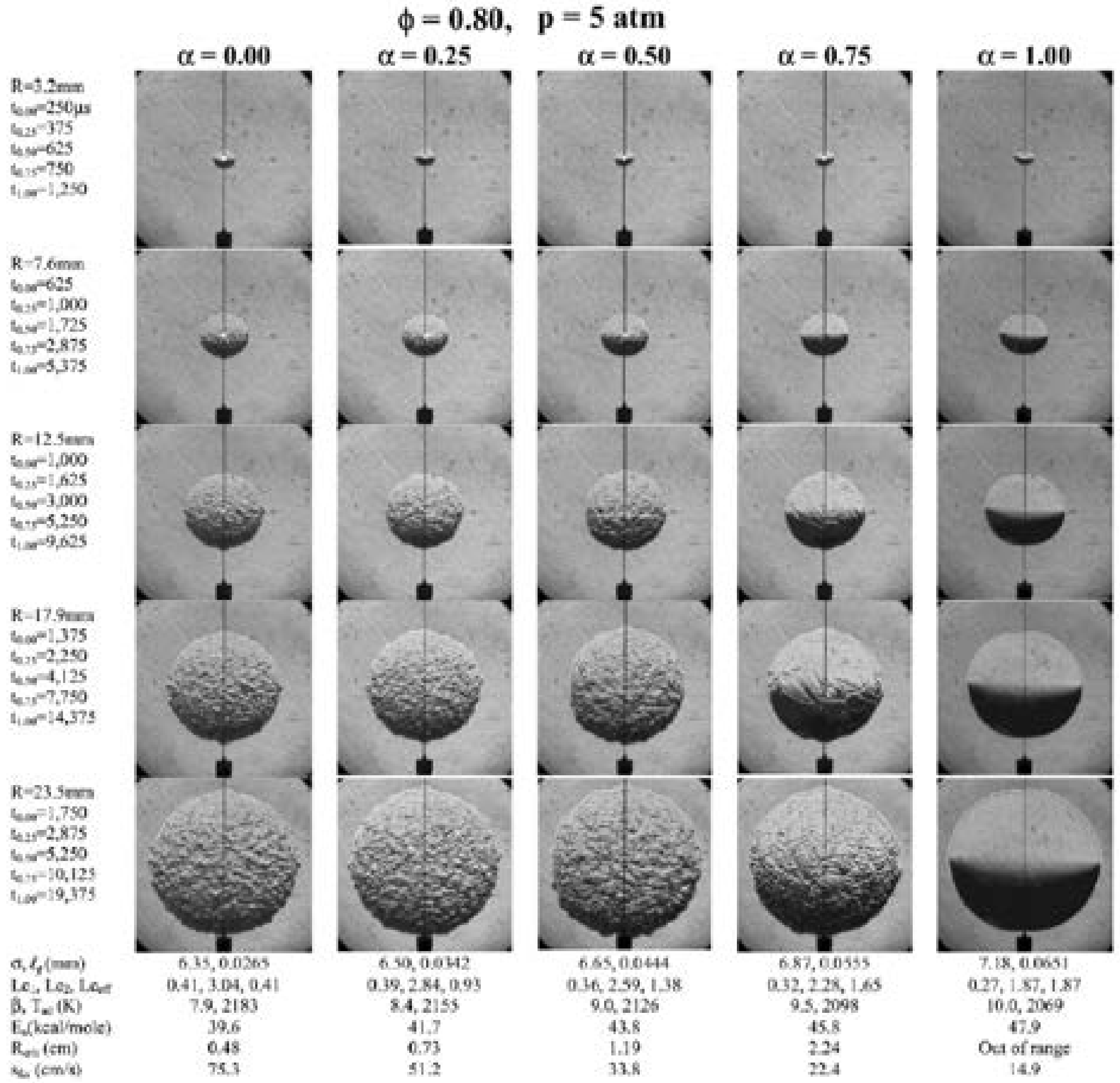

Figure 1.15 – Schlieren pictures of spherical hydrogen/propane flames expending in a combustion chamber with an overall pressure $p = 5$ atm. The parameter α denotes the content of propane in the initial mixture ($\alpha = 0$: hydrogen flame, $\alpha = 1$: propane flame) and the equivalence ratio of the mixture is set to $\phi = 0.8$. Figure reproduced from Law *et al.* [57].

Hydrogen is the smallest stable molecule of the universe. Its diffusivity is much higher than all others. This high diffusivity leads to preferential diffusion effects in CH_4/H_2/air mixtures [56, 58] and then to equivalence ratio inhomogeneities [59].

Thermo-diffusive instabilities are observed in lean hydrogen flames [57, 60]. Figure 1.15 shows that these instabilities increase with the hydrogen content in the fuel mixture and the operating pressure. The flammability limits of hydrogen/air mixtures are also hugely increased compared to hydrocarbon fuels [61]. As a consequence, hydrogen flames have the particularity to resist to very high strain rates before extinction [61].

1.5 NOx emissions

Hydrogen flames do not release CO_2 but they produce other pollutants. Nitrous oxides are pollutant emissions produced by combustion processes. They are toxic and cause damage to the respiratory system and asthma. They are also responsible for smog and ozone in urban air and acid rains. Moreover when they are emitted in the stratosphere, by an aircraft for example, nitrous oxides attack the ozone layer and increase ultraviolet radiations. NOx emission levels are generally presented as the summation of the concentrations of NO and NO_2, because most of NO is transformed in NO_2 later in the atmosphere. NO concentration in the burnt gases is generally much more important than NO_2 [62]. Several routes for NOx formations have been identified including thermal (Zeldovich), prompt (Fenimore), N_2O, NNH and fuel-bound nitrogen [63–66].

In most combustors, the predominant route is generally the Zeldovich mechanism. Thermal NOx formation can be described by three chemical kinetic steps [65]:

$$\begin{aligned} \mathrm{O} + \mathrm{N_2} &\leftrightarrows \mathrm{NO} + \mathrm{N} \\ \mathrm{N} + \mathrm{O_2} &\leftrightarrows \mathrm{NO} + \mathrm{O} \\ \mathrm{N} + \mathrm{OH} &\leftrightarrows \mathrm{NO} + \mathrm{H} \end{aligned} \tag{1.2}$$

NOx formation through the Zeldovich pathway only takes place at high temperature [62]. The initiation of the chemical reactions is due to the oxidation of N_2 molecules present in air.

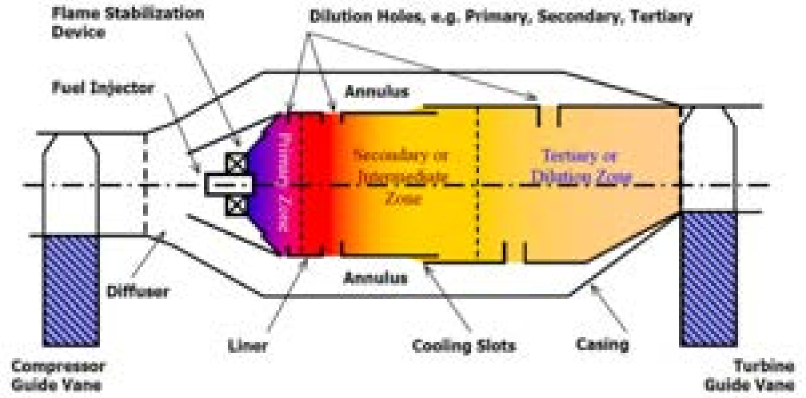

Figure 1.16 – Illustration of the dilution of combustion products with fresh air injected through holes in the combustion chamber walls. Figure reproduced from El-Hossaini *et al.* [67].

Several technologies have been developed to reduce thermal NOx production. They generally consist in decreasing the burnt gas temperature right out the combustion zone with the objective to reduce as much as possible the zone where the gas temperature is high, typically greater than 1800 K [68]. One simple system is to dilute the combustion products with air injected through several small holes in the combustion chamber walls as shown in Fig. 1.16.

Prompt NOx formation is described by the following two steps chemical kinetic mechanisms [65]:

$$\begin{aligned} \mathrm{CH} + \mathrm{N_2} &\leftrightarrows \mathrm{HCN} + \mathrm{N} \\ \mathrm{HCN} + \mathrm{O} &\leftrightarrows \mathrm{NCO} + \mathrm{H} \end{aligned} \tag{1.3}$$

Prompt NO cannot take place in pure hydrogen systems. The formation of NOx through the Fenimore pathway is initiated by CH^* radicals, and cannot consequently take place for hydrogen flames.

Another NOx formation way is the N_2O route, first described by Sarofim *et al.* [69] and later by Li *et al.* [65], described by:

$$\begin{aligned} \mathrm{N_2O} + \mathrm{M} &\leftrightarrows \mathrm{N_2} + \mathrm{O} + \mathrm{M} \\ \mathrm{N_2O} + \mathrm{H} &\leftrightarrows \mathrm{N_2} + \mathrm{OH} \\ \mathrm{N_2O} + \mathrm{O} &\leftrightarrows 2\mathrm{NO} \\ \mathrm{N_2O} + \mathrm{OH} &\leftrightarrows \mathrm{N_2} + \mathrm{HO_2} \end{aligned} \tag{1.4}$$

They may be significant at low temperatures and high pressure. More recently, a new route for NOx formation has been identified [66, 70–72]:

$$\begin{aligned} \mathrm{NNH + OH} &\leftrightarrows \mathrm{NH_2 + NO} \\ \mathrm{NH + O} &\leftrightarrows \mathrm{NO + H} \\ \mathrm{HNO + H} &\leftrightarrows \mathrm{NO + H_2} \\ \mathrm{HNO + OH} &\leftrightarrows \mathrm{NO + H_2O} \end{aligned} \tag{1.5}$$

In the case of hydrogen flames, the NOx formation through the Zeldovich pathway is preponderant [73]. Two parameters have been identified as important to describe the NOx emission levels through the Zeldovich pathway: the adiabatic flame temperature [52] and the residence time of the burnt gases in a hot zone (typically greater than 1800 K [68]), defined as the residence time in the flame [73, 74] or in the combustion chamber [75]. It is also convenient to convert NOx concentration into the mass of NOx released by unit of fuel mass. This index is denoted EINOX, and is defined for CH_4/H_2 mixtures as:

$$EINOX = 1000 \frac{\left(2 - X^f_{H2} / \left(X^f_{H2} + X^f_{CH_4}\right)\right) M_{NO_2} X_{NO}}{X_{H_2O} M_{Fuel}} \tag{1.6}$$

where X^f_{H2} is the hydrogen molar fraction in the fuel and M_{NO_2} and M_{Fuel} are respectively the molar weight of NO_2 and fuel. This index, normalized by the residence of burnt gases in the flame, is shown in many studies to scale with the power $-1/2$ of the residence time [73, 76].

1.6 Flame stabilization

Understanding the physical mechanisms driving flame stabilization is a main issue in the combustion scientific community. Several models have been proposed to explain the stabilization of lifted turbulent flames [77]. Vanquickenborne and van Tiggelen [78] argued that for lifted flames, fuel and oxidizer mix before ignition and the flame stabilizes on the stoichiometric line where the local flow velocity is equal to the turbulent flame speed. Another hypothesis is that the stabilization of lifted turbulent flames results from local flame extinction due to the quenching of laminar flamelets when the local value of the scalar dissipation rate falls below a critical threshold [79]. According to Byggstøyl and Magnussen [80], stabilization is controlled by local flame extinction at the smallest turbulence scales. For 20 years, a consensus has however been reached about the mechanisms leading to flame re-anchoring: the beginning of the lifted reaction zone is seen as an edge flame that propagates against the flow along the stoichiometric line [81] to reach a stabilization point, typically located at the injectors lips [82].

Edge flames are illustrated in Fig. 1.17. They were extensively studied in the last 20 years [84]. The most well-known is the idealized triple flame [83, 85]. Muñiz and Mungal [86] revisited the Vanquickenborne and van Tiggelen [78] model considering the leading-edge flame speed instead of the turbulent flame speed. In their experiments, they found that the leading-edge reaction front of a lifted flame can propagate towards the injector lips if the local velocity along the stoichiometric line connecting the flame to the injector is lower than the triple flame speed. Further experiments [87] have shown that the local velocity at the base of the leading edge flame is bounded by $3S_l$, where S_l is the laminar burning velocity at the equivalence ratio for which S_l is maximum. Figure 1.18 is reproduced from Muñiz and Mungal [86] and illustrates these observations.

In [83, 85], the authors concluded that leading-edge flames, which have similar characteristics than triple flames, are more consistent to describe flame re-anchoring than any models based on a turbulent flame speed. Ruetsch *et al.* [88] derived a relation to estimate the theoretical value of the propagation velocity of a triple flame. Cha and Ronney [83] measured the propagation speed of non-premixed edge flames for different fuels and different oxidizer dilutions and found that the relation proposed by Ruetsch *et al.* [88] corresponds for most cases to the maximum displacement speed reached by edge flames, except for CO_2 diluted mixtures. Results from Cha *et al.* [83] for $CH_4/O_2/N_2$ flames with $Z_{st} = 0.5$ are reproduced in Fig. 1.19. The measured

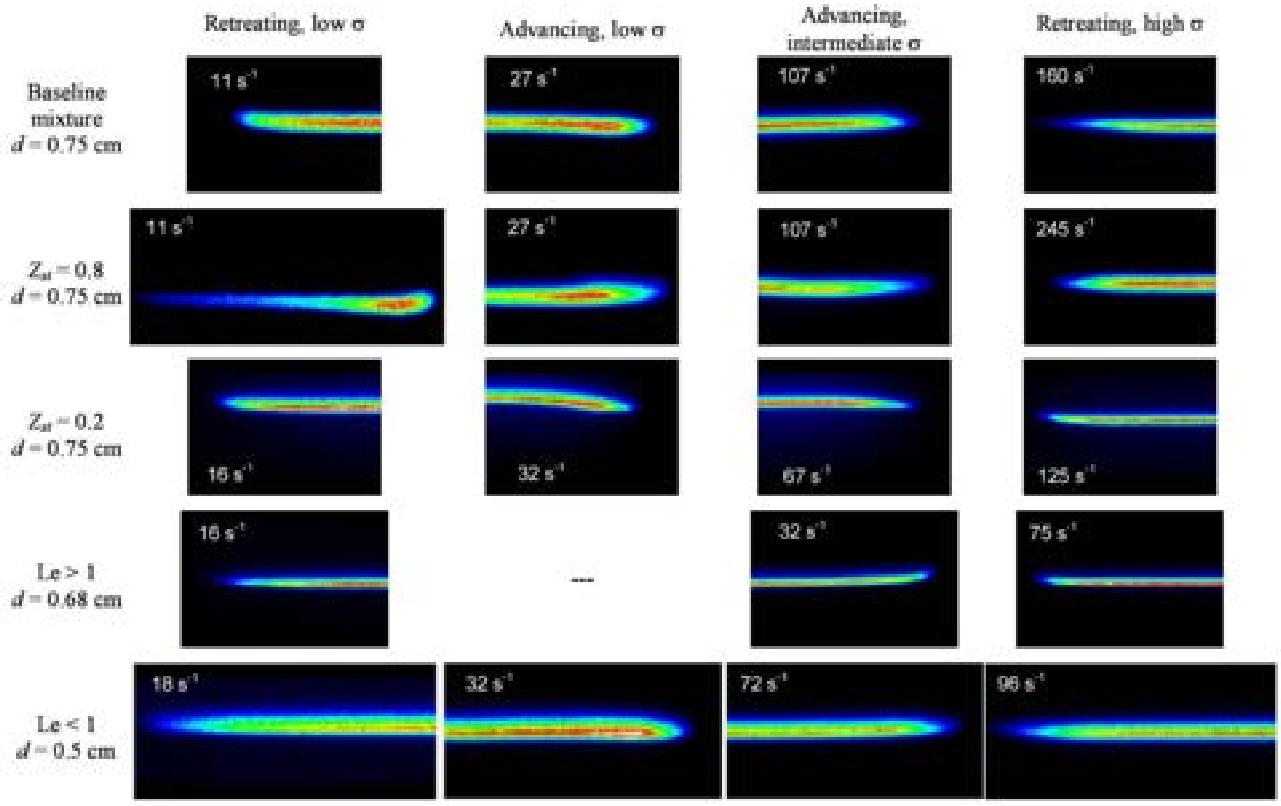

Figure 1.17 – $CH_4/O_2/N_2$ edge flame visualization for different strain rate σ, stoichiometric mixture fraction Z_{st} and Lewis number Le. Figure reproduced from Cha *et al.* [83].

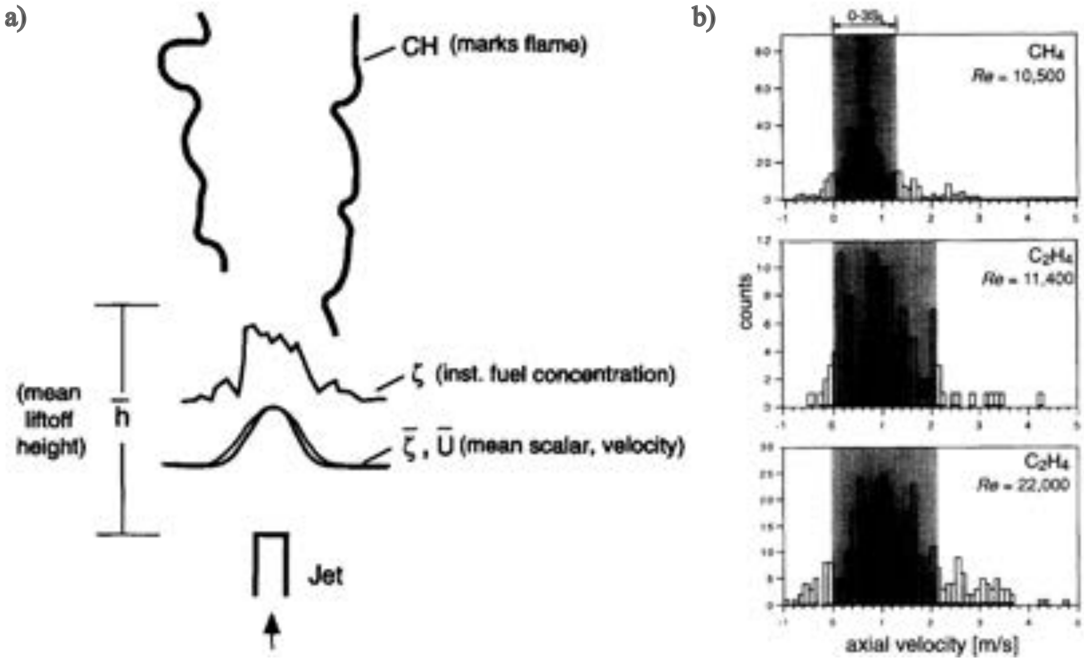

Figure 1.18 – (a) Sketch of velocity and scalar profiles measured in lifted-jet diffusion flames. (b) Histogram of the measured edge flame speed for CH_4 and C_2H_4 flames. Figure adapted from Muñiz and Mungal [86].

edge flame speed non-dimensionalized by the theoretical triple flame speed from [88] is plotted against the non-dimensionalized flame thickness ϵ. For intermediate values of ϵ, the measured edge flame speed is approximately equal to 0.8, i.e. a value slightly lower than the theoretical triple flame speed.

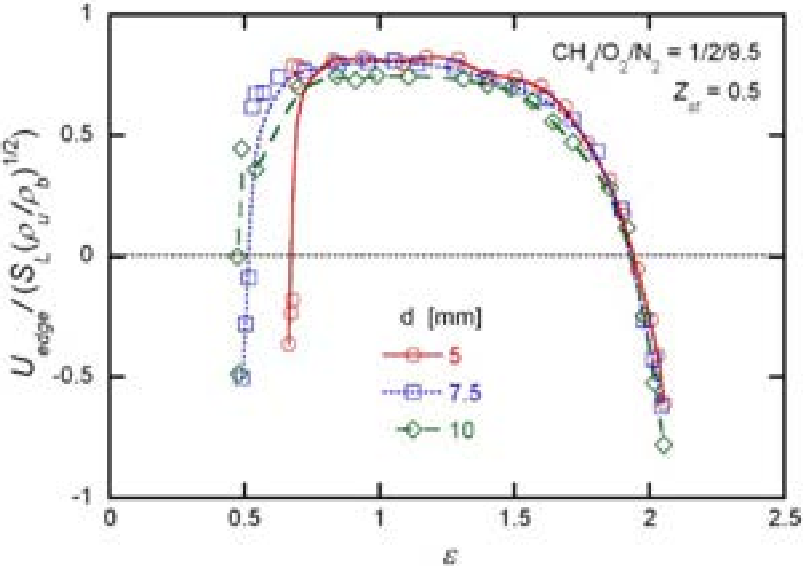

Figure 1.19 – Measured edge flame speed non-dimensionalized by the theoretical triple flame speed from Ruetsch *et al.* [88] plotted against the non-dimentionalized flame thickness ϵ. Figure reproduced from Cha *et al.* [83].

Further experiments have been conducted to unveil the different stabilization regimes of turbulent flames above coaxial injectors. These studies are generally carried out with a small air co-flow and without swirl. Brown *et al.* [87] confirm that the velocity of the leading edge of a lifted flame is in most cases bounded by $3S_l$. But for some cases, they observed that this local velocity better scales with a turbulent burning velocity S_T. Joedicke *et al.* [89] confirmed these observations for hydrocarbons lifted flames and highlighted the triple flame structure of the leading edge front in their experiments. They also showed that the flame leading edge does not exactly coincide with the location of the stoichiometric line, but lies on a line $Z \simeq 1.1Z_{st}$, where Z is the mixture fraction passive scalar and Z_{st} its stoichiometric value. Guiberti *et al.* [90] confirmed these observations using advanced laser diagnostics varying the pressure inside the combustion chamber. They identified two regimes. For unperfect mixing of air and oxidizer streams, the stoichiometric line is present at the axial location of the flame base and the local flow velocity of the leading edge of the lifted flame is slightly above $3S_l$. When premixing of the oxidizer and fuel streams is sufficiently advanced, this line does not exist anymore and combustion takes place in premixed conditions. In this latter case, the local velocity of the leading edge front is roughly equal to S_T, a turbulent flame speed estimated from empirical correlations. This last regime is observed above a critical value of the air co-flow velocity in their setup.

1.7 Motivations and content of the thesis

This work is motivated by the need of a safe, low-emission and low-cost hydrogen injector for gas turbines funded by the ERC advanced grant SCIROCCO no. 832248 (cerfacs.fr/SCIROCCO). A new injector was developed at IMFT in collaboration with Safran. The system is a coaxial injector with swirl inside both internal and annular channels used to inject hydrogen and air respectively. Work has started at the beginning of this thesis at TRL 0 (concept) to reach TRL 4 (with proof of the concept tested with laboratory scale prototype) at the end of this work. The manuscript is organized as follow.

Chapter 2: Experimental tools

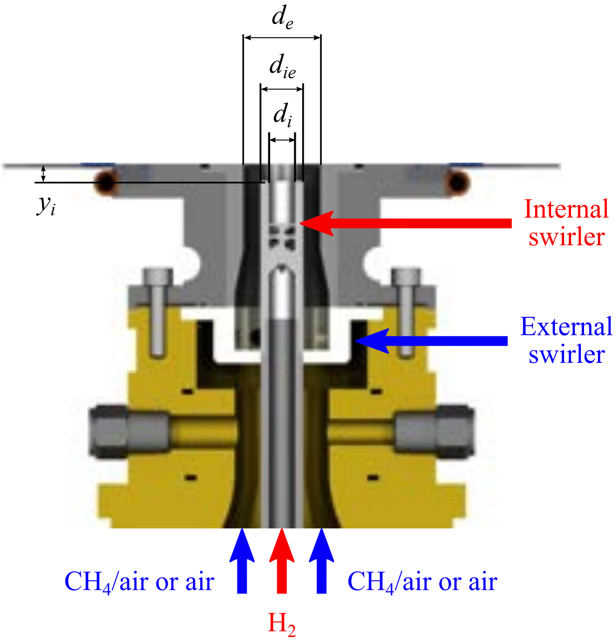

Chapter 2 describes the burner and the coaxial injectors used in this work. The external swirl level S_e is fixed for all experiments and the swirl number in the central channel S_i is varied. Two fuel injection strategies are considered. The first one, called DFDS for Dual Fuel Dual Swirl injector is powered by a CH_4/air mixture in the annular channel and hydrogen flowing inside the internal channel. The second one, called HYLON for HYdrogen LOw Nox injector has only air injected in the annular channel with here hydrogen through the central lance. The results gathered on a set of prototypes are presented in Chapter 3 to Chapter 7.

Chapter 3: Flame stabilization regimes

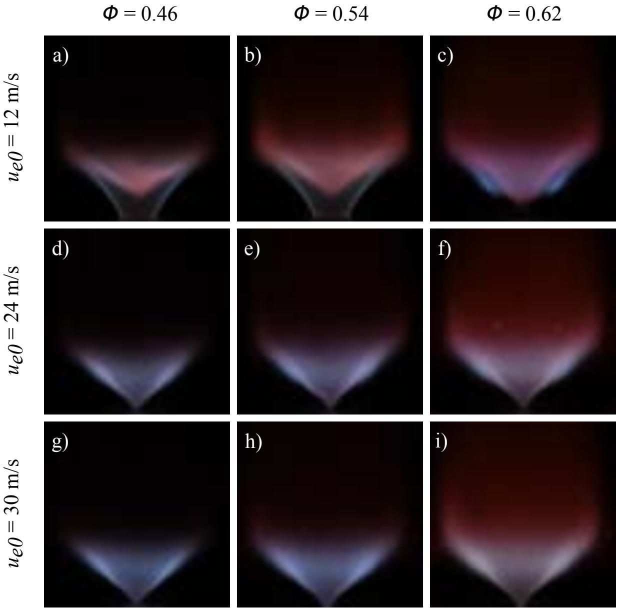

A parametric analysis is first conducted in Chapter 3 to identify the different flame stabilization regimes for the DFDS and HYLON injectors. Flame images in the visible and UV spectrum are used to highlight the influence of the hydrogen content X^f_{H2} in the CH_4/H_2 global fuel mixture, the inner swirl level S_i, the injector recess distance y_i between the outlet of the internal and external coaxial channels and the injection velocities u_e and u_i in the annular and central channels. The influence of these parameters is further analyzed to determine the best configuration in order to obtain aerodynamically stabilized flames over the largest range of operating conditions. These configurations are then determined for H_2/air flames produced with the HYLON injector for several combinations of inner swirl level S_i and hydrogen injector recess y_i.

Chapter 4: Cold flow velocity field

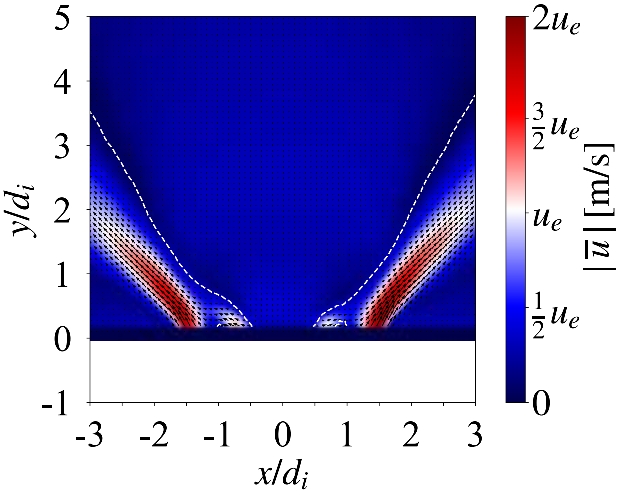

The aerodynamic stabilization of lifted flames is shown to be controlled by the structure of the velocity field near the burner outlet. In Chapter 4, the influence of each parameter studied in Chapter 3 is investigated using PIV measurements of the mean and RMS values of the velocity fields in cold flow conditions. The hydrogen flowrate in the central channel is initially replaced by air. Two strategies are compared: replacing the hydrogen flowrate by air keeping constant (i) the impulsion ratio J and (ii) the central injection velocity u_i. The second strategy is selected for reasons explained in Chapter 7. Additional experiments are then conducted with helium that has a molar weight closer to that of hydrogen in order to better reproduce the velocity field when hydrogen is injected through the central lance. These measurements are used to explain the observations made in Chapter 3. For two selected operating conditions, the presence of PVC instability in the cold flow is also finally studied.

Chapter 5: Cold flow mixing

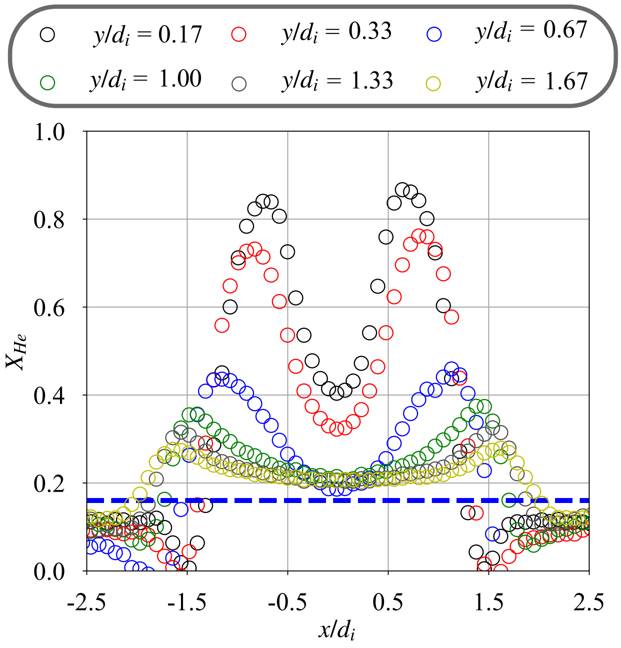

Mixing of hydrogen and air is then investigated for both the DFDS and HYLON injector configurations. In Chapter 5, a Raman scattering optical system is used to investigate how the two streams mix in cold flow conditions. As for the cold flow velocity measurements made in Chapter 4, hydrogen is replaced by helium in most experiments for safety reasons. The influence of the inner swirl level S_i is considered first. The impact of the velocity ratio $r_u = u_e/u_i$ and the density ratio $r_\rho = \rho_e/\rho_i$ is then analyzed. A model based on [91] is revisited and adapted to the case of dual swirl injectors. A mixing progress parameter η is deduced and compared to experimental measurements.

Chapter 6: Hot flow analysis

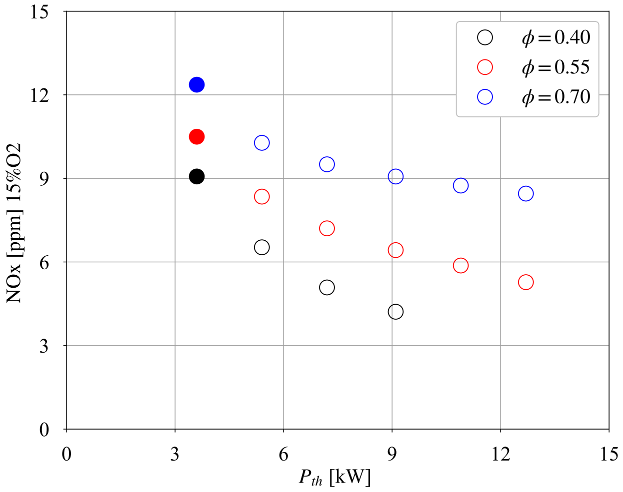

In Chapter 6, performances of the two injectors are examined in reactive conditions. For three selected operating conditions, the structure of the velocity field, the thermal boundary conditions, the burnt gas temperature at several locations and NOx emissions are measured. The effect of heat release on the structure of the flow field is first highlighted. The thermal boundary conditions for the three selected flames are then obtained for use in companion numerical flow simulations [92]. These boundaries include the temperatures of the metallic and quartz combustion chamber walls but also the burnt gases temperature at the outlet of the combustion chamber and in the ORZ. NOx and CO emissions are then determined for a large range of operating conditions. A scaling law is finally proposed to reduce the NOx emissions from H_2/air flames. The database created is made available to feed numerical flow simulations and has been proposed for a test case in the TNF database (tnfworkshop.org/data-archives).

Chapter 7: Modeling of flame re-anchoring

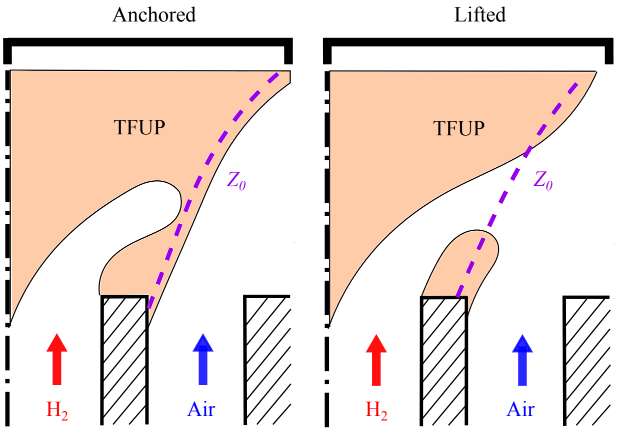

A low order model for flame re-anchoring is derived in Chapter 7. The model is called TFUP for Triple Flame Upstream Propagation. It focuses on the transitions from lifted to anchored flames, i.e. flame re-anchoring, where a leading edge flame is identified, traveling from the flame to the injector rim. The trends predicted by the model are first compared qualitatively to experimental observations. In a second time, a methodology is developed to apply this approach in a quantitative way to predict the operating conditions for which the flame should re-anchor to the injector lips. The predictions of the TFUP model are compared to the operating conditions for which the transition is observed in experiments.

This work is the first step for the design of a new H_2/air injection technology for gas turbines. It lays the foundation for future studies under more relevant thermodynamic conditions for gas turbine combustors.

1.8 Publications during the thesis

This work has led to a patent and the following publications and disseminations.

1.8.1 Scientific publications

T. Schuller, **S. Marragou**, G. Oztarlik, T. Poinsot and L. Selle, Influence of hydrogen content and injection scheme on the describing function of swirled flames, Combustion and Flame, 240: 111974, 2022.

S. Marragou, H. Magnes, T. Poinsot, L. Selle and T. Schuller, Stabilization regimes and pollutant emissions from a dual fuel CH_4/H_2 and dual swirl low NOx burner, International Journal of Hydrogen Energy, 47(44):19275–19288, 2022.

S. Marragou, H. Magnes, A. Aniello, L. Selle, T. Poinsot and T. Schuller, Experimental analysis and theoretical lift-off criterion for H_2/air flames stabilized on a dual swirl injector, Proceedings of the Combustion Institute, 39(4):4345-4354, 2023.

J. Kuhlmann, **S. Marragou**, I. Boxx, T. Schuller and W. Polifke, LES-based prediction of technically premixed flame dynamics and comparison with perfectly premixed mode, Physics of Fluids, 34(8):085125, 2022.

A. Aniello, D. Laera, **S. Marragou**, H. Magnes, L. Selle, T. Schuller and T. Poinsot, Experimental and numerical investigation of two flame stabilization regimes observed in a dual swirl H_2-air coaxial injector, Combustion and Flame, 249:112595, 2023.

A. Aniello, D. Laera, **S. Marragou**, T. Poinsot, T. Schuller and L. Selle, Influence of pilot H_2 injection on methane-air swirled flame stabilization and acoustic response, Combustion and Flame, Accepted.

H. Magnes, **S. Marragou**, A. Aniello, L. Selle, T. Poinsot and T. Schuller, Impact of air preheating on flame stabilization and NOx emissions from a dual swirl hydrogen injector, Proceedings of the ASME 2023, Accepted.

S. Marragou, H. Magnes, A. Aniello, T. Guiberti, L. Selle, T. Poinsot and T. Schuller, Modeling the stabilization regime of H_2/air flames above a coaxial dual swirl injector, Combustion and Flame, Accepted.

1.8.2 Patent

S. Richard, C. Viguier, **S. Marragou**, and T. Schuller, Dispositif d'injection de dihydrogène et d'air (FR Patent No FR2111267), Institut National de la Propriété Industrielle, 2021.

1.8.3 Public communications

During the thesis, a picture of hydrogen flame was submitted to the competition MECAPIXEL 2021 organized by CNRS. The picture presented in Fig. 1.20.a has reached the final of the public prize and has been exposed at the Academy of Sciences. Another picture was published in the magazine "Le petit illustré no.50: Europe, Regards croisés de chercheur-es." in an article on hydrogen combustion for aeronautical gas turbines as shown in Fig. 1.20.b.

VOLER DANS DES AVIONS À HYDROGÈNE ?

Nous avons tous et toutes envie de voyager et, pour aller loin, l'avion reste le premier choix. Mais les avions actuels contribuent au réchauffement climatique et le rêve est de pouvoir voler un jour dans un avion qui n'émettrait que de l'eau, c'est-à-dire dans un avion volant grâce à l'hydrogène. C'est notre sujet d'étude.

Figure 1.20 – (a) Exposition of the picture submitted to the picture contest MECAPIXEL 2021 organized by the CNRS. (b) Article on hydrogen combustion for gas turbines published in "Le petit illustré no.50: Europe, Regards croisés de chercheur-es.".

Chapter 2

Experimental tools

> “*Imagination is more important than knowledge.*”
>
> Albert Einstein

Overview

2.1 Experimental setup

2.1.1 Burner base

The experiments presented in this manuscript are carried out with the experimental test bench MIRADAS shown in Fig. 2.1 installed at IMFT [93–95]. The base of the burner corresponds to the so-called "Durox burner" installed at the EM2C laboratory [96–98].

It is composed of a mixing chamber at the bottom where the main flowrate, generally air or a mixture of air and methane, is injected radially through two opposite channels designated as "Main supply" in Fig. 2.1. This flow crosses the burner from the bottom to the top in a plenum of 64 mm diameter and 100 mm length. A perforated plate and a stack of three honeycomb grids are placed in order to break the largest turbulent structures and to condition the flow axially. The diameter of the plenum is reduced from 64 mm to 22 mm using a convergent section of 75 mm length. A fuel supply channel is introduced at the top of the plenum using two radial tubes from the external side of the plenum to the burner axis that are connected to the central fuel injector corresponding to the "Secondary supply" in Fig. 2.1. The distance between the outlet of the central tube and the outlet of the annular channel can be adjusted as described in the next section. A small straight extension section of 22 mm diameter is installed at the top of the convergent section to allow the installation of a microphone, a hot-wire and a thermocouple.

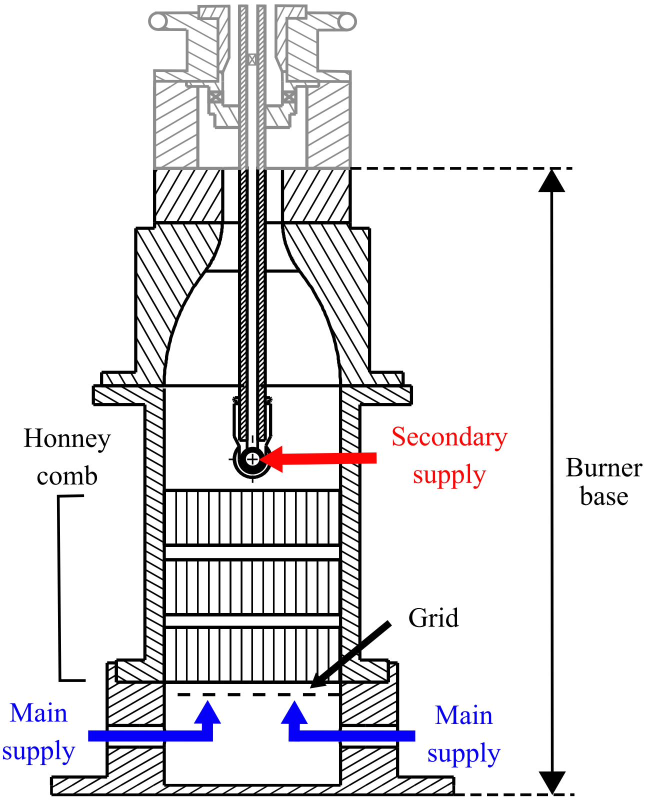

Figure 2.1 – Schematic of the burner base of the MIRADAS test bench.

Different injectors can be installed at the top of the burner base. The one shown in Fig. 2.1 corresponds to the HYLON injector that is described in the next section.

2.1.2 Injectors

The injectors used in this study are described in Fig. 2.2. The first one in Fig. 2.2.a is a coaxial dual swirl injector called DFDS for Dual Fuel Dual Swirl injector and burns CH_4/H_2/air mixtures. The second one shown in Fig. 2.2.b has the same geometry but only burns hydrogen. This version is called HYLON for HYdrogen LOw Nox and burns H_2/air mixtures.

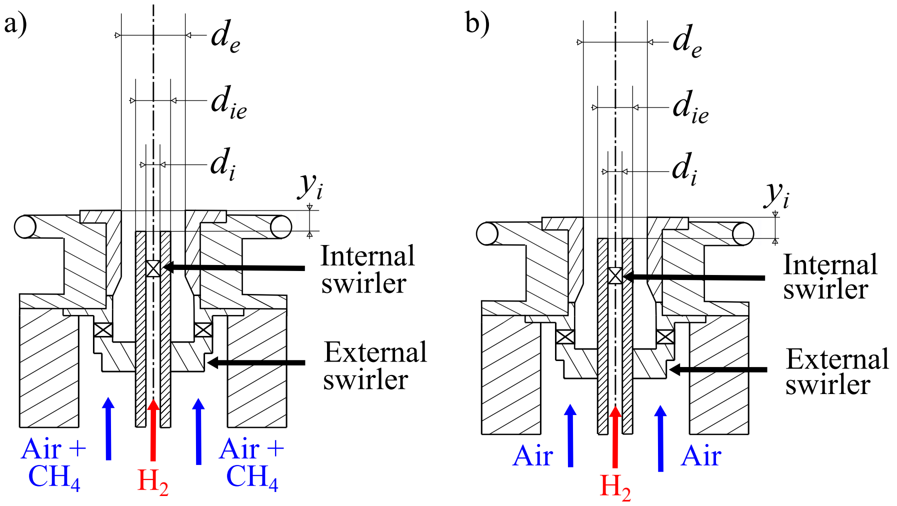

Figure 2.2 – Injectors used on the MIRADAS test bench for this study. (a) DFDS injector for CH_4/H_2/air combustion. (b) HYLON injector for combustion of H_2/air combustion.

Experiments with H_2/CH_4/air blends are carried out with the DFDS injector [95]. The geometry is shown in Fig. 2.2.a. This injector is coaxial. A methane and air mixture flows through the external channel, also called annular channel. Pure hydrogen is injected through the central channel. Both annular and central channels are swirled. The swirl motion is conferred to the annular CH_4/air flow with a radial swirler installed 42 mm below the annular channel outlet also corresponding to the location of the combustion chamber backplane. The central channel is equipped with an axial swirl vane placed 10 mm below the central channel outlet. The inner and external swirl levels produced by these swirl vanes are denoted S_i and S_e respectively. These swirlers are further described in the next section.

The swirl level produced by the external swirl vane is estimated from geometrical considerations and simplified hypothesis on the structure of the flow. It is fixed to $S_e = 0.67$ and is kept constant in all experiments of this work. The inner swirl level, estimated with the similar hypothesis, can be varied from $S_i = 0.0$ to $S_i = 0.9$. These estimations of the swirl level are described in the next section. The distance between the central and the annular channel outlets is denoted y_i. The value of the recess can be adjusted from $y_i = 0$ mm to $y_i = 8$ mm. In this study, the inner diameter $d_i = 6$ mm of the central tube, the external diameter $d_{ie} = 10$ mm of the central tube and the outer diameter $d_e = 18$ mm of the annular channel are kept constant.

Experiments are carried out by setting the reference bulk velocity u_{e0} and reference equivalence ratio ϕ_0 for the methane/air mixture injected through the annular channel of the DFDS burner. Values for u_{e0} are deduced from methane and air massflow regulators for an annular flow injected at ambient conditions in the annular channel of internal diameter d_{ie} and external diameter d_e. When hydrogen is injected, the total thermal power P_{th} and air mass flowrate $\dot{m}_a$ are kept constant. Methane is removed from the external channel and replaced by hydrogen injected through the central tube to get the desired fraction of power PHx originating from hydrogen:

$$PHx = \frac{\dot{m}_{H_2}\left(\Delta \dot{h}_f\right)_{H_2}}{\dot{m}_{H_2}\left(\Delta \dot{h}_f\right)_{H_2} + \dot{m}_{CH_4}\left(\Delta \dot{h}_f\right)_{CH_4}} \tag{2.1}$$

where $\dot{m}_{H_2}$ and $\dot{m}_{CH_4}$ are the mass flowrates of hydrogen and methane and $\left(\Delta \dot{h}_f\right)_{H_2} = 120$ MJ/kg and $\left(\Delta \dot{h}_f\right)_{CH_4} = 50$ MJ/kg are the low heating values of hydrogen and methane. As a consequence, the bulk velocity u_e in the annular channel and the global equivalence ratio ϕ at which the DFDS burner operates slightly differ from the reference values u_{e0} and ϕ_0 set for methane/air operation, when the hydrogen content PHx is increased.

The global equivalence ratio is defined as:

$$\phi = s\frac{\dot{m}_{CH_4} + \dot{m}_{H_2}}{\dot{m}_a}, \tag{2.2}$$

where $\dot{m}_a$ denotes the mass flowrate air. The stoichiometric ratio s is defined as:

$$s = \frac{\left(2 - 1.5X^f_{H2}\right)\left(W_{O_2} + 3.76W_{N_2}\right)}{X^f_{CH_4}W_{CH_4} + X^f_{H2}W_{H_2}} \tag{2.3}$$

where $X^f_{CH_4}$ and X^f_{H2} are the molar fractions of methane and hydrogen in CH_4/H_2 fuel blend and W_{O_2}, W_{N_2}, W_{CH_4} and W_{H_2} denote the molar masses of oxygen, nitrogen, methane and hydrogen.

When air is only flowing in the external channel, the DFDS injector is called HYLON for HYdrogen LOw Nox injector. The HYLON concept has been patented in 2021 [99]. It is the result of a collaboration between IMFT and Safran Helicopter Engine (SHE) to develop an injector adapted for the combustion of hydrogen in aeronautical gas turbines. During this study, the injector geometry has continuously been optimized. Modifications were first introduced to increase the operability of the HYLON injector and decrease NOx emissions for operations at atmospheric conditions. In a second time, modifications were made to adapt the injector to operation at pressurized and preheated air conditions. The results presented in this manuscript were used as a guideline for these optimizations.

2.1.3 Swirlers

Two different swirlers are used in this study for the DFDS and HYLON injectors. The first one for the annular flow, is a radial swirler as shown in Fig. 2.3. Figure 2.3.a shows a 3D view of the numerical model with a transverse cut view in Fig. 2.3.b. This swirler is 3D printed in resin. The central hole allows the passage of the central hydrogen injection tube. The swirl motion is created by channels inclined with an angle $\alpha_{se} = 42°$ with respect to the radial direction. An angle of $\alpha_{se} = 0°$ would provide no swirl $S_e = 0.0$.

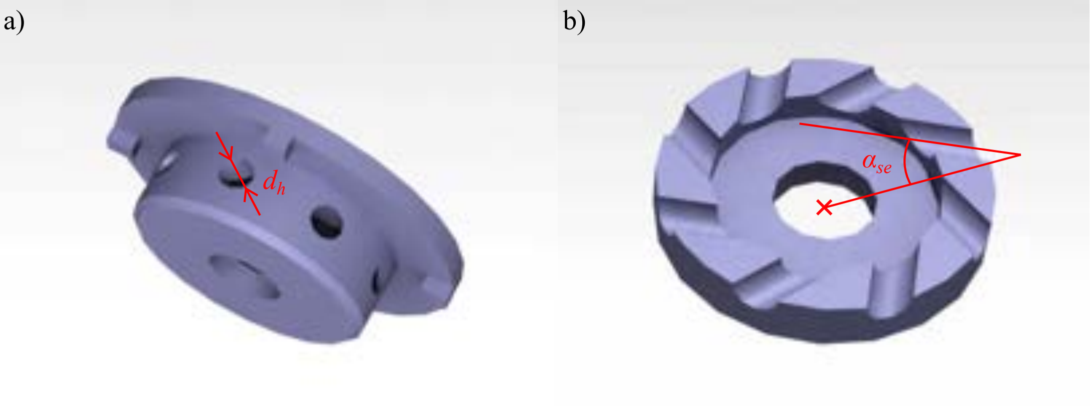

Figure 2.3 – Illustration of the radial swirler set in the main channel. (a) Isometric view of the CAO model. (b) Section cut view of the CAO model.

Figure 2.4.a describes the geometry considered to estimate the swirl number S_e produced by the radial swirler. First, section A in Fig. 2.4.a is considered. The diameter of the swirler holes is denoted d_h and is equal to 4 mm. The number of these holes is $n_h = 8$. The outer diameter of the external channel at the outlet of the swirler is equal to $d_0 = 22$ mm. The inner diameter of the external channel at the outlet of the swirler is equal to $d_{ie} = 10$ mm.

A common definition of the swirl number is to neglect turbulent and pressure effects [100]:

$$S = \frac{2}{d_0}\frac{\int_{d_i/2}^{d_0/2} \overline{u}_\theta \overline{u}_z r^2 dr}{\int_{d_i/2}^{d_0/2} \overline{u}_z^2 r dr} \tag{2.4}$$

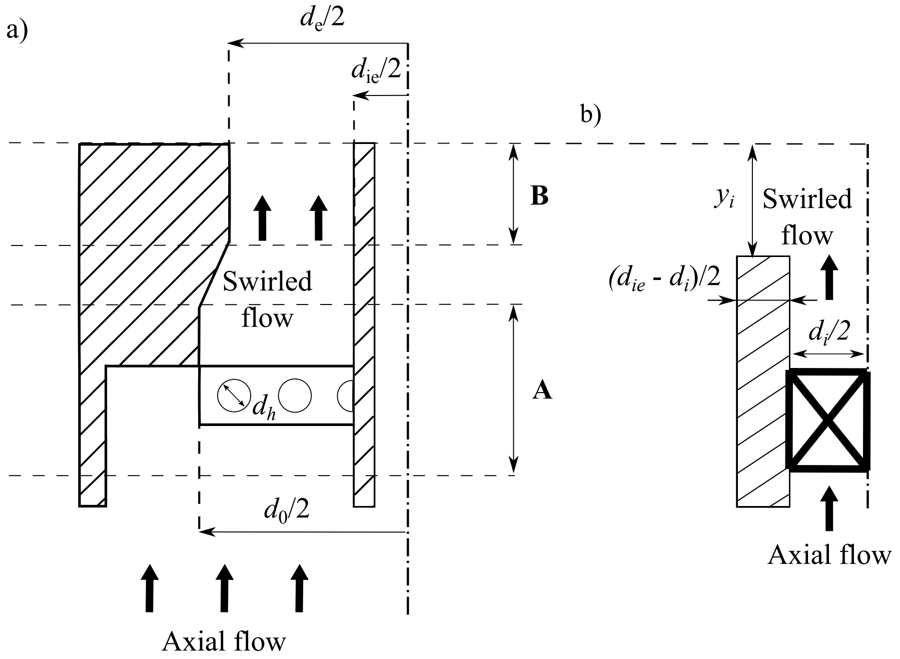

Figure 2.4 – (a) External channel geometry considered for the estimation of the external swirl number S_e. (b) Internal channel geometry considered for the estimation of the inner swirl number S_i.

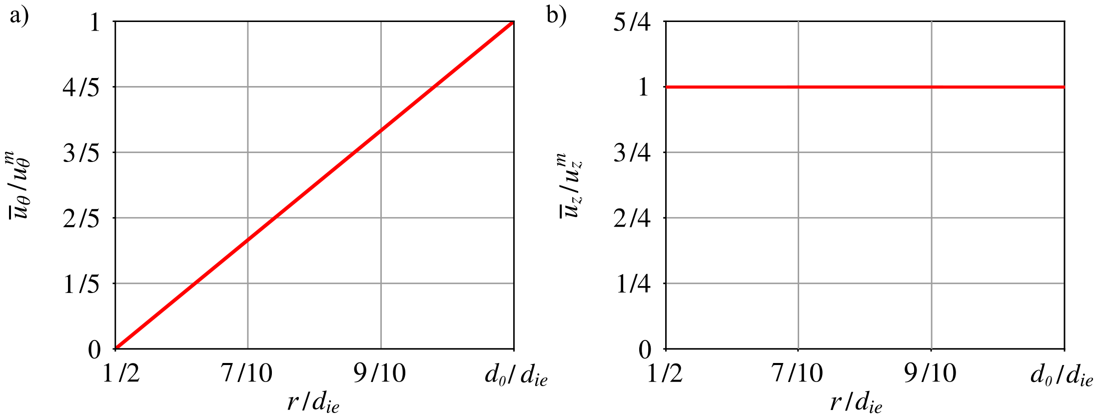

Figure 2.5 – Mean velocity profiles considered for the estimation of the swirl number S_e produced by the radial swirler. (a) Mean tangential velocity profile. (b) Mean axial velocity profile.

The mean tangential $\overline{u}_\theta$ and axial $\overline{u}_z$ velocity profiles need to be modeled to apply Eq. (2.4) and deduce the value of the swirl number. In Fig. 2.5.a, the mean tangential velocity $\overline{u}_\theta$ is assumed to increase linearly from 0 at the inner wall of the annular channel $r = d_{ie}/2$ to the maximum tangential velocity u_θ^m at the external wall of the channel $r = d_e/2$. The mean axial velocity profile $\overline{u}_z$ is assumed to be constant and equal to u_z^m in Fig. 2.5.b. In this case, one gets:

$$\begin{cases} \overline{u}_\theta = u_\theta^m \dfrac{2r - d_{ie}}{d_0 - d_{ie}} \\ \overline{u}_z = u_z^m \end{cases} \tag{2.5}$$

By inserting Eqs. (2.5) into Eq. (2.4) and integrating from $r = d_{ie}/2$ to $r = d_e/2$, the swirl level S_A at the outlet of section A in Fig. 2.4.a writes:

$$S_A = \frac{32 \sin(\alpha_{se})}{n_h d_h^2 (d_0 - d_{ie}) d_0} \left(\frac{d_0^4 - d_{ie}^4}{64} - d_{ie} \frac{d_0^3 - d_{ie}^3}{48} \right) \tag{2.6}$$

Before section B in Fig. 2.4.a, a convergent section is installed to reduce the annular channel diameter from d_0 to d_e. For an inviscid flow, mass flow and angular momentum conservations lead to an expression of the swirl level in section B:

$$S_B = S_A \frac{d_0}{d_e} \frac{d_e^2 - d_{ie}^2}{d_0^2 - d_{ie}^2} \tag{2.7}$$

Finally, the swirl number conferred by the radial swirl vane at the outlet of the annular injector is given by:

$$S_e = \frac{32 \sin(\alpha_{se})}{n_h d_h^2 (d_0 - d_{ie}) d_0} \left(\frac{d_0^4 - d_{ie}^4}{64} - d_{ie} \frac{d_0^3 - d_{ie}^3}{48} \right) \frac{d_0}{d_e} \frac{d_e^2 - d_{ie}^2}{d_0^2 - d_{ie}^2} \tag{2.8}$$

For all conditions investigated in this work S_e is fixed to $S_e = 0.67$.

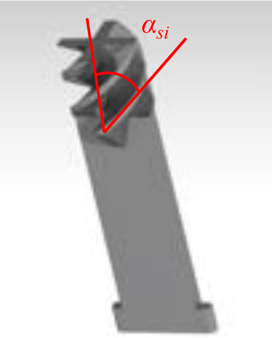

Figure 2.6 – Axial swirler inserted in the central hydrogen channel.

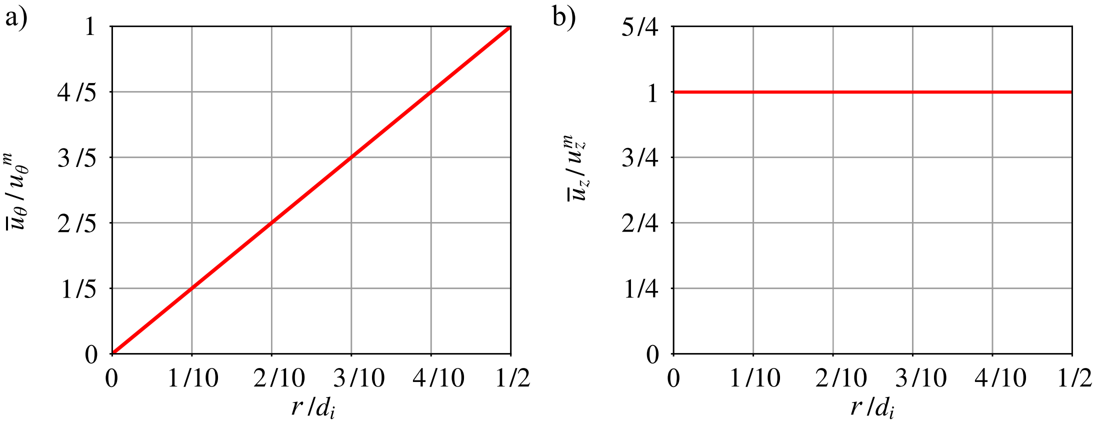

Figure 2.7 – Mean velocity profiles considered for the estimation of the swirl number S_i produced by the axial swirler. (a) Tangential velocity profile. (b) Axial velocity profile.

The same methodology is applied to estimate the swirl number S_i from the axial swirler placed inside the central tube as illustrated in Fig. 2.4.b. The swirler is shown in Fig. 2.6. Unlike the radial swirler, the central swirler can be varied. These swirlers are 3D printed in Inconel 718 as shown in Fig. 2.8 where the angle of the spin is varied from $\alpha_{si} = 0°$ (on the left) to $\alpha_{si} = 61°$ (on the right). To get an estimation of the swirl number, the velocity components are modeled as shown in Fig. 2.7 with a linear profile for the mean tangential velocity $\overline{u}_\theta$ and a constant velocity profile for the mean axial component $\overline{u}_z$ of the velocity:

$$\begin{cases} \overline{u}_\theta = u_\theta^m \dfrac{2r}{d_i} \\ \overline{u}_z = u_z^m \end{cases} \tag{2.9}$$

Combining Eq (2.4) and Eq. (2.9), the expression of the swirl number S_i at the outlet of the axial swirler is:

$$S_i = \frac{1}{2} \tan\left(\alpha_{si}\right) \tag{2.10}$$

Figure 2.8 – Isometric view of central hydrogen swirlers used in this study. (a) $\alpha_{si} = 0°$, $S_i = 0.0$. (b) $\alpha_{si} = 22°$, $S_i = 0.2$. (c) $\alpha_{si} = 39°$, $S_i = 0.4$. (d) $\alpha_{si} = 50°$, $S_i = 0.6$.

Four different swirlers were designed with $\alpha_{si} = 0°$, $\alpha_{si} = 22°$, $\alpha_{si} = 39°$, $\alpha_{si} = 50°$ and $\alpha_{si} = 61°$ leading to internal swirl numbers $S_i = 0.0$, 0.2, 0.4, 0.6 and 0.9.

2.1.4 Flow control

Flow regulation is achieved using thermal-mass flow controllers piloted with a home made Labview program. Air, hydrogen and methane flowrates are regulated with flow controllers Brooks SLA 585x. The helium, argon and nitrogen flowrates are regulated with flow controllers Bronkhorst F201-AV-x. Three configurations are used in this work shown in Figs 2.9 and 2.10. In each case, the fuel and air supply lines are equipped with a manual vane, an electrovalve and a gas regulator before the thermal mass flow controller.

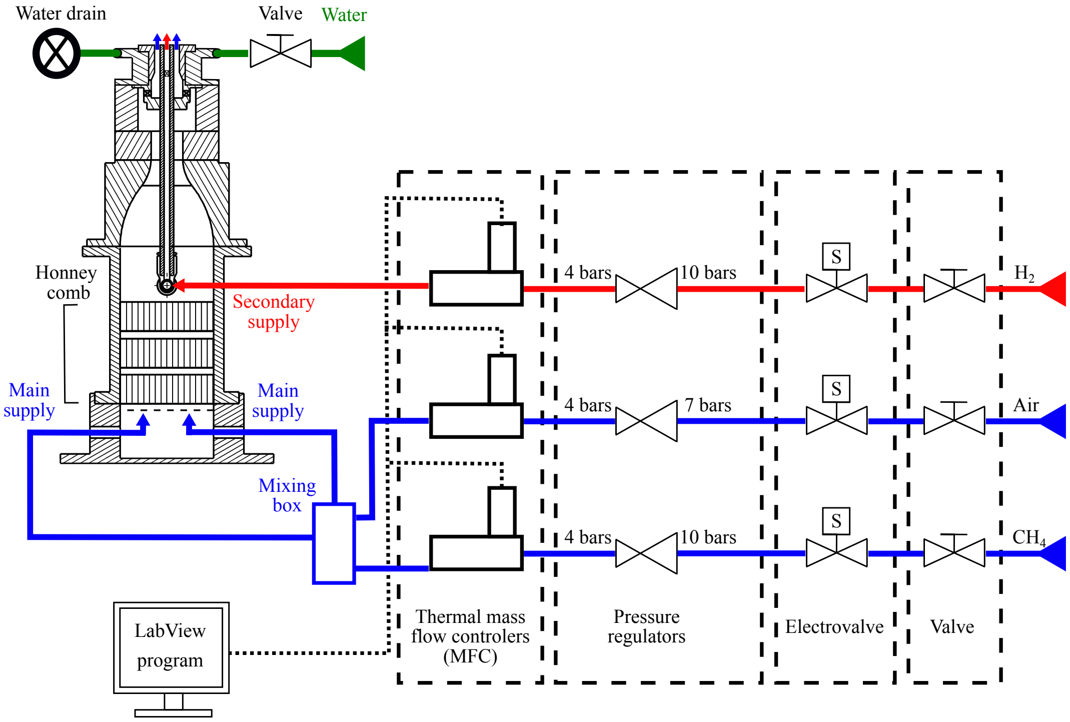

Figure 2.9 – Diagram of the flow control system of the MIRADAS test bench equipped with the DFDS injector.

Figure 2.9 shows the flow control diagram for the MIRADAS test bench equipped with the DFDS injector. The DFDS injector is powered by a methane and air mixture in the external annular channel (blue path in Fig. 2.2.a) and pure hydrogen inside the inner injection channel (red path in Fig. 2.2.a). In this configuration, three flow controllers Brooks are used. The gas supply lines of methane and hydrogen are pressurized at 10 bars. The air supply line is pressurized at 7 bars. A manual valve is used at the inlet of the flow control system and an electrovalve ensures a second security. The pressure is adjusted to 4 bars before the flow controllers. Methane and air are mixed inside a box before injection at the bottom of the plenum. A cooling system installed below the combustion chamber backplane uses a water flowrate adjusted by a manual valve.

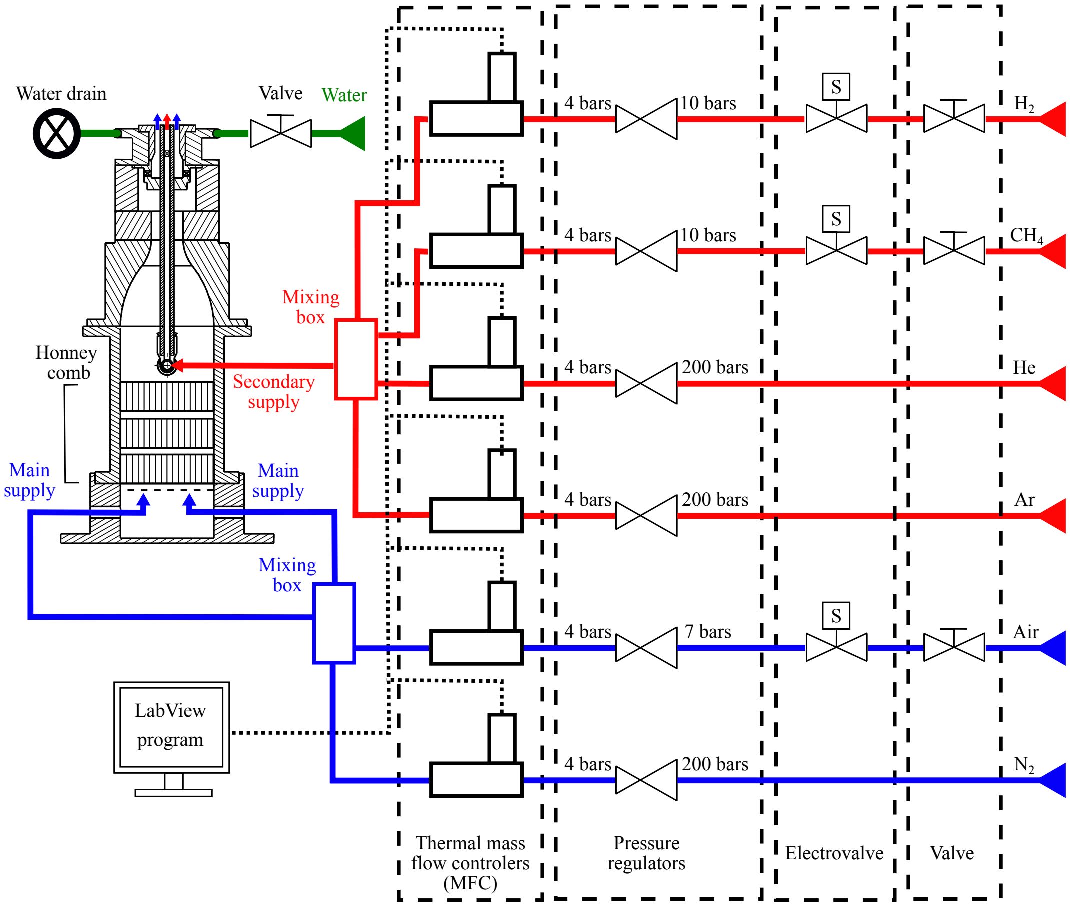

Figure 2.10 – Diagram of the flow control system of the MIRADAS test bench equipped with the HYLON injector for experiments with diluted gases.

When the HYLON injector is set on the MIRADAS test bench, only air is injected inside the external channel. The system is operated in this case without methane in Fig. 2.9.

Additional experiments with the HYLON injector were conducted with diluents to modify the mixture reactivity. These additional gases are added to both channels and the flow control system is illustrated in Fig. 2.10. The central injection tube can be supplied with hydrogen, methane, helium and argon and the annular channel with air and nitrogen. The inert gases (helium, argon and nitrogen) are stored in gas cylinders at 200 bars. These gases are depressurized to 4 bars before the flow controllers. In both channels, gases are perfectly mixed inside a box before injection through the HYLON injector.

2.1.5 Combustion chamber

The studied flames are confined in a combustion chamber with large optical access to the reaction zone. The chamber shown in Fig. 2.11 has a square cross section with an inner width $d_q = 78$ mm and a length from the backplane to the bottom of a burnt gases exhaust nozzle equal to $L_q = 150$ mm. The chamber is equipped with 4 fused silica windows. The thickness of the quartz windows is equal to 8 mm and the sealing between the quartz and the metallic pillars of the chamber is assured with glass wool. The fused silica has the advantage to have a transmission efficiency close to 93% from 280 nm (UV) to 800 nm (IR) as indicated by the spectral transmitance plotted in Fig. 2.12 of the windows used in this work. They are in particular well suited for combustion diagnostics as OH^* imaging recorded at 308 nm, PIV, Rayleigh and Raman scattering and thermometry with optical devices. Moreover, laser diagnostics are considerably simplified with flat windows rather than tubes because reflections and optical deformations are drastically reduced.

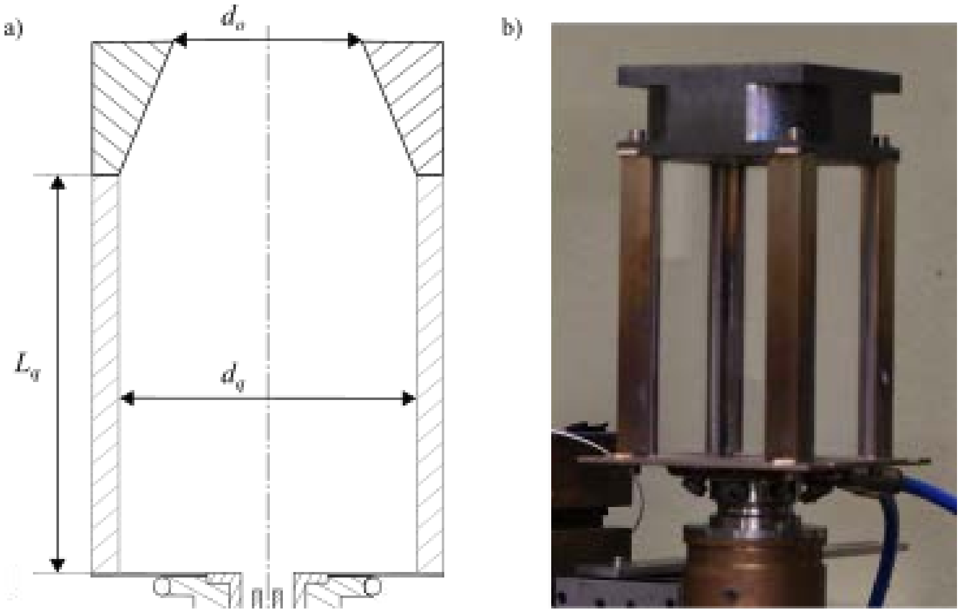

Figure 2.11 – (a) Schematic of the square combustion chamber. (b) Square combustion chamber equipped with 4 plane quartz windows.

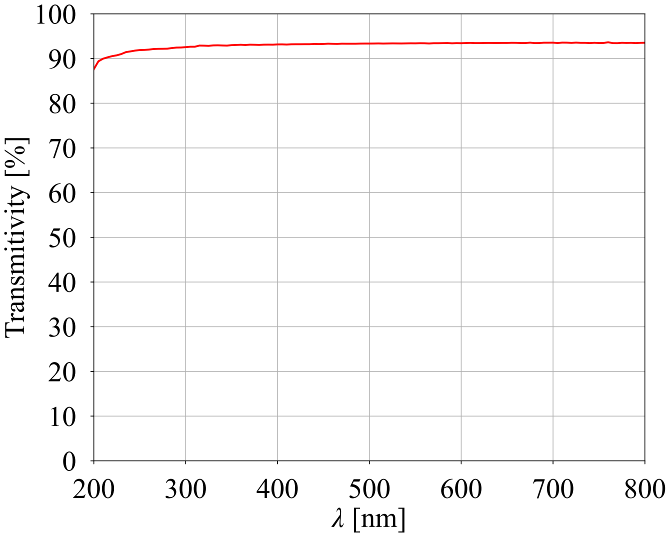

Figure 2.12 – Spectral transmittance of the Sceram 8 mm fused silica windows used in this study.

2.2 Diagnostics

2.2.1 Data acquisition

Analog electrical signals from different sensors are sampled with a terminal block National Instrument BNC 2120 shown in Fig. 2.13. It has 8 BNC analog input channels and 2 BNC analog output channels. A channel for a thermocouple is also available and several channels providing digital input/output, timing output and function generator output are available. Only the analog channels and the thermocouple input are used in this study. This system is controlled by a home-made Labview program to set the sampling rate F_s and the number of samples acquired n_s. The recorded data are saved in ASCII files format with a double precision (i.e. 16 decimals). All channels are synchronized.

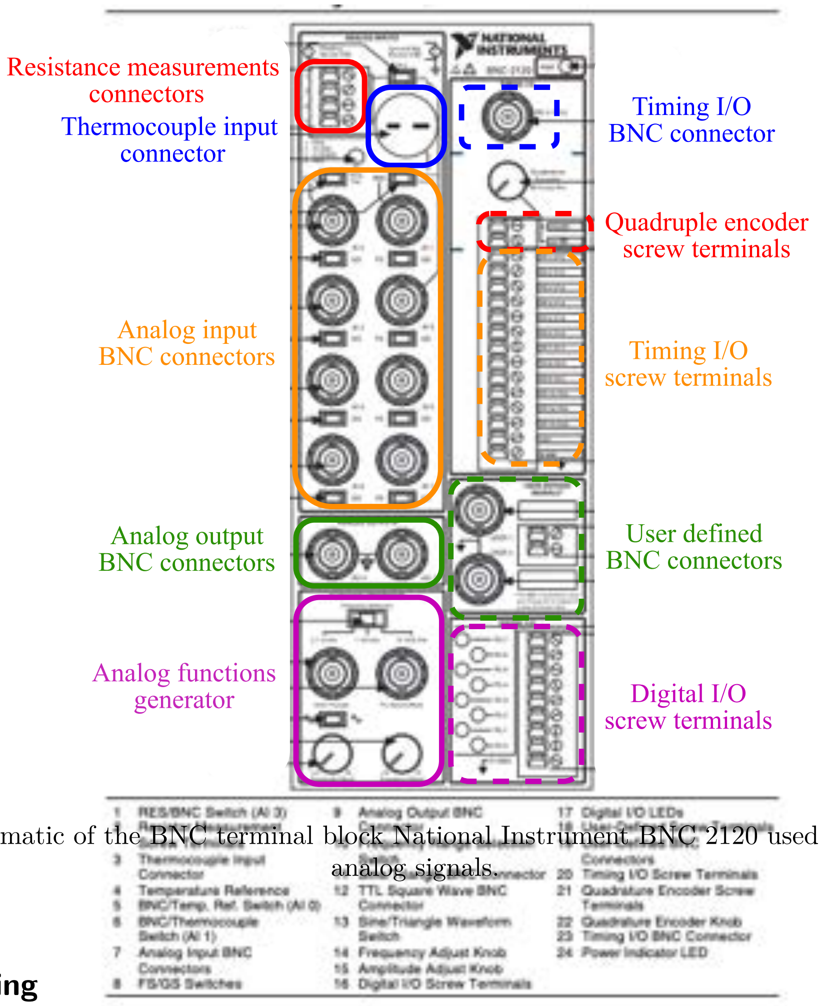

Figure 2.13 – Schematic of the BNC terminal block National Instrument BNC 2120 used for the acquisition of analog signals.

2.2.2 Flame imaging

2.2.2.1 Direct imaging

Direct flame imaging in the visible band is achieved with a commercial Nikon D7500 equipped with a lens Nikkor 105/2.8G AF-S IF-ED VR MICRO shown in Fig. 2.14. This camera has a wide focal aperture and a mode without color correction. The wide focal aperture allows to take flame images with small exposure times to get pictures of flames with a low intensity, as it is the case for lean H_2/air flames.

To illustrate the effect of different settings of the camera, tests are made with the same flame varying the focal aperture f, the exposure time τ and the value of the Iso parameter. They are presented in Fig. 2.14. At the top, the Iso parameter is set to 1250, the exposure time to $\tau = 1/4$ s and the focal aperture is progressively decreased. At the left, the focal aperture is $f/36$ and the flame is not visible on the picture, because no sufficient light reaches the photosensor. When the aperture is progressively opened, from left to right, the flame appears on the picture due to the increased fraction of light from the flame collected by the photosensor. The best settings are here obtained for $f/4.5$. In the middle row, the focal aperture is set to

Figure 2.14 – Nikon D7500 with the lens Nikkor 105/2.8G AF-S IF-ED VR MICRO used for direct flame imaging in this work.

$f/5$ and the Iso to 1250. Here, the exposure time is step by step increased. For $\tau = 1/60$ s of exposure, the flame is only slightly visible on the picture. When the exposure time is increased to $\tau = 1$ s, the picture is overexposed. The optimal settings are obtained for an exposure time $\tau = 1/4$ s. Finally the focal aperture is set to $f/3.2$ and the exposure time to $\tau = 1/20$ s. The values of Iso are increased from 100, in which case the flame does not appear on the picture, to 20000, in which case the picture is overexposed. The best picture is obtained for an Iso value equal to 2000.

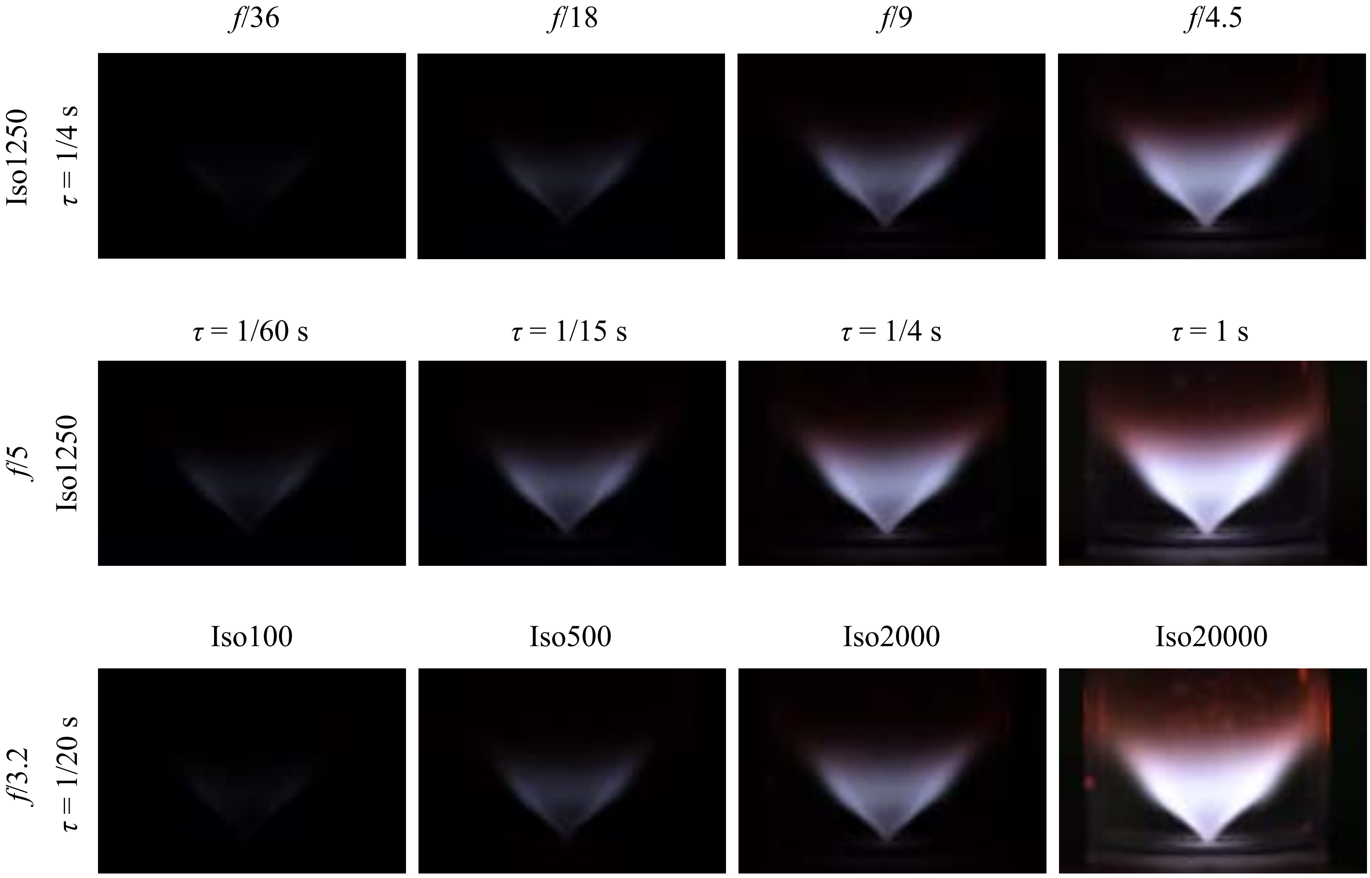

Figure 2.15 – Effects of the settings of the Nikon D7500 on the flame pictures.

2.2.2.2 CH* and OH* imaging

Chemiluminescence corresponds to the spontaneous light emission produced from a chemical reaction in the hot region of the flow [101]. The emitted light originates from radicals transitioning from an excited state to a ground state. Typically in hydrocarbon flames such as CH_4/air flames, the principal radicals present in the hot reaction zone are CH* and OH*. They are considered by the community as good tracers of the heat release rate location [102]. Moreover, in perfectly premixed systems, the intensity of the chemiluminescence of these radicals is also found to be proportional to the heat release rate [102]. This remarkable property is used in many studies.

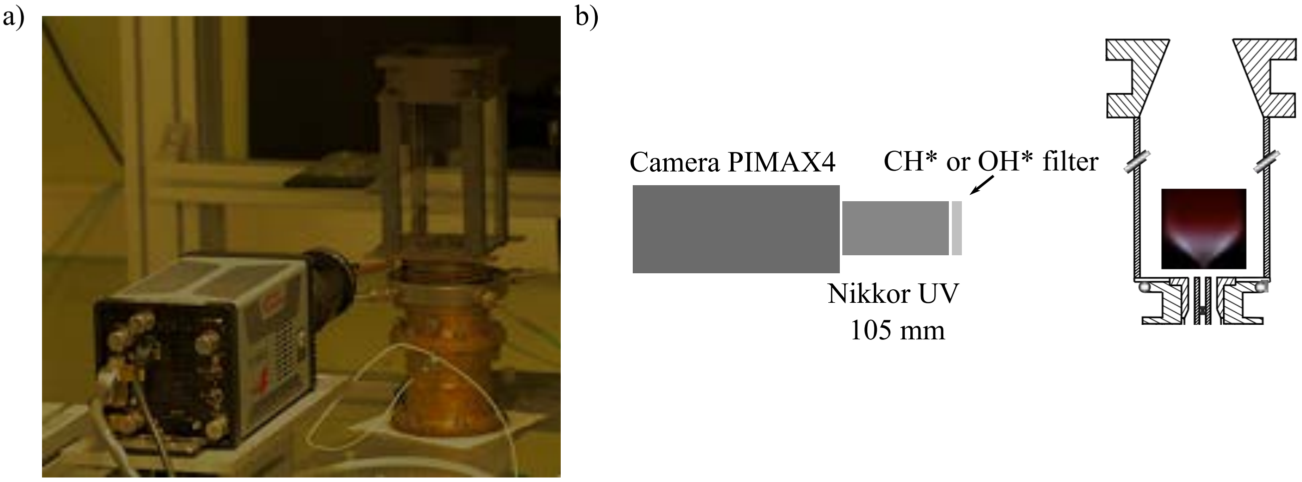

Figure 2.16 – Intensified Princeton Instrument PI-MAX4 camera sensible in the UV band in front of the DFDS burner. (a) Picture of the setup. (b) Schematic of the setup.

In unsteady perfectly premixed systems, the fluctuation level of heat release rate $\dot{Q}'/\overline{Q}$ is often determined from the integrated luminosity signal of CH* or OH* radicals [24, 94, 103]. For hydrogen combustion, due to the absence of carbon atoms, the heat release rate location can only be estimated with OH* radicals. The light emitted by this radical is a narrow peak around 308 nm that requires equipment able to record images in the UV spectrum. These images are recorded with an intensified Princeton Instrument PI-MAX4 camera. The camera is equipped with a UV lens Nikkor Rayfact UV-105 Multispectral lens, 105 mm f/4.5 and a narrow bandpass OD4 optical filter Asahi XHQA310 centered around $\lambda = 310 \pm 10$ nm.

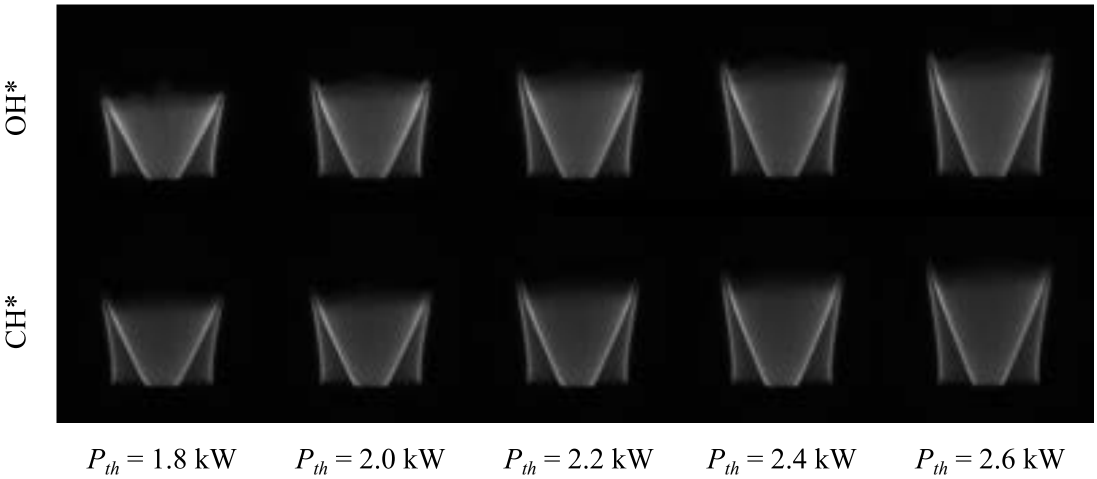

Figure 2.17 – Example of OH* and CH* images of laminar premixed M-flames stabilized on a cylindrical bluff-body. CH_4/H_2/air flames with a mass fraction of H_2 in the fuel blend equal to $Y_{H2}^{f} = 0.15$ and an equivalence ratio $\phi = 0.59$.

An example of flame images filtered around the emission wavelength of naturally exited OH* (310 nm) and CH* (430 nm) radicals is provided in Fig. 2.17. The flames are laminar premixed M-flames and burn a mixture of CH_4/H_2/air that is perfectly premixed before the reaction zone. The mass fraction of H_2 in the fuel blend is $Y^f_{H2} = 0.15$ and the equivalence ratio $\phi = 0.59$. They are stabilized with a M-shape on the burner rim at the external side and on a cylindrical rod officiating as bluff body at the center. The two filtered images, i.e. filtered around OH* and CH* emissions, are roughly identical. In Fig. 2.17, the thermal power is increased from the left to the right, keeping the equivalence ratio constant. The pictures are line-of-sight integrated and the reaction layer thickness is, for both cases, well visible.

2.2.3 Thermometry

2.2.3.1 Contact thermocouple

Contact thermocouples are one of the simplest and oldest electrical systems to measure temperatures. A contact thermocouple device is shown in Fig. 2.18. According to Seeback effect, the electrical potential difference at the thermocouple junction only depends on temperature.

Figure 2.18 – Image of an isolated contact type K thermocouple.

This difference of electrical potential is generally of the order of some millivolts and is typically measured with a Permanent Magnet Moving Coil (PMMC) instrument. For a couple of dissimilar metals as for example Chromel/Alumel for the type K thermocouples used in this work, the difference of potential between the two wires is proportional to the difference of temperature between the two junctions. The cold junction acts as a reference temperature (typically 0°C). To reduce inaccuracies, most thermocouples are now installed with instruments that provide automatic reference compensation. The type K thermocouples used in this thesis for the measurements of the temperature on the solid parts of the burner allow measurements up to 1300 K.

Thermal paste is applied on the quartz window where temperature measurements are made. This paste enables to optimize the quality of the thermal contact between the contact thermocouple and the window. An example of temperature profile is displayed for a reference flame in Fig. 2.19. This flame is anchored to the HYLON hydrogen injector tube with a thermal power $P_{th} = 3.9$ kW and a global equivalence ratio $\phi = 0.46$, produced by an injector with an inner swirl $S_i = 0.6$ and an injector recess $y_i = 4$ mm. The red dashed line is a polynomial fit of temperature measured at discrete locations. The maximum temperature $T_s \approx 640$ K for $y \approx 55$ mm corresponds to the flame tip impinging on the combustion chamber walls. These data were used compared to simulations by Aniello *et al.* [92].

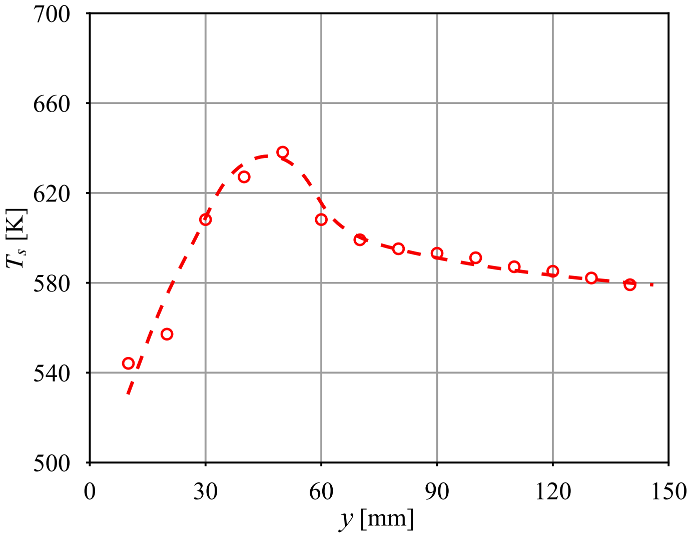

Figure 2.19 – Surface temperature measured with the contact thermocouple along the external side of the combustion chamber, at the middle width of the quartz window. Anchored H_2/air flame with a thermal power $P_{th} = 3.9$ kW and a global equivalence ratio $\phi = 0.46$. Symbols: Raw data. Dashed line: Fitted data.

2.2.3.2 Double bead thermocouple

Measurements of the local temperature of hot gases is more challenging than for solid components. It can be achieved with standard thermocouples when the gas temperature is low. When the temperature inside the combustion chamber increases, the error due to the thermal radiation from the thermocouple to the combustor solidwalls becomes important, and a method to correct this bias is needed to deduce the actual temperature of the hot gases. Moreover if the temperature is very high as in the burnt gases, the thermocouple needs to be adapted to this harsh environment. For example, R-type thermocouples made with platine and rhodium allow measurements up to 1800 K.

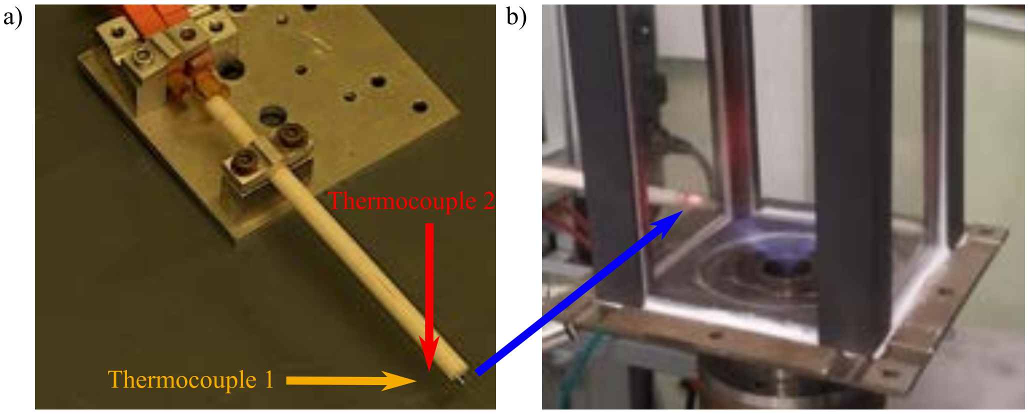

Figure 2.20 – Picture of a double bead thermocouple. (a) Support with double bead thermocouple used in this work. (b) Double bead thermocouple set in the hot combustion products in the MIRADAS setup.

Figure 2.20 shows how thermal radiation affects the thermocouple beads. The convective heat flux between the gas and the bead φ_{cv} is positive. Radiative heat transfer also takes place between the thermocouple and the combustor walls. Considering that the temperature of the bead T_b is higher than the temperature of the combustor walls T_w ($T_b > T_w$), the radiative heat flux at the bead surface is negative ($\varphi_{rad} < 0$). Consequently, the temperature of the thermocouple bead is smaller than the temperature of the hot gases ($T_w < T_b < T_g$). For smaller temperatures, the bead of the thermocouple is approximately at the thermal equilibrium with the gas and $T_b \approx T_g$ because the losses by radiative flux are low ($\varphi_{rad} \approx 0$). When φ_{rad} cannot be neglected, a correction is needed to realize accurate measurements of the gas temperature.

The Reduced Radiation Error method from Brohez *et al.* [104] is used in these experiments to mitigate the effects of the thermal radiation. It has already been successfully used by A. Degenève [105]. The same values for the thermo-physical properties of the thermocouple are chosen here. All the gas properties are estimated with Cantera and the velocity is estimated as the mean velocity at the measurement location based on the total flowrate and thermal expansion. Shaddix [106] explains that convective heat transfer takes place both at the surface of the bead and along the wires of the thermocouple. He showed that the thermal flux along the wires is negligible when the ratio between the bead and the wire diameter verifies $d_b/d_w < 3$. In the case of the double bead thermocouple used in this work, this ratio is equal to $d_{b2}/d_{w2} = 2.3$ and $d_{b1}/d_{w1} = 3.6$ respectively for the small and the large bead: $d_{b1} > d_{b2}$ and $d_{w1} > d_{w2}$.

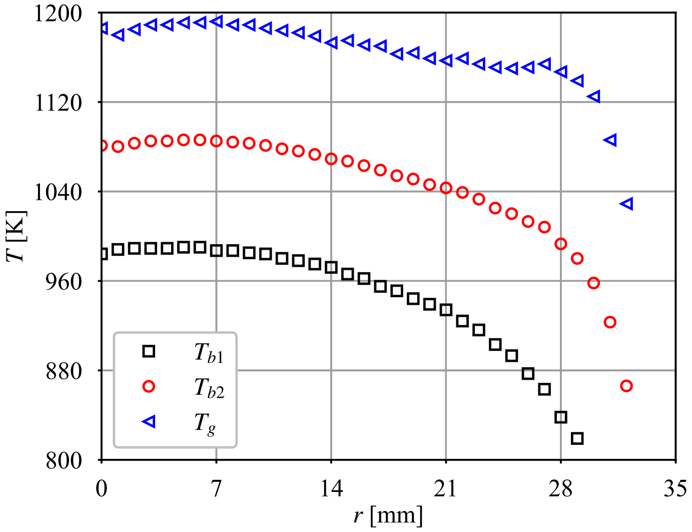

Figure 2.21 – Gas temperature profiles at the outlet of the combustion chamber. The measurements are made with a double bead thermocouple. T_{b1} and T_{b2} are the measured values respectively with the biggest and smallest bead. T_g is the corrected value of the gas temperature with the RRE method.

An example of measurement with the double bead thermocouple system described above is provided in Fig. 2.21 when they are set in the combustion chamber as in Fig. 2.20. The temperatures denoted T_{b1} and T_{b2} are respectively the temperatures provided by thermocouple 1 and 2. As $d_{w1} > d_{w2}$ and $d_{b1} > d_{b2}$, consequently thermocouple 1 looses more energy by radiation than thermocouple 2, due to its greater surface, and $T_{b1} < T_{b2}$. The corrected gas temperature T_g, in blue in Fig. 2.21, is always greater than the ones measured with thermocouples 1 and 2. It is an estimation of the gas temperature without loss by thermal radiation of the thermocouple wire and the bead. Effects of the wall radiation that affects the measurements close to the walls where $r \geq 28$ mm are clearly visible.

2.2.3.3 Double wavelength pyrometer

Hot surfaces with temperatures higher than $T > 250°\mathrm{C}$ are also determined in this work with a double wavelength pyrometer. For a single wavelength pyrometer, the emissivity of the surface needs to be known to measure the surface temperature. With a double wavelength pyrometer, this quantity is not needed. Only the slope of the spectral emissivity ratio between the two wavelengths is needed, and the assumption that this ratio is equal to unity is generally made. Moreover, a decrease of the optical transmissivity between the pyrometer and the measurement spot does not affect the measured temperature with a double wavelength pyrometer. These characteristics allow easy and accurate measurements of the surface temperature. The system used in this work is a Fluke Process Instruments E2RL-F2-V-0-0 Endurance Series. This instrument has the advantage to have a wide range of temperature measurements, from $T = 250°\mathrm{C}$ to $T = 1200°\mathrm{C}$. A laser pointer is included in the system to ease pointing of the measurement spot. This device is particularly suitable for measurements of hot surfaces of combustion chamber.

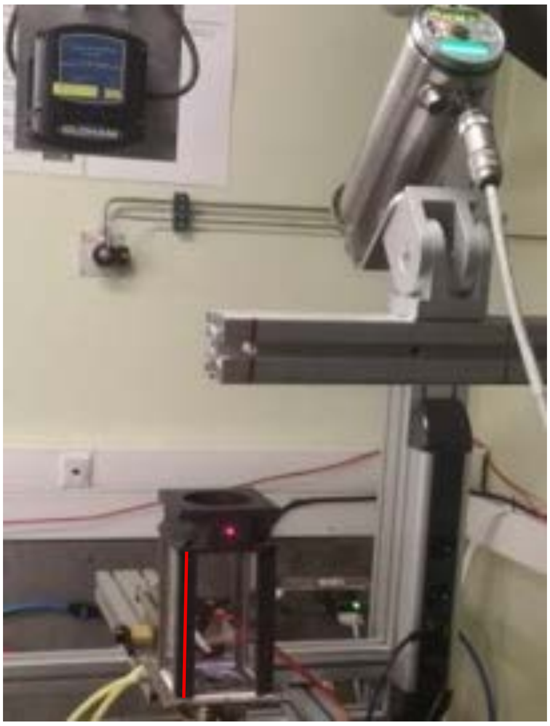

Figure 2.22 – Double wavelength pyrometer installed for the measurement of the surface temperature of the convergent section at the top of the combustion chamber during operation with a hydrogen/air flame.

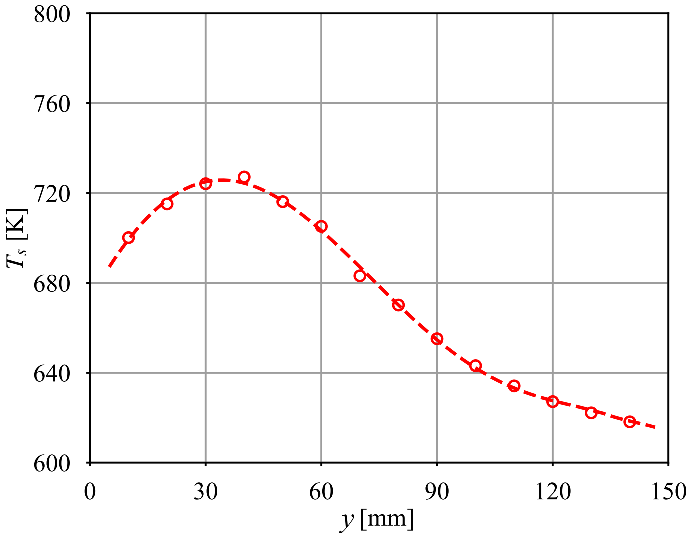

Figure 2.23 – Surface temperature measured with the double wavelength pyrometer along the external side of the combustion chamber on the red line shown in Fig. 2.22. Anchored H_2/air flame with a thermal power $P_{th} = 3.9$ kW and a global equivalence ratio $\phi = 0.46$. Symbols: Raw data. Dashed line: Fitted data.

An example of surface temperature measurements using the double wavelength pyrometer is provided in Fig. 2.23. These measurements are carried out along the red line in Fig. 2.22. As for the measurements along the quartz windows with the contact thermocouple shown in Fig. 2.19, the temperature increases with the distance to the combustion chamber backplane, reaches a maximum for $y \approx 40$ mm, and decreases further downstream. Compared to the temperature along the quartz windows, the position of the maximum temperature is slightly shifted downstream. These temperature profiles are analyzed in detail in the following.

2.2.4 Velocimetry

2.2.4.1 Hot-wire

Time resolved local velocimetry measurements in cold flow conditions were made with a constant temperature anemometer. The velocity of the flow needs to be large enough to assume a forced convection regime of the fluid on the heated solid body of the probe [107]. The materiel used in this study is a Dantec Dynamics 55P16 probe and a Dantec Dynamics MiniCTA. A calibrated curve of the velocity with respect to the voltage measured at the Wheatstone bridge of the MiniCTA is shown in Fig. 2.24.

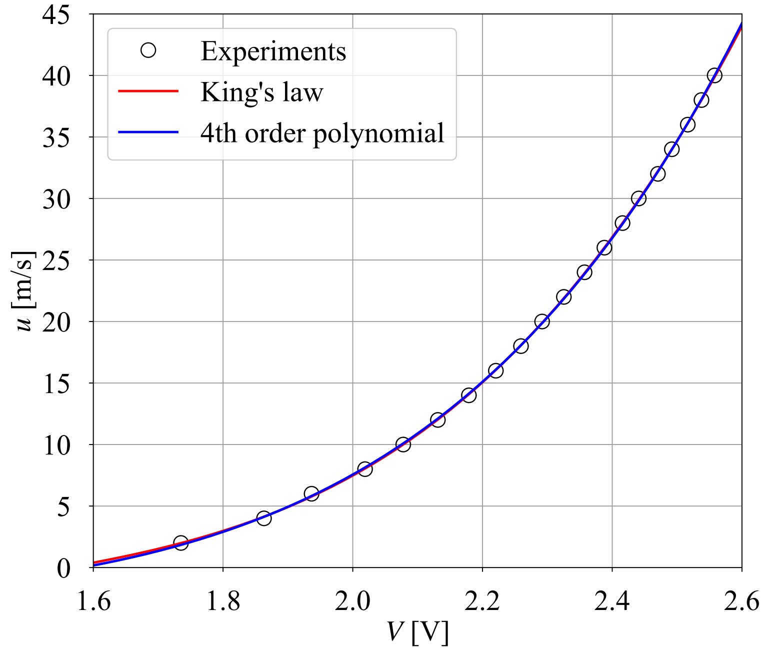

Figure 2.24 – Example of calibration with the determination of the King's law (see Eq. (2.11)) and 4th order polynomial (see Eq. (2.12)) constants from experiments.

Before measurements, the probe needs to be calibrated to set the relation between the measured velocity and the output probe voltage using a calibration system providing a known, stable and precise velocity. This is achieved with the calibration system Dantec Dynamics Streamline. The velocity is varied on the desired range of calibration and the corresponding output voltage is recorded for each velocity value. Then, the link between the output probe voltage and the measured velocity can be achieved with the so-called King's law or with a 4th order polynomial expression. The first one is the historical expression used for the hot-wire calibration and is defined by:

$$u = \left(\left(V^2 - A\right)/B\right)^{1/n} \tag{2.11}$$

where u is the local flow velocity, V is the output probe voltage and A, B and n are constants that need to be experimentally determined. Dantec Dynamics also provides an alternative expression to link the output probe voltage and the measured velocity:

$$u = a + bV + cV^2 + dV^3 + eV^4 \tag{2.12}$$

where a, b, c, d and e are constants that need to be experimentally determined.

An example of calibration with Eqs. (2.11) and (2.12) is illustrated in Fig. 2.24. The velocity range of calibration is set from $u = 2$ to 40 m/s. The two expressions provide very close results.

An example of measurement setup and measured velocity signal is provided in Fig. 2.25. In Fig. 2.25.a, the hot-wire is installed at the outlet of a laminar premixed burner. Figure 2.25.b shows an example of recorded signal during acoustic forcing of the flow. Here, the forcing frequency is set to $f = 230$ Hz. These data are used in [94] to determine the Flame Transfer Function.

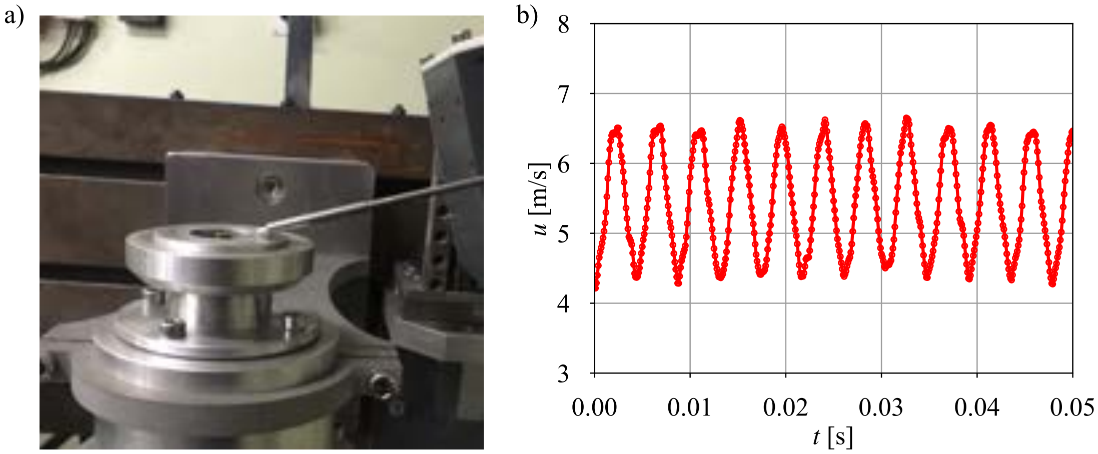

Figure 2.25 – (a) Hot-wire probe installed at the outlet of a laminar premixed burned. (b) Example of velocity measurements using a hot-wire during acoustic forcing of the flow at $f = 230$ Hz taken from [94].

2.2.4.2 Particle Image Velocimetry (PIV)

A Particle Image Velocimetry system is used to explore the velocity field in cold and reactive conditions. The principle of the technique is to illuminate particles seeded in the flow with two very short laser shots and to record the two images of the laser light scattered by the seeded particles in the normal direction to the 2D laser sheet. The delay between the two laser pulses must be precisely controlled and known. Then, a cross-correlation post-processing algorithm is applied to the two recorded images to calculate the mean displacement of the particles over small interrogation windows between the two snapshots. Knowing the delay and the particle displacement between the two snapshots, the velocity can be deduced. Several PIV post-processing algorithms have been developed [108]. PIV is a mature technique and powerful commercial algorithms are available. The post-processing PIV software Davis from LaVision is used in this study (lavision.de/en/products/davis-software). Two different PIV setups are used for cold and reactive flow conditions which are described in the following. In both cases, the measurements are realized in the axial plane of the burner.

2.2.4.3 PIV in cold flow conditions

The PIV system used for the flow velocity measurements in cold flow conditions is described here. The system in Fig. 2.26, features a double-head laser Big Sky CFR200 producing laser light with a wavelength equal to 532 nm, a laser sheet generator manufactured by LaVision and a CCD double-shot camera equipped with a bandpass filter 532±10 nm. Because multiple PIV measurement campaigns have been conducted during this work, two different cameras have been used: a PCO 2000 CCD and a PCO Sensicam QE. A bandpass filter in front of the camera is used to isolate only the scattered laser light by the seeded particles. The seeding particles are micrometric oil droplets produced with an air nebulizer for each injection channel. The oil used is a mineral oil Edwards Ultragrade Performance 15, well adapted for flow seeding for optical diagnostics as shown in Durox *et al.* [109].

The two pictures recorded during the two laser pulses are post-treated using the software LaVision Davis with interrogation windows of size 32×32 pixels and an overlap of 50%. An illustration is shown in Fig. 2.27, with the two raw images at the left and the resulting PIV snapshot at the right. The seeding of the flow with micrometric oil droplets is homogeneously distributed in these snapshots and with a reasonable density. The time between the two laser pulses is calculated in order to obtain a maximum displacement of 75% of the interrogation windows (32×32 pixels), based on the maximum local velocity expected. In the case presented in Fig. 2.27, the delay set between the laser pulses is 12 μs.

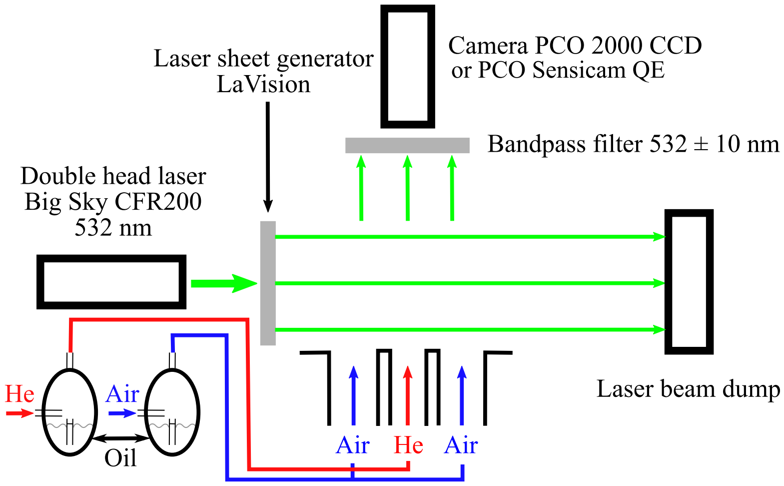

Figure 2.26 – Particle Image Velocimetry optical system used in this work for the 2D flow velocity fields in cold flow conditions.

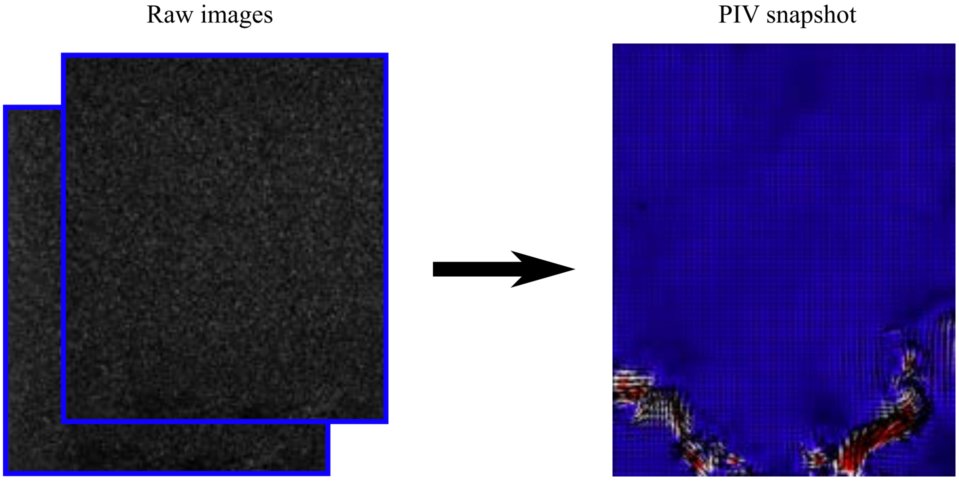

Figure 2.27 – Raw PIV images and the resulting instantaneous flow velocity field after post-processing.

2.2.4.4 PIV in reactive conditions

For measurements in reactive conditions, the experimental setup shown in Fig. 2.28 is used. The main difference with the experimental setup used for the cold flow experiments is the seeding system. A LaVision seeding system allows to seed the flow with micrometric solid particles. The particles used in this work are alumina (Al_2O_3) type DX with a diameter equal to 1 μm provided by Laborympex. The camera used in this work for PIV measurements in reactive conditions is a PCO 2000 CCD. The PIV interrogation windows size is set to 32×32 pixels with an overlap equal to 50%. The delay between the two laser pulses is determined for each flowrate with the same method as for the PIV measurements in cold flow conditions.

Figure 2.29 shows two examples of raw images and resulting PIV snapshots. Figure. 2.29.a shows a bad flow seeding. On the raw images on the left, the seeding density is very high in the jet and several zones with a low density of particles are visible on the images. The resulting PIV snapshot on the right is very noisy and several local velocities are badly estimated, as for example at the base of the right arm of the swirled jet, a zone where the seeding density is very high on the raw images on the left figure. In reactive conditions, the homogeneity of the seeding is more difficult to achieve because of the large thermal expansion of the gas through the reaction layer, leading to an increase of the volume by a factor of about six. Consequently it is difficult to achieve a good seeding in both fresh and burnt gas zones. In Fig. 2.29.b, an example of acceptable flow seeding is provided. The resulting PIV snapshot is much less noisy and the velocity vectors deduced from the post-processing of the raw images yields information all along the jet arms.

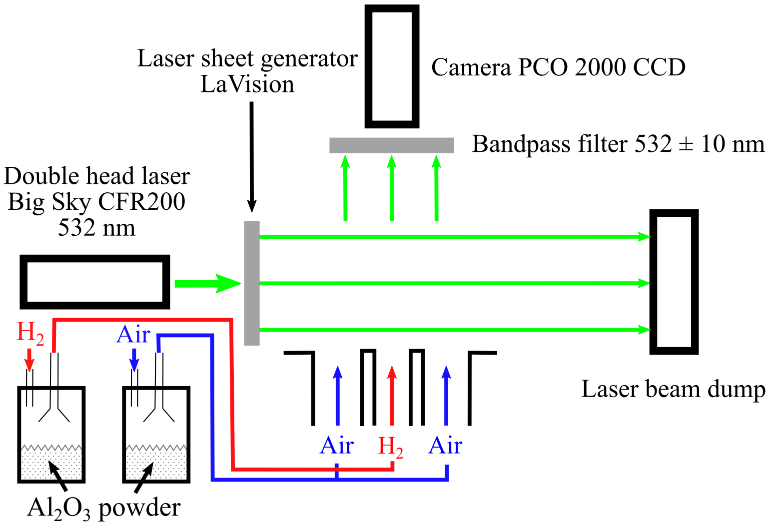

Figure 2.28 – Particle Image Velocimetry optical system used in this work for the 2D flow velocity fields in reactive conditions.

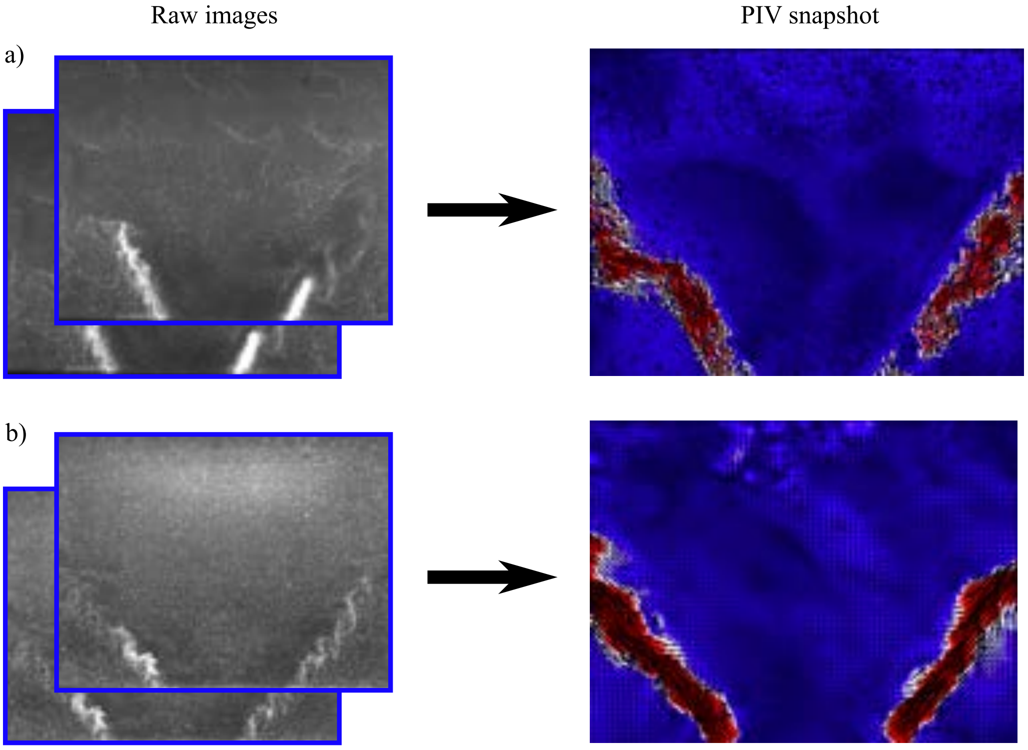

Figure 2.29 – PIV images and the resulting instantaneous flow velocity field after post-processing. (a) Bad flow seeding. (b) Acceptable flow seeding.

2.2.5 Gas concentration

2.2.5.1 Burnt gas analyzer

CO and NOx emissions are measured at the outlet of the combustion chamber using a commercial flue gas analyzer ECOM J2KN. Options are added to the base version to get measurements in burnt gases with temperature up to 1100°C and concentrations of hydrogen up to 20000 ppm. The analyzer is equipped with an air dryer and a soot filter.

Figure 2.30 – ECOM J2KN flue gas analyzer.

The ECOM JK2N is shown in Fig. 2.30. The type of sensor technology, range, resolution and accuracy of the measurements for each molecule are provided in Tab. 2.1. CO concentrations are measured with Non-Dispersive InfraRed (NDIR) sensor with a range of measurable concentration from 0 to 63000 ppm, a resolution of 1 ppm and an accuracy of ±3vol.%. For NO and NO_2 concentrations, an electrochemical cell (EC) is used, with a resolution of 0.1 ppm and an accuracy equal to ±5vol.%. The range of measurable concentrations is 0-500 ppm for NO and 0-100 ppm for NO_2.

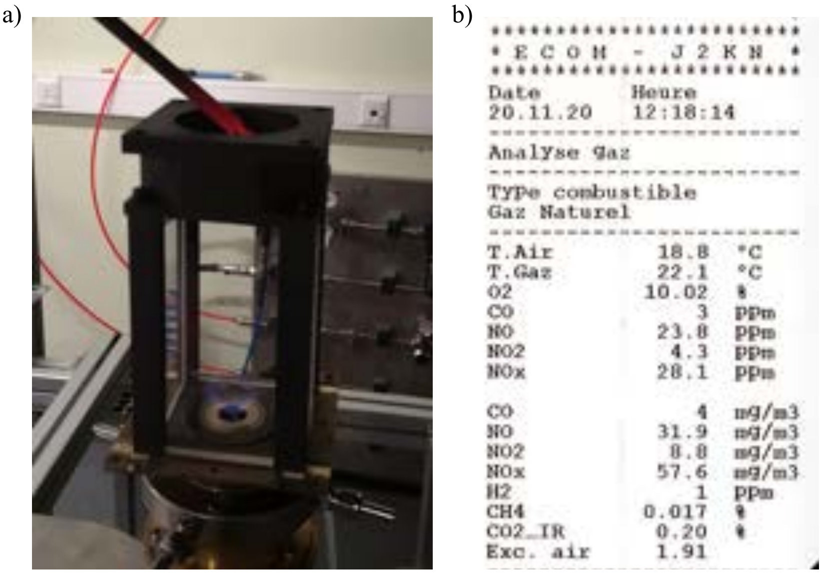

```
**************************
* E C O M  -  J 2 K N    *
**************************
Date         Heure
20.11.20     12:18:14
--------------------------
Analyse gaz
--------------------------
Type combustible
Gaz Naturel
--------------------------
T.Air             18.8   °C
T.Gaz             22.1   °C
O2               10.02   %
CO                   3   ppm
NO                23.8   ppm
NO2                4.3   ppm
NOx               28.1   ppm

CO                   4   mg/m3
NO                31.9   mg/m3
NO2                8.8   mg/m3
NOx               57.6   mg/m3
H2                   1   ppm
CH4              0.017   %
CO2_IR            0.20   %
Exc. air          1.91
```

Figure 2.31 – (a) ECOM J2KN flue gas analyzer installed at the outlet of the combustion chamber. (b) Report of the measured values printed by the ECOM J2KN flue gas analyzer.

Figure 2.31.a shows the ECOM J2KN flue gas analyzer installed on a burner in operation. The gas sampling probe is placed slightly upstream the outlet of the combustion chamber to avoid dilution of burnt gases with external fresh air. The measurement report printed by the device is shown in Fig. 2.31.b. All the measured concentrations of NO, NO_2, CO and H_2 are given in ppmv. For NO, NO_2 and CO, measured concentration are also provided in mg/m^3 by the instrument. The values for O_2, CO_2 and CH_4 concentrations are provided by the device in volumetric percentage. The gas temperature is displayed in Celsius degrees.

Table 2.1 – Sensor principle, range, resolution and accuracy of the measure for each molecule analyzed by a ECOM J2KN from the manufacturer. EC: Electrochemical Cell, NDIR: Non-Dispersive InfraRed, NiCr-Ni: thermocouple type NiCr-Ni.

Measured value	Principle	Range	Resolution	Accuracy
O_2	EC	0-21 vol.%	0.1 vol.%	±0.3 vol. %
CO	NDIR	0-63000 ppm	10 ppm	±3%
CO_2	NDIR	0-20 vol.%	0.1 vol.%	±3 vol. %
NO	EC	0-500 ppm	0.1 ppm	±5 vol. %
NO_2	EC	0-100 ppm	0.1 ppm	±5 vol. %
H_2	EC	0-20000 ppm	1 ppm	±5 vol. %
CH_4	NDIR	0-3 vol.%	0.001 vol.%	±3 vol. %
T_{gas}	NiCr-Ni	0-1100°C	0.1°C	±2°C

2.2.5.2 Raman scattering

Raman scattering in the cold flow is used to analyze mixing between oxidizer and fuel streams with the optical setup shown in Fig 2.32.

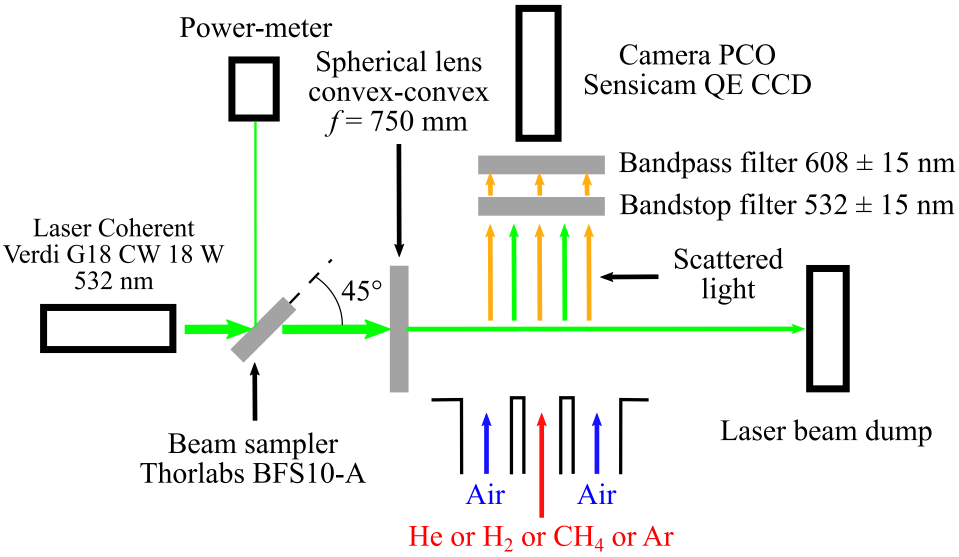

Figure 2.32 – Optical setup used for 1D1S Raman scattering.

It comprises a continuous Coherent Verdi G18 laser producing a p-polarized laser beam at $\lambda = 532$ nm. A part of the laser beam is deviated with a Thorlabs BFS10-A beam sampler to a Thorlabs S425C power meter to monitor the stability of the laser source. The beam is focused in the center of the combustion chamber using a convex-convex spherical lens of 750 mm focal length. The focused laser beam passes through fine slits made in aluminium sidewalls of the combustion chamber and painted in black to limit any reflections. The luminosity of the laser beam, laser reflections and the Rayleigh scattered light are filtered out by a notch optical filter Edmund Optics 532 ± 15 nm OD4. The remaining scattered light is filtered around 605 nm with an OD4 Edmund Optics 86367 15 nm bandpass filter. This optical system enables to record the light scattered by N_2 molecules within air by Raman anti-stokes effect around 607 nm. This wavelength corresponds, for an excitation wavelength of 532 nm, to the only vibrational-rotational band of the dinitrogen molecule with a Raman shift equal to 2328.72 cm^{-1} [110]. Images of the Raman anti-stokes scattered signal are collected with a PCO Sensicam QE equipped with a Nikkor 105 mm f/2.8G lens. Calibrations are made with a set of pure gases before each measurement to deduce the relation between the light intensity and N_2 molar fraction. Since the O_2 to N_2 ratio is constant in air, these data can be used to deduce the mixture fraction. Measurements are first conducted with hydrogen injected in the central lance and air in the annular channel and compared to measurements when hydrogen is replaced with helium. Most measurements are made with helium injected through the central channel but additional measurements are carried out with hydrogen, methane or argon in the central tube.

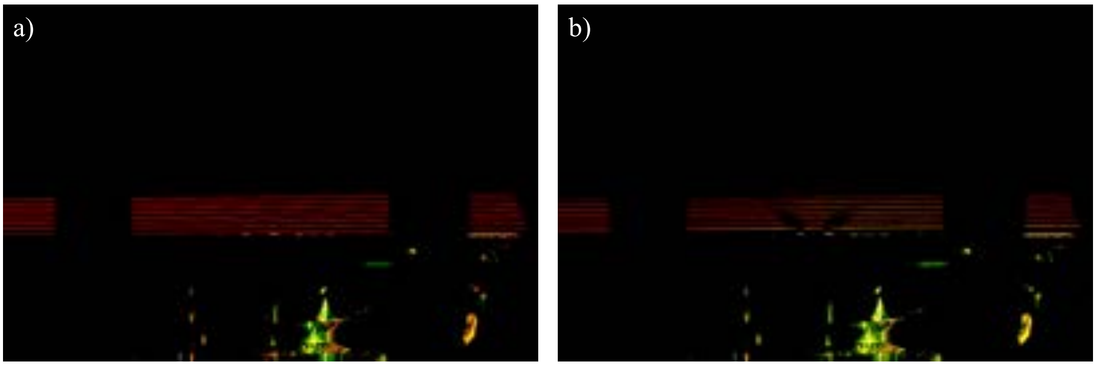

Figure 2.33 – Illustration of scattered light by Raman effect on N_2. (a) Only air is injected through the annular channel and no flow in the central tube. (b) Air is injected through the annular channel and helium in the central tube.

An illustration of Raman scattering from nitrogen is shown in Fig. 2.33. The pictures are taken with a Nikon D7500 and a lens Nikkor 105/2.8G AF-S IF-ED VR MICRO. The lens is equipped with a 605 nm OD4 Edmund Optics 86367 15 nm bandpass filter. The scattered light is recorded with a long exposure time $\tau = 30$ s, during which the height of the focused laser beam is step by step increased. In Fig. 2.33.a, only air is injected through the annular channel without flow in the central tube. The scattered light is uniform on each line, i.e. at the different steps covered by the laser, indicating an uniform concentration of N_2. Figure 2.33.b shows the same experiment repeated with a central injection of helium. In these experiments, the central injector is flush mounted with the combustion chamber backplane $y_i = 0$ mm and a swirl motion $S_i = 0.6$ is conferred to the central flow. The drop of dinitrogen concentration in the expanding central jet is visible on the picture of the scattered light.

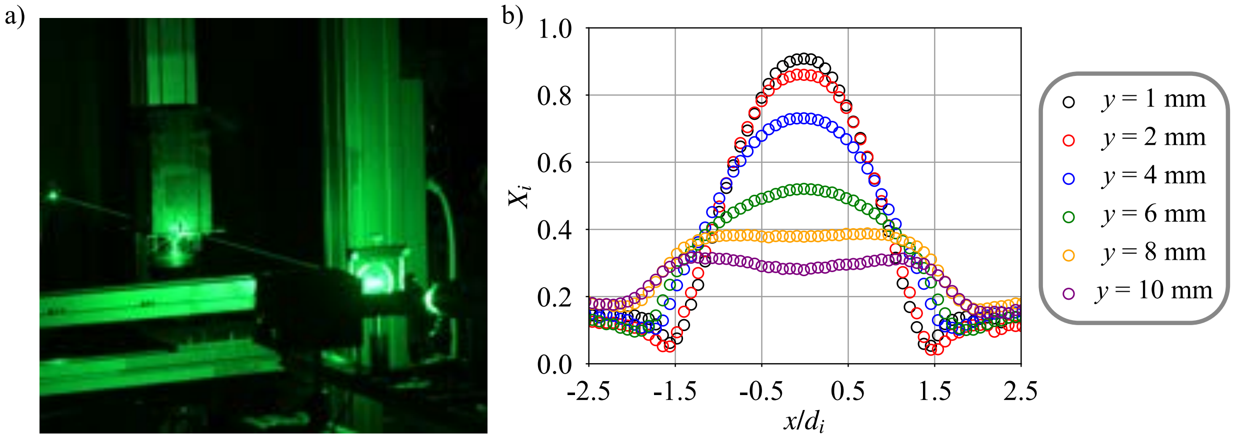

Figure 2.34 – (a) Picture during measurement with the Raman scattering system. (b) Measured concentration profiles of helium along the vertical axis with a flush mounted central injector $y_i = 0$ mm and without swirl in the central jet $S_i = 0.0$. The central injection velocity is set to $u_i = 34$ m/s and the annular injection velocity to $u_e = 28.5$ m/s.

The system in operation with the HYLON combustion chamber is illustrated in Fig. 2.34.a. Figure 2.34.b shows the measured concentration profiles of helium at different heights above the burner with a flush mounted central injector $y_i = 0$ mm and without swirl in the central jet $S_i = 0.0$. The progressive mixing between the annular and the central jet is revealed by increasing the distance of the measurement from the combustion chamber backplane y.

2.2.6 Conclusion

These diagnostics are used in the following chapters to explore the structure of the flow field in cold flow and reactive conditions when the MIRADAS setup is equipped with the DFDS injector and the HYLON injector.

Chapter 3

Flame stabilization regimes

> *"If you want to find the secrets of the universe, think in terms of energy, frequency and vibration."*
>
> Nikola Tesla

Overview

3.1 Flame archetypes

The DFDS and HYLON injectors produce four different flame archetypes shown in Fig. 3.1. This diversity of flame shape is due to the number of parameters that can be varied in the setup: the inner swirl level, the injector recess, the injection velocities and the gas concentrations in each channel.

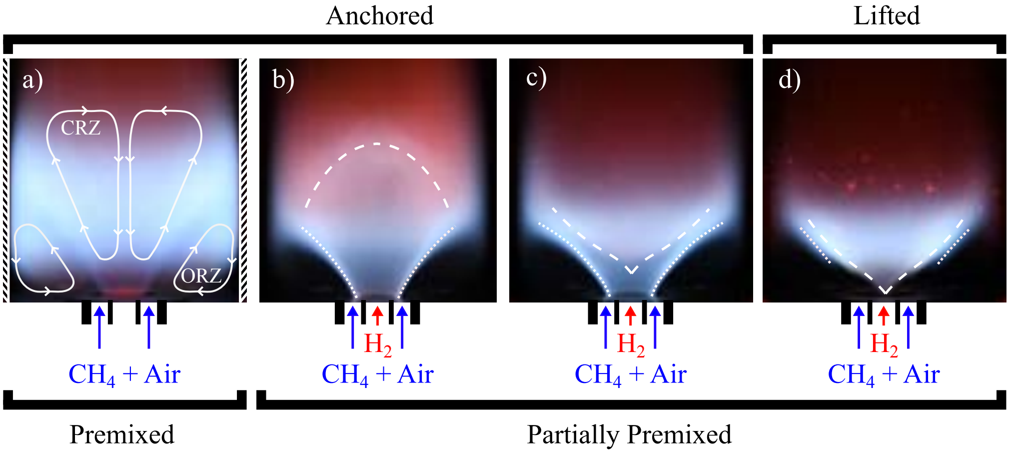

Figure 3.1 – Flame archetypes stabilized on the DFDS burner. (a) Premixed CH_4/air swirling flame with drawings of the Central Recirculation Zone (CRZ) and Outer Recirculation Zone (ORZ). The location of the sidewalls correspond to the hatched on the left and right sides of the image. (b) Attached flame with non-swirling central hydrogen jet. (c) Attached flame with a swirling central hydrogen jet. (d) Lifted flame with a swirling central hydrogen jet. Dotted lines: shear layer stabilized flame. Dashed lines: central reaction layer.

The first archetype is shown in Fig. 3.1.a. It corresponds to a fully premixed methane/air Ref case which is anchored on the hydrogen injector lip for all flow and geometrical configurations of the burner explored in this work. In this case, nothing is injected in the central tube lance and a methane/air mixture is injected in the annular channel. The blue luminosity of the reaction layer corresponds to the chemiluminescence of the CH^* radical (around 430 nm), which is a good tracer of the reaction front location [102]. The three other archetypes in Figs. 3.1.b, 3.1.c and 3.1.d correspond to partially premixed injection conditions in which a fraction of the methane flowrate is removed from the external channel and replaced by hydrogen injected through the central fuel lance. Figures 3.1.b and 3.1.c encompass partially premixed flames slightly protruding inside the external annular injector along the central hydrogen lance. These flames are designated as anchored on the hydrogen injector rim. The flame in Fig. 3.1.b is stabilized on the hydrogen nozzle rim by a reaction layer between the central pilot hydrogen jet and the annular methane/air jet. The reaction layer in the center is stabilized at the top of a weak central recirculation zone (CRZ). This flame archetype is only observed for non-swirling hydrogen jets when $S_i = 0.0$. They feature two distinct diffusion reaction fronts. The first one, on the external side of the flame (white dotted lines in Fig. 3.1.b), extends from the base to the top of the flame and takes place at the stoichiometric interface between the methane/air mixture injected in the annular channel and the hydrogen in the center. The second one, at the top of the flame (white dashed lines in Fig. 3.1.b), has a dome shape. To produce this flame archetype, the central injection velocity needs to be sufficient. The dome shape of the reaction front at the top of the flame is due to the unswirled central hydrogen jet that penetrates deeply into the CRZ. This reaction layer takes place at the stoichiometric interface between hot vitiated gases, produced by the first reaction front and recirculating in the CRZ, and pure hydrogen, injected through the central lance. These flames produce high NOx emissions typical of diffusion flames.

The flame in Fig. 3.1.c features the same diffusion reaction layers anchoring the flame on the hydrogen nozzle and takes a M-shape. The difference with Fig. 3.1.b is the reaction layer in the center of the flow (white dashed lines), which is now stabilized close to the apex of the CRZ and takes a V-shape. This archetype is observed for swirled hydrogen jets featuring a strong CRZ. The V-shape of the central reaction front is attributed to the swirled central injection of hydrogen that leads to a fast expansion of the jet at the outlet of the hydrogen injector.

The last flame archetype is shown in Fig. 3.1.d. Here, the reaction front in the shear layer between the central hydrogen jet and the annular jet is detached from the hydrogen nozzle (white dotted lines). Only a partially premixed flame is active in the center of the flow, which is aerodynamically stabilized above the coaxial injector at a small lift-off height above the hydrogen nozzle. This pattern is observed for swirled hydrogen jets with a high hydrogen injection velocity. This flame shape has the advantage to produce a low thermal stress on the injector lips, due to the relatively large distance between the flame and the injector lips leading to low NOx emission levels thanks to the mixing distance allowed by the aerodynamic stabilization. Small diffusion branches are also visible on the external side of the flame in certain cases (see white dotted lines).

3.2 Influence of inner swirl

Consider first the DFDS injector with the internal hydrogen lance flush mounted with the external annular channel outlet, i.e. $y_i = 0$ mm. Figure 3.2 shows the effect of the inner swirl level S_i for different hydrogen contents injected through the central tube. The global hydrogen content is varied from 0% corresponding to the Ref case with a premixed CH_4/air mixture injected through the annular channel to 100% (PH100). In this latter case, the fuel is hydrogen which is only injected through the central channel corresponding to the HYLON injector configuration. A swirl level $S_e = 0.67$ is applied to the external CH_4/air stream. In the top row in Fig. 3.2, the internal channel is equipped with an axial swirl vane with a trailing edge angle $\alpha_{si} = 0^\circ$ resulting to a swirl level $S_i = 0.0$ in the central hydrogen injection channel. This fake internal swirl vane produces a pressure drop in the hydrogen channel and creates a wake flow downstream the swirler blades. In the bottom row of the figure, the central channel is equipped with an axial swirl vane with a trailing edge angle $\alpha_{si} = 61^\circ$ producing a swirl level $S_i = 0.9$ in the central injection channel. Here, the reference bulk velocity in the external channel is set to $u_{e0} = 24$ m/s and the reference equivalence ratio to $\phi_0 = 0.75$. The corresponding total thermal power is kept constant to $P_{th} = 10.3$ kW. The external bulk injector velocity and the equivalence ratio slightly decrease when the content of hydrogen is increased. The values of the impulsion ratio $J = \left(\rho_e u_e^2\right) / \left(\rho_{H_2} u_i^2\right)$ are indicated at the bottom of the figure. The impulsion ratio J has been shown in some studies to be an important parameter controlling flame liftoff above co-axial injectors [111, 112]. In this configuration, it decreases when the fraction of H_2 increases.

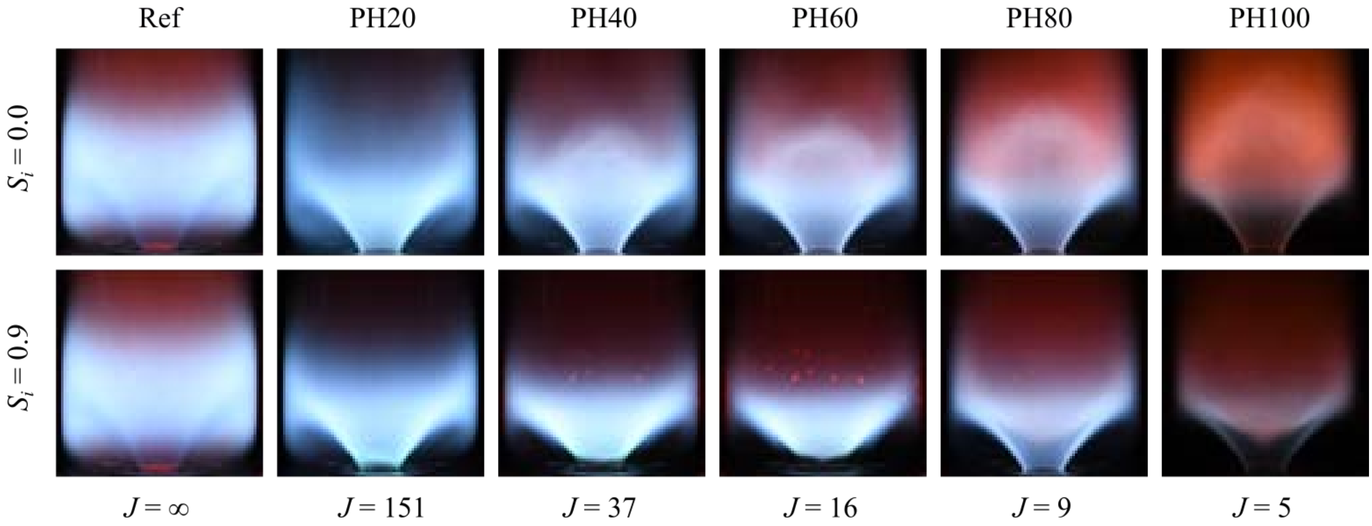

Figure 3.2 – Effect of the inner swirl level for different hydrogen contents using the DFDS injector. The reference bulk velocity is set to $u_{e0} = 24$ m/s and the reference equivalence ratio to $\phi_0 = 0.75$. The injector is flush mounted with the combustion chamber backplane (i.e. $y_i = 0$ mm). Natural flame emission recorded in the visible spectrum.

For this configuration obtained for $u_{e0} = 24$ m/s, $\phi_0 = 0.75$ and without injector recess $y_i = 0$ mm, the top row of Fig. 3.2 shows that all flames are anchored to the central fuel injector as in Figs. 3.1.a and 3.1.b. The flame topology for cases Ref and PH20 in Fig. 3.2 corresponds to the flame archetype shown in Fig. 3.1.a for low hydrogen injection velocities. For higher hydrogen injection velocities, the CRZ for cases PHxx with $xx \geq 40$ is destabilized by the high axial momentum of the central hydrogen jet and the flame takes the shape shown in Fig. 3.1.b. Varying the bulk velocity u_e in the external annular channel or the equivalence ratio does not change the stabilization mode despite large variations of the momentum ratio J. Differences between flames in the top row of Fig. 3.2 are only observed close to the combustion chamber sidewalls and at the top of the flame. The premixed methane/air Ref case on the left features reaction layers stabilized in the ORZ as depicted in Fig. 3.1.a close to the quartz wall that progressively disappear when the hydrogen content increases. As the hydrogen content increases, the velocity of the jet pushes the central reaction zone downstream and a halo forms at the top of the flame as shown in Fig. 3.1.b. For pure hydrogen injection PH100, the hydrogen injection velocity $u_i = 36.3$ m/s exceeds the bulk velocity $u_e = 22.3$ m/s in the annular channel leading to a drop in the momentum ratio to $J = 5$. Without internal swirl vane $S_i = 0.0$, the high momentum of the central fuel jet that penetrates deep into the recirculation zone destabilizes the CRZ when the momentum ratio J drops [111, 113, 114]. The structure of the central jet interacting with the CRZ is a counter-flow streams, where the axial position of the stagnation point depends on the impulsion ratio between the two jets. As a consequence, destabilization of the CRZ increases with the power originating from hydrogen. This is visible in the flame images at the top in Fig. 3.2. The height of the dome shape formed by the reaction front at the top of the flame is pushed further downstream when the central injection velocity increases. Similar observations are made with an injector recess equal to $y_i = 4$ mm.

Figure 3.2 at the bottom, shows flame images with a swirl vane producing a swirl level equal to $S_i = 0.9$ inside the central injection [112, 115, 116]. The Ref case is identical to the case without swirl as in the top row of Fig. 3.2 because no flow is injected through the central lance. The case PH20 is also very similar to the case without swirl in the top row of Fig. 3.2. These two flames correspond again to the flame archetype shown in Fig. 3.1.a. However, as the hydrogen content is further increased, flame topologies become quite different. First, for PH40 and PH60, the halo of luminosity at the top of the flames observed without internal swirl has completely disappeared in the images at the bottom row in Fig. 3.2. For PH40, the flame is lifted above the burner, but one still distinguishes a weak blue/green luminosity close to the central injector lip. Instantaneous snapshots reveal that this pale brightness is associated to a reaction layer that intermittently attaches to the central injector lip, as already observed by Yuasa [115] for methane and hydrogen flames. Increasing further the hydrogen content to reach PH60, the flame becomes fully aerodynamically stabilized above the coaxial injector and more compact as the flame archetype shown in Fig. 3.1.d. This shape is attributed to the strong CRZ that protrudes along the burner axis leading to high radial velocities and high strain rates at the lips of the central fuel lance [116]. The radial deflection of the hydrogen flow leads to a fast mixing between the methane/air mixture exhausting from the annular channel and the swirled hydrogen jet above the fuel lance [117, 118]. By further increasing the hydrogen content to PH80 and PH100, the flame re-attaches to the central injector rim and corresponds to the flame archetype shown in Fig. 3.1.c. Several explanations are possible to explain the flame re-anchoring to the injector lip for high hydrogen contents. This may be due to the low impulsion ratio J, as also identified in [116] for methane oxyflames, or due to a competition between flame front propagation at the leading edge of the flame and the flow, as already investigated in several studies for non swirling flames [86, 90]. Flame stabilization is further investigated in the following to identify the mechanisms responsible for flame re-anchoring.

In the remaining part of the section, the configuration with air in the annular channel and hydrogen in the central channel is adopted (i.e. the HYLON injector) and the resulting flame images are shown in Fig. 3.3. The annular bulk velocity is set to $u_e = 28.5$ m/s and the equivalence ratio fixed to $\phi = 0.46$. The corresponding total thermal power is $P_{th} = 9.7$ kW. The injector is flush mounted with the combustion chamber backplane (i.e. $y_i = 0$ mm). The inner swirl level is varied from $S_i = 0.0$ to $S_i = 0.9$ in Fig. 3.3. Without swirl motion conferred to the central hydrogen flow, the structure of the flame is again identical to the case shown in Fig. 3.1.a (see white dashed lines) with a central reaction zone that takes the form of a dome. In Figs. 3.3.b to 3.3.d, conferring a swirl motion to the central channel leads to shorter flames and a V-shape structure of the central reaction zone as delimited by the white dashed lines in Fig. 3.1.c. Figure 3.3 also shows that the flame shape and the global dimensions are marginally affected by the increase of the inner swirl level from $S_i = 0.4$ to $S_i = 0.9$. The main difference between these flames is the central reaction

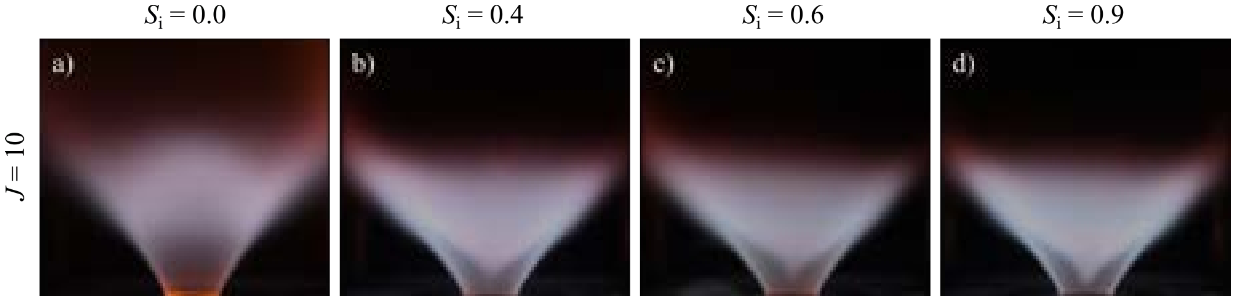

Figure 3.3 – Effect of the inner swirl level on the flame shape using the HYLON injector. The inner swirl level is varied from $S_i = 0.0$ (a) to $S_i = 0.9$ (d). The bulk velocity is set to $u_e = 28.5$ m/s and the reference equivalence ratio to $\phi = 0.46$. The injector is flush mounted with the combustion chamber backplane, i.e. $y_i = 0$ mm. Natural flame emission recorded in the visible spectrum.

zone that is pushed upstream when the swirl level increases. This effect is attributed to the increase of the transverse pressure gradient due to the increase of the swirl level in the central channel.

For the case without swirl motion conferred to the central hydrogen stream, flames are always anchored to the hydrogen rim independently of the range of momentum ratio J that was covered $J > 1$. These experiments made without injector recess $y_i = 0$ mm show that applying a swirl motion to the inner hydrogen channel is a necessary condition to lift the flame above the injector, in both DFDS and HYLON configurations, for the range of operating conditions explored in this study. But without injector recess, these tests also show that the range of operating conditions with lifted flames is narrow, especially with the HYLON injector that is only powered by hydrogen.

3.3 Influence of injector recess

The impact of the injector recess is first considered with the DFDS injector. The inner swirl level is fixed to $S_i = 0.9$ in this section. Figure 3.4 illustrates the influence of the injector recess on the stabilization regime for a reference bulk velocity in the annular channel $u_{e0} = 24$ m/s and a reference equivalence ratio $\phi_0 = 0.75$. Flame stabilization regimes are compared for different hydrogen contents and for hydrogen injectors with different recess $y_i = 0$ mm and $y_i = 4$ mm. The top row of Fig. 3.4 is the same as the bottom row of Fig. 3.2.

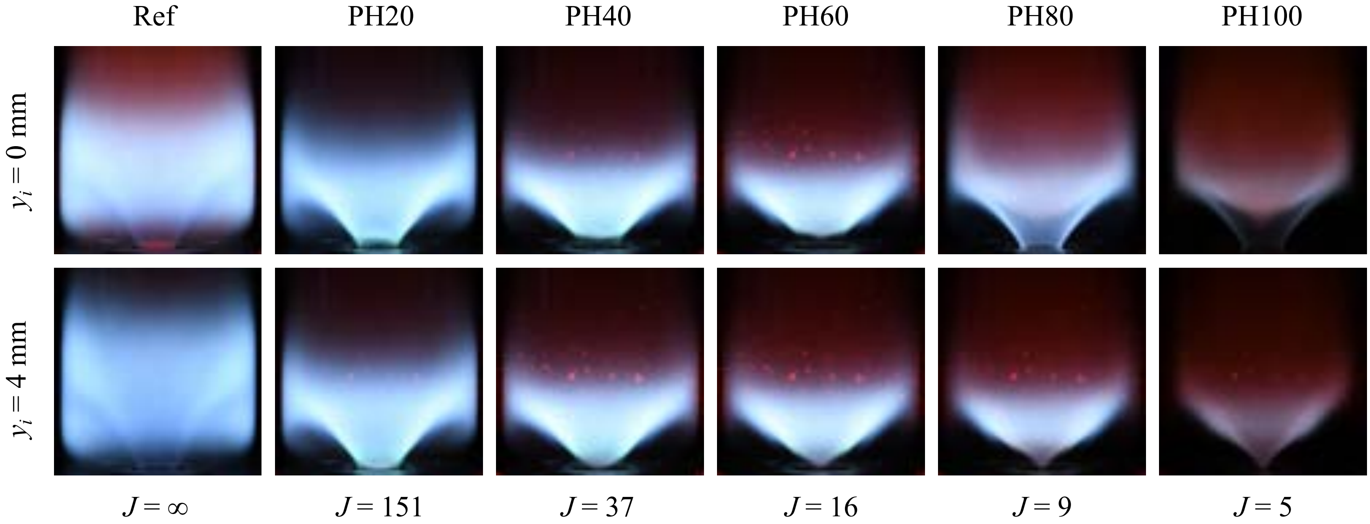

Figure 3.4 – Effect of the injector recess y_i for different hydrogen contents using the DFDS injector. The reference bulk velocity is set to $u_{e0} = 24$ m/s and the reference equivalence ratio to $\phi_0 = 0.75$. The inner swirl level is $S_i = 0.9$. Natural flame emission recorded in the visible spectrum.

Figure 3.4 at the bottom shows the shapes of the flames when the recess distance is set to $y_i = 4$ mm. For PH20, the flame is intermittently lifted but the mean image shows that it is preferentially stabilized inside the annular injector. For higher hydrogen contents, all flames are aerodynamically stabilized above the burner with a flame root lying close to the outlet of the co-axial DFDS burner above the central hydrogen lance. For PH40, the base of the flame has a rounded shape that becomes sharper and more compact in the radial direction for higher hydrogen injection velocities with PH60, PH80 and PH100.

The wider operability range with aerodynamically stabilized flames can hardly be explained at this stage of this study. However, the following observation is made. For a fixed hydrogen bulk velocity, the strong recirculation along the centerline inside the CRZ leads to a strong flow blockage and consequently to a flow acceleration that is reported on the external side of the injector. This hypothesis will be further investigated when exploring the structure of the velocity field in Chapter 4.

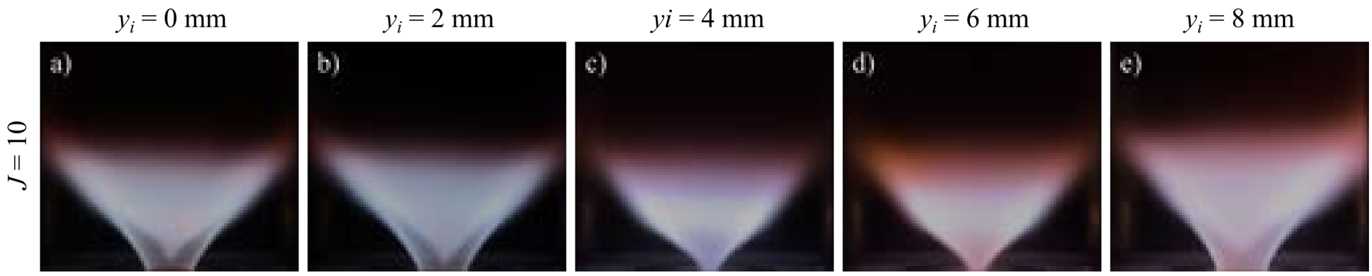

Figure 3.5 – Effect of the injector recess with the HYLON injector. The injector recess is varied from $y_i = 0$ mm (a) to $y_i = 8$ mm (e). The air bulk velocity is set to $u_e = 28.5$ m/s and the equivalence ratio to $\phi = 0.46$. The inner swirl level is $S_i = 0.9$. Natural flame emission recorded in the visible spectrum.

Experiments are now repeated with the HYLON injector for H_2/air flames. Increasing the injector recess from $y_i = 0$ to 2 mm, the base of the CRZ protrudes further upstream inside the flow in Fig. 3.5. Increasing the recess distance helps to lift the flame. The flame initially anchored in Figs. 3.5.a and 3.5.b is lifted in Figs. 3.5.c and 3.5.d. Interestingly for $y_i = 8$ mm in Fig. 3.5.e, the flame re-attaches to the hydrogen injector rim. This cannot easily be explained without further investigation. These observations serve as a baseline to the rest of this study.

In conclusion, it has been shown that the injector recess y_i drastically increases the range of operability of the burner with aerodynamically stabilized flames. An injector with recess and with inner swirl allows to lift H_2/air flames, while when y_i is set to 0 mm, no configuration has been found to produce H_2/air lifted flames.

3.4 Influence of injection velocities

The geometrical configurations of the DFDS and HYLON injectors with swirl motion and recess, yielding the widest operability range with aerodynamically stabilized flames are analyzed. The influence of global equivalence ratio ϕ and external channel bulk injection velocity u_e on the stabilization mode and shape taken by the flames is explored for two hydrogen contents. The first case is PH40 with methane/air mixture in the external annular channel and pure hydrogen in the central lance. The molar fraction of hydrogen in the fuel blend corresponds in this case to $X_{H2}^{f} = 0.67$. The second one PH100 is only powered by hydrogen with $X_{H2}^{f} = 1.00$ through the central lance and air flowing in the annular channel.

Figure 3.6 shows nine operating points corresponding to reference bulk velocities $u_{e0} = 12$, 24 and 30 m/s and global equivalence ratio $\phi = 0.51$, 0.60 and 0.69. In Figs. 3.6.a and 3.6.b, flames are anchored to the central hydrogen lance, corresponding to the flame archetype shown in Fig. 3.1.c. In these cases, the hydrogen injection velocity is low, $u_i = 5.4$ and 6.4 m/s in Figs. 3.6.a and 3.6.b respectively, compared to the external injection velocity $u_{e0} = 12$ m/s. The CRZ above the central injector is weak. The radial velocity of the swirled hydrogen flow at the central tube outlet is too low to quench the combustion reaction above the injector lip [116]. All other flames in Fig. 3.6 are lifted due to the higher hydrogen injection velocities. The flow close to the central tube outlet is in these cases submitted to higher radial hydrogen velocities

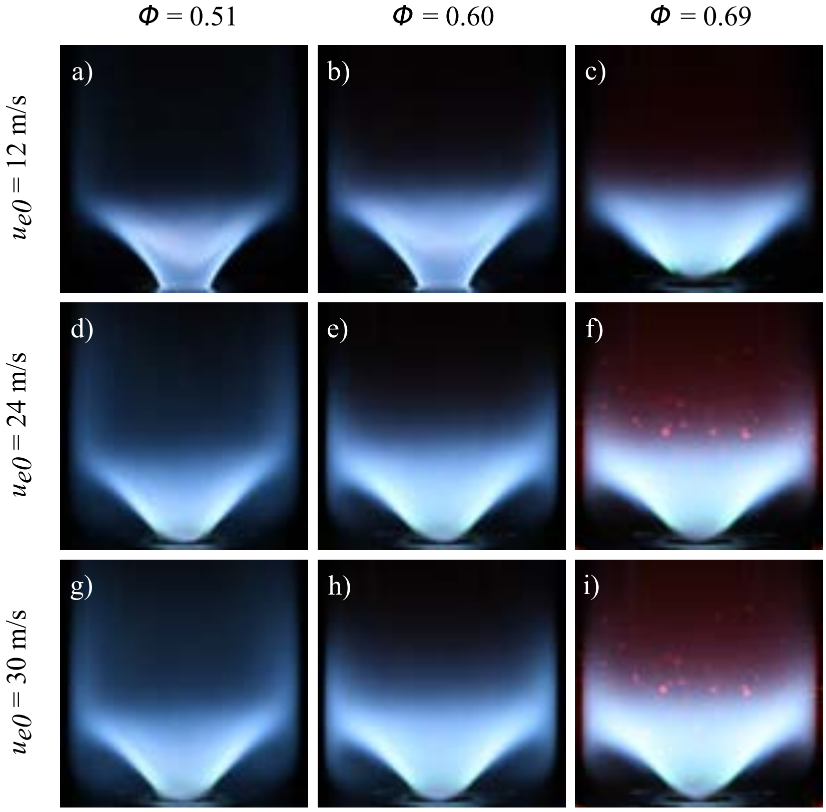

Figure 3.6 – Impact of the external bulk velocity u_{e0} and equivalence ratio ϕ on flame stabilization for $S_i = 0.9$, $y_i = 4$ mm and PH40 case. Natural flame emission in the visible spectrum. Flames are labeled (a) to (i) as function of the reference velocity u_{e0} in the external channel and global equivalence ratio ϕ.

and combustion has more difficulty to take place. An aerodynamic stabilization mode above the injector becomes more favorable. The lifted flames have a V-shape in Figs. 3.6.c to 3.6.i. Combustion may also take place in the ORZ of the burner when the equivalence ratio or the external bulk velocity increases as in Figs. 3.6.e to 3.6.i. This figure also shows that for a CH_4/H_2 fuel blend with 40% of power originating from hydrogen, increasing the equivalence ratio at constant external injection velocity u_{e0} (Figs. 3.6.a, 3.6.b and 3.6.c) or increasing the hydrogen bulk injection velocity at fixed equivalence ratio ϕ (Figs. 3.6.a, 3.6.d and 3.6.g) helps lifting the flame.

Figure 3.7 shows the shape taken by the flames sharing the same reference bulk velocities, reference equivalence ratios and thermal powers as in Fig. 3.6, but when only hydrogen is injected through the central tube to power the burner (PH100). As for PH40, the flames in Figs. 3.7.a and 3.7.b are anchored to the lips of the central hydrogen lance and feature two different reaction branches. The ones stabilized in the shear layer of the swirled flow are sharp with a blue/gray colour attributed to naturally excited $H_2O_2^*$ molecules [119]. The other V-shape structure stabilized in the center of the flow further downstream is orange/red. Schefer and al. [120] attribute this orange/red radiation to H_2O^* chemiluminescence. All other flames in Fig. 3.7 are aerodynamically stabilized above the burner, but take slightly different shapes compared to Fig. 3.6. Flames in Fig. 3.7 are more compact due to the higher reactivity and burning velocity of pure H_2 compared to the H_2/CH_4 blends. The blue luminosity visible in the ORZ for PH40 in Fig. 3.6 disappears for PH100 in Fig. 3.7. The flame root also protrudes further upstream along the burner axis for pure hydrogen with a narrower radial extension. As already observed in Fig. 3.6 for PH40, increasing the equivalence ratio at constant external injection velocity (Figs. 3.7.a, 3.7.b and 3.7.c) or increasing the hydrogen injection velocity at fixed equivalence ratio (Figs. 3.7.a, 3.7.d and 3.7.g) helps lifting the flame. The only difference is that the hydrogen lift-off velocity, i.e. the minimum velocity at which hydrogen needs to be injected to obtain a lifted flame, increases with the power originating from hydrogen combustion. This is attributed to the higher reactivity of the pure H_2 flames compared to the H_2/CH_4 flames studied in Fig. 3.6.

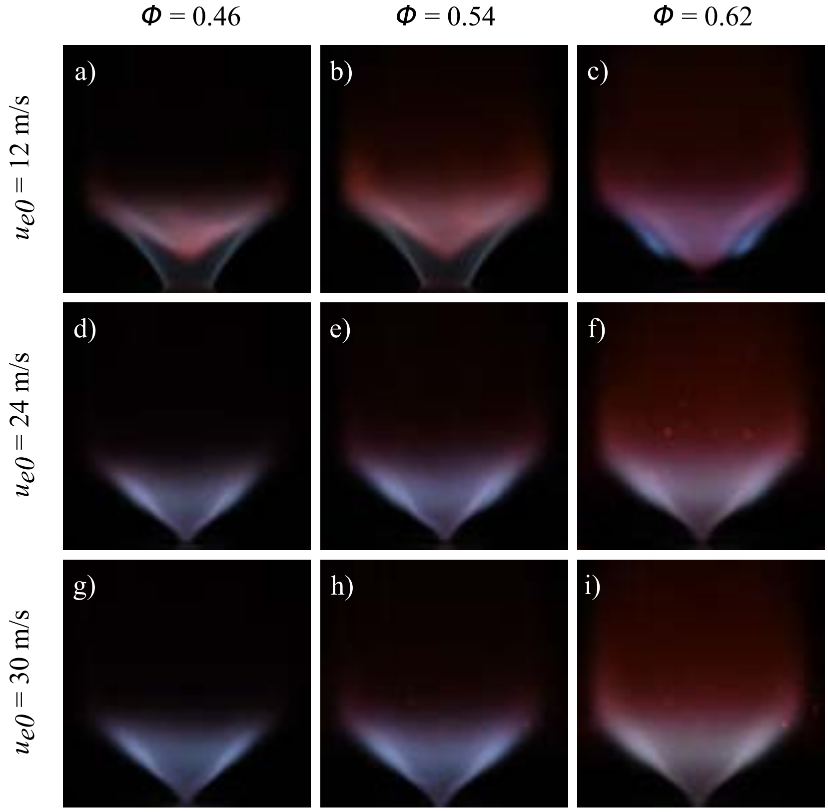

Figure 3.7 – Impact of the external bulk velocity u_{e0} and equivalence ratio ϕ on flame stabilization for $S_i = 0.9$, $y_i = 4$ mm and PH100 case. Natural flame emission in the visible spectrum. Flames are labeled (a) to (i) as function of the reference velocity u_{e0} in the external channel and global equivalence ratio ϕ.

These series of experiments highlighting shape transitions also help understanding the origin of the structure of the reaction layers of the V-shaped aerodynamically stabilized flames powered by pure hydrogen in Fig. 3.7. When the equivalence ratio is increased from $\phi = 0.46$ to $\phi = 0.62$ and the external annular injection velocity is fixed to $u_{e0} = 12$ m/s, Fig. 3.7 shows that the orange/red V-shaped structure close to the combustion axis progressively protrudes further upstream inside the CRZ at the expense of the blue/gray reaction layers stabilized in the external shear layer of the annular swirled jet that progressively vanishes at the flame bottom. Progressing now along a path at fixed equivalence ratio $\phi = 0.62$ in Fig. 3.7 and increasing the air velocity to $u_{e0} = 24$ m/s in the annular channel further reduces the reactivity of the external blue reaction layer that is pushed further downstream and completely disappears for $u_{e0} = 30$ m/s. In the mean time, the base of the flame progresses further upstream towards the injector. These nine flames, including flames (a) and (g) in Fig. 3.7 serve as references for experiments and numerical flow simulations of the HYLON injector [92].

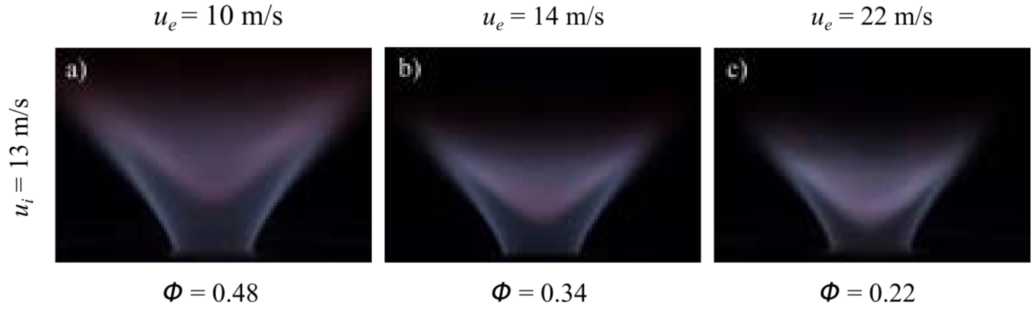

Figure 3.8 – Impact of the air injection velocity u_e for a fixed hydrogen injection velocity $u_i = 13$ m/s. The inner swirl level is $S_i = 0.6$ and the injector recess is $y_i = 4$ mm. The air bulk velocity is varied from $u_e = 10$ m/s to $u_e = 22$ m/s from (a) to (c). Natural flame emission in the visible spectrum.

For a given hydrogen flowrate, it is interesting to explore if blowing more air in the external channel can be used to trigger transition from anchored to lifted flames. Except blowing at excessively high air flowrates, it was found that increasing the air velocity u_e cannot be used to trigger easily a transition from an anchored to a lifted flame. This is illustrated in Fig. 3.8 for an anchored flame on the hydrogen injector. The inner swirl level is $S_i = 0.6$ and the injector recess is $y_i = 4$ mm. The hydrogen velocity is fixed to $u_i = 13$ m/s and the air velocity is varied from $u_e = 10$ m/s to 22 m/s in Figs. 3.8.a to 3.8.c. The momentum ratio varies in these experiments from $J = 9$ to 41. The flame shortens as u_e increases due to the increase of the recirculation velocity inside the CRZ with the bulk velocity u_e, but the flame remains attached to the hydrogen injector nozzle. This relative insensitivity to the air velocity may originate from a small recirculation region located along the external wall of the hydrogen channel due to the relatively strong swirl $S_e = 0.67$ imparted to the annular air stream. This zone causes an aerodynamic flow blockage in the annular air channel and has been identified in companion LES simulations. Boundary layer separation takes place at the extremity of the air annular channel as shown in [92] because the thickness of the boundary layer increases along the vertical axis due to the transverse pressure gradient created by the swirl motion imparted to the air flow [121]. Examination of transitions from lifted to anchored flames shows that they also slightly depend on the air co-flow velocity. For a fixed geometry and fuel injection velocity the hydrogen threshold injection velocity u_i above which the flame switches from a lifted to an anchored flames, i.e. flame re-anchoring, increases linearly with the air bulk velocity u_e.

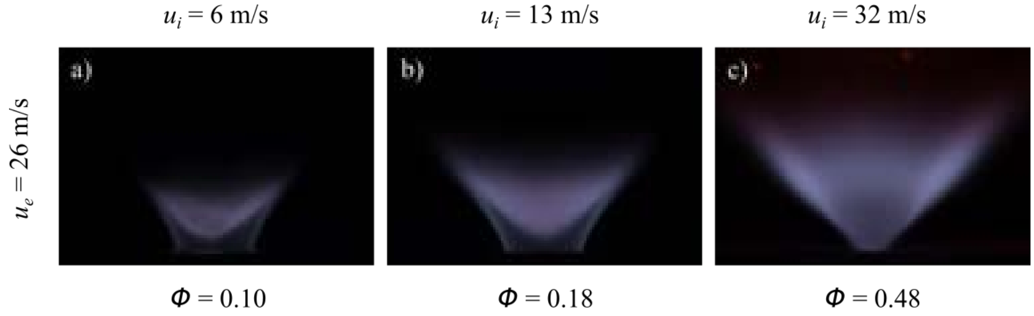

Figure 3.9 – Impact of the hydrogen injection velocity u_i for a fixed air injection velocity $u_e = 26$ m/s. The inner swirl level is $S_i = 0.6$ and the injector recess is $y_i = 4$ mm. The central injection velocity is varied from $u_i = 6$ m/s to $u_i = 32$ m/s from (a) to (c). Natural flame emission in the visible spectrum.

Effect of the hydrogen injection velocity u_i is now explored in Fig. 3.9 by fixing the air flowrate and varying the hydrogen flowrate. The inner swirl level is $S_i = 0.6$ and the injector recess is $y_i = 4$ mm. The air injection velocity is set to $u_e = 26$ m/s and the hydrogen velocity is increased from $u_i = 6$ to 32 m/s. At low hydrogen injection velocities, the flame is anchored on the hydrogen injector in Fig. 3.9.a for $u_i = 6$ and 13 m/s and switches to a lifted flame in Fig. 3.9.c for $u_i = 32$ m/s for hydrogen injection velocities higher than $u_i = 18$ m/s. Above this threshold value for the hydrogen velocity u_i, the flame remains lifted if it is initially in this stabilization regime. A different value is found for a geometrical configuration with a different internal swirl number S_i or injector recess y_i. This threshold hydrogen velocity leading to a lifted flame also slightly depends on the air velocity. However, for a fixed burner geometry, the hydrogen velocity u_i appears clearly as the main parameter controlling flame stabilization. This dependence is quantified in the following section.

3.5 Stabilization map

For a fixed swirl number $S_e = 0.67$ of the external air stream, the main parameters altering flame stabilization are the internal swirl number S_i, the hydrogen injector recess distance y_i and the hydrogen injection velocity u_i. Figure 3.10.a plots the hydrogen threshold velocity u_i above which lifted flames are observed as a function of the injector recess y_i for different levels of internal swirl S_i. The air bulk velocity is set to $u_e = 26$ m/s in these experiments.

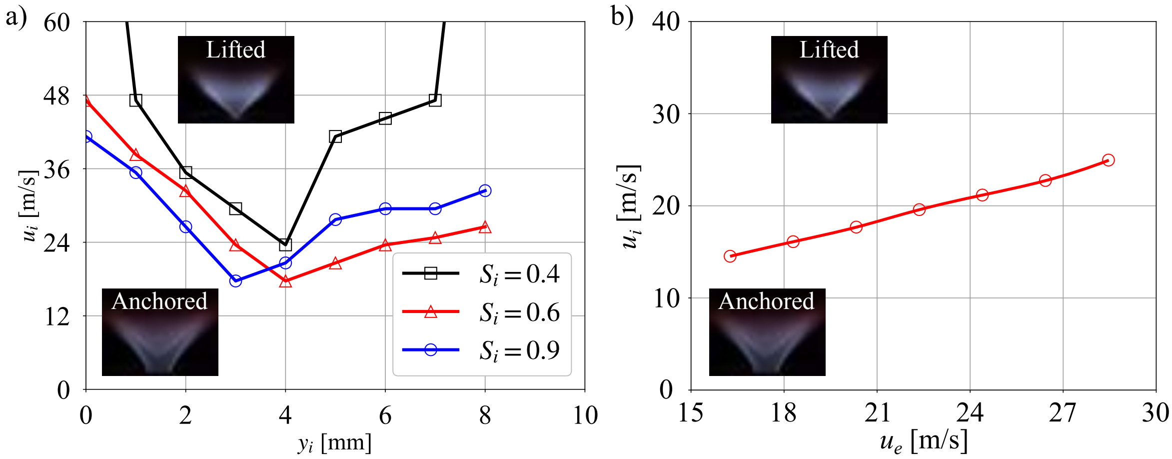

Figure 3.10 – (a) Transition from lifted to anchored stabilization mode as a function of the injector recess y_i and threshold hydrogen velocity u_i for three values of internal swirl number $S_i = 0.4$, 0.6 and 0.9. External air velocity $u_e = 26$ m/s. (b) Transition from lifted to anchored stabilization mode as a function of the air bulk velocity u_e. The inner swirl level is set to $S_i = 0.6$ and the injector recess to $y_i = 3$ mm.

Without internal swirl $S_i = 0.0$, flames remain anchored on the hydrogen injector rim for all tested values of recess distance and hydrogen injection velocity. For a moderate internal swirl number $S_i = 0.4$, flames are still anchored on the hydrogen injector rim without recess, but can be lifted with recess. For this internal swirl level, the optimal value is obtained for a recess $y_i = 4$ mm. In this case, blowing hydrogen with a velocity higher than $u_i = 24$ m/s leads to lifted flames. This threshold value for the hydrogen velocity above which flames are lifted above the hydrogen injector is designated in the following as the lift-off hydrogen velocity. For a higher internal swirl number $S_i = 0.6$, the optimal recess distance $y_i = 4$ mm remains unaltered, but the lift-off hydrogen velocity drops to $u_i = 18$ m/s. When the internal swirl number is further increased to $S_i = 0.9$, the optimal recess shifts to $y_i = 3$ mm, but the lift-off hydrogen velocity $u_i = 18$ m/s remains unchanged. These results are shown to linearly depend on the air flow velocity in Fig. 3.10.b.

3.6 Conclusion

A parametric analysis of flame stabilization regimes has been carried out. The main parameters driving flame stabilization mode have been identified for configurations with a fixed injector diameter and fixed swirl level in the air channel. The swirl level inside the hydrogen lance, the recess distance of the central hydrogen lance with respect to the annular channel outlet, the hydrogen content and the velocities in both external and central channels have been varied. The influence of each parameter has been studied independently to isolate each impact on flame stabilization. The main observations are:

- A swirl motion conferred to the central flow is a necessary condition to lift hydrogen flames above the injector.
- The probability to stabilize a lifted flame decreases with the increase of hydrogen content.
- A small injector recess greatly enlarges the operability of the burner with aerodynamically stabilized lifted flames.
- The injection velocity of hydrogen needs to exceed a threshold to obtain lifted flames.
- This threshold level for the hydrogen injection velocity linearly depends on the external channel injection velocity.
- An optimum for the injector recess distance exists for each value of the swirl level conferred to hydrogen stream.

In the following chapters, these observations are used to guide experiments made on the velocity field and low order modeling.

CHAPTER 4

Cold flow velocity field

> *"I am one of those who think that science is of great beauty. A scientist in his laboratory is not only a technician: he is also a child placed in front of a natural phenomena which impress him like fairy tales."*
>
> MARIE CURIE

Overview

Particle Image Velocitmetry (PIV) is used to characterize the mean and RMS values of the velocity field in the axial plane of the burner under cold flow conditions. The setup including the seeding system is described in Chapter 2. For safety reasons, PIV measurements in cold flow conditions are carried out by replacing the central flow of hydrogen by the same volumetric flowrate of air in the first part of this section, and then by helium in the second part. This second strategy leads to a jet momentum closer to operation with hydrogen and a better quality of the seeding for particles injected through the central tube. In this later case, the momentum of the central jet is however still higher than with hydrogen injection due to the higher molar weight of helium. Tests are first made to explore the impact of these choices on the structure of the flow field at the burner outlet.

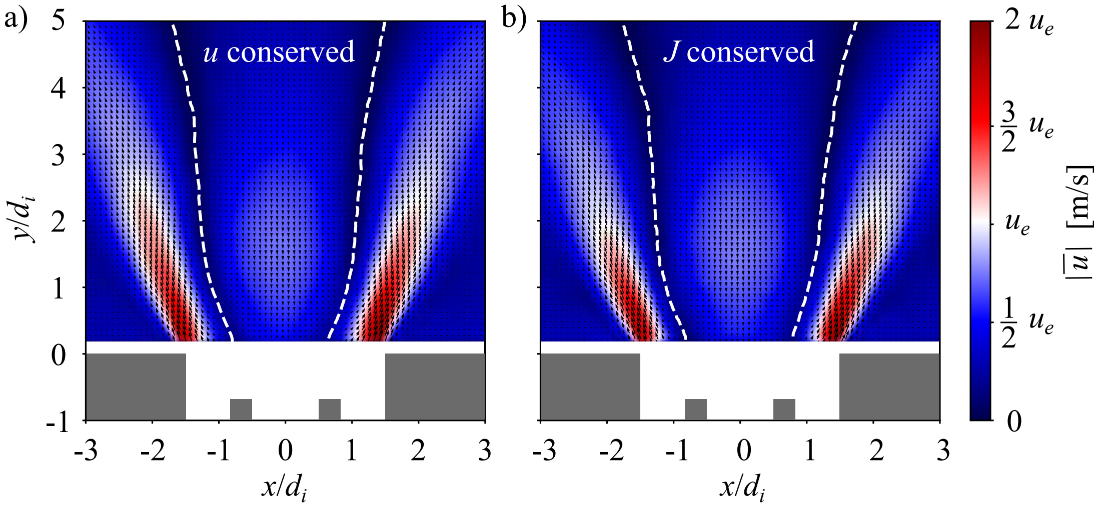

Figure 4.1 – Mean velocity field in the axial plane for an internal swirl level $S_i = 0.6$ and a central injector recess $y_i = 4$ mm. Air is injected in the internal and external channels with (a) the same bulk velocity $u_i = 34$ m/s and (b) the same momentum ratio $J = 10.1$ as the reactive case with hydrogen injected through the central tube. Results are normalized by the bulk air velocity $u_e = 28.5$ m/s in the external channel. The white dashed lines delineate the boundary of the CRZ where $u_z = 0$ m/s.

Figure 4.1 shows the flow field measured in the axial plane for a swirl level $S_i = 0.6$, a recess $y_i = 4$ mm and an air bulk velocity $u_e = 28.5$ m/s. Figure 4.1.a shows the case where the bulk velocity $u_i = 34$ m/s in the central tube is equal to the reference operating point in reactive conditions with hydrogen injected through the central tube. Figure 4.1.b shows the case where the momentum ratio $J = 10.1$ is kept constant between the two streams in cold (air/air) and reactive (H_2/air) conditions by adapting the central flowrate. The structure of the flow field is similar in both cases. The intensity of the recirculation in the CRZ and the swirling jet spread angle in Fig. 4.1.b are slightly higher than in Fig. 4.1.a i.e. when the velocities remain fixed. These differences are small. For reasons explained in Chapter 7, the injection velocities are conserved in most experiments in cold flow conditions.

4.1 Influence of inner swirl

It has been concluded in Chapter 3 that conferring a swirl motion to the central hydrogen flow is a necessary condition to lift a flame above the injector. In the following tests, the injector is flush mounted with the combustion chamber backplane with $y_i = 0$ mm. PIV data are used to explore conditions leading to a stable and strong CRZ when the central fuel injection tube is equipped with a swirler. The coordinates (x, y) are made dimensionless by the inner diameter of the central injector d_i. Data shown for the velocity fields are averaged over a minimum of 800 instantaneous snapshots. Three values of the inner swirl level varying from $S_i = 0.0$ to $S_i = 0.9$ are considered.

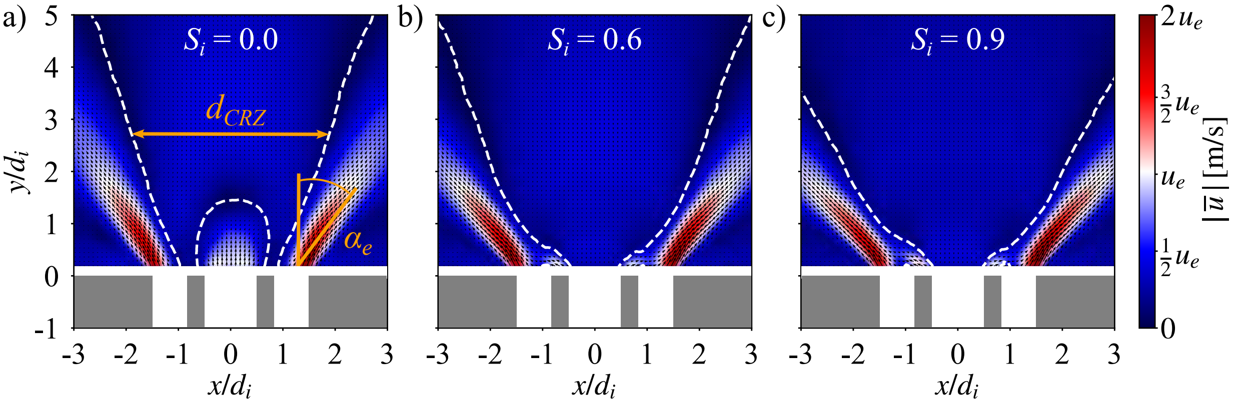

Figure 4.2 – Mean velocity field in the axial plane for an inner swirl level varying from $S_i = 0.0$ (a) to $S_i = 0.9$ (c) without hydrogen injector recess $y_i = 0$ mm. Data are normalized by the bulk air velocity $u_e = 28.5$ m/s in the external channel. The central injection velocity is $u_i = 34$ m/s. The white dashed lines delineate the boundary of the CRZ where $u_z = 0$ m/s. Air is injected in the central and external channels.

Figure 4.2 shows data collected for $u_e = 28.5$ m/s and $u_i = 34$ m/s, corresponding to flame G in Fig. 3.7.g. PIV data are only valid 1 mm above the burner outlet in Fig. 4.2. Without inner swirl $S_i = 0.0$, the CRZ produced by the annular swirling jet in Fig. 4.2.a is pushed downstream by the central jet, as already discussed in [111, 113]. Without recess, hydrogen flames are all anchored to the central injector rim for all the operating points explored. When the central jet is swirled, as in Fig. 4.2.b with $S_i = 0.6$, the size of the CRZ drastically increases and penetrates inside the central tube leading to a strong flow blockage at the outlet of the internal injector between $-0.5 \leq x/d_i \leq 0.5$. This flow blockage is accompanied by large radial velocities close to $x/d_i = 0.5$, corresponding to the radial position of the central injector lip [116]. As a consequence, the angle of the swirling jet arms widens. In this case, the expanding central jet cuts the low velocity zone above the injector lips observed in Fig. 4.2, that prevents the flame to re-anchor. In Fig. 4.2.c, the swirl level is increased to $S_i = 0.9$, the diameter of the CRZ increases and the radial velocities above the injector lips too. Moreover, increasing the inner swirl level S_i increases also the angle α_e of the jet flow. Values of the angle α_e of the jet flow are reported in Tab. 4.1 as a function of the inner swirl level S_i.

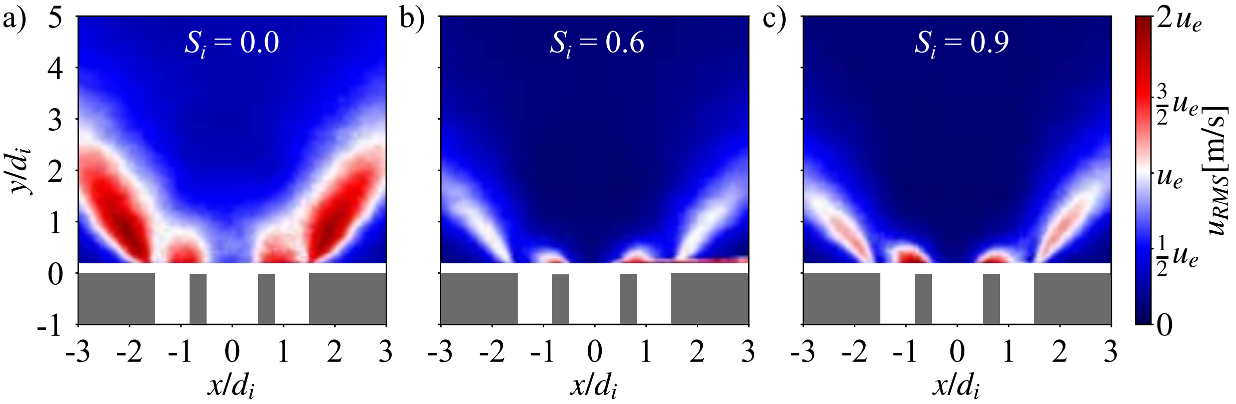

Figure 4.3 – RMS velocity field in the axial plane for an inner swirl level varying from $S_i = 0.0$ (a) to $S_i = 0.9$ (c) without hydrogen injector recess $y_i = 0$ mm. The fields are normalized by the bulk air velocity $u_e = 28.5$ m/s in the external channel. The central injection velocity is $u_i = 34$ m/s. Air is injected in the central and external channels.

The impact of the swirl level in the central injection channel on the RMS velocity field is now analyzed. Without swirl imparted to the central jet, the flow is highly fluctuating in Fig. 4.3.a. The annular swirled flow exhibits RMS fluctuations of the order of $2u_e$, i.e. values close to the maximum value of the local mean velocity in Fig. 4.2.a. Moreover, in the wake above the central injector lip, i.e. between the central and the external flow, another zone with high velocity fluctuations is visible in Fig. 4.3.a in a region where the mean velocity remains low. The central unswirled jet exhibits low RMS velocity fluctuations. When a swirl level $S_i = 0.6$ is conferred to the central flow in Fig. 4.3.b, the RMS velocity fluctuations in the jet arms are substantially reduced. Now, large fluctuations are only measured in the wake of the hydrogen injector lips. This is attributed to the flow acceleration caused by the flow blockage of the CRZ at the outlet of the central injector. In the CRZ, RMS fluctuations remain very low $u_{RMS} < 1/2u_e$. When the inner swirl level is increased to $S_i = 0.9$, Fig. 4.3.c is very similar to Fig. 4.3.b except that the RMS values slightly increase in both central and annular jets. These data confirm that the CRZ is more stable with less fluctuations when a swirl is imparted to the central injection.

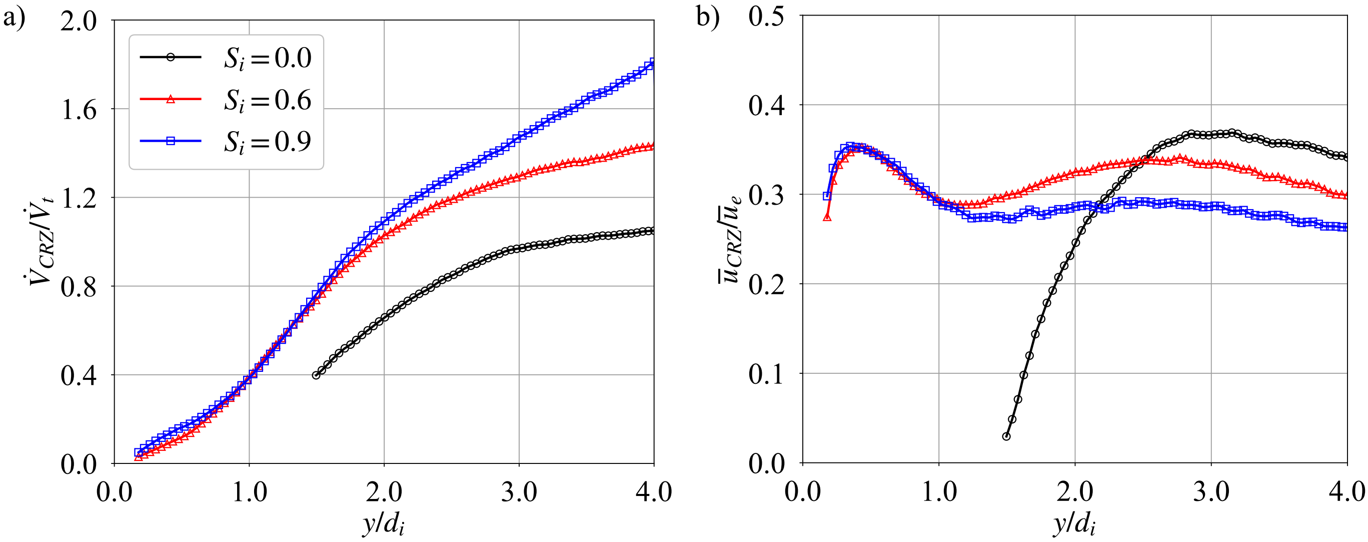

Figure 4.4 – Impact of the inner swirl level S_i on the CRZ. (a) Normalized recirculation volumetric flowrates $\dot{V}_{CRZ}/\dot{V}_t$ in the CRZ. (b) Normalized velocities $\overline{u}_{CRZ}/\overline{u}_e$ in the CRZ along the centerline at $x = 0$ mm.

Data in Fig. 4.2 are further scrutinized. The recirculating flow in the CRZ and the velocity along the centerline are examined. The recirculating volumetric flowrate $\dot{V}_{CRZ}$ is normalized by the total inlet flowrate $\dot{V}_t = \dot{V}_e + \dot{V}_i$ where $\dot{V}_e$ and $\dot{V}_i$ are the volumetric flowrates through the external and internal injection channels. Figure 4.4.a shows that the central jet penetrates up to $1.5d_i$ along the burner axis when no swirl $S_i = 0.0$ is conferred to the central flow. The maximum recirculating flowrate $\dot{V}_{CRZ}$ is equal in this case to the total inlet flowrate $\dot{V}_t$, $\dot{V}_{CRZ}/\dot{V}_t = 1.0$ for axial locations $y > 3d_i$. When swirl is conferred to the central flow, the flowrate recirculating in the CRZ increases. Figure 4.2 shows that the CRZ extends from the central injector outlet to the upper limit of the PIV window when $S_i = 0.6$ or 0.9. High fidelity 3D simulations indicate that the CRZ penetrates slightly inside the central injector tube [92]. From $y/d_i = 0.0$ to $y/d_i = 1.5$, the normalized recirculation flowrates are approximately equals for $S_i = 0.6$ and 0.9. For distances from the injector lip higher than $y/d_i > 1.8$, the recirculation flowrate $\dot{V}_{CRZ}$ is higher than the total inlet flowrate $\dot{V}_t$, i.e. $\dot{V}_{CRZ}/\dot{V}_t > 1.0$, and increases with the internal swirl level S_i. The fact that more flow recirculates than the total injected flowrate shows how strongly the swirler drives the recirculating flow. As conclusion, the stability of the CRZ and the flowrate recirculating inside the CRZ are enhanced by the installation of a swirling vane inside the central injector. Furthermore, Fig. 4.4.b also indicates that the increased flowrate recirculating through the CRZ is mainly due to the increase of the CRZ diameter (see Fig. 4.2) because the velocities in the CRZ are slightly lower for the case with inner swirl.

Figure 4.5 indicates that the recirculating flowrate shown in Fig. 4.4 is correlated with the diameter of the CRZ. So far experiments were conducted with air in the external and internal channels. To analyze a more representative structure of the central hydrogen jet in cold flow conditions, additional PIV measurements are carried out by replacing the central hydrogen flow by the same volumetric flowrate of helium, a gas with a density closer to hydrogen. The PIV window is also adjusted to zoom on the central jet and increase spatial resolution. Results for the effect of the inner swirl level on the central jet are presented in Fig. 4.6. As the configuration is symmetric with respect to the burner axis only the right part of the flow field is presented in Fig. 4.6.

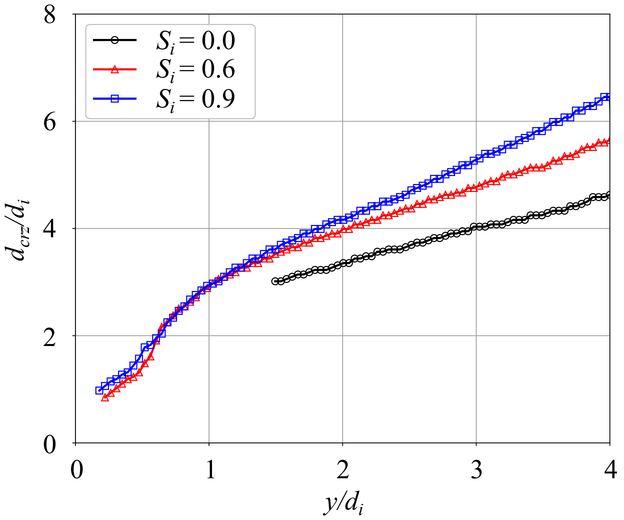

Figure 4.5 – Impact of the inner swirl level S_i on the normalized diameter of the CRZ d_{CRZ}/d_i along the normalized vertical axis y/d_i.

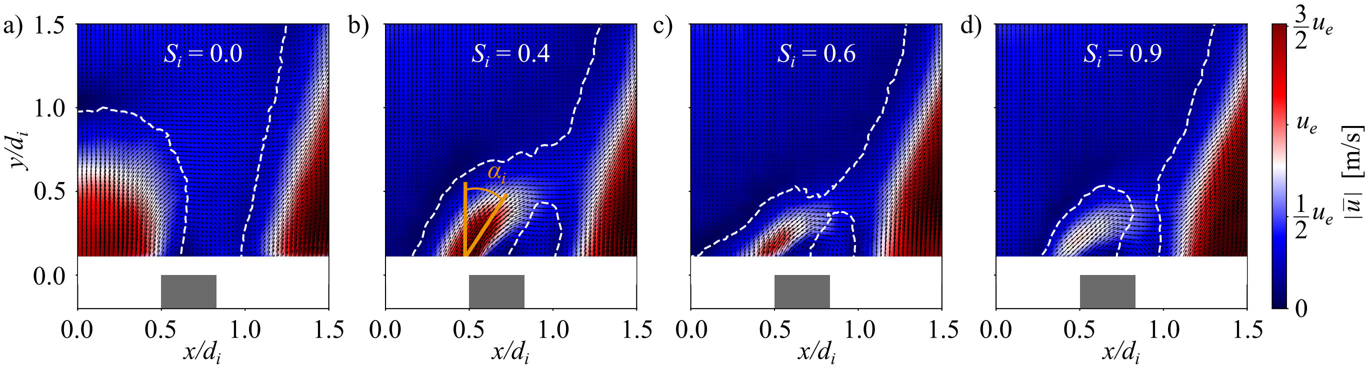

Figure 4.6 – Mean velocity field in the axial plane close to the central injector outlet for an inner swirl level varying from $S_i = 0.0$ (a) to $S_i = 0.9$ (d) without hydrogen injector recess $y_i = 0$ mm. The fields are normalized by the bulk air velocity $u_e = 28.5$ m/s in the external channel. The central injection velocity is $u_i = 34$ m/s. The white dashed lines delineate the boundary $u_z = 0$ m/s of the CRZ. Air is injected in the external channel. Helium is injected in the central lance.

Globally, the same trends are observed for the evolution of the flow in the near field of the injector outlet when the swirl level in the central channel is increased. The better resolution of the measurements allows a better characterization of the central jet. The increase of the central jet angle α_i with the inner swirl level S_i can now be measured accurately and the values are reported in Tab. 4.1. The angle of the central jet α_i increases with the swirl level. Moreover, the flow blockage at the outlet of the central lance increases with the inner swirl level. A small recirculation zone appears above the injector lips. Figure 4.2 already showed that the angle of the annular jet flow α_e increases slightly with the inner swirl level. These data are used in the following to model mixing between the two jets.

4.2 Influence of injector recess

The internal swirl level is now fixed to $S_i = 0.6$ to explore the effect of the recess distance y_i of the internal injector with respect to the annular channel outlet. Figure 4.7 shows the structure of the mean velocity field when the recess increases from $y_i = 0$ to $y_i = 8$ mm. The wide CRZ in Fig. 4.7.a without recess $y_i = 0$ mm pushes the annular flow radially that features an angle $\alpha_e = 42°$ with respect to the burner axis. The recirculation velocity in the CRZ reaches in this case values close to $|u_e|/4$ on the burner axis. For the cases with a recess $y_i = 2$, 4 or 8 mm, the flow field inside the injector is not visible, but Figs. 4.7.c

Table 4.1 – Angles of the central and annular jets at the outlet of the injector for $u_e = 28.5$ m/s and $u_i = 34$ m/s with an inner swirl number varied from $S_i = 0.0$ to 0.9. The central injector is flush mounted $y_i = 0$ mm with the combustion chamber backplane.

S_i	0.0	0.4	0.6	0.9
α_i [deg]	8	32	41	48
α_e [deg]	39	-	42	47

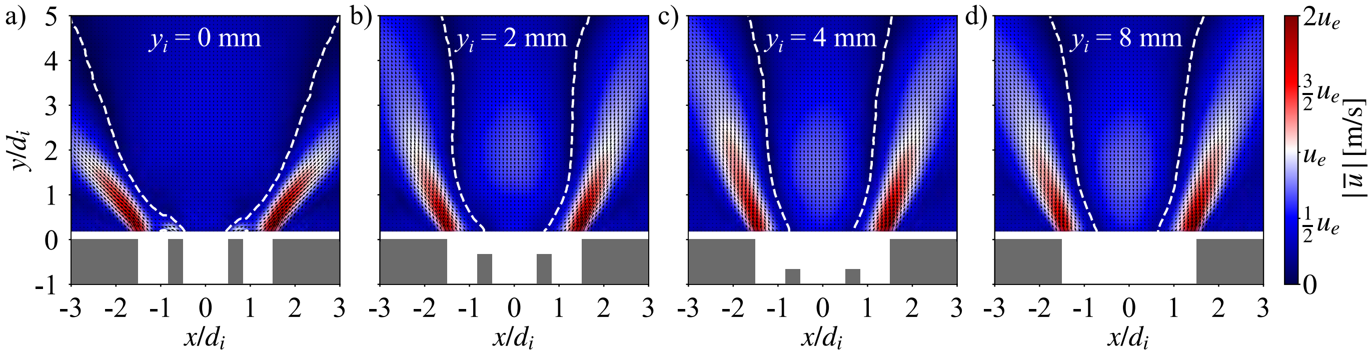

Figure 4.7 – Mean velocity field in the axial plane when the internal injector recess is varied from $y_i = 0$ mm (a) to $y_i = 8$ mm (d) for a fixed inner swirl number $S_i = 0.6$. The fields are normalized by the bulk air velocity $u_e = 28.5$ m/s in the external annular channel. The central injection velocity is $u_i = 34$ m/s. The white dashed lines delineate the boundary $u_z = 0$ m/s of the CRZ. Air is injected in the central and external channels.

to 4.7.d clearly show that the swirling jet flow does not expand as much as in the case without recess shown in Fig. 4.7.a. The annular jet stream angle takes in these cases the same value $\alpha_e = 19°$. The two velocity fields in Fig. 4.7.c for $y_i = 4$ mm and Fig. 4.7.d for $y_i = 8$ mm are indeed very similar despite the different values of the recess y_i of the internal injector. With recess, the CRZ becomes thinner and the recirculation velocity increases and reaches values slightly higher than $|u_e|/2$ along the burner axis. This leads to a higher flow blockage of the hydrogen stream with higher radial velocities at the hydrogen nozzle outlet favoring flame lifting. Effect of injector recess becomes marginal for $y_i \geq 4$ mm.

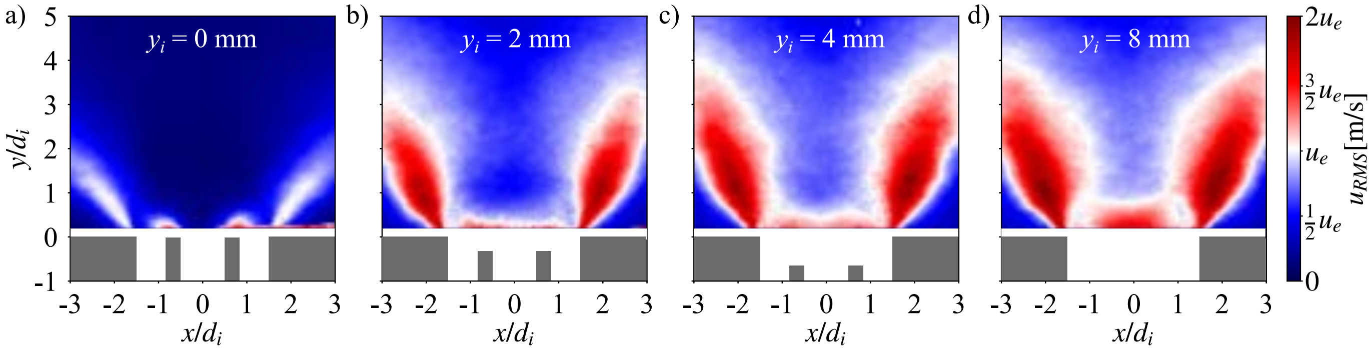

Figure 4.8 – RMS velocity field in the axial plane when the internal injector recess is varied $y_i = 0$ mm (a) to $y_i = 8$ mm (d) for a fixed inner swirl number $S_i = 0.6$. The fields are normalized by the bulk air velocity $u_e = 28.5$ m/s in the external annular channel. The central injection velocity is $u_i = 34$ m/s. Air is injected in the central and external channels.

The corresponding RMS values of the mean fields shown in Fig. 4.7 are presented in Fig. 4.8. When the injector recess is increased to $y_i = 2$ mm in Fig. 4.8.b, the RMS fluctuations in the main flow substantially increase. Large fluctuations in the CRZ are also measured at the outlet of the annular flow. The RMS values increase also in the CRZ with the injector recess. The same trend is observed when the recess is increased to $y_i = 4$ mm and $y_i = 8$ mm. The RMS values in the main flow and in the CRZ increase. As for the mean velocity fields presented in Fig. 4.7, the impact of the injector recess y_i on the flow structure is small when $y_i \geq 4$ mm. Looking at the RMS values, a difference is visible in the CRZ at the outlet of the annular injector.

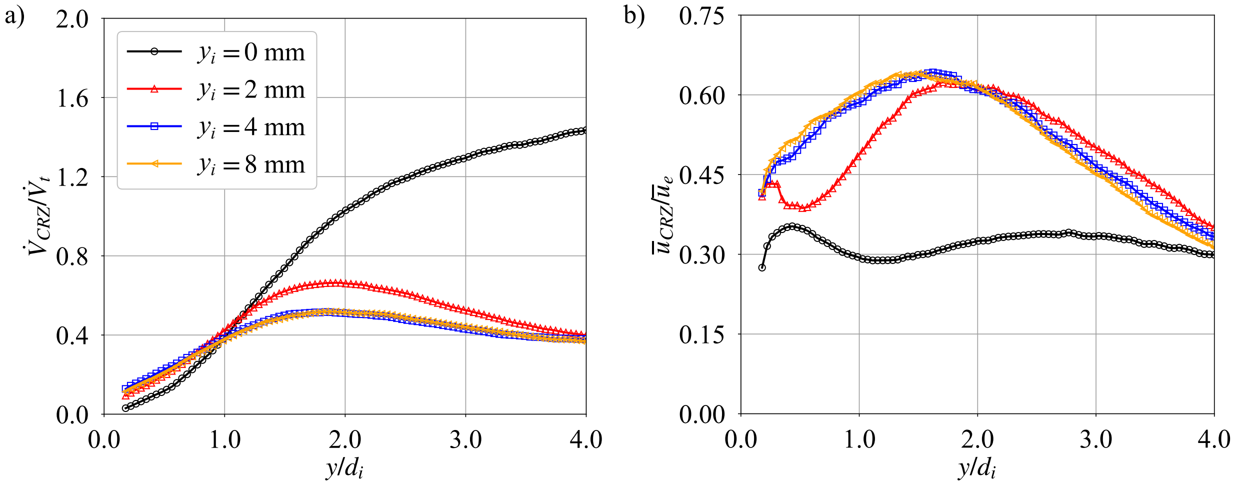

Figure 4.9 – Impact of the injector recess y_i on the recirculating flow in the CRZ. (a) Normalized recirculation flowrates $\dot{V}_{CRZ}/\dot{V}_t$ in the CRZ. (b) Normalized velocities $\overline{u}_{CRZ}/\overline{u}_e$ in the CRZ along the centerline $x = 0$ mm.

In Fig. 4.9.a, the normalized recirculation flowrates $\dot{V}_{CRZ}/\dot{V}_t$ are drawn for different values of the injector recess y_i. The flowrates recirculating through the CRZ are slightly enhanced close to the annular channel outlet for distances $y/d_i < 1.0$. However, further downstream for $y/d_i > 1.0$, increasing the injector recess has a huge effect on the recirculating flowrate. Increasing the injector recess substantially decreases the recirculating flowrate for $y/d_i > 1.0$. As noticed in Figs. 4.7 and 4.8, the velocity fields for $y_i = 4$ mm and $y_i = 8$ mm are very similar. Conversely, the mean velocity along the centerline is increased when the injector recess increases, as shown in Fig. 4.9.b.

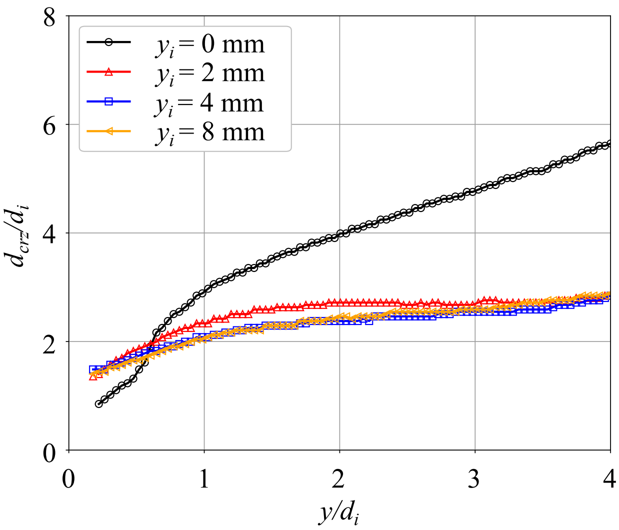

Figure 4.10 – Impact of the injector recess y_i on the normalized diameter of the CRZ d_{CRZ}/d_i along the normalized vertical axis y/d_i.

Figure 4.10 confirms that the recirculating flowrate in the CRZ is mainly correlated with the diameter of the CRZ. As observed in Fig. 4.7, the injector recess decreases the diameter of the CRZ and the differences become small for $y_i \geq 4$ mm.

Table 4.2 – Angle of the central jet α_i and angle the annular jet α_e at the outlet of the injector for $u_e = 28.5$ m/s and $u_i = 34$ m/s with an inner swirl number $S_i = 0.6$. The injector recess is varied from $y_i = 0$ mm to 8 mm.

y_i [mm]	0	2	4	8
α_i [deg]	41	-	-	-
α_e [deg]	42	29	19	19

4.3 Influence of air velocity

The influence of the air velocity on the mean velocity field near the injector outlet is investigated. The PIV window is reduced to zoom near the outlet of the injector in order to characterize the structure of the central jet.

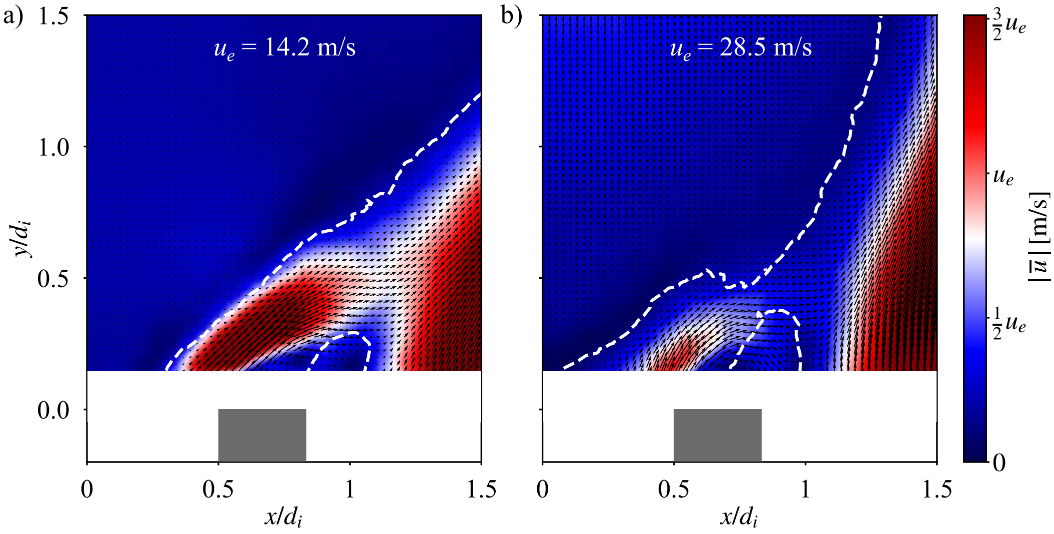

Figure 4.11 – Mean velocity field in the axial plane close to the central injector outlet for two air bulk velocities $u_e = 14.2$ m/s (a) and $u_e = 28.5$ m/s (b). The central injection velocity is $u_i = 34$ m/s. The inner swirl level is set to $S_i = 0.6$ without hydrogen injector recess $y_i = 0$ mm. The fields are normalized by the bulk air velocity in the external channel. The white dashed lines delineate the boundary $u_z = 0$ m/s of the CRZ. Air is injected in the external channel. Helium is injected in the central lance.

Figure 4.11 shows results for two air bulk velocities $u_e = 14.2$ m/s and $u_e = 28.5$ m/s. The central injection velocity is set to $u_i = 34$ m/s, the injector recess to $y_i = 0$ mm and the inner swirl level to $S_i = 0.6$. Despite the small size of the dataset for the impact of air velocity on the velocity field, some important observations can be made from Fig. 4.11. The spreading angle of the swirling jet α_e cannot be measured precisely due to the limited size of the PIV window. But one clearly sees that the angle of the outer jet α_e increases when the air bulk velocity is reduced. This leads to a higher pressure gradient leading to a small increase of the central jet angle α_i and to a slight increase of the diameter of the CRZ close to the injector outlet. Moreover, the velocity in the CRZ increases with the air bulk velocity. The velocity recirculating along the centerline inside the CRZ is always slightly lower than $1/2u_e$ for the two cases investigated in Fig. 4.11.

4.4 Influence of central velocity

The influence of the central injection velocity is investigated for a fixed air bulk velocity $u_e = 28.5$ m/s. The injector recess is set to $y_i = 0$ mm and the inner swirl level to $S_i = 0.6$.

In Fig. 4.12, the central injection velocity is varied from $u_i = 17$ m/s to $u_i = 45$ m/s: the central jet is weak for the case where $u_i = 17$ m/s and its angle with the vertical axis $\alpha_i = 61°$ (see Tab. 4.3) is large

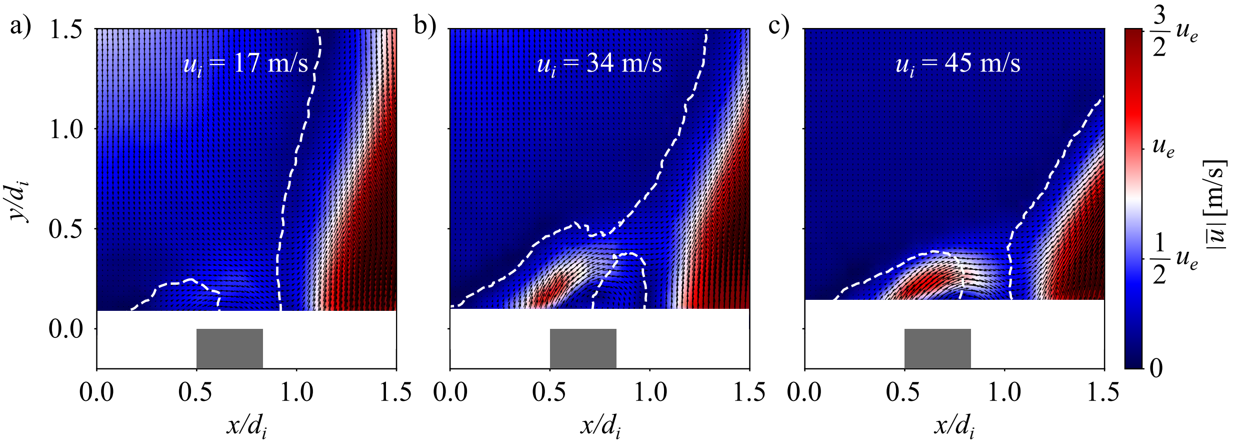

Figure 4.12 – Mean velocity field in the axial plane close to the central injector outlet when the air bulk velocity is varied from $u_i = 17$ m/s (a) to $u_e = 45$ m/s (c). The inner swirl level is set to $S_i = 0.6$ without hydrogen injector recess $y_i = 0$ mm. The fields are normalized by the bulk air velocity $u_e = 28.5$ m/s in the external annular channel. The white dashed lines delineate the boundary of the CRZ where $u_z = 0$ m/s. Air is injected in the external channel. Helium is injected in the central lance.

Table 4.3 – Angles of the central and annular jets at the outlet of the injector for $u_e = 28.5$ m/s and $y_i = 0$ mm. The central injection velocity is varied from $u_i = 17$ m/s to $u_i = 45$ m/s.

u_i [m/s]	17	34	45
α_i [deg]	61	41	50
α_e [deg]	-	42	-

compare to all other cases studied previously. It is attributed to the axial momentum of the central jet which is low compared to the axial momentum of the flow recirculating inside the CRZ. Moreover, the small recirculation zone above the injector lips is reduced when the central injection velocity is increased. The exact angle of the external main flow cannot be accurately estimated with the present data, but it is clear that the angle of the annular jet α_e increases with the central injection velocity u_i. The measured central jet angles α_i from Fig. 4.12 are reported in Tab. 4.3. They are used in the following.

4.5 Precessing vortex core

Precessing Vortex Cores (PVC) are coherent flow structures which are often observed in swirling flows [23, 25, 33, 34]. Their presence is investigated here in cold flow conditions with the setup shown in Fig. 4.13. Two hot-wire probes are positioned in the axial plane at a radial distance $r = 6$ mm from the centerline and with an angle separating the two hot-wire probes equal to 180°. The distance from the backplane is set to $y = 1$ mm. An analysis using the Cross Spectral Power Density (CPSD) between the signals recorded by the hot-wire probes is used to detect correlation between the signals at a single frequency that should be linearly related to the flowrate and the swirl level [23, 42] for a PVC with a phase difference between the two signals equal to π.

First, the experiments are made for two reference cases corresponding to an equivalent cold flow of flames A and G presented in Fig. 3.7.a and 3.7.g respectively. The recess is set to $y_i = 4$ mm and the inner swirl level to $S_i = 0.6$. As for PIV measurements in cold flow conditions presented previously, the central flow of hydrogen is replaced in these experiments by the same volumetric flowrate of helium. Two experiments with and without central injection are compared. Results are presented in Fig. 4.14 for case A and in Fig. 4.15 for the flame G. Without central flow, the results are plotted in red. Results with a flowrate injected through the central channel are in blue.

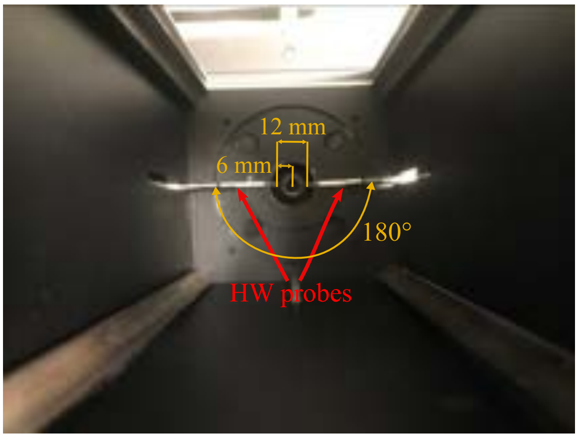

Figure 4.13 – Double hot-wire setup installed for the detection of the PVC.

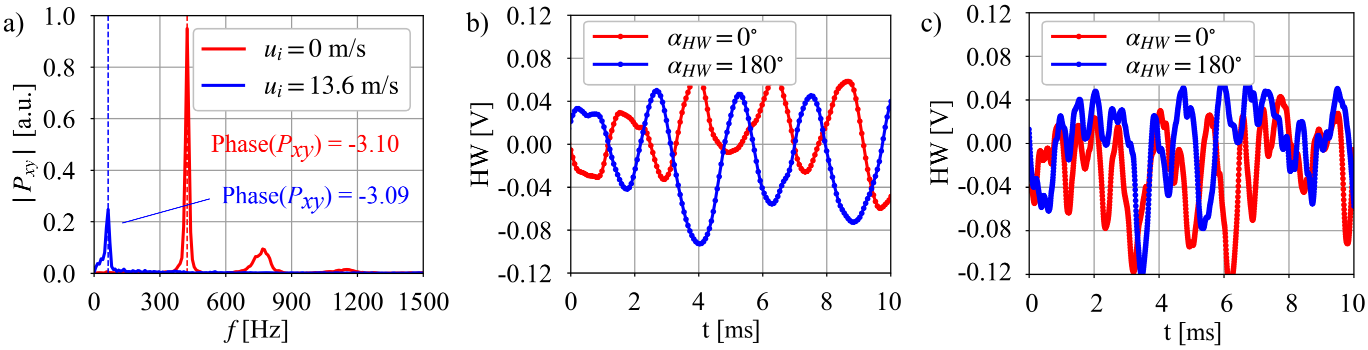

Figure 4.14 – PVC characterization for case A ($u_e = 11.6$ m/s, $S_i = 0.6$ and $y_i = 4$ mm) with hydrogen replaced by the same volumetric flowrate of helium. (a) Modulus of the CPSD between the two hot-wire signals. (b) Filtered hot-wire signals without central flow $u_i = 0$ m/s. (c) Filtered hot-wire signals with central flow $u_i = 13.6$ m/s.

Without central injection, Fig. 4.14.a shows for case A a strong correlation between the two hot-wire signals at 424 Hz with a phase difference close to π. Additional tests not shown here confirm that this is the signature of a PVC. The small phase difference with π is attributed to measurements precision, particularly the precision of the probe positions. With central injection, the peak value of the modulus of the CPSD between the two signals is reduced by a factor 4 and shifts to a much lower frequency 64 Hz. The phase difference remains close to π. In this case, the central injection has a huge effect on the PVC instability, as already observed in [122]. The coherent peak detected for 64 Hz may originate from a small PVC instability of the central flow looking at the phase opposition of the hot-wire signals but this cannot be confirmed with the available data. Figures 4.14.b and 4.14.c show the corresponding two hot-wire signals. They are filtered with a low-pass zero-phase shift Butterworth to avoid any phase shift. The filter cut-off frequency is set to $f_{LP} = f_{PVC} + 80$ Hz. In Fig. 4.14.b, the case without central flow $u_i = 0$ m/s is considered. The two signals correspond to quasi-harmonic oscillations out of phase by π. The presence of a PVC is clear. With central injection, Fig. 4.14.a shows the presence of a dominant frequency one order of magnitude lower than in the case without central injection. The signals shown in Fig. 4.14.c are noisy and the phase shift is not clear. The central injection seems to suppress the PVC instability, at least the one associated to the air stream flow.

Figure 4.15 shows the results obtained for case G. The frequency peaks in Fig. 4.15.a are shifted to 1048 Hz and 152 Hz, respectively for the case without and with central injection, due to the increase of flowrate (the impulsion ratio is kept constant to $J = 5.05$). The modulus of the CPSD peak between the two signals when a central flow is imparted to the central tube is divided approximately by 20 with respect to the case without central injection. For each case, the phase difference remains however close to π. The filtered signals presented in Fig. 4.15.b show the presence of a PVC without central injection, but the results are again not clear in the case with central injection in Fig. 4.15.c.

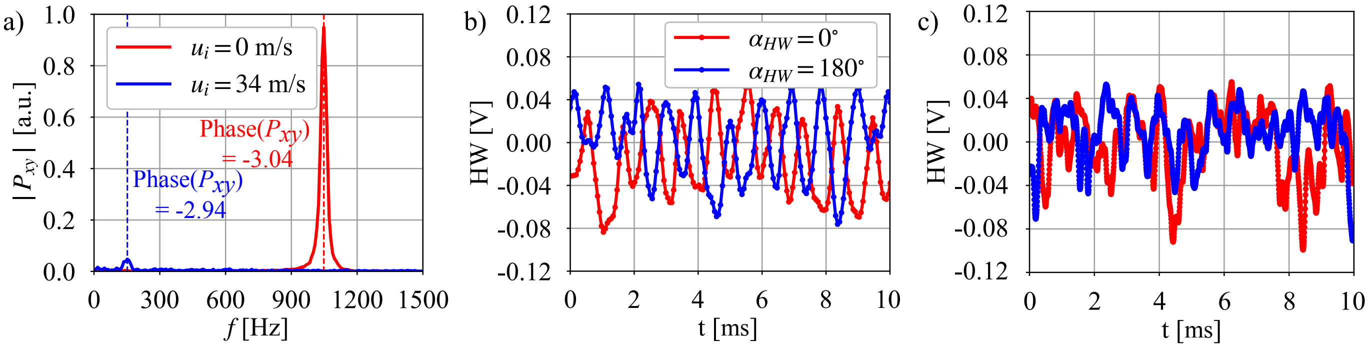

Figure 4.15 – PVC characterization for case G ($u_e = 28.5$ m/s, $S_i = 0.6$ and $y_i = 4$ mm) with hydrogen replaced by the same volumetric flowrate of helium. (a) Modulus of the CPSD between the two hot-wire signals. (b) Filtered hot-wire signals without central flow $u_i = 0$ m/s. (c) Filtered hot-wire signals with central flow $u_i = 34$ m/s.

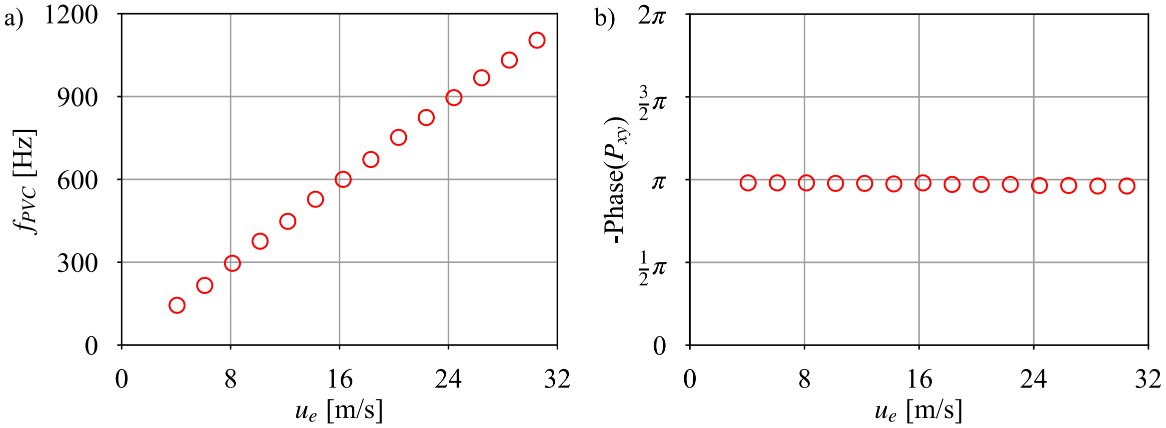

Figure 4.16 – (a) PVC frequency f_{PVC} plotted against the air bulk velocity u_e. (b) Phase shift between the two hot-wire signals plotted against the air bulk velocity u_e. No central injection $u_i = 0$ m/s.

Now the presence of the PVC in cold flow conditions without central injection is verified for the range of air bulk velocity u_e explored in this work from $u_e = 4$ m/s to 31 m/s (Fig. 4.16): the phase shift between the two hot-wire signals is close to π in Fig. 4.16.b. Figure 4.16.a shows that the frequency of the PVC f_{PVC} increases linearly with the air bulk velocity u_e as noticed in [49], as expected for a hydrodynamic instability. The Strouhal number $S_t = f_{PVC} d_e / u_e$ for this mode is $S_t = 900 \times 0.018/24 = 0.675$, a typical value for PVC [123]. This Strouhal number is constant for the range of air bulk velocities investigated.

In conclusion, the presence of a PVC instability is confirmed for the geometry and the flowrates considered in this work. It is shown that the PVC instability associated to the air channel is substantially altered when a central flow is imparted to the central injector.

4.6 Conclusion

A characterization and an analysis of the velocity flow field in cold flow conditions has been carried out in order to understand how the inner swirl level S_i, the injector recess y_i, the air and hydrogen injection velocities u_e and u_i affect the velocity field. When it is possible, a link with the observations made in the Chapter 3 has been made. The conclusions can be resumed as follow:

- When no swirl is present in the central flow $S_i = 0.0$, the central jet penetrates deeply into the CRZ and a relatively large low velocity zone establishes above the central injector lips.
- When a swirl motion is conferred to the central flow $S_i > 0.0$, this zone is cut by the central jet expanding radially right out at the central injector outlet. This explains the necessity of an inner swirl to lift the flame above both DFDS and HYLON injectors, as concluded in Chapter 3. This also explains the large influence of the central injection velocity on the flame stabilization regime.

- When a recess is applied to the central injector, the diameter of the CRZ d_{CRZ} decreases and the recirculation velocity on the centerline u_{CRZ} increases.
- For a recess $y_i \geq 4$ mm, the flow becomes insensitive to the injector recess distance.
- An increase of the air bulk velocity u_e decreases the angle of the annular swirled jet. Conversely, an increase of the central injection velocity u_i increases this angle.
- A PVC is detected in cold flow conditions without central injection $u_i = 0$ m/s, but is destroyed by a swirled central jet.
- The PVC frequency f_{PVC} scales linearly with the air injection velocity u_e.

These data have been used to validate companion numerical flow simulations in Aniello *et al.* [92].

It is worth mentioning that is most of these experiments, hydrogen injected through the central channel has been replaced by air or helium for safety reasons to investigate the velocity flow field in cold flow conditions. It has been verified that replacing hydrogen by air with the same central injection velocity u_i or the same momentum ratio J provides similar results when the injector features a recess. The strategy with the same injection velocity as the reactive case with hydrogen is however preferred for both measurements with air and helium injected through the central lance. The reasons are clarified in Chapter 7.

Chapter 5

Cold flow mixing

> *"Nothing in life is to be feared, it is only to be understood. Now is the time to understand more, so that we may fear less."*
>
> Marie Curie

Overview

To understand the stabilization mechanisms of a flame, the concentration field in the combustion chamber is an important information, in addition to the velocity field [90]. In this section, the 1D1S Raman system described in Chapter 2 is used to infer the concentration profiles of the gas injected through the central injector at different distances from the injector outlet. A parametric analysis is carried out varying the inner swirl level S_i, the injector recess y_i and the injection velocities u_e and u_i in each channel, with the same guideline as in the Chapter 4. The influence of the gas density injected by the central lance is investigated too. At the end of this chapter, the model for the mixing of coaxial jets proposed by Villermaux and Rehab [91] is revised and adapted to the case of swirling jets.

5.1 Comparison between operations with helium and hydrogen

For obvious safety reasons, experiments in cold flow conditions are preferred using helium instead of hydrogen. The question arises whether mixing between H_2/air jets can be studied with He/air injectors. Experiments are first conducted to determine if measurements with helium injected through the central tube provide similar results as with hydrogen.

Table 5.1 – Impulsion ratio between the CRZ and the unswirled central jet $S_i = 0.0$ without injector recess $y_i = 0$ mm for three central injection velocities $u_i = 17$, 34 and 45 m/s calculated for hydrogen and helium. The air bulk velocity is set to $u_e = 28.5$ m/s.

Gas	H_2	He	H_2	He	H_2	He
u_i [m/s]	17	17	34	34	45	45
u_{CRZ} [m/s]	10.8	10.8	10.8	10.8	10.8	10.8
J_{CRZ}	5.94	2.97	1.49	0.74	0.85	0.42

Concentration profiles of He and H_2 are compared for a configuration without recess $y_i = 0$ mm and without inner swirl $S_i = 0.0$. The results are presented for different central flowrates. Figure 5.1 shows differences between the concentration profiles of helium and hydrogen. Close to the injector $y/d_i = 0.17$, the concentration profiles inside the central jet are very close, but differences are visible in the ORZ close to the combustion chamber backplane $|x/d_i| \geq 1.5$. These differences in the CRZ disappear further downstream for $y/d_i \geq 0.67$. For $y/d_i = 0.67$, the two concentration profiles are close for $u_i = 17$ m/s in Fig. 5.1.b but differ for $u_i = 34$ m/s and $u_i = 45$ m/s in Figs. 5.1.d and 5.1.f. This is attributed to the effect of the CRZ on the central jet. The interaction between the unswirled central jet and the CRZ forms a counter-flow. Measurements in Fig. 4.4.b indicate that the mean velocity in the CRZ u_{CRZ} is approximately equal to $0.38u_e$. The corresponding impulsion ratios $J_{CRZ} = \rho_{air}/\rho_i \left(u_{CRZ}^2/u_i^2\right)$ are reported in Tab. 5.1. The CRZ flow clearly alters the central jet for the low flowrates in Fig. 5.1.b. It is due to the high impulsion ratio between the CRZ and the central jet (see Tab. 5.1). In the intermediate case for $u_i = 34$ m/s, the impulsion ratio J_{CRZ} is of the order of unity: $J_{CRZ} = 1.49$ for hydrogen and $J_{CRZ} = 0.78$ for helium. Both jets are influenced by the CRZ acting as a counter-flow and large differences are visible on the concentration profiles plotted in Fig. 5.1.d. These differences reduce for higher injection velocities in Fig. 5.1.f but are not negligible. It is attributed to the value of J_{CRZ} of the order of unity for the hydrogen injection ($J_{CRZ} = 0.85$). These differences will disappear for higher injection velocities or lower velocity of the CRZ when the air bulk velocity is reduced, implying a reduction of u_{CRZ}.

Figure 5.2 shows results for the same configuration as in Fig. 5.1, with a swirl motion added to the central stream. When swirl $S_i = 0.6$ is imparted to the central jet, differences between hydrogen and helium profiles reduce. Figure 5.2 shows very close concentration profiles for experiments made with hydrogen and helium. Only small differences subsist along the burner axis. When the central jet is swirled, hydrogen can be replaced by helium with a sufficient confidence to study the mixing between the two jets away from the burner axis and extrapolate the results to the hydrogen case.

In the case of operation with a recess y_i of the central injector, Fig. 5.3 shows that differences in the concentration profiles of hydrogen and helium are only close to the burner axis. This zone is not of interest

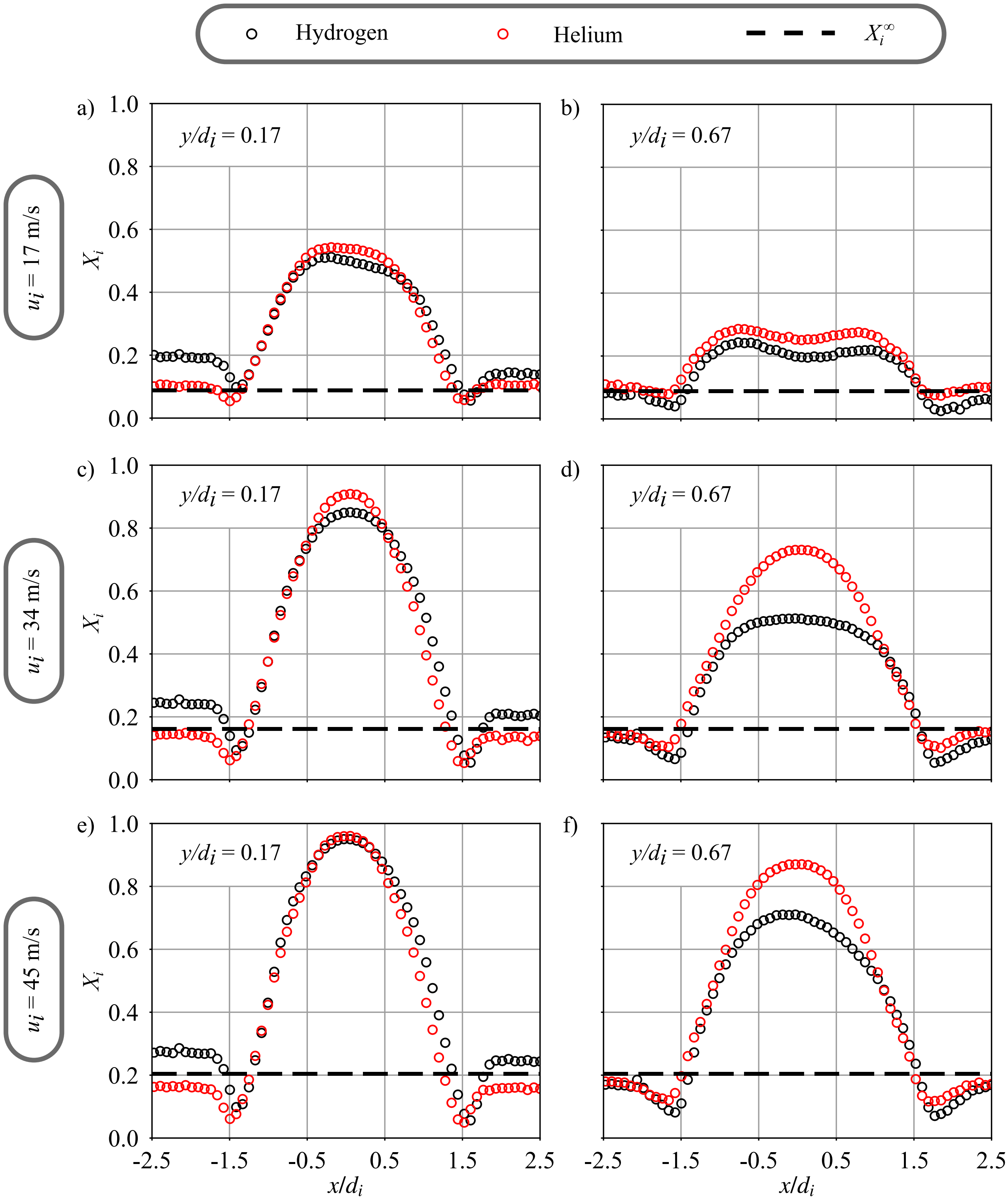

Figure 5.1 – Evolution of the mean helium and hydrogen molar concentration profiles along the vertical axis for different central injection velocities u_i. The injector is flush-mounted with the combustion chamber backplane $y_i = 0$ mm and the inner swirl level is $S_i = 0.0$. The air bulk velocity is set to $u_e = 28.5$ m/s. The black dashed line is the theoretical molar concentration of helium and hydrogen X_i^∞ if the two streams are perfectly premixed.

for the understanding of flame stabilization mechanisms. These zones are located in the shear layer between the annular and the central flows as indicated by Chapter 3 when the flame switches between V and M shapes.

In the remaining part, experiments are only conducted with helium injected through the central tube,

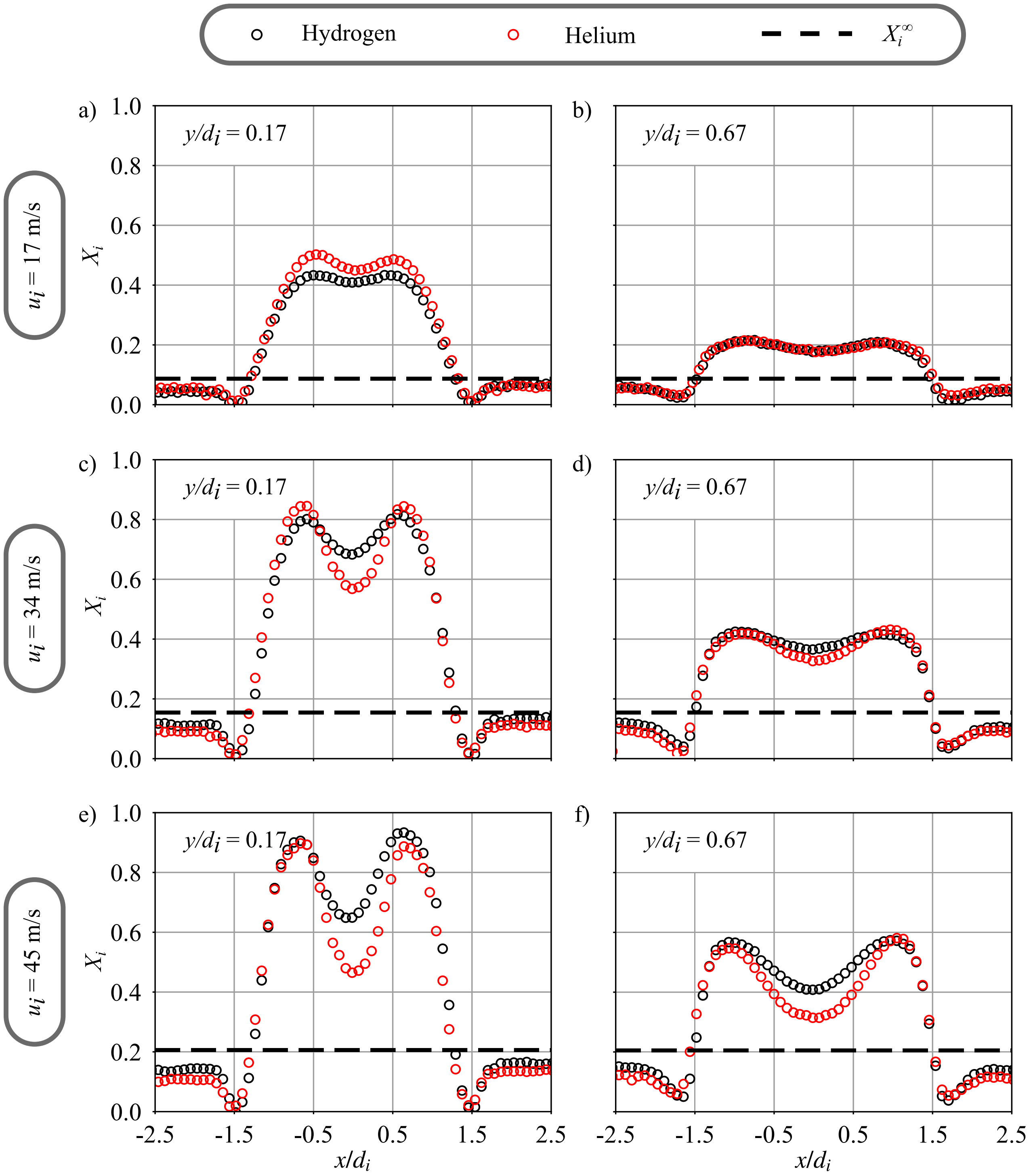

Figure 5.2 – Evolution of the mean helium molar concentration profiles along the vertical axis for three central injection velocities $u_i = 17$, 34 and 45 m/s. The injector is flush-mounted with the combustion chamber backplane $y_i = 0$ mm and the inner swirl level is $S_i = 0.6$. The air bulk velocity is set to $u_e = 28.5$ m/s. The black dashed line is the theoretical molar concentration of helium and hydrogen X_i^∞ if the two flows are perfectly premixed.

except for investigation on the influence of density ratio on mixing for which the central injector is supplied with different gases.

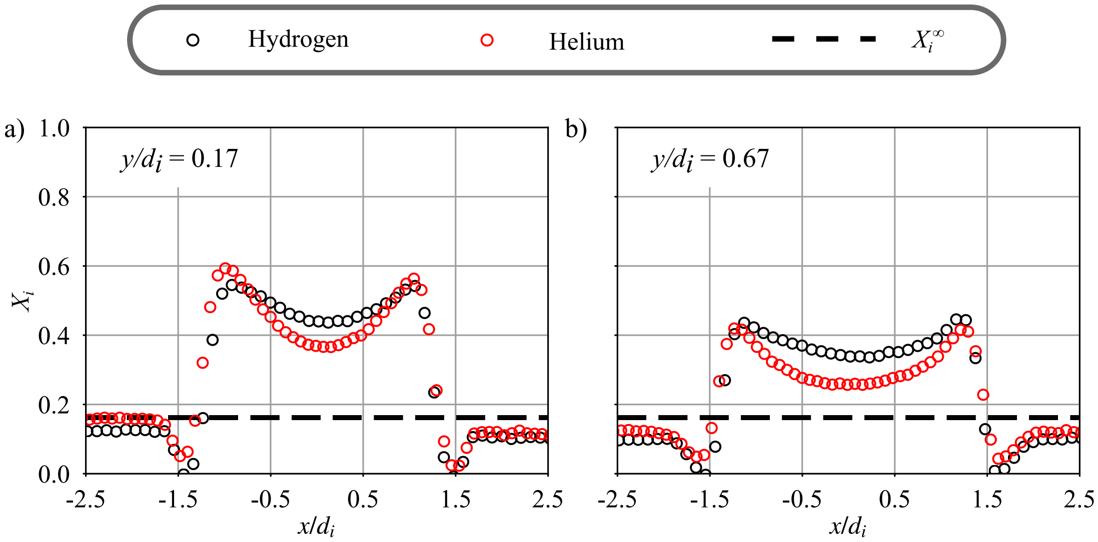

Figure 5.3 – Mean helium and hydrogen molar concentration profiles along the vertical axis. (a) $y/d_i = 0.17$. (b) $y/d_i = 0.67$. The injector recess distance is set to $y_i = 4$ mm and the inner swirl level is $S_i = 0.6$. The air bulk velocity is set to $u_e = 28.5$ m/s and the central bulk velocity to $u_i = 34$ m/s. The black dashed line is the theoretical molar concentration of helium and hydrogen X_i^∞ if the two flows are perfectly premixed.

5.2 Influence of inner swirl

The influence of the inner swirl motion on the mixing between the coaxial jets is now analyzed. The swirl motion conferred to the annular stream of a coaxial injector is known to enhance the mixing between the annular and the central jet due to enhancement of the entrainment velocity [124], enhancement of turbulent mixing by higher turbulent fluctuations [125] and enhancement of large-scale structures as PVC [126]. The effect of a swirl motion conferred to the central injection is not well documented. Only a recent study with a dual swirl injector and a variable recess of the central injector characterizes the mixing between two coaxial swirled jets [127]. In this study, the annular channel is flowing with a mixture of hydrogen and air and the central injection channel with ammonia and air.

Figure 5.4 shows the impact of the inner swirl level on the mixing between the central and annular flows. The hydrogen flow is replaced by the same volumetric flowrate of helium, as for PIV measurements in cold flow conditions described previously. It has been shown that mixing away from the burner axis can be studied by replacing hydrogen with helium. Mixing between the two streams is very fast, justifying the choice to study mixing only in the near field of the injector outlet for $y/d_i < 2$..

First, the central injector is flush-mounted $y_i = 0$ mm with the combustion chamber backplane, the air bulk velocity is set to $u_e = 28.5$ m/s and the central bulk velocity to $u_i = 34$ m/s, that corresponds to the inlet flowrates of the flame G presented in Fig. 3.7.g. In Fig. 5.4.a, concentration profiles for central swirl levels $S_i = 0.0$, 0.4, 0.6 and 0.9 are presented. For a small distance $y/d_i = 0.17$ from the injector outlet, the maximum of the peaks of molar concentration of helium injected through the central injector is close to unity. Without swirl, the concentration profile is typical of a central unswirled jet. The molar concentration profile of helium exhibits a Gaussian profile centered on the centerline. It drops to 0 at the location of the annular jet and reaches in the ORZ a value close to the molar concentration X_i^∞ reached if the two flows are fully mixed. As the distance to the burner outlet increases, the profile for $S_i = 0.0$ becomes larger in Figs. 5.4.b to 5.4.f and peak value decreases. This is due to air entrainment that dilutes the central jet [91]. The concentration profile flattens for $y/d_i = 1.33$ and becomes convex at the top for $y/d_i = 1.67$ due to the influence of the CRZ of the annular swirled flow.

When swirl is imparted to the central flow, radically different profiles are observed. Just above the outlet of the injector for $y/d_i = 0.17$, the profiles have a M-shape in Fig. 5.4.a. The helium concentration in the external shear layer of the annular jet and the ORZ is similar to that observed without inner swirl. In the central region, two symmetric peaks are visible, and a decrease of the molar concentration of helium

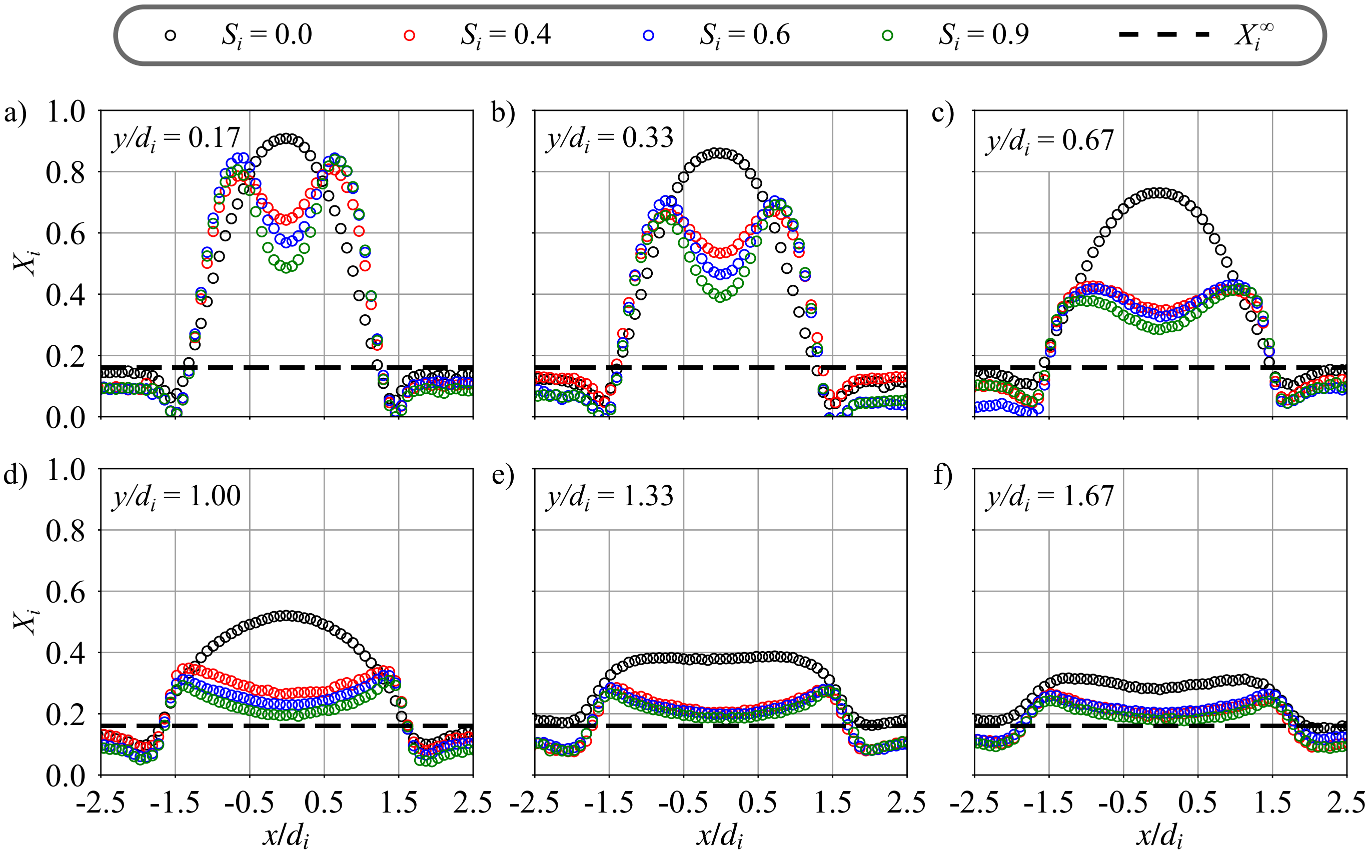

Figure 5.4 – Evolution of the mean helium molar concentration profiles along the vertical axis for different levels of inner swirl from $S_i = 0.0$ to $S_i = 0.9$ with the injector flush-mounted with the combustion chamber backplane $y_i = 0$ mm. The air bulk velocity is set to $u_e = 28.5$ m/s and the central bulk velocity to $u_i = 34$ m/s. The black dashed line is the theoretical molar concentration of helium X_i^∞ if the two flows are perfectly premixed.

is measured around the centerline. The symmetric peaks are due to the radial expansion of the central jet when swirl is imparted to the central flow. The decrease of the molar concentration of helium around the centerline is due to the penetration of the CRZ up to the central injector outlet, as confirmed by PIV measurements for the same conditions in Fig. 4.2. Peak values are close to the maximum reached along the centerline without swirl for $y/d_i = 0.17$. Increasing the distance to the injector outlet, the difference between the peak values and the concentration reached on the centerline decreases. With $S_i > 0.0$, the maximum value of the mole concentration of helium decreases much more faster than in the unswirled case, and tends to a top hat profile in Fig. 5.4.f for $y/d_i = 1.67$. Typically, for $y/d_i = 0.67$ in Fig. 5.4.c, the maximum concentration reached for swirled cases is half of the value measured without inner swirl. These experiments confirm that conferring swirl to the central stream drastically improves mixing of coaxial jets.

To compare the mixing enhancement provided by the inner swirl, a mixing progress variable is defined as follow:

$$C = \frac{1 - \max\left(X_i\right)}{1 - X_i^\infty} \tag{5.1}$$

In the core of the central jet of helium before mixing with the air flow $C = 0$, i.e. mixing has not started. Far away from the injector outlet $\max(X_i) = X_i^\infty$, the two flows are perfectly mixed $C = 1$, i.e. mixing is complete. Figure 5.5 shows the evolution of the mixing progress variable C along the vertical axis y for the different values of the inner swirl level investigated in this work. In the near field of the injector outlet $y/d_i \leq 1$, mixing is faster when swirl motion is imparted to the central flow. The normalized recirculating velocity u_{CRZ}/u_e, the normalized recirculating flowrate $\dot{V}_{CRZ}/\dot{V}_t$ and the normalized diameter of the CRZ d_{CRZ}/d_i reach close values near the injector outlet for $y/d_i \leq 1.5$ in Figs. 4.4 and 4.5. But substantial

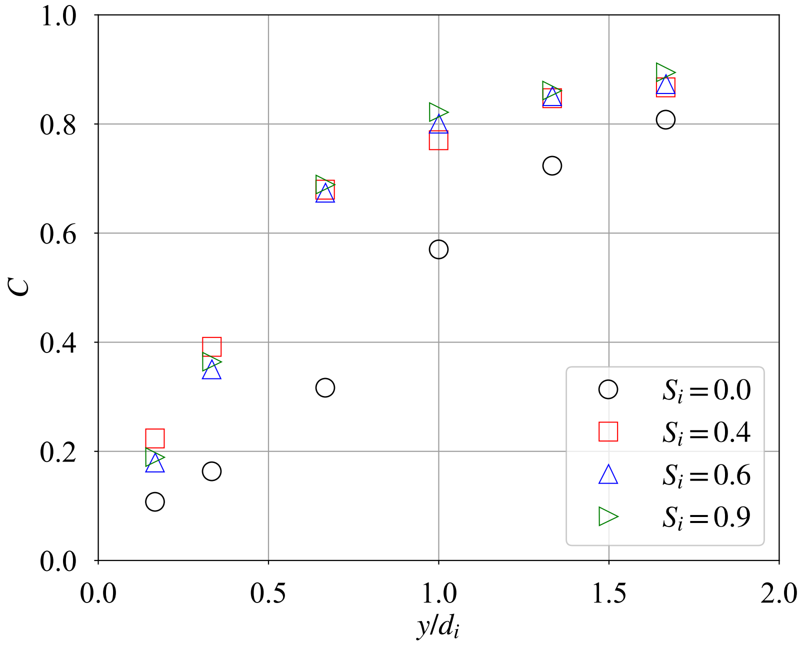

Figure 5.5 – Evolution of the mixing progress variable C with the distance from the burner outlet for different swirls $S_i = 0.0$ to $S_i = 0.9$ with the injector flush-mounted with the combustion chamber backplane $y_i = 0$ mm. The air bulk velocity is $u_e = 28.5$ m/s and the central bulk velocity is $u_i = 34$ m/s.

differences are observed for the mean and RMS velocity fields of the annular jet near the injector outlet: the RMS values are greatly enhanced without inner swirl motion and drop when an inner swirl motion is conferred to the central flow. It is well known that turbulence in the shear layer enhances mixing between two streams [125]. The PVC enhances mixing through large-scale structures [126]. In the near field of the injector, mixing does not seem to be controlled by the PVC that disappears (or is strongly attenuated) when the central jet is swirled. Mixing appears to be more correlated with the central jet and the CRZ characteristics. At the location of the flame above $y/d_i \approx 0.8$ for lifted flames enhancement of the mixing due to inner swirl is considerable: $C\left(S_i > 0.0\right)/C\left(S_i = 0.0\right) \approx 2$ for $y/d_i = 0.67$ and $C\left(S_i > 0.0\right)/C\left(S_i = 0.0\right) \approx 1.4$ for $y/d_i = 1.00$. This is particularly promising for the development of injectors with hydrogen injected as late as possible to limit the risk of flashbacks and, in the mean time, ensure a fast mixing before combustion to limit NOx emissions.

5.3 Influence of injector recess

In this section, the swirl level in the central tube is set to $S_i = 0.6$ and the influence of the injector recess y_i is investigated. Experiments are conducted for the same flowrates $u_e = 28.5$ m/s and $u_i = 34$ m/s as in the previous section.

Mixing is first analyzed at $y/d_i = 0.17$ above the burner outlet. Figure 5.6.a shows that the maximum value of Helium concentration decreases when the injector recess increases from $y_i = 0$ to 4 mm, due to the increase of the mixing distance. It is shown in experiments not presented here that, for an injector recess $y_i \geq 4$ mm, the gain of mixing at the outlet of the air channel (i.e. at the enter of the combustion chamber) decreases when the injector recess is further increased. The mixing between the two gases is evolved again when enters in the combustion chamber, due to the abrupt enlargement of the section. In Fig. 5.6.b, the inverse behaviour is observed, keeping constant the distance between the measure and the central injector outlet. It is shown that the mixing rate decreases increasing the injector recess. These results highlight that the mixing efficiency in the annular tube is less than in the combustion chamber. To conclude, the injector recess considerably improves mixing between the two streams before the inlet of the combustion chamber.

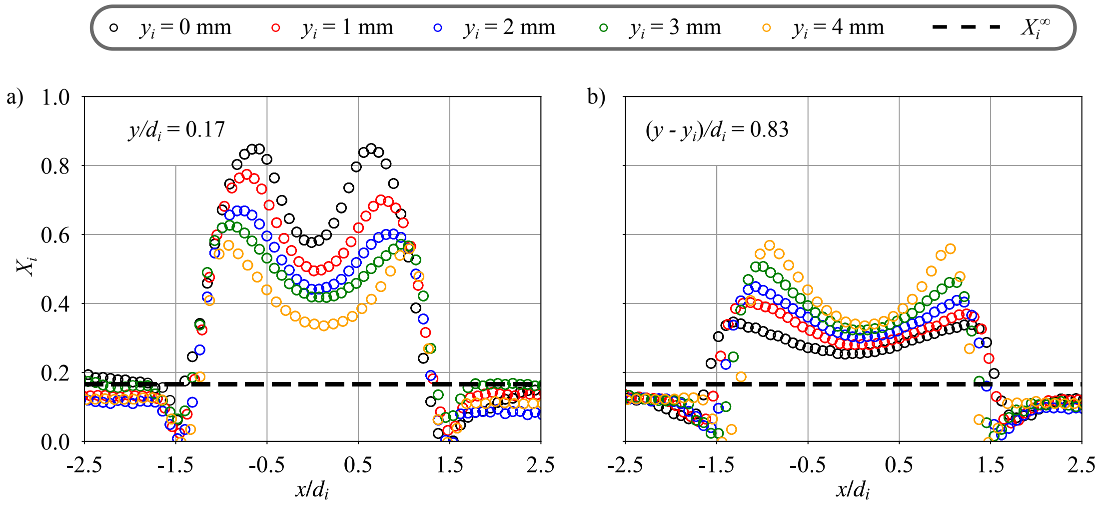

Figure 5.6 – Mean helium molar fraction for injector recess varied from $y_i = 0$ mm to $y_i = 4$ mm with a swirl level in the central channel $S_i = 0.6$. (a) $y/d_i = 0.17$. (b) $(y - y_i)/d_i = 0.83$. The air bulk velocity is $u_e = 28.5$ m/s and the central bulk velocity is $u_i = 34$ m/s . The dashed line is the theoretical molar concentration of helium X_i^∞ if the two flows are perfectly premixed.

5.4 Influence of air velocity

The influence of the air bulk velocity is investigated now. The inner swirl level is set to $S_i = 0.6$ and the injector is flush mounted with respect to the combustion chamber inlet $y_i = 0$ mm.

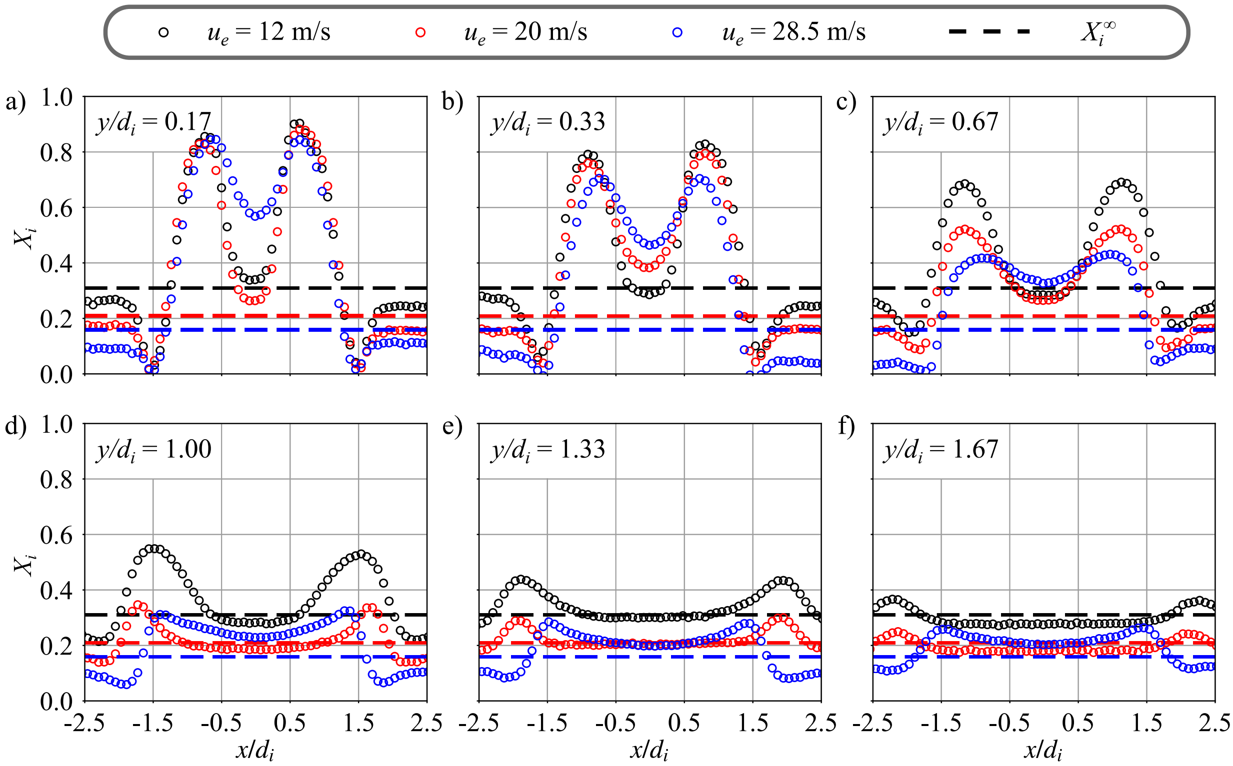

Figure 5.7 – Evolution of the mean helium molar fraction at different heights y/d_i above the burner for three air bulk velocities $u_e = 12$, 20 and 28.5 m/s. The injector is flush-mounted with the combustion chamber backplane $y_i = 0$ mm and the swirl level in the central channel is $S_i = 0.6$. The central bulk velocity is $u_i = 34$ m/s. The dashed lines are the theoretical molar concentrations of helium X_i^∞ if the two flows are perfectly premixed.

Three different air bulk velocities are considered while all other parameters are kept constant. The injector recess is set to $y_i = 0$ mm and the central injection velocity is kept constant equal to $u_i = 34$ m/s. Profiles of the molar fraction of helium are presented in Fig. 5.7. The molar fraction of well mixed gases X_i^∞ differs for the three cases studied because the central flowrate of helium is fixed, but the air flowrate varies. The values of X_i^∞ are equals for $u_e = 12$, 20 and 28.5 m/s respectively to $X_i^\infty = 0.31$, 0.21 and 0.16. Figure 5.7.a shows that in the ORZ, the molar fraction of helium is close to the theoretical value X_i^∞. The peaks are comparable for $y/d_i = 0.17$ but the values in the CRZ are quite different for the three air bulk velocities investigated. The influence of the air bulk velocity on the mixing rate appears clearly when the measurement location is shifted downstream in Fig. 5.7.b to 5.7.d. Increasing the air bulk velocity increases the mixing rate for $y/d_i \leq 1$.

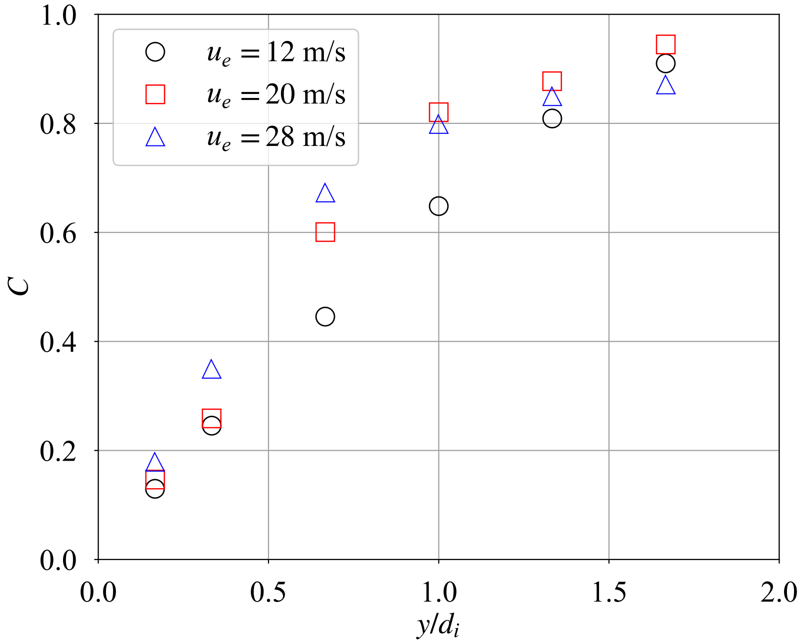

Figure 5.8 – Evolution of the mixing progress variable C above the burner for three air bulk velocities $u_e = 12$, 20 and 28.5 m/s. The injector is flush-mounted with the combustion chamber backplane $y_i = 0$ mm. The swirl level in the central channel is $S_i = 0.6$. The central bulk velocity is $u_i = 34$ m/s.

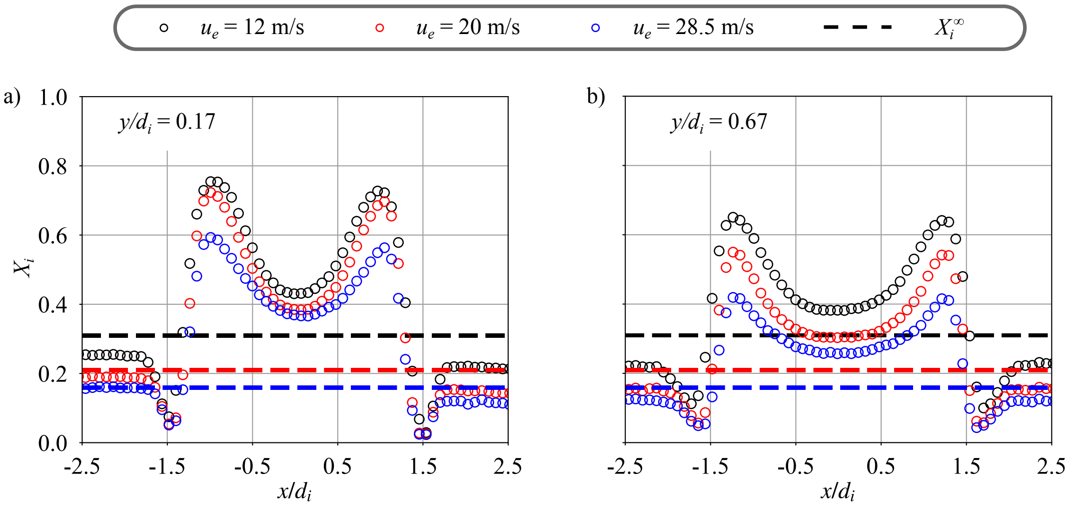

Figure 5.9 – Evolution of the mean helium molar above the burner for three air bulk velocities $u_e = 12$, 20 and 28.5 m/s. The injector recess is set to $y_i = 4$ mm and the swirl level in the central channel is $S_i = 0.6$. The central bulk velocity is $u_i = 34$ m/s. The dashed lines are the theoretical molar concentrations of helium X_i^∞ if the two flows are perfectly premixed.

The progress variable C calculated with the data in Fig. 5.7 is presented in Fig. 5.8. Mixing is enhanced by the increase of the air bulk velocity in the near field of the injector outlet $y/d_i \leq 1$. In the region, upstream flame apex stabilization $y/d_i \approx 1$, increasing the air bulk velocity has a favorable effect on the mixing rate.

The same experiments are repeated with an injector recess $y_i = 4$ mm. The same inner swirl level and flowrates are used. The results presented in Fig. 5.9 confirm the previous conclusions. The mixing rate increases also with the air bulk velocity but the concentration profiles are sharper with an injector recess.

5.5 Influence of central velocity

The influence of the helium injection velocity on the mixing is investigated in this section. The geometrical configuration $S_i = 0.6$, $y_i = 0$ mm is conserved. The air bulk velocity is set to $u_e = 28.5$ m/s.

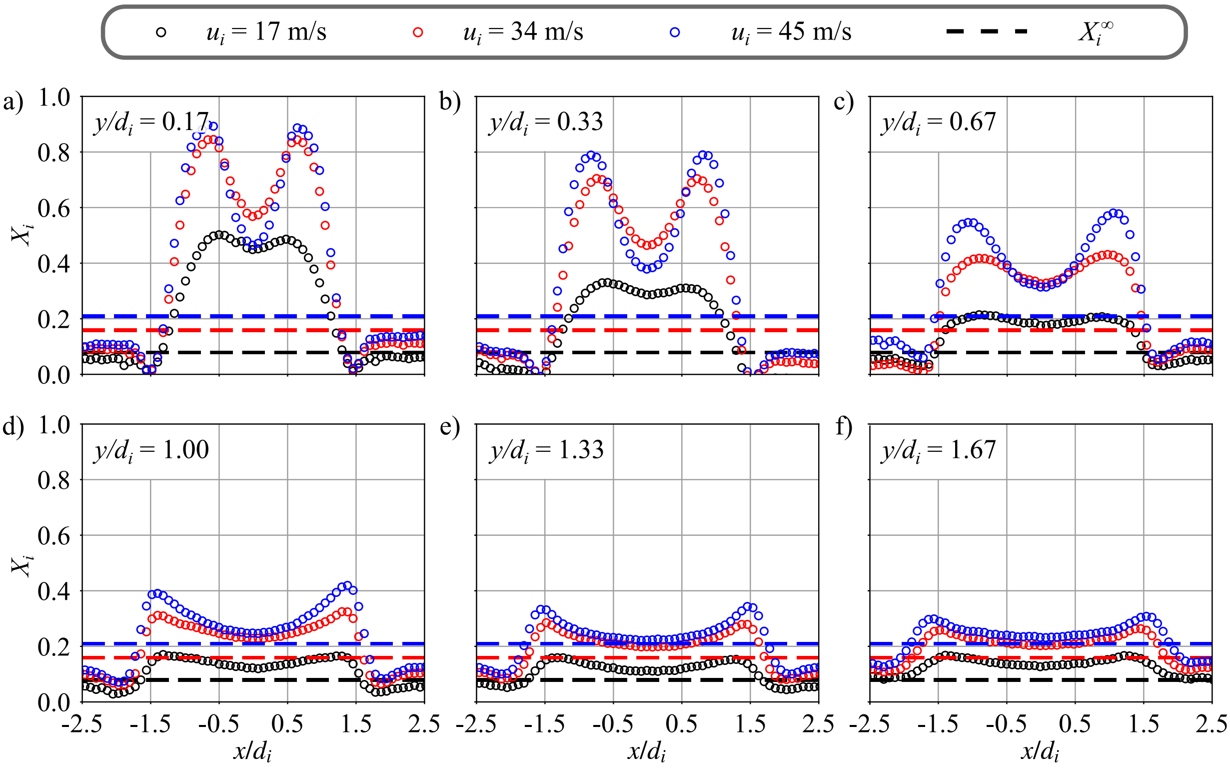

Figure 5.10 – Evolution of the mean helium molar above the burner for three central injection velocities $u_i = 17$, 34 and 45 m/s. The injector is flush-mounted with the combustion chamber backplane $y_i = 0$ mm and the swirl level in the central channel is $S_i = 0.6$. The air bulk velocity is $u_e = 28.5$ m/s. The dashed lines are the theoretical molar concentrations of helium X_i^∞ if the two flows are perfectly premixed.

Profiles of the molar fraction of helium are presented in Fig. 5.10. Increasing the helium injection velocity decreases the mixing rate. In the first millimeters downstream the injector outlet, the mixing rate is higher for low helium injection velocities. The progress variable will help to interpret these measurements.

The progress variable calculated from data shown in Fig. 5.10 is presented in Fig. 5.11. Mixing improves when the central injection velocity is reduced. These results are difficult to interpret without ambiguity because the impulsion ratio and consequently the global molar concentration X_i^∞ vary between the different cases studied. This is further studied and clarified in the following.

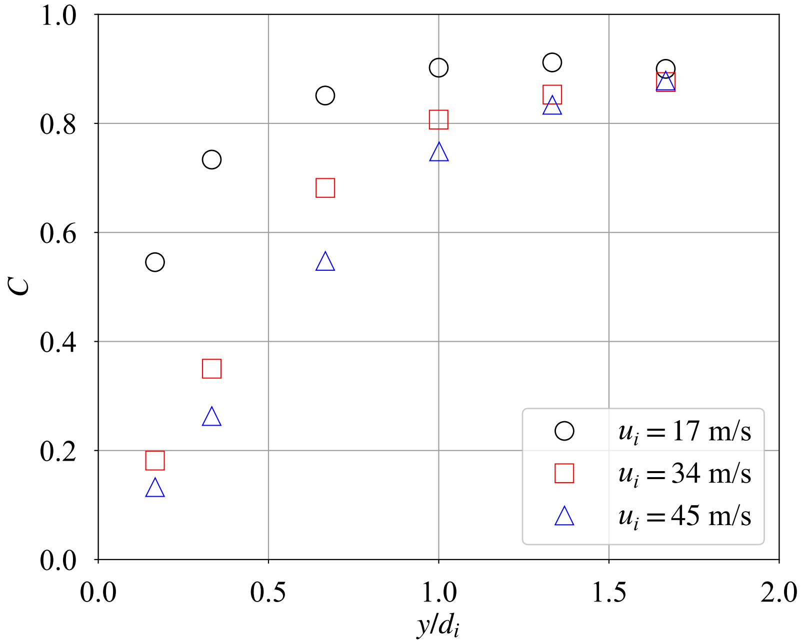

Figure 5.11 – Evolution of the mixing progress variable C for three central injection velocities $u_i = 17$, 34 and 45 m/s. The injector is flush-mounted with the combustion chamber backplane $y_i = 0$ mm and the swirl level in the central channel is $S_i = 0.6$. The air bulk velocity is $u_e = 28.5$ m/s.

5.6 Influence of velocity ratio

In Fig. 5.12, the gases injected are air in the external channel and helium in the central lance. For three values of the impulsion ratio, the flowrates are increased proportionally. Consequently, the density ratio between the two streams is fixed to $r_\rho = \rho_e/\rho_i = 7.2$ and only the effect of the velocity ratio $r_u = u_e/u_i$ is studied. Here, the velocity ratio r_u is varied from $r_u = 0.55$ to $r_u = 0.95$. The swirl level is set to $S_i = 0.6$ and the injector recess to $y_i = 4$ mm. Figure 5.12 shows that the helium molar concentration profiles barely change varying the total flowrate for a given impulsion ratio J, i.e. velocity ratio r_u here. These observations are coherent with theory and previous studies [91, 128–130]. They can be use to interpret the results presented previously. The increase of the mixing rate with the air bulk velocity observed in Fig 5.8 is due to the increase of the velocity ratio r_u. Conversely, the decrease of the mixing rate observed in Fig. 5.11 when the central injection velocity is increased is due to the decrease of the velocity ratio r_u. This corroborates that the scaling parameter proposed by Villermaux *et al.* [91] is at least partially valid for non-swirling co-axial jets for the case of this dual swirl injector. The effect of the density ratio needs to be investigated now.

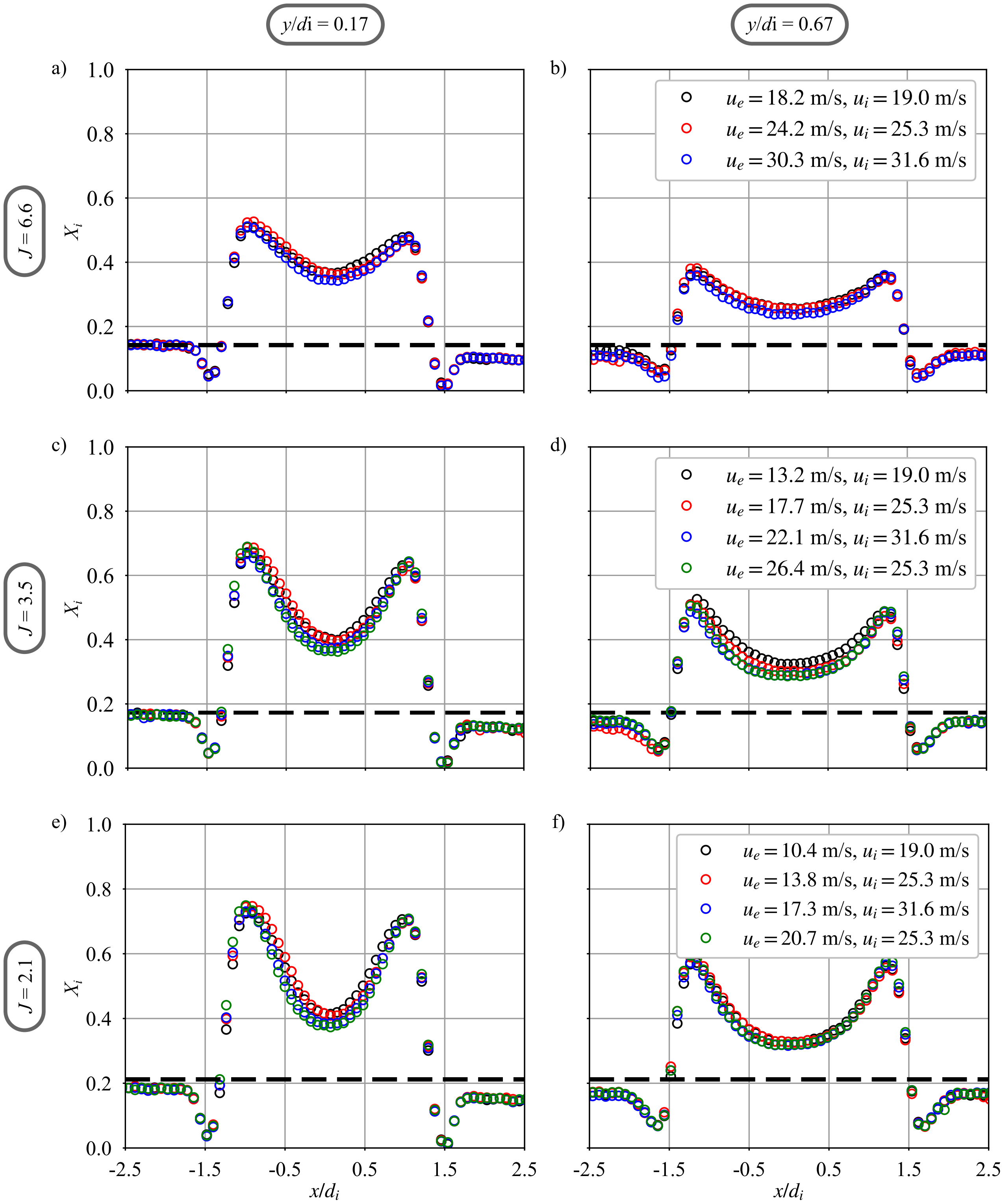

Figure 5.12 – Mean helium molar concentration profiles for different impulsion ratios at two height above the burner $y/d_i = 017$ (left) and $y/d_i = 0.67$ (right). (a-b) $J = 6.6$. (c-d) $J = 3.5$. (e-f) $J = 6.6$. The injector recess is $y_i = 4$ mm and the internal swirl level is $S_i = 0.6$. The dashed line is the theoretical molar concentration of helium X_i^∞ if the two flows are perfectly premixed.

5.7 Influence of density ratio

It is generally admitted that the impulsion ratio needs to be conserved to reproduce the same mixing rate between two coaxial channels. It is shown in [91] that the length to reach local stoichiometry L_s scales with $J^{1/2}$. Here, varying the density of the gas injected through the channel, the impulsion ratio J and the velocity ratio r_u are conserved in the two sets of experiments. The density variation of the gas injected by the central channel is achieved with different gases: hydrogen ($\rho_{H_2} = 0.08988$ kg/m^3), helium ($\rho_{He} = 0.16753$ kg/m^3), methane ($\rho_{CH_4} = 0.7173$ kg/m^3) and argon ($\rho_{Ar} = 1.7835$ kg/m^3). The gas density ratio $r_\rho = \rho_e/\rho_i$ between the two channels is varied from $r_\rho = 0.7$ to $r_\rho = 14.4$

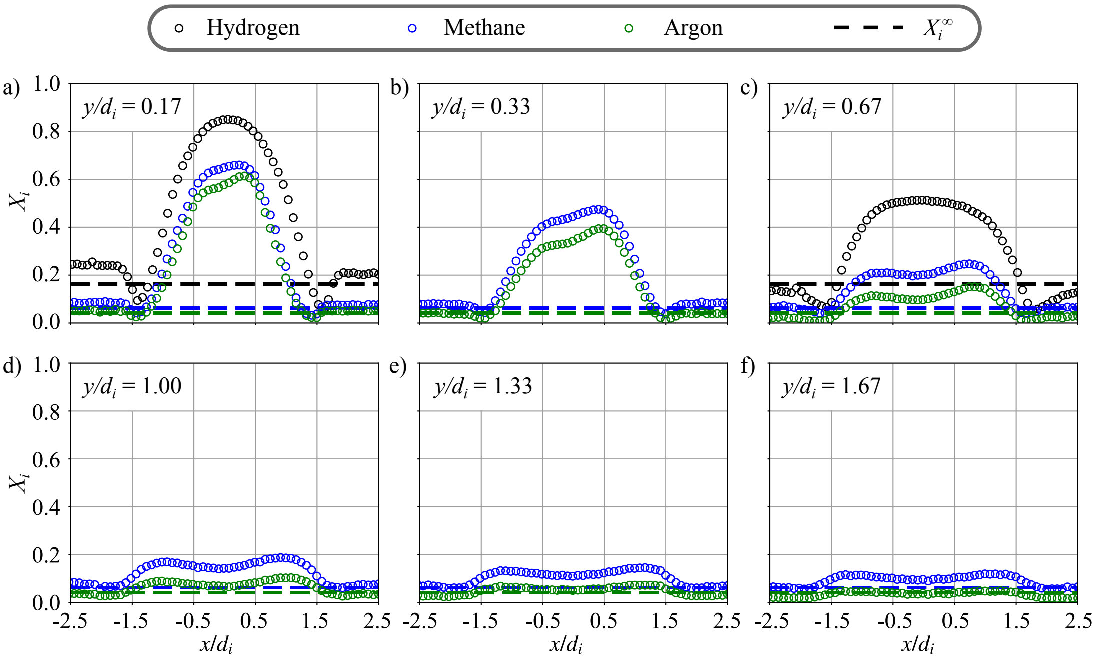

Figure 5.13 – Evolution of the mean molar concentration profiles above the burner for three gases injected through the central lance: hydrogen ($r_\rho = 14.4$), methane ($r_\rho = 1.8$) and argon ($r_\rho = 0.7$). The impulsion ratio is kept constant to $J = 10.1$. The injector is flush-mounted with the combustion chamber backplane $y_i = 0$ mm and no swirl is imparted to the central jet flow $S_i = 0.0$. The air bulk velocity is $u_e = 28.5$ m/s. The dashed lines are the theoretical molar concentrations of helium X_i^∞ if the two flows are perfectly premixed.

The evolution of mixing is plotted in Figs. 5.13 and 5.14 for different gases injected through the central channel without swirl motion $S_i = 0.0$. The gas in the annular channel is always air. In Fig. 5.13, measurements are made with a constant impulsion ratio $J = 10.1$. The mixing rate is greatly affected by the gas density ratio r_ρ, due to the decrease of the velocity ratio r_u. Large differences are visible from $y/d_i = 0.17$ to 1.67. It is concluded that the impulsion ratio J is not a driving parameter for the mixing of coaxial jets in the presence of a CRZ. Moreover, it is interesting to note the influence of the CRZ on the concentration profiles of methane and argon which are injected with a velocity much smaller than the hydrogen case, due to the conservation of the impulsion ratio J.

The same experiments are then repeated with a constant central injection velocity $u_i = 34$ m/s, leading to a constant velocity ratio $r_u = 0.8$. The results are presented in Fig. 5.14. The concentration profiles are close for $y/d_i \leq 0.33$ but differ for higher distances y/d_i. It is attributed to the competition between the recirculation flow and the central jet. For constant injection velocities, as in Fig. 5.14, only the central gas density influences the impulsion ratio between the central injection and the central recirculation. The influence of the CRZ is more visible for light gases, for which the impulsion ratio is higher.

The influence of the inner swirl level on the previous conclusions is investigated. The same experiments as in Fig. 5.13 with a swirl motion $S_i = 0.6$ to the central flow are carried out and the results are presented in Fig. 5.15. When the impulsion ratio J between the two channels is conserved, mixing is much faster for higher gas density in the central channel. It is again due to the increase of the velocity ratio r_u. As in

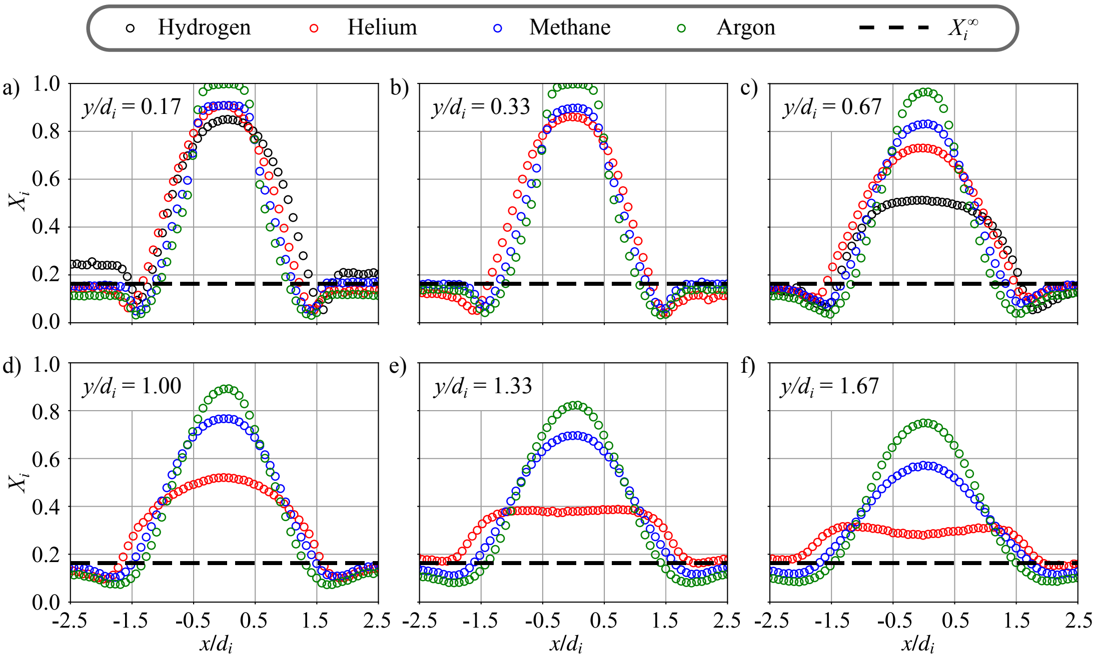

Figure 5.14 – Evolution of the mean molar concentration profiles above the burner for four gases injected through the central lance: hydrogen ($r_\rho = 14.4$), helium ($r_\rho = 7.2$), methane ($r_\rho = 1.8$) and argon ($r_\rho = 0.7$). The central injection velocity is kept constant to $u_i = 34$ m/s and the annular bulk velocity is $u_e = 28.5$ m/s leading to a constant velocity ratio $r_u = 0.8$. The injector is flush-mounted with the combustion chamber backplane $y_i = 0$ mm and no swirl is imparted to the central channel $S_i = 0.0$. The dashed line is the theoretical molar concentration of helium X_i^∞ if the two flows are perfectly premixed.

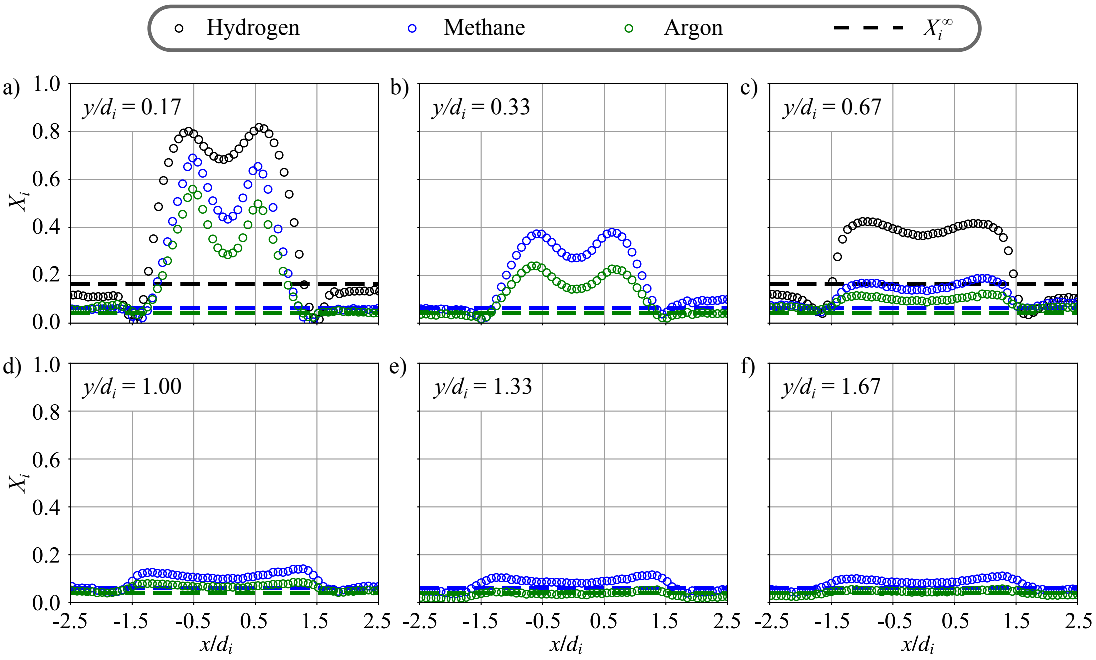

Figure 5.15 – Evolution of the mean molar concentration profiles above the burner for three gases injected through the central lance: hydrogen ($r_\rho = 14.4$), methane ($r_\rho = 1.8$) and argon ($r_\rho = 0.7$). The impulsion ratio is kept constant to $J = 10.1$. The injector is flush-mounted with the combustion chamber backplane $y_i = 0$ mm and the swirl level in the central channel is $S_i = 0.6$. The air bulk velocity is $u_e = 28.5$ m/s. The dashed lines are the theoretical molar concentrations of helium X_i^∞ if the two flows are perfectly premixed.

Fig. 5.13, large differences on the gas concentration profiles are visible from $y/d_i = 0.17$ to 1.67, and the conclusion is made that mixing is not comparable in this case.

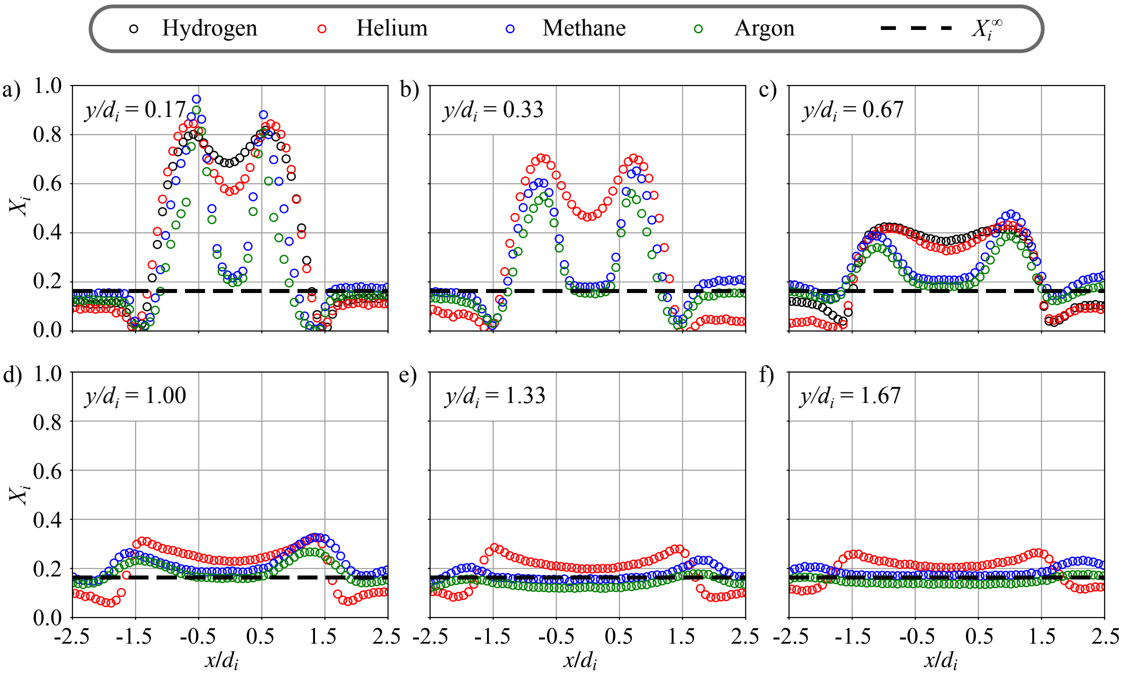

Figure 5.16 – Evolution of the mean molar concentration profiles above the burner for four gases injected through the central lance: hydrogen ($r_\rho = 14.4$), helium ($r_\rho = 7.2$), methane ($r_\rho = 1.8$) and argon ($r_\rho = 0.7$). The central injection velocity is kept constant to $u_i = 34$ m/s and the annular bulk velocity is $u_e = 28.5$ m/s leading to a velocity ratio $r_u = 0.8$. The injector is flush-mounted with the combustion chamber backplane $y_i = 0$ mm and the swirl level in the central channel is $S_i = 0.6$. The dashed line is the theoretical molar concentration of helium X_i^∞ if the two flows are perfectly premixed.

The same experiments are now repeated with a constant central injection velocity for the different gases investigated. Results are presented in Fig. 5.16. Mixing between the two jets progresses approximately with the same rate because r_u and X_{st} are kept constant in Fig. 5.16. Differences are also visible, especially for argon. It can be due to a small modification of the central jet angle α_i. This is investigated in details in the following. Despite the large variation of the density ratio from $r_\rho = 0.7$ to $r_\rho = 14.4$, it is concluded that mixing of the two dual swirl coaxial streams is comparable when the velocity ratio r_u is kept constant.

5.8 Mechanisms and scaling laws of the mixing

The previous observations are considered to highlight the mechanisms driving the mixing in the case of dual swirl coaxial injector, with the injector flush mounted $y_i = 0$ mm with the combustion chamber backplane. An effort is made to determine scaling laws in a general way, as much as possible. The model proposed by Villermaux and Rehab [91] is revisited and adapted to the case of swirling flows.

In Fig. 5.17.a, the initial model proposed by Villermaux and Rehab [91] is schematically illustrated. The geometry is axisymmetric. This model considers a central jet without jet divergence $\alpha_i = 0°$ with a non-swirling co-flow. A surface exchange denoted A_{ee} between the two streams is considered and illustrated with a red line in Fig. 5.17.a. In the case of two circular and co-axial jets considered by Villermaux and Rehab [91], the surface exchange A_{ee} is cylindrical. This model considers that the central jet is diluted along the vertical axis y by entrainment of gas from the annular co-flow with a velocity of entrainment u_{ee}. In the original paper [91], several assumptions are made:

1. The entrainment velocity u_{ee} is assumed to be proportional to the annular bulk velocity u_e: $u_{ee} \sim u_e$.
2. The velocity ratio is assumed to be much greater than unity: $r_u = u_e/u_i >> 1$.

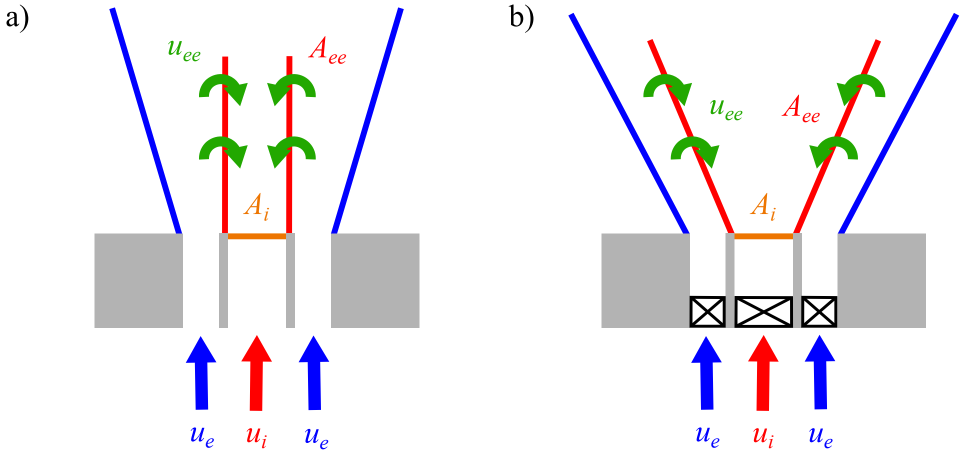

Figure 5.17 – Schematic of the modeling approach to scale the mixing progress variable C. (a) From Villermaux and Rehab [91] valid for $S_i = 0.0$. (b) Two swirled streams in each injection channel.

From the definition of the molar concentration X_i of the gas injected through the central tube, one can write:

$$X_i = \frac{n_i}{n_i + n_e} = \frac{\dot{V}_i}{\dot{V}_i + \dot{V}_e} = \frac{u_i A_i}{u_i A_i + u_{ee} A_{ee}} \tag{5.2}$$

It comes, considering $r_u >> 1$:

$$X_i \sim \frac{1}{(y/d_i)\, r_u} \tag{5.3}$$

In this work, the same modeling approach is adopted and adapted to the case of swirled flows. Moreover, for the operating points explored in this study, the assumption $r_u >> 1$ is relaxed. Here, the exchange area corresponding to the interface between the central and the annular jets is modeled as an inverted truncated cone, that can be expressed as follow:

$$A_{ee} = \pi \left(y \tan(\alpha_i) + d_i \right) \frac{y}{\cos(\alpha_i)} \tag{5.4}$$

From Eq. (5.2), it comes for X_i:

$$X_i \sim \frac{1}{1 + 4\delta \left(y/d_i \tan(\alpha_i) + 1 \right) (y/d_i) \left(r_u / \cos(\alpha_i) \right)} \tag{5.5}$$

where δ corresponds to the ratio between the entrainment velocity and the bulk air velocity $\delta = u_{ee}/u_e$ and needs to be determined. It finally comes for the mixing progress variable C:

$$C \sim \left(1 - \frac{1}{1 + 4\delta \left(y/d_i \tan(\alpha_i) + 1 \right) (y/d_i) \left(r_u / \cos(\alpha_i) \right)} \right) / \left(1 - X_i^{\infty} \right) = \eta \tag{5.6}$$

The scaling variable is denoted η in the following. Note that this relation is equivalent to Eq. (5.3) proposed by Villermaux and Rehab [91] when $r_u >> 1$ and $\alpha_i = 0°$. In contrast to [91], the parameter δ is needed because the simplification $r_u >> 1$ cannot be used here. The value of δ is found to be equal to $\delta = 1/4$ for all operating conditions explored. This value is determined indirectly from mixing measurements for the hydrogen case with $S_i = 0.6$, $y_i = 0$ mm, $u_e = 28.5$ m/s and $u_i = 34$ m/s and then applied to all other cases. Figure 4.6.a shows that the central jet expands radially directly at the outlet of the injector even for the case without inner swirl $S_i = 0.0$ and the angle of this jet differs for 0° as reported in Tab. 4.1. The choice is made in this section to consider only the operating points for which PIV measurements are available for helium/air case, and, consequently, the angle of the central jet is well known. The assumption is made that the angle of the central jet α_i depends only on the inner swirl level S_i and the velocity ratio

Table 5.2 – Angles of the central jet α_i with the vertical axis used in Figs. 5.18, 5.19 and 5.20.

S_i	0.0	0.4	0.6	0.6	0.6	0.9
u_i	All	34	17	34	45	34
α_i [deg]	8	32	64	41	50	48

r_u. The angle α_i is considered as independent of the velocity ratio r_u for the unswirled case. For the data presented in the following, the air bulk velocity u_e is kept constant to $u_e = 28.5$ m/s and consequently only the mean injection velocity u_i in the central channel acts on the velocity ratio r_u. These angles are reported in Tab. 5.2.

First the case without swirl in the inner injector $S_i = 0.0$ is considered. The mixing progress variable C is plotted for this case in Fig. 5.18 when the velocity ratio is then varied from $r_u = 0.8$ to $r_u = 3.8$ and the density ratio from $r_\rho = 0.7$ to $r_\rho = 14.4$. The results are presented for different gases injected in the central channel and for two strategies. In the first one the central injection velocity is kept constant equal to $u_i = 34$ m/s, i.e. the velocity ratio is kept constant to $r_u = 0.8$ because the air bulk velocity is fixed to $u_e = 28.5$ m/s. In the second strategy, the impulsion ratio kept constant to $J = 10.1$. The reference case is hydrogen.

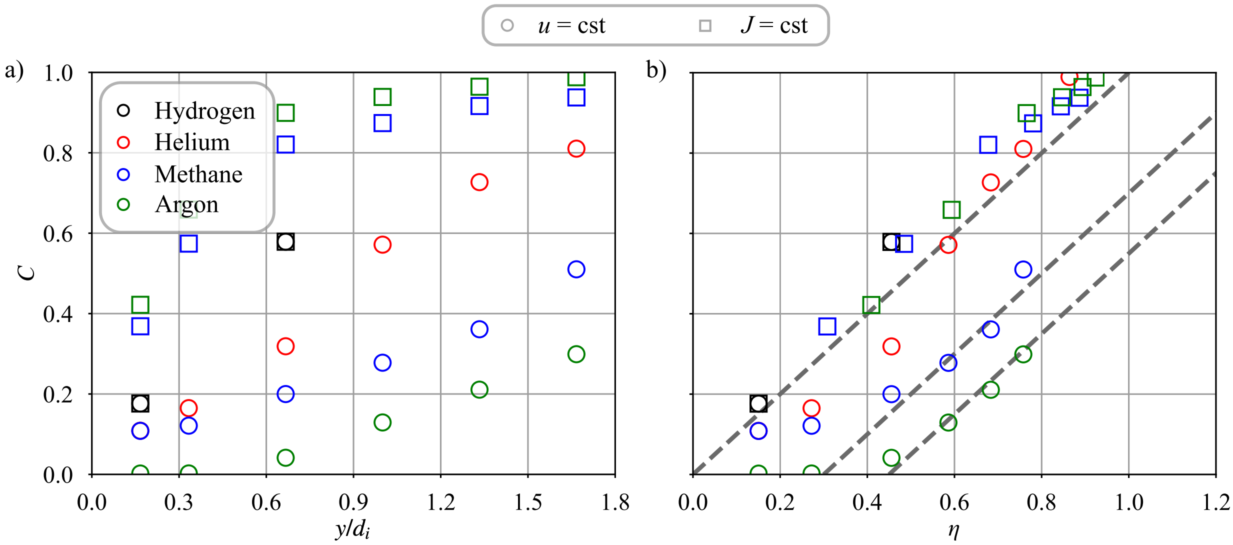

Figure 5.18 – Mixing progress variable without swirl conferred to the central stream $S_i = 0.0$. The velocity ratio is varied from $r_u = 0.8$ to $r_u = 3.8$ and the density ratio from $r_\rho = 0.7$ to $r_\rho = 14.4$. (a) Results plotted against the distance from the injector outlet non-dimensionalized by the inner injector diameter y/d_i. (b) Results plotted against the mixing variable η.

The data are plotted in Fig. 5.18.a as a function of the dimensionless axial coordinate y/d_i. For the four gases injected through the central channel, the two strategies ($u = $ cst and $J = $ cst) are presented, except for helium operation with $J = $ cst. For the reference hydrogen case, the two strategies lead to the same injection velocities and the points are superimposed. The mixing is faster for gases with a higher density, here methane and argon, when the impulsion ratio J is conserved. This is due to the decrease of the injection velocity implied by the conservation of the value of the impulsion ratio J. As shown previously, mixing is enhanced when the velocity ratio r_u increases, i.e. when the central injection velocity u_i decreases if the air bulk velocity u_e remains fixed. Conversely, for a constant velocity ratio, the mixing rate decreases when the density ratio decreases i.e. the density of the gas injected through the central channel increases. Mixing of the methane and argon jets (for $u = $ cst) starts further downstream than for hydrogen and helium injection, due to the strong impulsion of these jets. This is to denoted core jet zone in [91]. When these results are plotted against the mixing scaling variable η in Fig. 5.18.b, all the mixing variables exhibit the same unity slope. The light gases and low velocity injection cases collapse on a same line, only the case of methane and argon with $u = \text{cst}$ are shifted to the right, due to the late beginning of the mixing. The slopes of the lines for these two cases are unity too. Here the angle α_i used for the determination of the mixing scaling variable η is $\alpha_i = 8^\circ$ for all operating conditions.

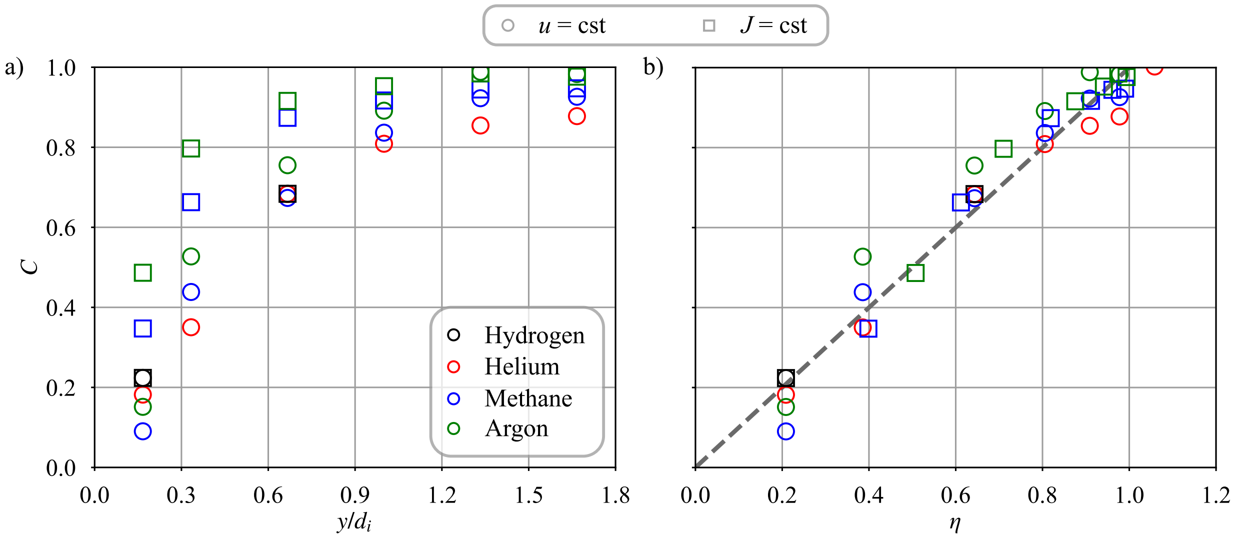

Figure 5.19 – Mixing progress variable with swirl conferred to the central stream $S_i = 0.6$. The velocity ratio is varied from $r_u = 0.8$ to $r_u = 3.8$ and the density ratio from $r_\rho = 0.7$ to $r_\rho = 14.4$. (a) Data plotted against the axial distance to the injector outlet non-dimensionalized by the inner injector diameter y/d_i. (b) Data plotted against the mixing variable η.

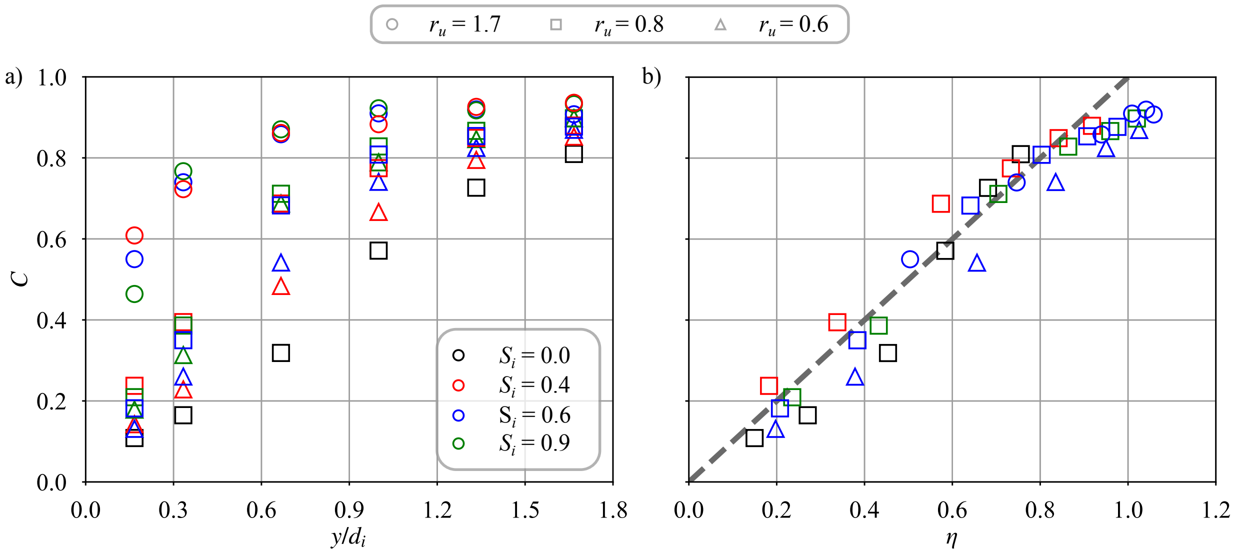

Figure 5.20 – Mixing progress variable for helium injected in the central channel with a swirl level varied from $S_i = 0.0$ to $S_i = 0.9$. The velocity ratio is varied from $r_u = 0.6$ to $r_u = 1.7$. (a) Data plotted against the axial distance to the injector outlet non-dimensionalized by the inner injector diameter y/d_i. (b) Data plotted against the mixing variable η.

Now the swirl level in the inner channel is fixed to $S_i = 0.6$. The results are presented in Fig. 5.19. In Fig. 5.19.a when a swirl is added to the central channel, the mixing progress is similar when the velocity ratio r_u is kept constant, despite the large variation of the density ratio r_ρ. Again, when the impulsion ratio is kept constant, increasing the density of the gas injected through the central channel leads to a decrease of the central injection velocity and the mixing between the two jets progresses faster. When these data are plotted against the mixing scaling variable η in Fig. 5.19.b, the points collapse around a single line of unity slope as in Fig. 5.18.b. In all these cases the jets mix directly at the outlet of the injector due to the penetration of the CRZ in the central injector. This leads to the collapse of all the points around a single line.

The model is now compared to a larger set of measurements with an inner swirl level varying from $S_i = 0.0$ to $S_i = 0.9$ and the velocity ratio from $r_u = 0.6$ to $r_u = 1.7$. The gas injected through the central channel is only helium, corresponding to a fixed value of the density ratio $r_\rho = 7.2$. Figure 5.20.a, shows a large diversity of mixing for the different cases considered. When the mixing scaling variable η is used to plot the data in Fig. 5.20.b, all these points collapse again on a same line, with a slope equal to unity. The mixing scaling variable η well describes the mixing progress for a wide range of operating points.

5.9 Conclusion

Mixing between the central and external channels of the HYLON injector has been investigated in cold flow conditions in order to better understand how the inner swirl level S_i, injector recess distance y_i and air and hydrogen injection velocities u_e and u_i affect the mixing between the central and annular flows. The results can be resumed as follow:

- The inner swirl motion $S_i > 0.0$ increases substantially the mixing rate between the central and the annular streams, especially in the first millimeters above the central injector outlet.
- A high inner swirl $S_i \geq 0.6$ only enhances slightly the mixing compared to a moderate swirl level, typically $S_i = 0.4$.
- An injector recess favors a partial premixing before the flow penetrates in the combustion chamber. But the mixing rate in the mixing tube between the outlet of the central injector and the inlet of the combustion chamber is less than inside the combustion chamber.
- Increasing the annular air injection velocity enhances mixing. Increasing the central injection velocity reduces mixing.
- The velocity ratio and the angle of the central jet control the progress of the mixing. These conclusions have been validated for cases where the injection diameters and the annular swirl level are kept constant.
- A model inspired from [91] has been developed to examine the impact of the inner swirl level S_i, velocity ratio r_u and gas density ratio r_ρ on the mixing rate. An adimensional mixing progress variable η has been deduced.
- When the mixing progress variable C is plotted against η, all the data collapse on a single line of unity slope after the beginning of the mixing between the two jets.

These measurements allow to understand how each parameter influences the mixing of coaxial jets. The results can be used to improve the design of coaxial swirl injectors.

Chapter 6

Hot flow analysis

> *"Intelligence is, unfortunately! always an enigma, but no more than stupidity."*
>
> Alan Turing

Overview

6.1 Flow velocity measurements

6.1.1 Results on selected operating points

For the validation of high fidelity numerical simulations of the HYLON injector [92], PIV measurements in reactive conditions are carried out for three selected operating points. The PIV setup used for the measurements is described in Chapter 2.

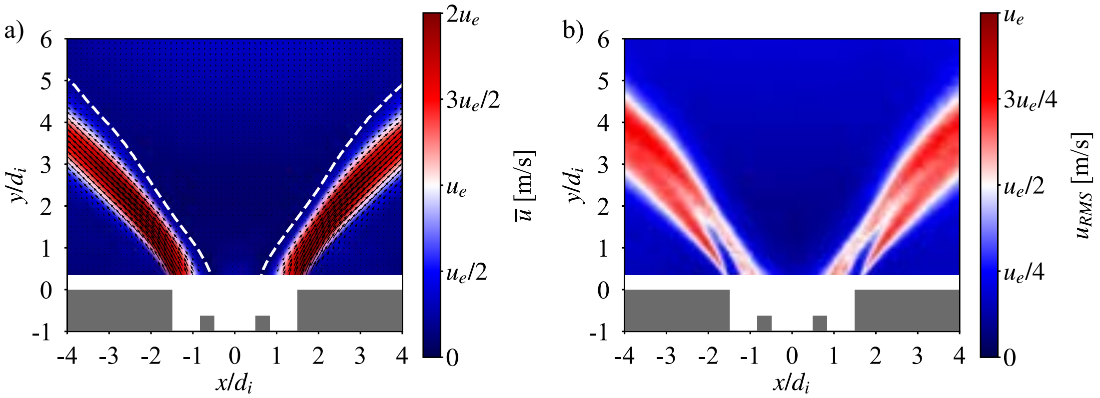

Figure 6.1 – Velocity field in reactive conditions in the axial plane for an inner swirl level $S_i = 0.6$ and a hydrogen injector recess $y_i = 4$ mm. The fields are normalized by the bulk air velocity $u_e = 11.4$ m/s in the external channel. The central injection velocity is $u_i = 13.6$ m/s. These operating conditions correspond to flame A presented in Fig. 3.7.a, anchored to the injector lips. (a) Mean velocity field. The white dashed lines denote the location where the axial velocity $u_z = 0$ m/s, delineating the CRZ. (b) RMS velocity field.

The first selected operating point is flame A presented in Fig. 3.7.a. The flame is anchored to the injector lips and has been simulated by A. Aniello in [92]. The mean and RMS velocity fields are presented in Fig. 6.1. The air velocity is set to $u_e = 11.4$ m/s and the hydrogen injection velocity to $u_i = 13.6$ m/s. The inner swirl level is $S_i = 0.6$ and the injector recess is $y_i = 4$ mm. The CRZ is always present around the centerline of the flow, and the recirculating velocity along the centerline $x = 0$ mm is approximately equal to $0.4u_e$. The diameter of the CRZ at the bottom of the PIV window is approximately equal to the inner diameter of the central injector $d_{CRZ} \approx d_i = 6$ mm. The maximum velocity in the jet arms is slightly greater than $2u_e$.

Figure 6.1.b shows that the maximum RMS value of the velocity is close to $3u_e/4$ indicating intense turbulence. On the external side of the jet, from the base to the top, fluctuations appear at the outlet of the annular injector in a thin layer and develop further downstream in the shear layer between the ORZ and the main jet. In the shear layer between the main jet and the CRZ, lower fluctuations are measured at the bottom of the PIV window before developing further downstream at $y/d_i > 1.5$. For axial distance $y/d_i \geq 3$, large fluctuations are present in all the jet which becomes fully turbulent.

The second reference case is flame G presented in Fig. 3.7.g where the flame is lifted. This is the second operating point simulated in [92]. The mean and RMS values of the flow velocity field are shown in Fig. 6.2. The inner swirl level and the injector recess are the same as for flame A ($S_i = 0.6$ and $y_i = 4$ mm). The annular injection velocity is $u_e = 28.5$ m/s and the hydrogen injection velocity is equal to $u_i = 34$ m/s. The general structure of the mean and RMS values of the flow velocity field is similar to ones for flame A presented in Fig. 6.1, but some differences are also visible. The maximum values reached by the velocity, non-dimensionalized by $2u_e$ for the mean field and by u_e for the RMS fluctuations, are similar to ones for flame A. For flame A, anchored to the injector lips, thermal expansion due to heat release occurs right the central injector outlet. For flame G, lifted above the injector lips, the thermal expansion takes place further downstream. Consequently, the thickness of the jet flow is, for $y/d_i \leq 1.5$, lower than for flame A. Moreover, the diameter of the CRZ at the bottom of the PIV window is larger $d_{CRZ} \approx d_{ie} = 10$ mm, leading to a higher flow blockage at the outlet of the annular injector. The impact of heat release on the flow field is further investigated below.

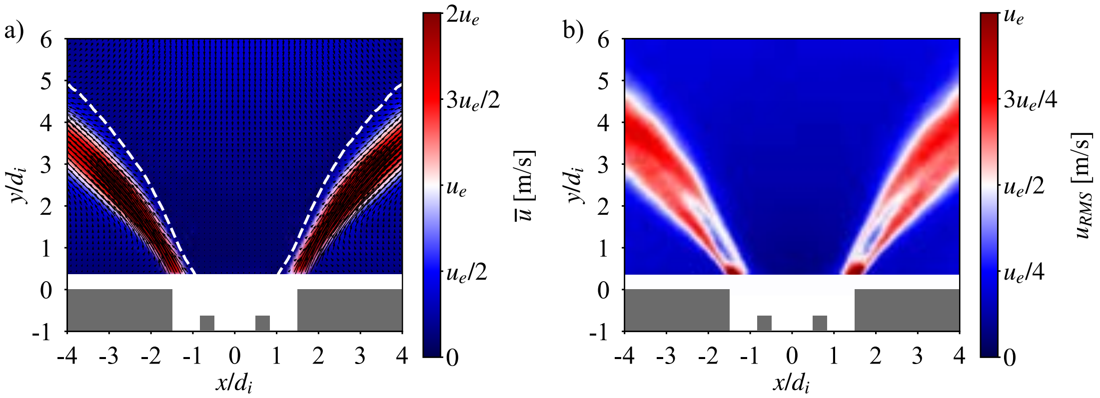

Figure 6.2 – Velocity field in reactive conditions in the axial plane for an inner swirl level $S_i = 0.6$ and a hydrogen injector recess $y_i = 4$ mm. The fields are normalized by the bulk air velocity $u_e = 28.5$ m/s in the external channel. The central injection velocity is $u_i = 34$ m/s. These operating conditions correspond to flame G presented in Fig. 3.7.g, lifted above the injector lips. (a) Mean velocity field. The white dashed lines denote the location where the axial velocity $u_z = 0$ m/s, delineating the CRZ. (b) RMS velocity field.

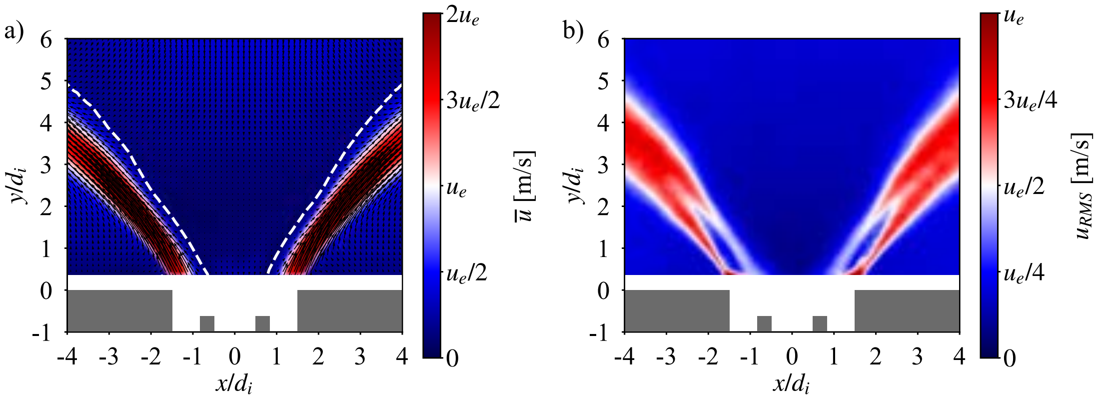

Figure 6.3 – Velocity field in reactive conditions in the axial plane for an inner swirl level $S_i = 0.6$ and a hydrogen injector recess $y_i = 4$ mm. The fields are normalized by the bulk air velocity $u_e = 28.5$ m/s in the external channel. The central injection velocity is $u_i = 34$ m/s. Operating conditions correspond to flame G presented in Fig. 3.7.g, but in a situation where the flame is forced to anchor to the injector lips. (a) Mean velocity field. White dashed lines denote the location where the axial velocity $u_z = 0$ m/s, delineating the CRZ. (b) RMS velocity field.

To visualize the influence of the flame front on the velocity field, flame G in Fig. 3.7.g can be forced to anchor on the injector lips in certain conditions. Typically this is the case after a hard ignition when the burner is ignited with a torch at the top of the combustion chamber at full power with both air and hydrogen flowrates fully established. With this ignition scheme the flame is anchored for the same operating point presented in Fig. 6.2 in which case the flame is lifted. Results are presented in Fig. 6.3. Several differences appear, due to the heat release rate located further upstream with a flame stabilized on the injector lips. The thickness of the jet flow at the bottom of the PIV windows is much more larger than in the lifted case in Fig. 6.3, due to thermal flow expansion. The diameter of the CRZ at the base of the PIV window is smaller with a value slightly greater than d_i due to the earlier gas expansion. The RMS fluctuations in Fig. 6.3.b are slightly lowered by the presence of the flame in the main flow for $y/d_i \leq 2$. This modification of the flow field when the flame is anchored leads to a hysteresis for the transitions from anchored to lifted flame. The lift-off velocity determined in Chapter 3 when a lifted flame reanchors to the injector rim is not the same when the flame is anchored. One needs to blow more air to lift the flame from the injector.

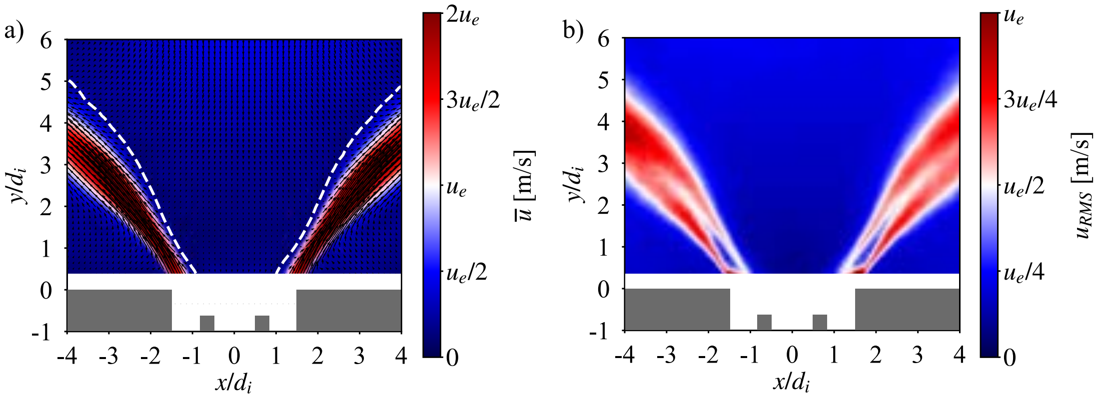

Figure 6.4 – Velocity field in reactive conditions in the axial plane for an inner swirl level $S_i = 0.6$ and a hydrogen injector recess $y_i = 4$ mm. The fields are normalized by the bulk air velocity $u_e = 27.9$ m/s in the external channel. The central injection velocity is $u_i = 45.4$ m/s. These operating conditions correspond to flame I presented in Fig. 3.7.i, lifted above the injector lips. (a) Mean velocity field. The white dashed lines denote the location where the axial velocity $u_z = 0$ m/s, delineating the CRZ. (b) RMS velocity field.

The third and last selected operating point is flame I shown in Fig. 3.7.i where the flame is also lifted (Fig. 6.4). The inner swirl level and the injector recess are still the same as in previous experiments. The air injection velocity is set to $u_e = 27.9$ m/s and the hydrogen injection velocity to $u_i = 45.4$ m/s. Non-dimensionalized by $2u_e$ for the mean velocity field and by u_e for the RMS fluctuations, the resulting velocity fields are very similar as those obtained for flame G presented in Fig. 6.2. The mean angle α_e of the main flow slightly increases compared to flame G but the figure confirms that the non-dimentionalized velocity field mainly depends on the total flowrate, the injector recess, the swirl level and the flame stabilization.

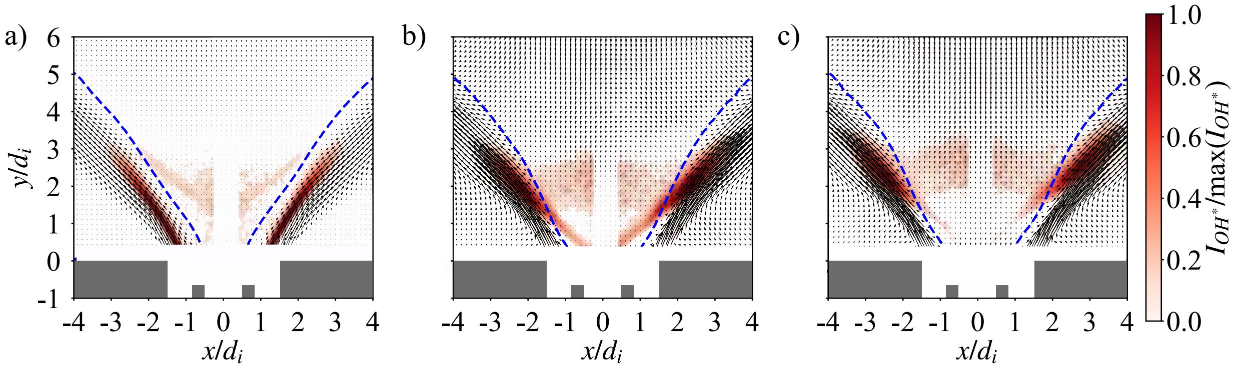

Figure 6.5 – Mean velocity fields with Abel deconvolutions of the OH* signals superimposed to the velocity vectors. The blue dashed lines denote the location where the axial velocity is $u_z = 0$ m/s, delineating the CRZ. The inner swirl level is set to $S_i = 0.6$ and the injector recess to $y_i = 4$ mm. (a) Flame A. (b) Flame G. (c) Flame I.

Figure 6.5 shows Abel deconvoluted OH* images superimposed to the mean velocity fields measured in reactive conditions. The blue dashed lines delineate the CRZ. The first case in Fig. 6.5.a is flame A, anchored to the injector lips. The OH* signal indicates the location of the heat release rate [102] in the shear layer between the main jet and the CRZ. A thin reaction layer is stabilized at a roughly constant distance with the CRZ frontier $u_z = 0$ m/s. A weak reaction front is also stabilized at the CRZ as described in Fig. 3.1.a. As explained in Chapter 3 and confirmed by numerical flow simulations in [92], the two reaction layers burn in diffusion mode. When the flame is lifted for flame G in Fig. 6.5.b and I in Fig. 6.5.c, the reaction layer stabilized at the CRZ, is pushed further upstream close to the burner outlet. The reaction front in the shear layer between the jet and the CRZ is stabilized further downstream. This reaction takes place at stoichiometry [92]. Its position is a good tracer of the position of the stoichiometric mixture fraction line at the inner side of the central hydrogen jet. Compared to the case of the anchored flame in Fig. 6.5.a, the reaction front in the shear layer is thicker in Fig. 6.5.b and 6.5.c. and in a partially premixed combustion mode. The stabilization height of these flames mainly depends on the mixing distance to reach stoichiometry. As shown in Chapter 5, this distance depends on the ratio between air and hydrogen injection velocities, denoted $r_u = u_e/u_i$. This is why flame I in Fig. 6.5.c is stabilized slightly further upstream than flame G in Fig. 6.5.b, due to its higher velocity ratio r_u and consequently the smaller mixing distance to reach stoichiometry. A drops of the CRZ diameter d_{CRZ} is observed in the wake of the flame position for $y/d_i \approx 1$ in Fig. 6.5.b and Fig. 6.5.c.

6.1.2 Comparison with cold flow measurements

To conclude this section, a comparison between cold and reactive flow measurements is carried out.

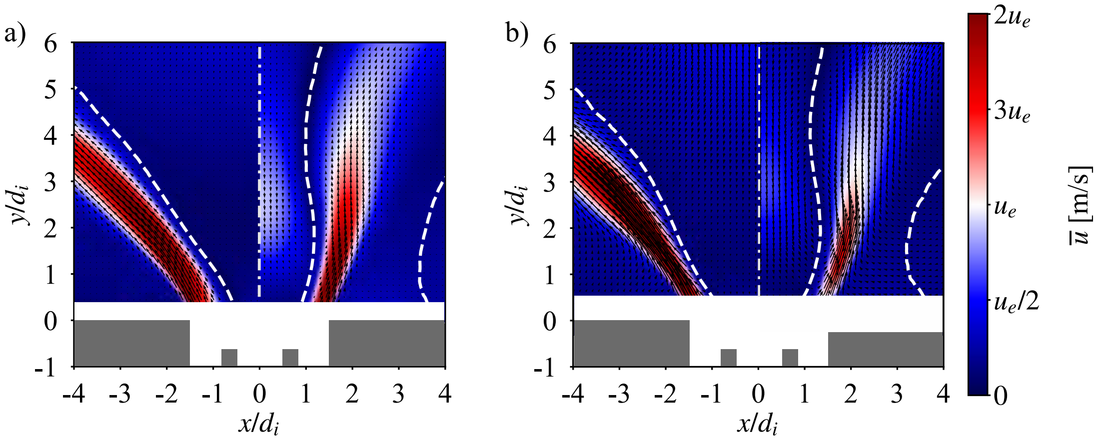

Figure 6.6 – Comparison of the velocity fields in cold (right) and reactive (left) conditions in the axial plane for an inner swirl level $S_i = 0.6$ and a hydrogen injector recess $y_i = 4$ mm. The fields are normalized by the bulk air velocity. The white dashed lines denote the location where the axial velocity $u_z = 0$ m/s, delineating the CRZ. (a) Flame A, anchored to the injector lips. (b) Flame I, lifted above the injector.

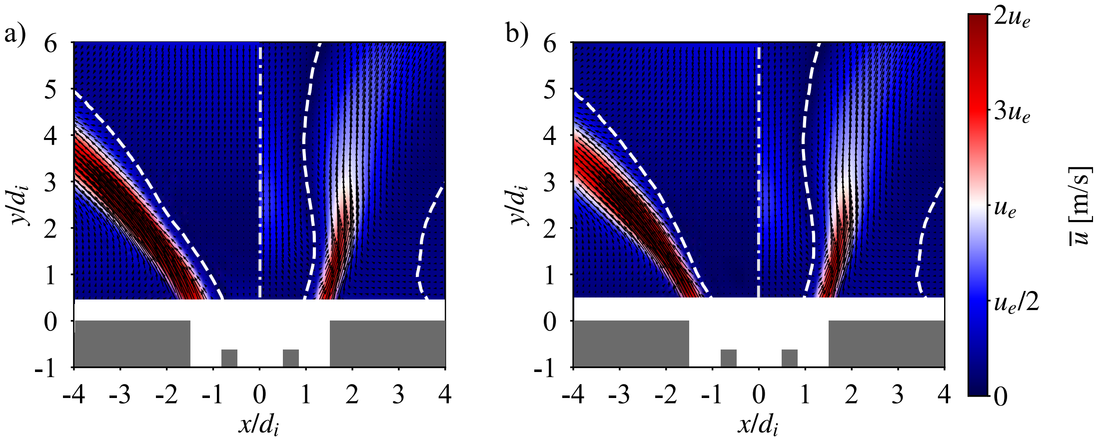

Figure 6.7 – Velocity fields in cold (right) and reactive (left) conditions in the axial plane for an inner swirl level $S_i = 0.6$ and a hydrogen injector recess $y_i = 4$ mm. The operating point corresponds to flame G obtained for $u_e = 28.5$ m/ and $u_i = 34$ m/s. Data are normalized by the bulk air velocity. The white dashed lines denote the location where the axial velocity $u_z = 0$ m/s, delineating the CRZ. (a) Flame anchored to the injector lips. (b) Flame lifted above the injector.

The comparison between cold and reactive velocity fields for flame A (anchored flame) and flame I (lifted flame) is shown in Fig. 6.6. In the two cases, the structure of the flow is strongly affected by the flame.

In reactive conditions shown at the left of each figure, the angle of the jet α_e increases due to the thermal expansion of the gas. Then, the recirculation velocities in the CRZ are reduced and the diameter of the CRZ increases. Moreover, the ORZ is pushed to the external sides and is not visible in the interrogation window in reactive conditions. For flame A in Fig. 6.6.a, anchored to the injector lips, a reduction of the CRZ diameter at the bottom of the PIV window is observed, due to the presence of heat release at the bottom of the window. When the flame is lifted as in Fig. 6.6.b, the diameter of the CRZ in reactive conditions is comparable to the one in cold flow conditions.

The same comparison is carried out for the flame G in Fig. 6.7, for anchored and lifted cases. The same conclusions are drawn than for the flames A and I in Fig. 6.6 for the CRZ size and the ORZ location.

6.2 Temperature measurements

Gas and wall surface temperature measurements have been carried out for the three reference flames A, G and I. Gas temperatures are measured with a double bead thermocouple and surface temperatures with a contact thermocouple for quartz windows and a double wavelength pyrometer for metallic walls (see Chapter 2). The temperature of the combustion chamber walls is determine to set the thermal boundary conditions in numerical flow simulations [92]. The burnt gases temperature at different locations is also determined inside the ORZ and at the combustor outlet. All temperature measurements presented in this chapter correspond to mean values averaged over 2 seconds of acquisition once steady state is reached, i.e. after the thermal equilibrium was reached.

6.2.1 Combustion chamber walls temperature

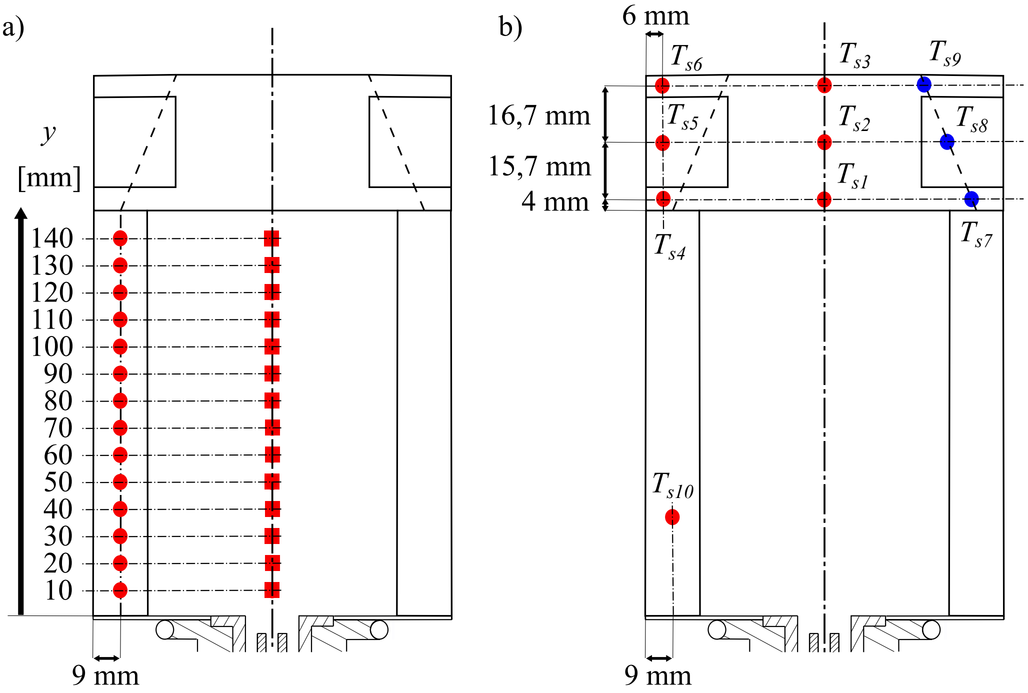

Figure 6.8 – Combustion chamber with locations of the surface temperature measurements. Circle symbols: Measurements made with a double wavelength pyrometer. Square symbols: Measurements with contact thermocouples. Red symbols: External surface of the combustion chamber. Blue symbols: Internal surface of the combustion chamber. (a) Measurements along the external metallic pillar of the combustion chamber and quartz window along the vertical axis. (b) Measurements at selected locations.

The locations where the surface temperatures are measured along the metallic walls and the quartz windows of the combustion chamber are presented in Fig. 6.8.a. Figure 6.8.b shows the locations where the hot gases temperatures are determined outside (red symbols) and inside (blue symbols) the exhaust nozzle at the top of the combustion chamber (see Tab. 6.1 from T_{s1} to T_{s9}) and the location where the temporal evolution of the surface temperature T_{s10} of the combustion chamber is controlled.

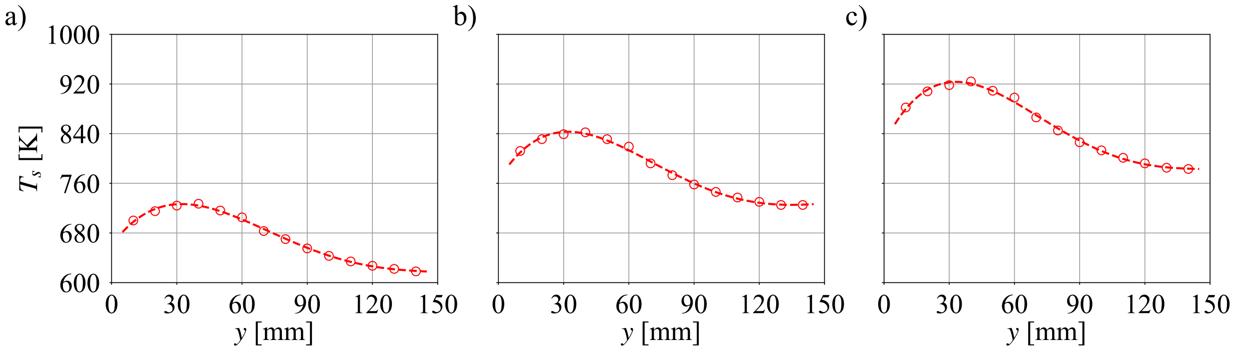

Figure 6.9 – Surface temperature along the external side of a metallic pillar of the combustion chamber (see circle symbols in Fig. 6.8.a). Measurements made with a double wavelength pyrometer. (a) Flame A. (b) Flame G. (c) Flame I. Symbols: Raw data. Dashed line: Fitted data.

Figure 6.9 shows the surface temperature along a metallic pillar of the combustion chamber (see Fig. 6.8.a, red circle symbols) made with the double wavelength pyrometer described in Chapter 2. Measurements are reported for flames A, G and I. In the three cases, the surface temperature T_s reaches a maximum close to $y \approx 30$ mm and decreases downstream. The maximum temperatures are respectively $T_s = 727$, 842 and 924 K for flames A, G and I. They tend to constant values further downstream which are equal respectively to $T_s = 618$, 725 and 783 K.

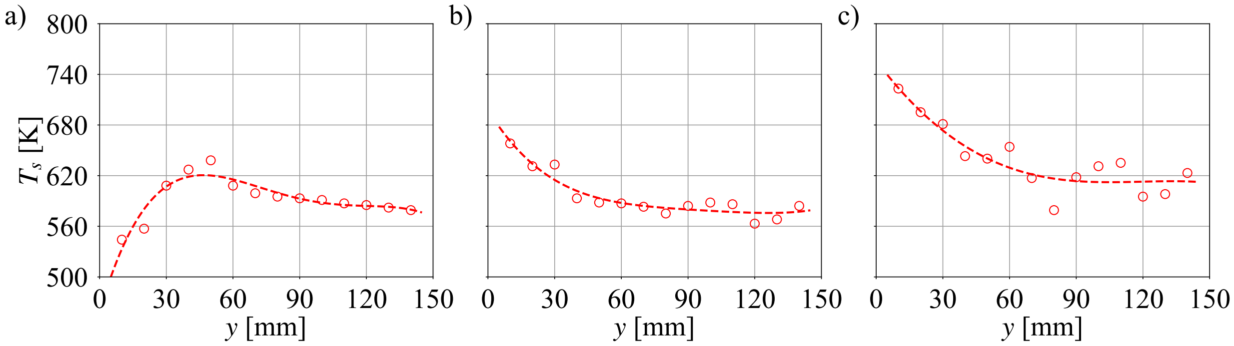

Figure 6.10 – Surface temperature along the external side of a quartz window (see square symbols in Fig. 6.8.a). Measurements made with a contact thermocouple. (a) Flame A. (b) Flame G. (c) Flame I. Symbols: Raw data. Dashed line: Fitted data.

Measurements are also reported along the external surface of the quartz window, at the center of the window along the vertical axis (see red square symbols in Fig. 6.8.a). They are made with a contact thermocouple. Thermal paste is applied on the quartz surface to enhance the thermal contact between the thermocouple and the window. These measurements could not be made with the double wavelength pyrometer because the quartz is transparent to the wavelengths used by the pyrometer. Results are presented in Fig. 6.10. For flame A in Fig. 6.10.a, a similar temperature profile as along the metallic pillar is observed with a drop of approximately 100 K. The results are more intriguing for flames G and I presented in Figs. 6.10.b and 6.10.c. The surface temperature is maximum at the bottom of the quartz window and decreases monotonically downstream. Interpretation of the different behaviors is difficult without further investigations. For flames A, G and I, the maximum temperature is equal to $T_s = 638$, 658 and 723 K.

Again the temperature decreases and reaches further downstream a value which is equal to $T_s = 579$, 584 and 623 K for flame A, G and I respectively.

Table 6.1 – Surface temperature T_{s1} to T_{s9} along the exhaust nozzle shown in Fig. 6.8.b. Measurements are made with a double wavelength pyrometer.

Flame	T_{s1} [K]	T_{s2} [K]	T_{s3} [K]	T_{s4} [K]	T_{s5} [K]	T_{s6} [K]	T_{s7} [K]	T_{s8} [K]	T_{s9} [K]
A	619	618	633	600	618	619	655	645	642
G	724	723	715	706	723	688	765	750	747
I	796	791	780	761	791	733	847	820	808

Additional surface temperatures are reported in Tab. 6.11. The location of the measurements spots for T_{s1} to T_{s9} is indicated in Fig. 6.8.b. These data are used to set the thermal boundary conditions in companion numerical flow simulations [92].

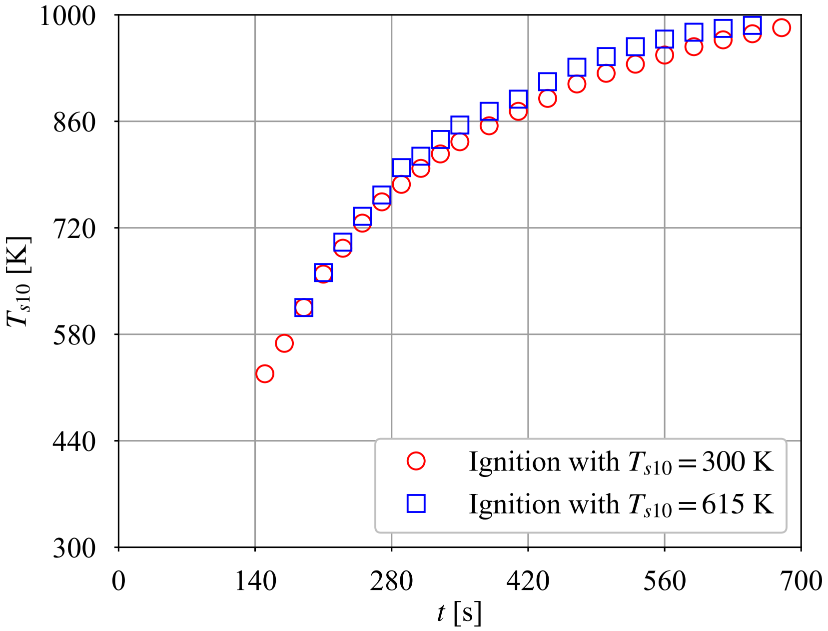

Figure 6.11 – Evolution of the surface temperature T_{s10} at the location indicated in Fig. 6.8.b for a lifted flame with $\phi = 0.66$ and $P_{th} = 14$ kW. The injector recess is set to $y_i = 4$ mm and the inner swirl level to $S_i = 0.6$.

The time taken by the system to reach thermal equilibrium after ignition is estimated with measurements of T_{s10} in Fig. 6.8.b. Two sets of experiments are presented in Fig. 6.11. The first one (red circle symbols), corresponds to ignition of the burner initially cold, i.e at ambient temperature $T_{s10} \approx T_0 \approx 300$ K. Measurements begin when the temperature reaches $T_{s10} = 523$ K, which is the minimum temperature that can measure the double wavelength pyrometer. The temperature increases and reaches $T_{s10} \approx 980$ K after 700 s of operation. The burner is then extinguished and the temperature decreases slowly down to $T_{s10} = 615$ K. The burner is then re-ignited and the temporal evolution of the surface temperature is reported on the same figure with blue square symbols. The first measurement is placed at the instant at which the temperature measured with a burner ignited at $T_{s10} = 300$ K is equal to $T_{s10} = 615$ K. A similar evolution of the temperature is observed and the equilibrium temperature is approximately the same. These results indicate that the thermal state is insensitive to the history of the system followed to reach thermal equilibrium.

6.2.2 Burnt gas temperature

The double bead thermocouple presented in Chapter 2 is used to determine the gas temperatures. Three sets of experiments are carried out to determine the temperature profiles at the outlet of the combustion chamber and the temperature in the ORZ at two axial locations.

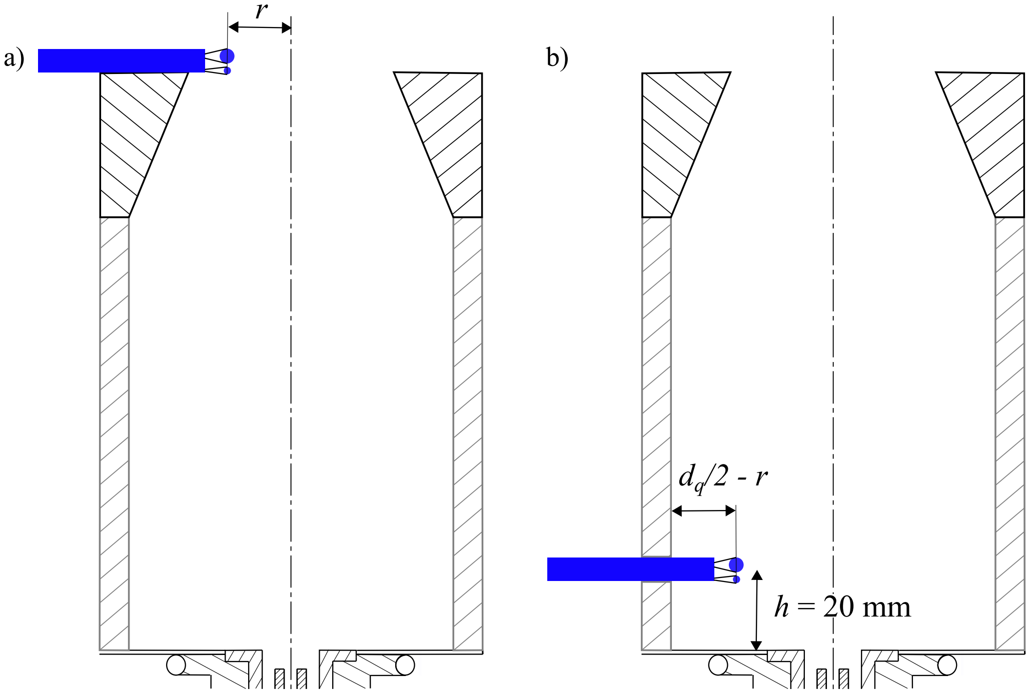

Figure 6.12 – Schematic illustration of the combustion chamber with location of the gas temperature measurements with the double bead thermocouple, shown in blue in the figure. (a) Measurements at the outlet of the combustion chamber. (b) Measurements at the top of the ORZ.

Figure 6.12 indicates the position of the double bead thermocouple (in blue in the figure). Figure 6.12.a shows the position of the thermocouple for measurements of the gas temperature at the outlet of the combustion chamber. Figure 6.12.b shows the position of the double bead thermocouple for measurements of the gas temperature in the ORZ at 20 mm from the combustion chamber backplane. In both cases, the radial position can be varied.

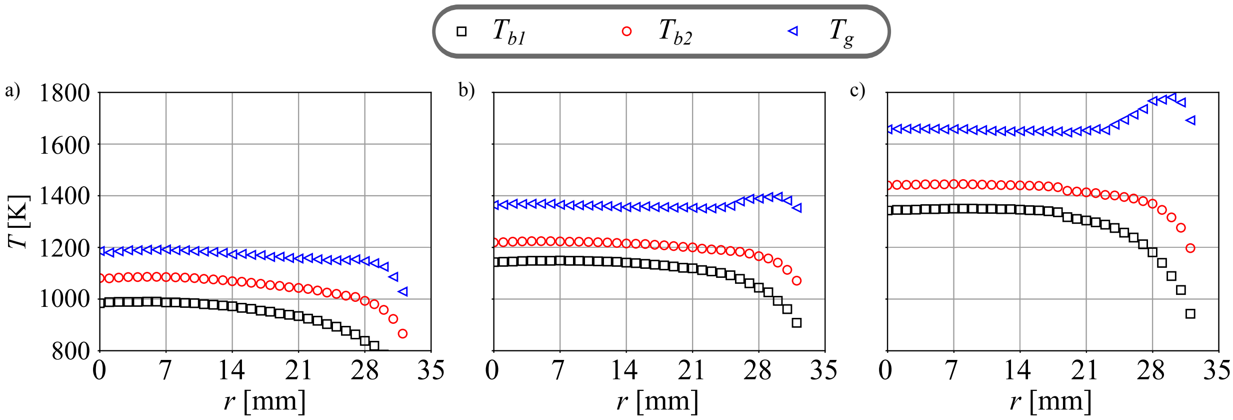

Figure 6.13 – Gas temperature profiles at the outlet of the combustion chamber. The measurements are realized with a double bead thermocouple. (a) Flame A. (b) Flame G. (c) Flame I.

The exhaust gas temperatures for flames A, G, and I are plotted in Figs. 6.13.a, 6.13.b and 6.13.c. The temperature T_{b1} (black square symbols) denotes the temperature of thermocouple 1 with the bigger bead. The temperature T_{b2} (red circle symbols) corresponds to thermocouple 2 with the smaller bead. The corrected gas temperature using the RRE method described in Chapter 2 is plotted with blue triangular symbols. For flame A in Fig. 6.13.a, the temperatures measured with thermocouples 1 and 2 are respectively close to 1000 K and 1100 K between $r = 0$ mm (the centerline) to $r = 20$ mm. Close to the exhaust nozzle walls ($r = d_q/2 = 36.5$ mm), the temperature decreases progressively. The corrected gas temperature profile T_g is flat and close to 1200 K from $r = 0$ to $r = 29$ mm, and decreases close to the external wall. Measurements for flame G, in Fig. 6.13.b, are similar but shifted to higher temperatures. The mean temperature detected by the biggest thermocouple (thermocouple 1) is approximately $T_{b1} \approx 1150$ K, and $T_{b2} \approx 1200$ K for thermocouple 2. The corrected gas temperature profile shows a plateau around $T_g \approx 1380$ K. A small increase and then a decrease is observed close to walls. This may result from an error due to the proximity of a hot radiating wall close to the measurement location. Even through flames A and G show the same global equivalence ratio $\phi = 0.46$, the increase of thermal power from flame A to flame G leads to an increase of the mean temperature of the burnt gases at the outlet of the combustion chamber. This can be due to several effects. First, the flame A is anchored to the injector lips and burns in diffusion mode: the flame temperature of diffusion flames decreases with the increase of strain rate [131, 132]. Another explanation is the residence time 2.5 times greater for flame A estimated with the total flowrate, leading to higher thermal losses of the gas before the combustion chamber outlet. Moreover, due to differences of flame stabilization regime and of heat release rate distribution, the flow field structure is affected and can altering in turn the thermal losses of the gas. The third reference case, flame I in Fig. 6.13.c is lifted as the flame G in Fig. 6.13.b. The equivalence ratio is increased to $\phi = 0.62$ to reach this operating condition. Due to the higher flame temperature, the temperature profiles are shifted to higher values. The maximum measured temperatures are $T_{b1} \approx 1380$ K and $T_{b2} \approx 1420$ K respectively with the thermocouples 1 and 2. The corrected gas temperature is close to $T_g \approx 1650$ K from $r = 0$ mm to $r = 22$ mm. As for flame G in Fig. 6.13.b, an overshoot is measured close to the combustion chamber walls. This temperature overshoot needs to be interpreted with caution as explained above.

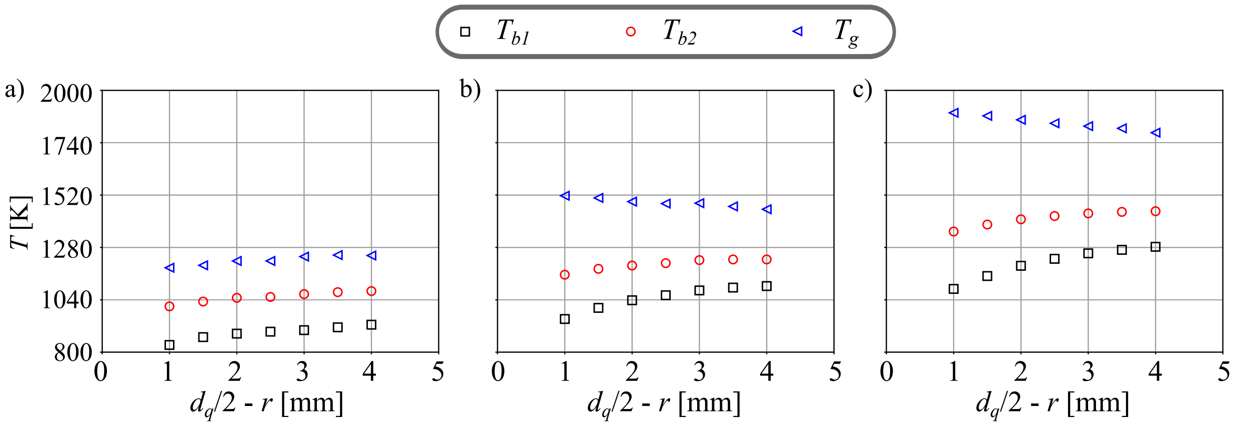

Figure 6.14 – Gas temperature profiles at the top of the ORZ. The measurements are realized with a double bead thermocouple. (a) Flame A. (b) Flame G. (c) Flame I.

The thermocouples are now installed at the bottom of the ORZ, 20 mm above the combustion chamber backplane as indicated in Fig. 6.12.b. The circular ceramic protecting the thermocouple wires is inserted in the combustion chamber through a hole drilled in the quartz window. The radial position of the thermocouple is adjusted using a micrometric displacement table. The temperature is measured from the quartz wall surface up to 4 mm away from the wall towards the center of the burner. Results for flames A, G and I are presented in Fig. 6.15. For the flame A in Fig. 6.15.a, the corrected gas temperature increases slightly when the thermocouple is moved away from the quartz window. The mean gas temperature is equal to $T_g = 1221$ K. For flame G in Fig. 6.15.b, the temperature decreases slightly when the thermocouple is moved away from the quartz window. The mean gas temperature is $T_g = 1486$ K. The increased gas temperature with flame G despite the same global equivalence ratio of flames A and G may have different origins. It might be due to the decrease of the flame temperature with the strain rate for diffusion flames, the increase of thermal losses of the gas with the increase of residence time, or the effect of the heat release rate location on the flow field. For flame I featuring a higher global equivalence ratio $\phi = 0.62$, the mean temperature measured in the burnt gases is $T_g = 1851$ K. For flames G and I, lifted above the injector lips, the measured gas temperatures are close to the adiabatic flame temperature estimated with Cantera for freely propagating premixed flames with an equivalence ratio set equal to the global equivalence ratio. For flame G, the ratio of measured gas temperature T_g to adiabatic flame temperature T_{ad} is equal to $T_g/T_{ad} = 0.97$, and $T_g/T_{ad} = 0.99$ for flame I. These measurements are made a few millimeters away from the reaction zone, explaining that the measured values are close to the adiabatic flame temperatures.

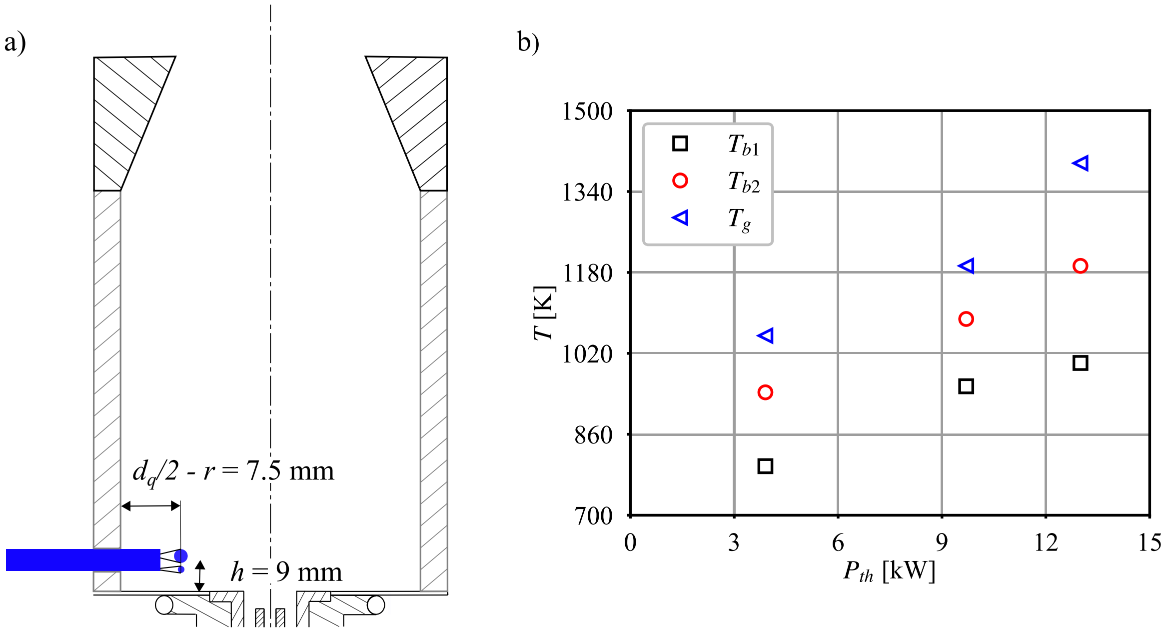

Figure 6.15 – Measurements of gas temperature inside the ORZ with a double bead thermocouple. (a) Flame A. (b) Flame G. (c) Flame I.

An additional measurement is taken in the core of the ORZ, 9 mm above the combustion chamber backplane and 7.5 mm from the quartz window. This position is shown in Fig. 6.15.a. Results are presented in Fig. 6.15.b. The thermocouple beads are approximately in the center of the ORZ. Temperatures are plotted against the thermal power $P_{th} = 3.9$, 9.7 and 13 kW for flame A, G and I. The temperature of flame A $T_g = 1058$ K is lower than $T_g = 1193$ K measured for flame G, despite the same global equivalence ratio. The highest temperature $T_g = 1396$ K is measured for flame I.

6.3 Pollutant measurements

6.3.1 CH_4/H_2/air flames on DFDS injector

Pollutant emission levels are described in this section. Only CO and NOx emissions are investigated, considering these molecules as the main pollutant emissions from CH_4/H_2/air flames. Note that CO_2 is mainly proportional to the methane content and is not considered as pollutant. Measurements are made with the flue gases analyzer described in Chapter 2. All measurements are normalized by a volumetric fraction of 15% of O_2 in the flue gases. Each value is averaged over at least 45 seconds once steady conditions inside the combustor are met for the selected operating condition.

6.3.1.1 Influence of inner swirl level and injector recess

Figure. 6.16 shows NOx (Fig. 6.16.a) and CO (Fig. 6.16.b) concentrations in flue gases as a function of the fraction of power originating from hydrogen combustion P_{H_2}/P_{th} for two internal swirl levels and two injector recess. Experiments presented in Fig. 6.16 are conducted with a constant thermal power $P_{th} = 10.3$ kW. The reference annular bulk velocity is set to $u_{e0} = 24$ m/s and the reference equivalence ratio to $\phi_0 = 0.75$. These flames were investigated in Figs. 3.2 and 3.4 of Chapter 3.

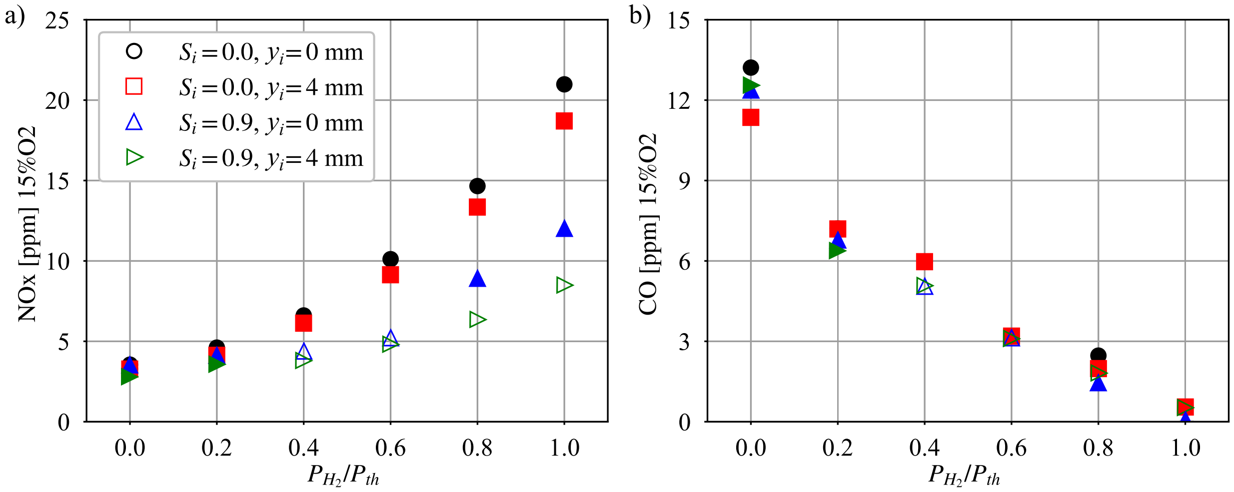

Figure 6.16 – Pollutant emission levels normalized for 15%O_2 as a function of hydrogen content P_{H_2}/P_{th} for $u_{e0} = 24$ m/s and $\phi_0 = 0.75$. The inner swirl level is varied from $S_i = 0.0$ to $S_i = 0.9$ and the injector recess from $y_i = 0$ mm to $y_i = 4$ mm. Filled symbols: Anchored flames. Empty symbols: Lifted flames. (a) NOx emission levels. (b) CO emission levels.

NOx measurements are plotted in Fig. 6.16.a. The lowest detected concentration is approximately 3 ppm for the fully premixed methane flames. A similar result for dual-swirl premixed burner is already noticed in [133]. The NOx concentration increases with the hydrogen content injected in the burner. When no swirl motion is imparted to the central hydrogen flow ($S_i = 0.0$), with and without injector recess y_i, NOx emission levels increase rapidly with hydrogen enrichment. For fuel blends with a hydrogen content $P_{H_2}/P_{th} \leq 0.2$, NOx emissions are approximately the same for the different geometrical configurations of the DFDS burner. For higher hydrogen contents, there is a clear impact of the burner geometry on NOx emissions. They increase much more rapidly when hydrogen is injected without swirl, with only a minor effect of the recess distance.

As expected, CO emissions in Fig. 6.16.b drop with the hydrogen content in the fuel blend. There is no clear dependence of CO emissions with the values of the internal swirl level or injector recess distance. CO emissions do not seem to be correlated with the flame stabilization mode. A residual concentration of CO, less than 1 ppm, is still observed for hydrogen flames, but this level also corresponds to the precision of the CO measurement chain.

When the hydrogen stream is swirled with $S_i = 0.9$, NOx emissions increase less with the hydrogen content injected in the burner. In this case, the injector recess also makes a difference for fuel blends with a hydrogen content higher than PH80. One can link these behaviors to the way the flame is stabilized on the DFDS burner. For PH80 and PH100, the flame reattaches to the central injector rim for the DFDS burner without recess ($y_i = 0$ mm) and remains aerodynamically stabilized with $y_i = 4$ mm recess. When the flame is anchored to the central hydrogen injection rim, NOx emissions reach higher levels than when the flame is aerodynamically stabilized above the burner. The strong swirl conferred to the hydrogen flow leads to a better mixing with air before combustion. In this latter case, as also shown in Chapter 5, increasing the recess distance of the hydrogen lance outlet with respect to the burner outlet further improves mixing of the internal fuel and external oxidizer streams before combustion leading to a reduction by more than 2.5 of NOx emissions with respect to a non swirling hydrogen jet (when $S_i = 0.0$ and $y_i = 0$ mm).

6.3.1.2 Influence of thermal power and global equivalence ratio

One now further analyzes the most promising geometrical configuration explored in this work obtained for $S_i = 0.6$ and $y_i = 4$ mm. CO and NOx emissions are characterized for two reference equivalence ratios $\phi_0 = 0.65$ in Fig. 6.17.a and $\phi_0 = 0.75$ in Fig. 6.17.b. As in the previous section, the hydrogen content P_{H_2}/P_{th} is varied from 0 (fully premixed methane/air operation) to 1 (hydrogen operation injected through the central tube). For each reference equivalence ratio, three different reference bulk velocities are explored: $u_{e0} = 12$, 24 and 30 m/s.

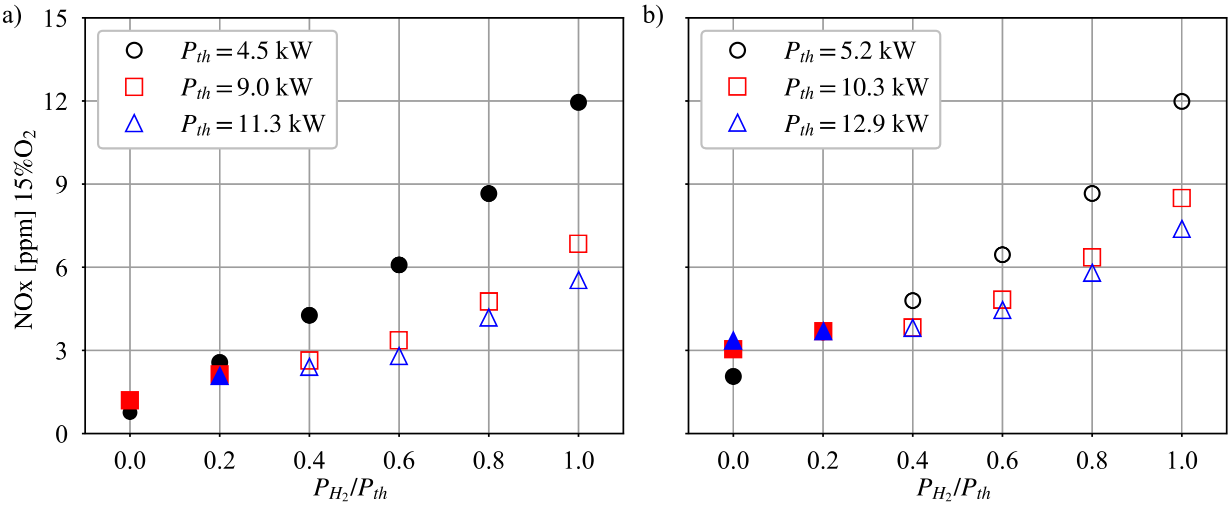

Figure 6.17 – NOx emission levels normalized for 15%O$_2$ as a function of the hydrogen content P_{H_2}/P_{th} for $S_i = 0.9$ and $y_i = 4$ mm. The thermal power is varied from $P_{th} = 4.5$ kW to $P_{th} = 12.9$ kW. Filled symbols: Anchored flames. Empty symbols: Lifted flames. (a) $\phi_0 = 0.65$. (b) $\phi_0 = 0.75$.

The plots in Fig. 6.17 show NOx emissions. Except in Fig. 6.17.a for $\phi_0 = 0.65$ and $P_{th} = 4.5$ kW where all flames are anchored to the injector lips, the flames in Fig. 6.17 are always lifted for $P_{H_2}/P_{th} \geq 0.4$. For the six sets of data, the NOx concentration increases when the hydrogen content increases. However, the observed trend is surprising because NOx emissions decrease when the bulk velocity u_{e0} increases, i.e. when the thermal power P_{th} increases, at constant reference equivalence ratio ϕ_0. For the lowest air velocity $u_{e0} = 12$ m/s when the reference equivalence ratio ϕ_0 is set to 0.65 in Fig. 6.17.a, NOx reaches 12 ppm for the hydrogen air flame, when, with a bulk velocity set to $u_{e0} = 30$ m/s, the NOx emission level drops to 5.5 ppm for $\phi_0 = 0.65$. For $\phi_0 = 0.75$ in Fig. 6.17.b, NOx concentration in the burnt gases reaches 12 ppm for the hydrogen air flame with $u_{e0} = 12$ m/s and drops to 7.5 ppm for $\phi_0 = 0.75$. For a fixed fuel blend and flame stabilization regime, NOx emissions increase with the equivalence ratio due to the associated increase of the adiabatic flame temperature as already reported in many studies [74, 134–136]. For $\phi_0 = 0.65$ (Fig. 6.17.a), the flame is anchored to the injector lips and burns in diffusion combustion regime, when, for $\phi_0 = 0.75$ (Fig. 6.17.b), the flame is lifted above the injector and burns in partially premixed combustion regime. The adiabatic temperature for the same inlet flowrates is higher when the flame is anchored (diffusion combustion) than when the flame is lifted (partially premixed combustion) because the adiabatic flame temperature is maximum for stoichiometric combustion, i.e. for diffusion flames or premixed combustion at stoichiometry. NOx concentrations drop when the injection velocities are both increased at a constant equivalence ratio. This feature cannot be attributed to the adiabatic flame temperature because the mixing between the two channels is unchanged when the velocity ratio between the two channels is conserved as shown in Chapter 5. This can be the effect of the residence time τ_R that drops with the total flowrate injected as observed in several previous studies on the scaling of NOx emissions [75, 134, 137]. NOx emission levels are mainly correlated with the injection flow velocity and the flame volume. Levels below 8 ppm that can be achieved with the HYLON burner are particularly low for a hydrogen/air burner operating at these equivalence ratios with a pure hydrogen stream injected only 4 mm before the burner outlet [138]. Industrial burners operate at lower equivalence ratios and secondary air dilutes the flue gases just after combustion to further decrease NOx emissions [139]. Moreover, no attempt has been made in this work to optimize the different swirl levels and the recess distance in order to minimize NOx emissions.

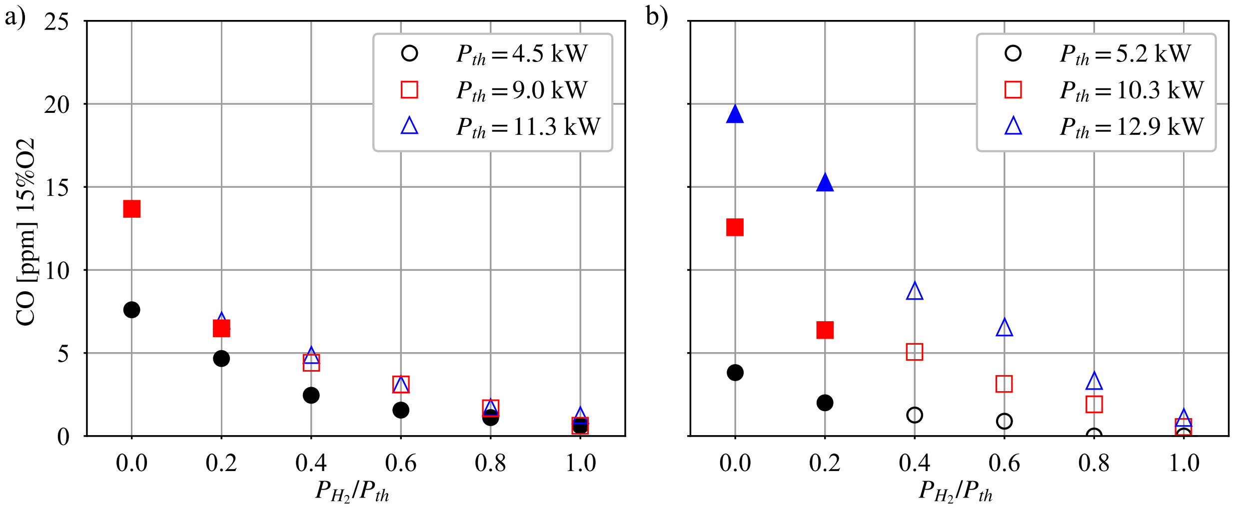

Figure 6.18 – CO emission levels normalized for 15%O_2 as a function of the hydrogen content P_{H_2}/P_{th} for $S_i = 0.9$ and $y_i = 4$ mm. The thermal power is varied from $P_{th} = 4.5$ kW to $P_{th} = 12.9$ kW. Filled symbols: Anchored flames. Empty symbols: Lifted flames. (a) $\phi_0 = 0.65$. (b) $\phi_0 = 0.75$.

Measurements of CO emission levels are presented in Fig. 6.18. As expected, the CO concentration goes to zero with hydrogen enrichment. When the bulk velocity u_{e0} increases, CO emissions increase as well, especially for the fully premixed methane/air flames. This is probably due to the quenching of the combustion reaction when the flame impinges the cold sidewalls of the combustion chamber leading to incomplete combustion. Reducing the bulk velocity u_{e0} by a factor two also reduces CO emissions by a factor of two for $\phi_0 = 0.65$ in Fig. 6.18.a and by a factor of three for $\phi_0 = 0.75$ in Fig. 6.18.b.

6.3.2 H_2/air flames on HYLON injector

6.3.2.1 Influence of thermal power and global equivalence ratio

We turn here to pure hydrogen flames. NOx emission levels with the HYLON configuration are now investigated, in which case only hydrogen injected by the central tube is used to power the burner and only air is injected through the external annular channel. In this section, the inner swirl level is set to $S_i = 0.6$ and the injector recess to $y_i = 4$ mm.

The influence of the global equivalence ratio is first investigated for a fixed thermal power. Results are presented in Fig. 6.19 for three thermal powers $P_{th} = 3.6$, 7.2 and 10.9 kW. The equivalence ratio varies from $\phi = 0.2$ to $\phi = 0.8$. For a fixed thermal power, NOx emissions increase with the global equivalence ratio ϕ as already noticed in the previous section. This is attributed to the increase of the adiabatic flame temperature, increasing the NOx formation through the Zeldovich pathway, which is the main origin of NOx emissions in H_2/air flames [140]. As shown in Fig. 6.18, for a fixed equivalence ratio, NOx emissions drop increasing the thermal power. Moreover, for a fixed thermal power when the equivalence ratio is varied, Fig. 6.19 shows that NOx emissions differ for anchored and lifted flames. For anchored flames, the main reaction front in the shear layer between hydrogen and air flames burn in a diffusion mode. The adiabatic temperature of this reaction layer is close to the stoichiometric value (it also depends on the strain rate). The lifted flames at $P_{th} = 7.2$ kW and 10.9 kW burn in partially premixed conditions and the adiabatic flame temperature increases with the equivalence ratio.

Figure 6.20 shows NOx emissions when the equivalence ratio is fixed and the thermal power increases. Three equivalence ratios are selected: $\phi = 0.40$, 0.55 and 0.70. The flame with the lower thermal power $P_{th} = 3.6$ kW is anchored to the injector lips and the other ones are lifted. For each equivalence ratio,

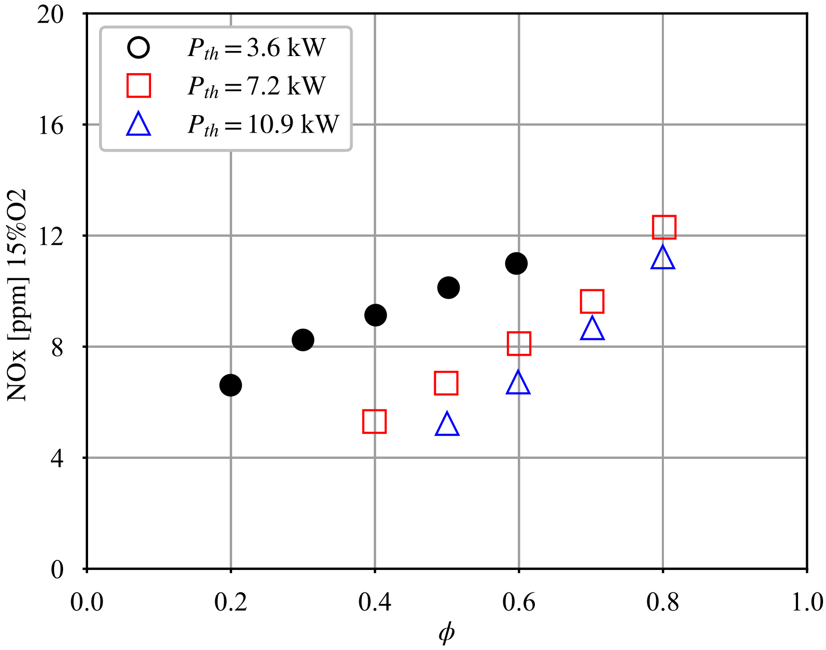

Figure 6.19 – NOx emission levels normalized for 15%O_2 as a function of the equivalence ratio ϕ for $S_i = 0.9$ and $y_i = 4$ mm. The thermal power is varied from $P_{th} = 3.6$ kW to $P_{th} = 10.9$ kW. Filled symbols: Anchored flames. Empty symbols: Lifted flames.

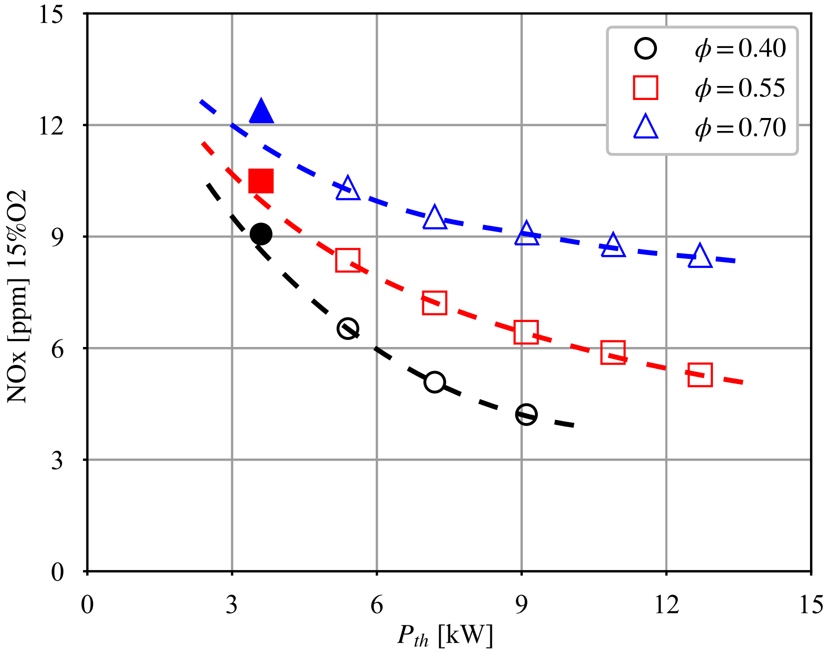

Figure 6.20 – NOx emission levels normalized for 15%O_2 as a function of the thermal power P_{th} for $S_i = 0.9$ and $y_i = 4$ mm. The equivalence ratio varies from $\phi = 0.40$ to $\phi = 0.70$. Filled symbols: Anchored flames. Empty symbols: Lifted flames. Symbols: Raw data. Dashed lines: Fitted data.

the highest NOx emissions are observed for the anchored flame at low thermal power. For higher thermal powers, the flames are lifted and NOx emission levels decrease monotonically with the increase of the thermal power. Dashed lines are superimposed on the plot for each equivalence ratio to ease visualizations of NOx emissions. The dashed lines are produced with a polynomial fit of order three on the data for lifted flames and then extended to lower thermal powers.

6.3.2.2 Influence of flame stabilization regime

It appears from the previous measurements that the flame stabilization influences the NOx emission levels.

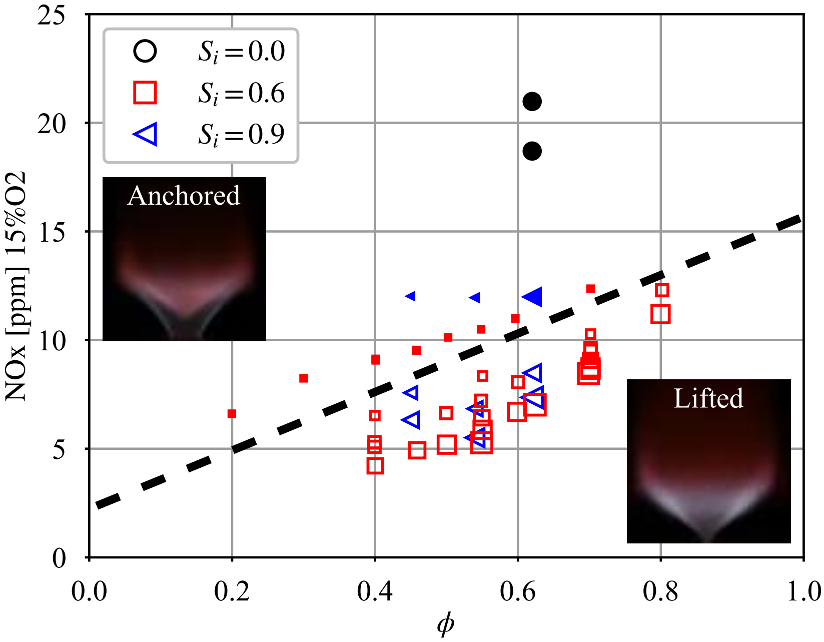

Figure 6.21 – Compilation of all the measured NOx emission levels on the HYLON injector plotted against the equivalence ratio ϕ. The swirl level is varied from $S_i = 0.0$ to $S_i = 0.9$.

Figure 6.21 compiles all NOx emissions measured with the HYLON injector burning H_2/air which are plotted against the global equivalence ratio ϕ. The size of the symbols is proportional to the thermal power. Data include measurements gathered for three swirl levels $S_i = 0.0$, 0.6 and 0.9. Data observed with injector recess $y_i = 0$ mm and $y_i = 4$ mm are also plotted. This figure confirms that for a fixed equivalence ratio, NOx emissions from anchored flames are always higher that for lifted flames. A linear frontier can be delineated with a black dashed line. Except for flames with $S_i = 0.0$, the thermal power is generally lower for anchored flames than for lifted flames. The lowest NOx emissions are reached for lifted flames with the highest thermal powers and the lowest equivalence ratios. The impact of the flame stabilization regime is attributed to the diffusion nature of the anchored flames, but it is clear that the thermal power and the equivalence ratio play an important too.

6.3.3 Scaling laws for NOx emissions

A scaling law for NOx emissions of H_2/air flames is proposed in this section. The principal route of formation of NOx in H_2/air flames is the Zeldovich pathway [140]. In this case, NOx emissions increase with the residence time of burnt gases in the hottest zone with a temperature typically higher than 1800 K. NOx emissions depend on the residence time in the hot gases τ_R and the flame temperature T_{ad} [52]. These two parameters are used in several studies to try to scale the NOx emissions of different flames. The residence time τ_R can either be defined as the time of residence of burnt gases in the flame volume as in [73, 134] or inside the combustion chamber as in [75]. The second definition is adopted in this work, neglecting the thermal losses before the outlet of the combustion chamber. Accounting for the thermal expansion of gases through the flame, the residence time τ_R can be estimated from the mean length of the combustion chamber L_{ch} divided by the mean gas velocity in ambient conditions ($T = 300$ K, $p = 1$ atm) $d_q^2/\pi/\left(u_e\left(d_e^2 - d_{ie}^2\right) + u_i d_i^2\right)$ and divided by the gas expansion ratio, equal for perfect gases to T_{ad}/T_0. The residence time τ_R is consequently defined as:

$$\tau_R = \frac{L_{ch} d_q^2}{\pi \left(u_e \left(d_e^2 - d_{ie}^2\right) + u_i d_i^2\right)} \frac{T_0}{T_{ad}} \tag{6.1}$$

NOx emission levels are modeled as follows:

$$\text{NOx} \sim T_{ad} \tau_R^{\beta} \tag{6.2}$$

where β is a constant that needs to be determined experimentally.

A value $\beta \approx 1/3$ is found in this work to collapse all NOx measurements for H_2/air flames investigated in this work. This value is close to that found by Oh *et al.* [76] ($\beta = 1/2.8$).

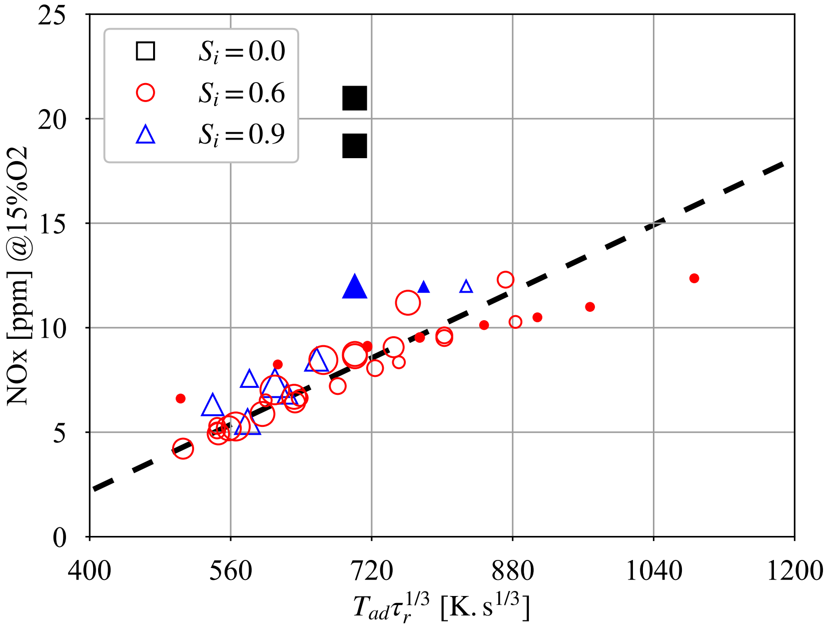

Figure 6.22 – NOx emissions of all H_2/air flames investigated in this section plotted against $T_{ad}\tau_R^{1/3}$. The size of the symbols is proportional to the thermal power of the flame. Filled symbols: Anchored flames. Empty symbols: Lifted flames. Symbols: Raw data. Dashed line: Fitted data.

Figure 6.22 shows that NOx levels for all the lifted flames, i.e. partially premixed flames, collapse around a single line. The anchored flames appearing as filled symbols in Fig. 6.22 obtained for $S_i > 0.0$ lie slightly offset with respect to all lifted flames with a slightly lower slope. This is certainly due to the diffusion combustion mode for which the adiabatic flame temperature estimated for fully premixed flames is no longer valid. Moreover, the two NOx measurements without inner swirl level $S_i = 0.0$ in filled black symbols do not collapse on the same line. This can be the effect of a greater residence time due to the penetration of the central jet in the CRZ or of the diffusion combustion mode.

This scaling law is currently improved on several test cases of NOx emission levels with different geometry and inlet air temperature, showing good results too. These results will be published in a scientific paper but are out of scope of this work.

6.4 Conclusion

The flow velocity field in hot flow conditions, the burnt gas temperature, the temperature of the combustion chamber and the pollutant emission levels (CO and NOx) have been measured and analyzed. These data have been used to understand the impact of heat release rate on the structure of flow field, validate numerical flow simulations and identify the effect of each parameter on the pollutant emission levels of CO and NOx.

The flow velocity fields in reactive conditions have been measured for these selected reference flames. A comparison with cold flow measurements has been made for each flame. Results can be resumed as follow:

- The mean expansion angle of the annular jet increases in reactive conditions compared to cold flow conditions.
- The recirculation velocity u_{CRZ} decreases in reactive conditions compared to cold flow conditions.
- The diameter of the CRZ at the bottom of the PIV window d_{CRZ} reduces when the flame is anchored to the injector leading to a lower flow blockage at the injector outlet. This reduction is believed to cause the observed hysteresis in the transition from anchored to lifted flames.
- These data have been used to validate numerical flow simulations.

Measurements of the burnt gas temperature and the temperature of the combustion chamber walls at for several locations have been carried out for the selected reference flames. The results can be resumed as follow:

- The temperature of the external surface of the quartz windows and the uprights metallic walls has been used as boundary conditions for numerical flow simulations.
- The time to reach thermal equilibrium of the combustion chamber takes about 700 s in the most cases.
- The temperature profiles at the outlet of the combustion chamber are nearly flat.
- The temperature of lifted flames at the top of the ORZ are close to the adiabatic flame temperature determined with Cantera for freely propagating premixed flames.
- For all cases, the burnt gas temperature increases with the thermal power P_{th} and the equivalence ratio ϕ. The increase with the thermal power for a fixed global equivalence ratio is attributed to lower residence time decreasing the thermal losses.

Finally CO and NOx emission levels have been measured for a wide range of configurations on both DFDS and HYLON injectors. The conclusions can be resumed as follow:

- NOx emissions are high without inner swirl motion ($S_i = 0.0$). The injector recess ($y_i > 0$ mm) only decreases slightly the NOx emissions when the flames remain anchored.
- With an inner swirl level and an injector recess ($S_i = 0.6$ and $y_i = 4$ mm), the NOx emission levels of H_2/air flames are divided by 2.5 compared to the case without inner swirl motion and without injector recess ($S_i = 0.0$ and $y_i = 0$ mm), due to the lifted stabilization mode.
- For both DFDS and HYLON injectors, NOx emissions increase with the equivalence ratio ϕ and drop with the increase of the thermal power P_{th}.
- CO emissions decrease with the H_2 content P_{H_2}/P_{th}, due to the decrease of C-atoms content in the fuel mixture. They also increase with the thermal power, i.e. with the central injection velocity, due to the increase of the strain rate.
- For a fixed equivalence ratio ϕ, NOx emissions from H_2/air flames are always lower for lifted flames than for anchored flames.
- For H_2/air flames, NOx emissions below 7 ppm are reached for a wide range of operating conditions when the flames are lifted.
- NOx emissions from H_2/air flames scale well with the adiabatic flame temperature and the residence time as $T_{ad}\tau_R^{1/3}$ when $S_i > 0.0$, especially when the flames are lifted.

These results provide useful data to validate numerical flow simulations as carried out by A. Aniello in [92]. They are made available in the TNF workshop (tnfworkshop.org/data-archives). On a more technological level, the low levels of NOx emissions measured for H_2/air flames validate the interest on the HYLON injector as a suitable, low-cost and safe technology for gas turbines fueled with hydrogen.

CHAPTER 7

Modeling of flame re-anchoring

"It doesn't matter how beautiful your theory is, it doesn't matter how smart you are. If it doesn't agree with experiment, it's wrong."

RICHARD FEYNMAN

Overview

7.1 Triple Flame Upstream Propagation (TFUP) model

Previous experiments revealed that the stabilization regime (anchored or lifted flames) mainly depends on the swirl numbers S_e and S_i in both injection channels, the central injector recess distance y_i, and the central injection velocity u_i. It was also shown in Chapter 3 that flames are more easily lifted when methane is added in the external oxidizer channel. A model is developed in this chapter with the aim to reproduce the observed features. Multiple models have been proposed in the last 30 years to describe stabilization mechanisms controlling diffusion flames. Here, we start from the triple flame approach which has been recognized as the most convincing one since the previous studies Kioni *et al.* [141, 142] or Muñiz and Mungal [86]. To develop this theory for flames with complex flow, a set of hypothesis is first made on the flow and the flame structures. The flow is considered as two dimensional and it is also hypothesized that the velocity field close to the HYLON injector outlet remains unchanged in cold and hot conditions when the flame is lifted. Following Muñiz and Mungal [86], an edge flame can anchor to the central injector lips separating the fuel from the oxidizer streams only if its leading edge displacement speed S_d is higher than the local flow velocity along the stoichiometric mixture fraction line Z_{st}. The maximum propagation speed of an edge flame S_d is assumed to match the triple flame speed [88]. This hypothesis is corroborated by measurements of the edge flame velocity carried out by Cha *et al.* [83] for strained edge flames.

However, as also already noticed in [86], an edge flame does not propagate systematically along the stoichiometric line Z_{st} [89], but along a mixture fraction Z_m line corresponding to the most reactive combustible mixture available in the zone where the flow velocity between the flame and the injector is lower than the flame displacement speed S_d. The preferred mixture fraction Z_m corresponds to the mixture that features the highest laminar burning velocity: for hydrogen/air flame, the maximum laminar burning velocity S_l^m is reached for $Z_m = 0.046$ that should be compared to the stoichiometric value $Z_{st} = 0.028$ and corresponds to a hydrogen/air rich mixture at equivalence ratio $\phi_m = 1.65$. If this mixture fraction does not exist between the flame and the injector lip, the edge flame will propagate along a mixture fraction line corresponding to a lower fuel concentration.

To summarize, a lifted flame can move upstream only if two conditions are met: (i) a flammable mixture fraction line Z_0 between the flame and the injector rim exists and (ii) the mixing fraction line $Z = Z_0$ is located, from the flame to the injector lip, inside a zone where the projection of the local flow velocity along this line $u_t = \mathbf{u} \cdot \mathbf{t}$, i.e. the flow velocity seen by the edge flame, is lower than its propagation velocity S_d.

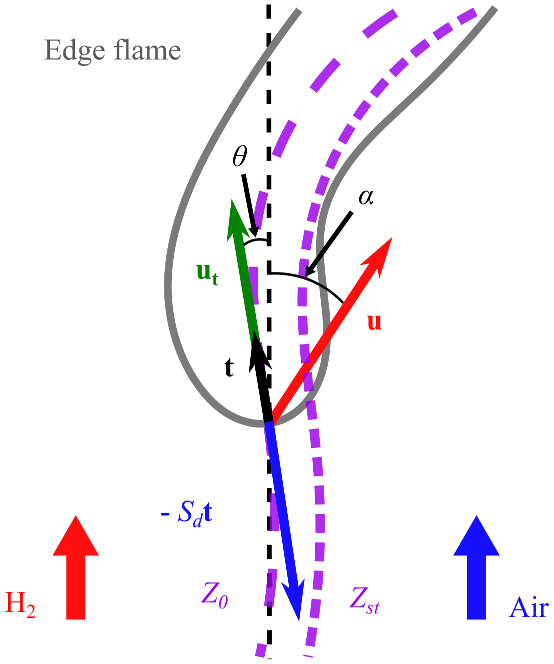

Figure 7.1 – Schematic of an edge flame with projection of the local flow velocity $\mathbf{u}$ in the laboratory frame along the flame propagation mixture fraction Z_0.

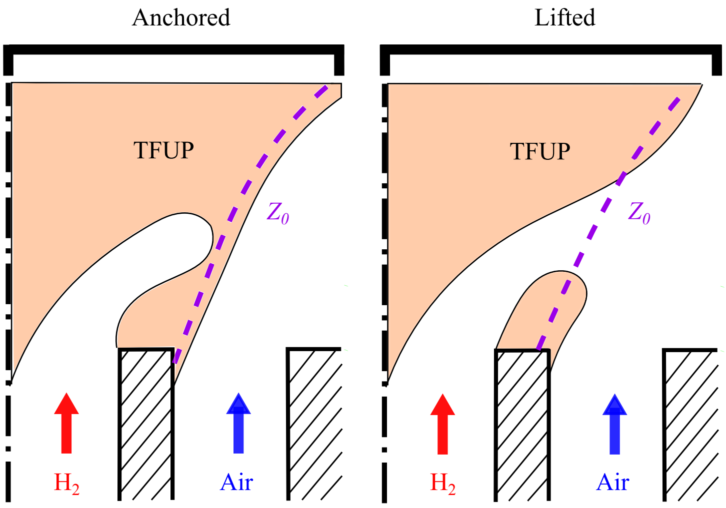

Figure 7.2 – Representation of the TFUP model for (a) an anchored flame and (b) a lifted flame. The edge flame propagation line Z_0 is drawn in purple dashed lines and the TFUP zone is colored in orange.

The unit vector **t** is tangent to the Z_0 iso-level. This latter condition delineates the boundary of the Triple Flame Upstream Propagation (TFUP) zone:

$$u_t \leq S_d \tag{7.1}$$

The edge flame speed S_d along the mixture fraction line Z_0 line is here estimated as follows [88]:

$$S_d = S_l^0 \left(\frac{\rho_u}{\rho_b}\right)^{1/2} \tag{7.2}$$

where S_l^0 is the laminar burning velocity at Z_0 and ρ_u/ρ_b the volumetric expansion ratio of gases through the flame calculated for Z_0. The mixture fraction Z_0 is equal to Z_m, the mixture fraction corresponding to the highest laminar burning velocity S_l^m unless Z_m is not reached inside the TFUP zone. In this latter case, Z_0 corresponds to the mixture fraction leading to the highest flame speed.

Notations used for these vector projections are introduced in Fig. 7.1. The angle θ of the flame propagation line Z_0 and the angle α of the local flow velocity with respect to the vertical axis are determined in the following experiments to get the local velocity $u_t = \mathbf{u} \cdot \mathbf{t}$ along the Z_0 line as:

$$u_t = |u| \cos(\alpha - \theta) \tag{7.3}$$

where $|u|$ is the magnitude of the flow velocity in the axial plane of the burner. Condition Eq. (7.1) for flame re-anchoring becomes:

$$|u| \cos(\alpha - \theta) \leq S_l^0 \left(\rho_u/\rho_b\right)^{1/2} \tag{7.4}$$

Figure 7.2 shows the two possible cases. In this diagram, the flame propagation line Z_0 corresponds to the purple dashed line. To propagate towards the hydrogen nozzle rim, the edge flame needs to overcome the velocity $u_t = \mathbf{u} \cdot \mathbf{t}$ of the local flow along the Z_0 line. The TFUP zone where the flame can propagate upstream is colored in orange. When the Z_0 line intersects the TFUP zone, the flame re-anchors following the path shown in Fig. 7.2.a. If the TFUP zone is disrupted close to the nozzle lip the flames remains lifted as in Fig. 7.2.b.

Values for ρ_u, ρ_b and S_l^0 at Z_0 are determined in the following with Cantera for freely propagating premixed flames at ambient conditions with the San Diego kinetic mechanism [51]. For a H_2/air flame at ambient conditions, the laminar burning velocity reaches his maximum $S_l^0 = S_l^m = 3.17$ m/s for $Z_0 == 0.046$ and $\rho_u/\rho_b = 6.37$. Equation (7.2) yields in this case a displacement speed equal to $S_d = 7.99$ m/s.

7.2 Indirect validations

To test the validity of the TFUP zone scenario, one possibility is to push the Z_{st} line into or outside the TFUP zone to check if this leads to the expected transition. Here, two sets of experiments were conducted in which the position of the stoichiometric mixture fraction line Z_{st} and the value of the theoretical triple flame speed S_d were modified to trigger a transition from one flame type to the other and test the validity of TFUP zone model.

7.2.1 Influence of Z_{st} line position

First, the influence of the position of the Z_{st} line with respect to the TFUP zone is explored. For the lifted flame shown in Fig. 7.3.a, the Z_{st} line should lie outside the TFUP zone according to Fig. 7.2.b. The objective is to trigger a transition to an anchored flame by shifting the position of the Z_{st} line towards the hydrogen injector so that it intersects the TFUP zone as in Fig. 7.2.a without altering the triple flame speed and the aerodynamic flow field, i.e. the boundary of the TFUP zone. To achieve this purpose, the hydrogen stream is diluted with argon. Due to the large difference in molar weight, a small volumetric fraction of argon in the hydrogen channel substantially alters the hydrogen mass fraction $Y_{H_2,i}$, but the triple flame speed S_d remains barely modified as indicated in Tab. 7.1.

Table 7.1 – Impact of argon dilution in the hydrogen stream inside the internal channel on the stoichiometric mixture fraction Z_{st} and triple flame speed S_d. Values for S_d are given in m/s.

Flame	ϕ	$X_{Ar,i}$	$Y_{Ar,i}$	$Y_{N_2,e}$	Z_{st}	S_d
F_1	0.46	0.00	0.00	0.76	0.028	6.1
F_2	0.43	0.07	0.61	0.76	0.069	5.9
F_3	0.39	0.15	0.78	0.76	0.114	5.6

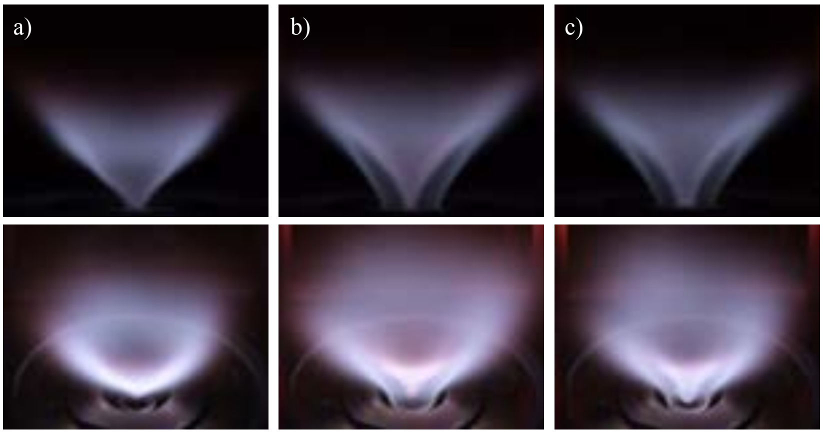

Figure 7.3 – Lifted to anchored flame transition triggered by shifting the Z_{st} line towards the hydrogen stream while keeping S_d roughly constant for the flames described in Tab. 7.1. The internal and external injection velocities are fixed to $u_i = 34$ m/s and $u_e = 28$ m/s. Images are given for two view angles to highlight the flame root. (a) Flame F_1. (b) Flame F_2. (c) Flame F_3.

In Fig. 7.3, hydrogen is progressively replaced by argon in the internal injection channel by increasing the argon mass fraction from $Y_{Ar,i} = 0.00$ to 0.73. This dilution barely changes the triple flame speed S_d, but leads to a large shift of the stoichiometric mixture fraction from $Z_{st} = 0.028$ to 0.114 that moves towards the hydrogen stream favoring its intersection with the TFUP zone and consequently also flame re-attachment. The injection velocities in the external and internal channels being in these experiments fixed to $u_e = 28$ m/s and $u_i = 34$ m/s, one may assume that the flow field is only weakly perturbed by the fuel dilution and in particular the location of the TFUP zone should not be modified between flames F_1 to F_3.

A transition from lifted to anchored flame is indeed observed between flames F_1 and F_2 in Figs. 7.3.a and 7.3.b. This result is particularly counter-intuitive as for many burners operating at globally lean conditions, fuel dilution generally leads to less well anchored flames. The opposite is observed here in agreement with the TFUP zone model prediction, which constitutes a good indication of the model validity. It is also worth noting that, even if the value of S_d slightly drops from flames F_1 to F_3 in Tab. 7.1, this small reduction favors flame detachment while the opposite is observed with flame re-attachment due to the large displacement of the stoichiometric line Z_{st} towards the burner centerline.

7.2.2 Influence of triple flame speed

The model is further tested by fixing the stoichiometric mixture fraction to $Z_{st} = 0.028$ as for pure hydrogen and air streams but this dilution scheme has a strong impact on the triple flame speed S_d through the laminar burning velocity [143]. The speed is reduced by half from $S_d = 6.1$ m/s for flame F_4 in Fig. 7.4.a to $S_d = 3.1$ m/s for flame F_6 in Fig. 7.4.c while the position of the stoichiometric line Z_{st} inside the flow remains unaltered as indicated in Tab. 7.2. The air and hydrogen velocities are here set respectively to $u_e = 15$ m/s and $u_i = 14$ m/s. The hydrogen injection velocity being lower than the lift-off hydrogen velocity $u_i = 18$ m/s, an anchored flame is observed for flame F_4 in Fig. 7.4.a for injection of air and hydrogen.

Table 7.2 – Impact of argon dilution of the hydrogen stream and nitrogen dilution in the air stream on stoichiometric mixture fraction Z_{st} and triple flame speed S_d. Values for S_d are given in m/s.

Flame	ϕ	$X_{Ar,i}$	$Y_{Ar,i}$	$Y_{N_2,e}$	Z_{st}	S_d
F_4	0.34	0.00	0.00	0.76	0.028	6.1
F_5	0.40	0.01	0.16	0.79	0.028	4.4
F_6	0.46	0.02	0.27	0.82	0.028	3.1

Both injection velocities u_e and u_i are kept constant increasing dilution of both flows. For this dilution scheme, the size of the TFUP shrinks as the triple flame speed S_d is reduced from flame F_4 to F_6 in Tab. 7.2. The position of the line $Z_{st} = 0.028$ inside the flow remaining unaffected, it does not intersect anymore the TFUP zone for a sufficient dilution rate.

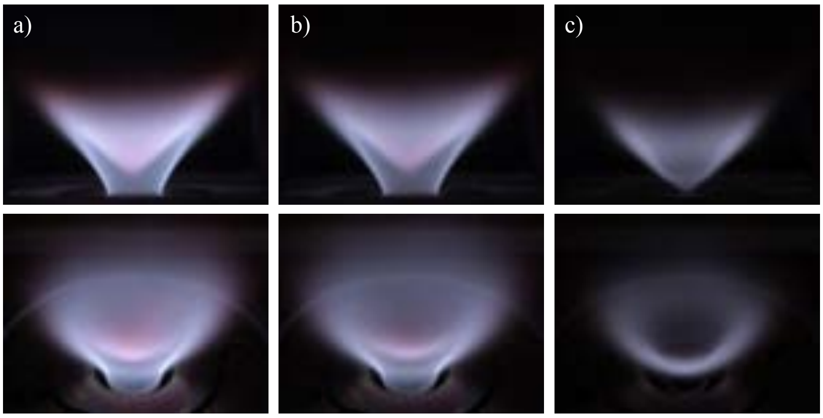

Figure 7.4 – Anchored to lifted flame transition triggered by reducing the triple flame speed S_d keeping Z_{st} constant for flames described in Tab. 7.2. The internal and external injection velocities are fixed to $u_i = 14$ m/s and $u_e = 15$ m/s. Images are given for two view angles to highlight the flame root. (a) Flame F_4. (b) Flame F_5. (c) Flame F_6.

This prediction from the TFUP zone model corresponds to what is effectively seen in Fig. 7.4 between flames F_5 and F_6. Due to a drop of the flame luminosity with dilution, images have been over-exposed to keep the same camera settings for all experiments with dilution. Figures 7.4.a and 7.4.b show that flames

F_4 and F_5 are well anchored on the hydrogen injector, the last one F_6 being lifted away from the hydrogen injector rim when the triple flame speed drops to $S_d = 3.1$ m/s (see Tab. 7.2).

These experiments shed light on the mechanisms leading to flame re-attachment on the hydrogen injector nozzle from the dual swirl coaxial injector. The influence of the internal swirl conferred to the hydrogen stream in the internal channel can be interpreted as follows. When hydrogen is injected without swirl, a relatively long TFUP zone, characterized by low axial velocities $u \leq S_d$, develops in the wake of the hydrogen injector lips (see Fig. 4.2.a). This low velocity region, where hydrogen mixes with air, contains the Z_{st} line and hydrogen flames remain anchored for all conditions explored. Adding swirl to the hydrogen stream leads to a flow blockage at the hydrogen injector outlet with a strong radial deflection of the hydrogen stream that has two major effects. The axial extension of the TFUP in the wake of the hydrogen injector shrinks (see Figs. 4.2.b and 4.2.c) and the Z_{st} line is pushed in the direction of the annular flow.

The hydrogen injector recess distance y_i enhances hydrogen recirculation velocities at the hydrogen injector outlet (see Fig. 4.7). Higher recirculation velocities in the CRZ lead to a stronger flow blockage at the hydrogen injector outlet accompanied by a larger radial deflection of the hydrogen stream towards the air stream. The annular air flow being confined, this also leads to higher air velocities at the hydrogen injector outlet leading to a further reduction of the size of the TFUP. Moreover, the position of the stoichiometric line Z_{st} with respect to the central tube outlet is also shifted influencing flame stabilization.

7.3 Direct validations

7.3.1 Experimental determination of TFUP zone

An estimation of the local angle θ of the edge flame propagation line with respect to y-axis is needed to deduce the TFUP boundaries from PIV measurements (see Fig. 7.1). Without the possibility to measure directly the location of this line with a sufficient spatial resolution with the diagnostics available at IMFT, its position is inferred from attached flames by detecting the flame front position. It has been verified with high fidelity simulations [92] that the diffusion branches from the base to the top of anchored flames well correspond to the location of the stoichiometric mixture fraction Z_{st} line. The angle between the Z_{st} line and the vertical axis is here assumed to be approximately the same as the angle of the edge flame propagation line, even though this line does not necessarily correspond exactly to the stoichiometric mixture fraction line.

Table 7.3 – Operating points with thermal power P_{th}, equivalence ratio ϕ, injection velocities u_e and u_i. The velocities are calculated for standard inlet gas conditions at T_0=20°C and p_0=1 atm.

Flame	P_{th} [kW]	ϕ	u_e [m/s]	u_i [m/s]
F_7	4.8	0.23	28.5	17.0
F_8	9.7	0.46	28.5	34.0
F_9	12.7	0.60	28.5	45.0

A sensitivity analysis is thus first conducted to compare the angles with the vertical axis deduced for different mixture fractions and analyze their impact on the boundary of the TFUP zone. The case of flame F_8 is considered for this purpose (Tab. 7.3). Flame images are recorded and then an Abel deconvolution is applied to infer the OH* distribution in the symmetry plane of the burner. The location of the flame front is deduced from the maximum of OH* intensity. Figure 7.5 shows results of the flame front detection algorithm obtained for flame F_8 with an inner swirl number $S_i = 0.9$.

Figure 7.5 shows the detected flame front in blue which is superposed to the Abel deconvoluted OH* image. To mimic the impact of various levels of the mixture fraction, these experiments are repeated when hydrogen is diluted with argon in the central lance as summarized in Tab. 7.4. Argon is chosen because of his large molar weight with respect to hydrogen. A small volumetric concentration of argon in the fuel substantially increases the value of the stoichiometric mixture fraction Z_{st} but barely alters the bulk flow

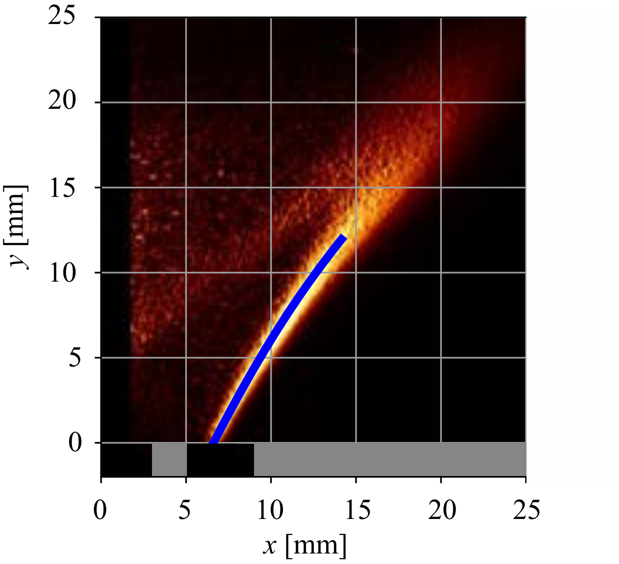

Figure 7.5 – Illustration of the methodology applied for the detection of the flame front location for flame F_8. Abel deconvoluted OH* image with the detected flame front superimposed in blue.

injection velocity inside the central lance. As a consequence, the flame position corresponding to the OH* peak intensity slightly moves towards the burner center when the argon concentration increases. The position of the detected flame front is plotted in Fig. 7.6.a for mixture fractions spanning from $Z_{st} = 0.028$, i.e. when pure hydrogen is injected, to $Z_{st} = 0.114$ for hydrogen diluted with $Y_{Ar,i} = 0.77$. The angles θ deduced from these plots are presented in Fig. 7.6.b. These figures show that despite the differences observed in Fig. 7.6.a for the mixture fraction lines when Z_{st} is varied, their impact on θ remains limited. The difference for the angle is less than 3° between all cases over the first 6 mm above the burner (y-axis).

Table 7.4 – Diluted F_8 flames with argon mass fraction $Y_{Ar,i}$ in the hydrogen lance: thermal power P_{th}, equivalence ratio ϕ, stoichiometric mixture fraction Z_{st}, and mixture fraction Z_m corresponding to the equivalence ratio at which the laminar burning velocity is maximum. The air injection velocity is $u_e = 28.5$ m/s and the central injection velocity is $u_i = 34.0$ m/s.

$Y_{Ar,i}$	P_{th} [kW]	ϕ	Z_{st}	Z_m
0.00	9.7	0.46	0.028	0.046
0.61	9.0	0.43	0.069	0.114
0.71	8.6	0.41	0.091	0.150
0.77	8.3	0.40	0.114	0.188

The impact of the chosen angle θ determined for different mixture fractions Z_{st} on the TFUP boundary is now assessed with the help of Eq. (7.4). Information on the velocity field, i.e. $|u|$ and α, is determined from PIV data. The edge flame speed $S_d = S_l^m(\rho_u/\rho_b)^{1/2}$ is deduced from Cantera simulations as described in the previous section.

To test only the influence of the angle θ, the value of $S_d = 7.99$ m/s is first fixed to the maximum triple flame displacement speed of a hydrogen/air flame. The location of the TFUP zone is presented in Fig. 7.7. Despite the large variation of the theoretical value of Z_{st} used for the determination of the angle θ, the boundary of the TFUP zone is only slightly affected. In the following, only the angle θ deduced for $Z_0 = Z_{st} = 0.028$ is used to infer the boundary of the TFUP zone that has been shown to be a valid approximation.

The following measurements are made in cold flow conditions to determine the mixture fraction inside the TFUP zone with 1D1S (1 Dimensional 1 Species) Raman scattering. Figure 7.8 compares the position of the stoichiometric mixture fraction $Z_0 = Z_{st} = 0.028$ at different heights above the burner when the central

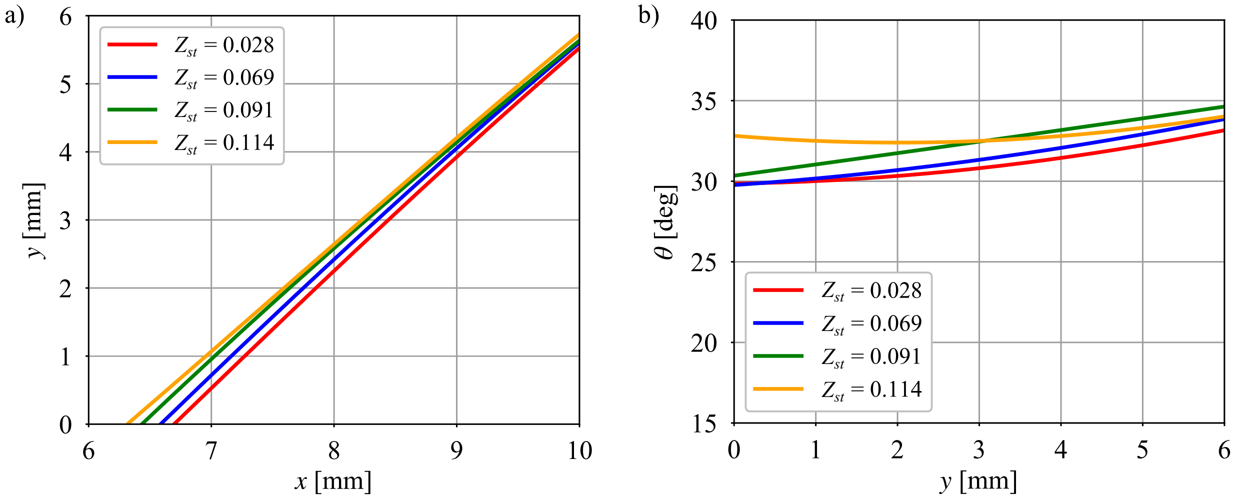

Figure 7.6 – Illustration of the methodology applied for the estimation of the propagation line angle θ with the vertical axis for flame F_8 (see Tab. 7.3) with an inner swirl level $S_i = 0.9$. (a) Detected flame front locations. (b) Flame angles θ for different values of the stoichiometric mixture fraction Z_{st}.

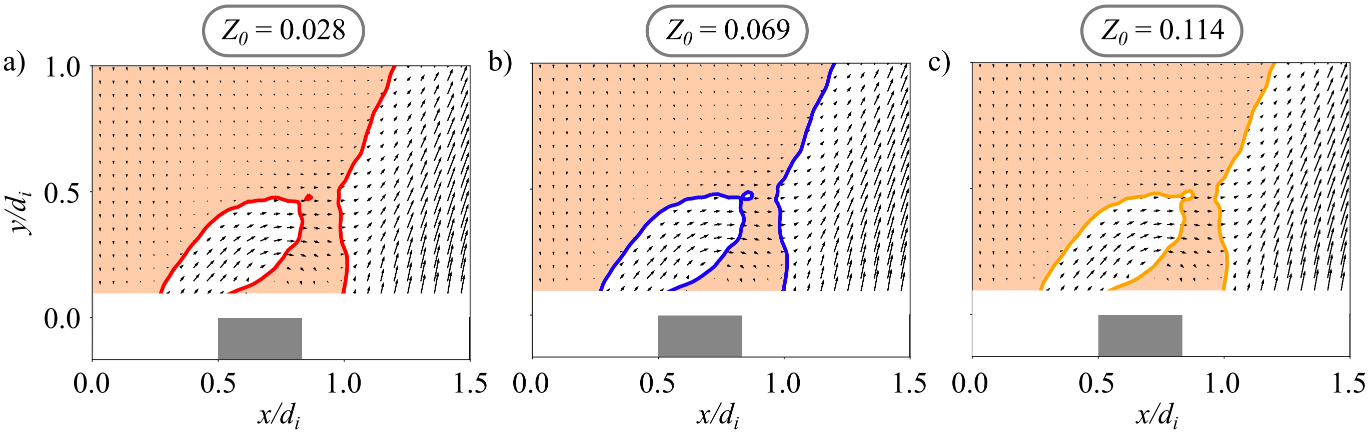

Figure 7.7 – Sensitivity of the TFUP zone boundary determined with $S_d = 7.99$ m/s to the angle θ of the propagation line Z_0 with respect to the vertical axis. The operating conditions correspond to flame F_8 with an inner swirl level $S_i = 0.9$ for H_2/air operation. The angle θ of the propagation line Z_0 is determined for: (a) $Z_0 = 0.028$, (b) $Z_0 = 0.069$ and (c) $Z_0 = 0.114$.

injector is fed with helium or hydrogen with the detected flame front deduced from OH^* images shown in Figs. 7.5. Conditions correspond to flame F_8 (see Tab. 7.3), with the same volumetric flowrates for the cold flow experiments when the hydrogen flow is substituted by helium as for PIV measurements. This figure indicates that the location of the mixture fraction of helium $Y_{He} = 0.028$ determined in cold flow conditions matches well the location of the stoichiometric mixture fraction $Z_{st} = 0.028$ when the burner is fed by hydrogen for all the swirl numbers $S_i = 0.0$ to $S_i = 0.9$ tested. It also confirms that the detected flame front used to determine the edge flame propagation line Z_0 well corresponds to the stoichiometric mixture fraction line Z_{st} measured by 1D1S Raman scattering in cold flow conditions for heights below 3 mm. Above 4 mm, the Z_{st} line in the cold flow and the location of the flame front begin to deviate from each other.

These tests indicate that helium can safely be used instead of hydrogen to determine the mixture fraction in the cold flow. This operation mode is preferred for obvious safety reasons. Moreover, it has been shown that the location of the stoichiometric line $Z_0 = 0.028$ measured by Raman scattering is always near the flame front inferred from OH^* images close to the hydrogen nozzle rim. In reacting conditions, the detected flame front is slightly shifted towards the external side leading to a slightly higher angle θ with respect to the vertical axis due to thermal expansion [144]. These small differences are however considered as acceptable

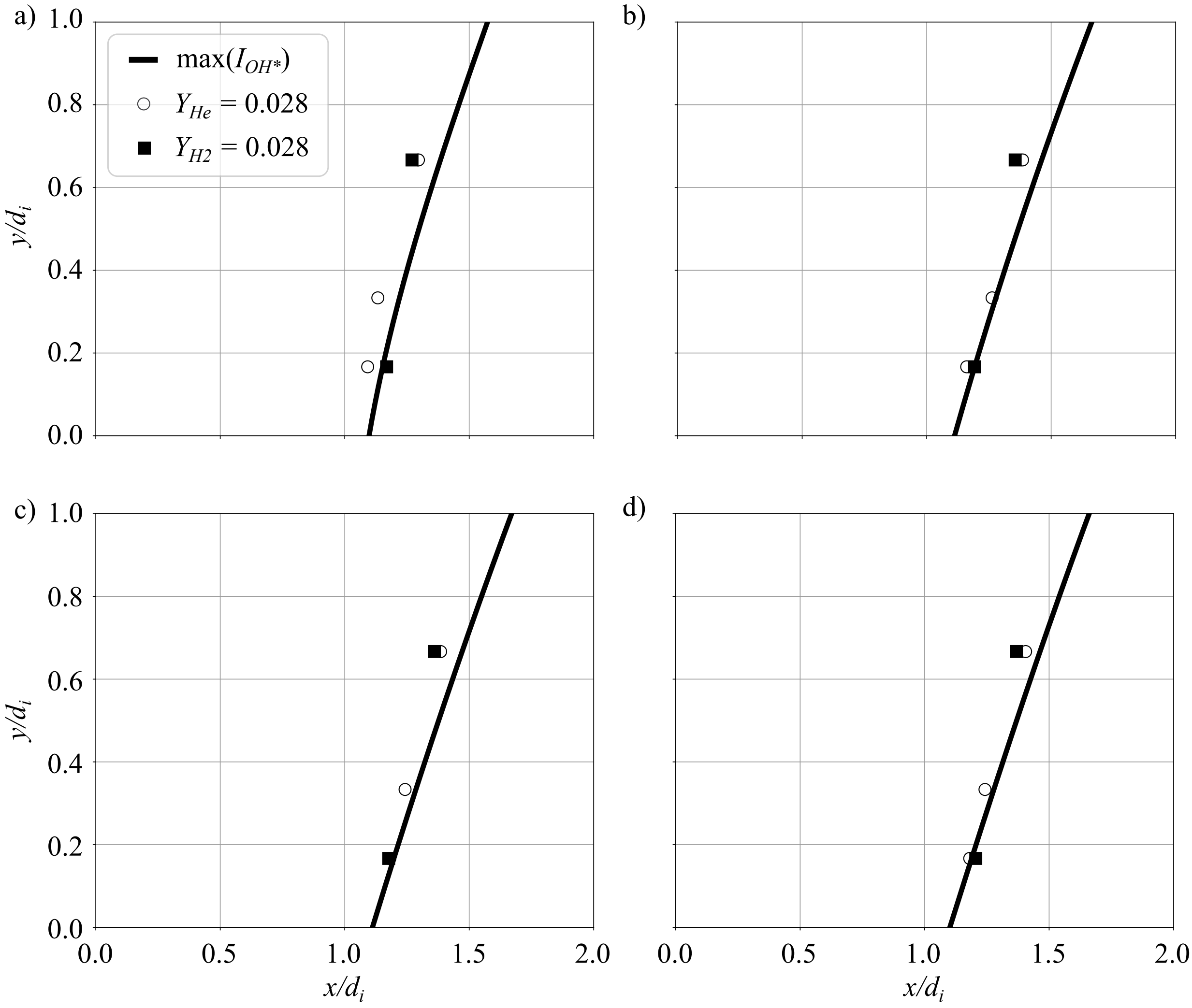

Figure 7.8 – Comparison of the flame front location deduced from OH* images with the mixture fraction = 0.028 for H_2 and He swirled jets deduced from 1D Raman scattering. Conditions F_8 (see Tab. 7.3) for (a) $S_i = 0.0$, (b) $S_i = 0.4$, (c) $S_i = 0.6$ and (d) $S_i = 0.9$.

and the angle θ of the edge flame propagation line is deduced in the following from OH* images.

These preliminary tests lead to the following method used to determine the boundary of the TFUP zone for the different cases explored:

1. The angle θ between the edge flame propagation line Z_0 and the vertical axis is first determined.
2. The velocity field in the axial plane of symmetry of the burner is determined with PIV in cold flow conditions when hydrogen is replaced by the same volumetric flowrate of helium.
3. The triple flame speed S_d is determined with Cantera and Eq. (7.2).
4. The TFUP zone boundary is superimposed to the velocity field using Eq. (7.4).

7.3.2 Validation of the TFUP model

Predictions from the TFUP model in cold flow conditions are now compared to observations of the flame stabilization regime when the inner swirl level S_i and the injection velocities are varied.

The case of flame F_8 in Tab. 7.3 is again first considered. The air bulk velocity is $u_e = 28.5$ m/s and the injection velocity in the central tube is $u_i = 34$ m/s. The inner swirl level is varied from $S_i = 0.0$ to $S_i = 0.9$. The colored lines in Fig. 7.9 correspond to the boundary of the TFUP zone on the air side where mixing between the pure hydrogen and air swirled jets takes place. The triple flame displacement speed used to draw this TFUP boundary corresponds to $S_d = 7.99$ m/s which corresponds to the maximum triple flame speed for H_2/air mixture. The markers correspond to the location of the mixture fraction $Z_m = 0.046$ at $y = 1$ and 4 mm above the burner outlet that are deduced from Raman scattering measurements in the cold flow. In all cases, the mixture fraction $Z_m = 0.046$ belongs to the TFUP zone at all distances y investigated. As a consequence, the edge flame velocity can be estimated with Eq. (7.2) for a mixture fraction $Z_m = 0.046$ corresponding to the maximum laminar flame burning velocity of H_2/air flames leading to a value $S_d = 7.99$ m/s. This consideration is used below. Figure 7.10 shows how the velocity field and the boundary of the TFUP zone change for increasing values of the inner swirl level (from top to bottom) and for decreasing values of the triple flame speed S_d (from the left to the right). The injection velocities $u_e = 28.5$ m/s and $u_i = 34$ m/s correspond here to flame F_8 in Tab. 7.3. For the configuration without inner swirl motion $S_i = 0.0$ conferred to the central flow at the top in Fig. 7.10, the edge flame can always find a propagation path to the injector lips inside the TFUP zone when the triple flame speed is decreased from $S_d = 6.0$ m/s to 4.5 m/s. A disruption of the TFUP zone is only found by further reducing the triple flame speed to $S_d = 1.2$ m/s, a case which is not shown in this figure. This very low threshold value of the triple flame speed S_d is due to the non swirling central hydrogen jet $S_i = 0.0$. In this case the very low flow velocities in the wake of the hydrogen injector rim foster flame anchoring to the injector.

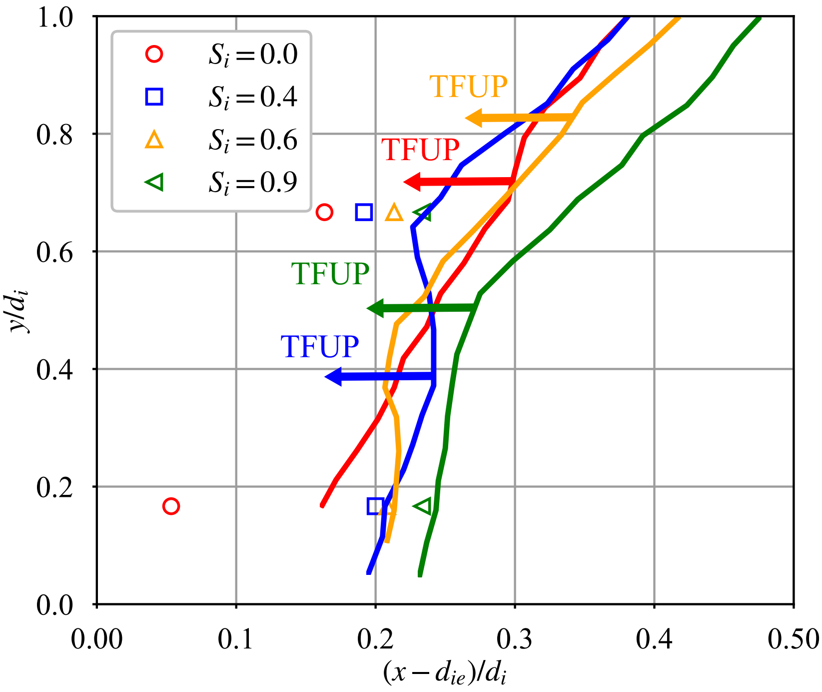

Figure 7.9 – Comparison of the location of the mixture fraction $Z_m = 0.046$ corresponding to the highest laminar burning velocity of H_2/air flames at ambient conditions with the limit of the TFUP zone on the air side for flame F_8 (see Tab. 7.3) at different inner swirl numbers S_i. The TFUP zone is drawn for H_2/air flames with $S_d = 7.99$ m/s.

In the second row in Fig. 7.10, the inner swirl number is slightly increased to $S_i = 0.4$. The swirl motion conferred to the hydrogen stream produces a fast expansion of the central jet at the hydrogen nozzle outlet and the TFUP zone in the wake of the hydrogen nozzle rim shrinks leaving only a small open channel for flame propagation when $S_d = 6.0$ m/s. The TFUP zone above the hydrogen injector lips is disrupted when S_d is further reduced between 5.5 m/s and 5.0 m/s. As consequence, the minimum triple flame speed S_d at which flame re-anchoring is predicted greatly increases when the hydrogen flow is swirled. For $S_i = 0.4$, the predicted minimum triple flame speed is $S_d = 5.2$ m/s. This trend is exacerbated in the last two rows in Fig. 7.10 when the inner swirl number is further increased to $S_i = 0.6$ and $S_i = 0.9$. Transitions from lifted to re-anchored flames are predicted for a minimum triple flame speed $S_d = 5.6$ m/s and $S_d = 5.8$ m/s respectively.

To compare these predictions with the observed transitions, further experiments are carried out by mod-

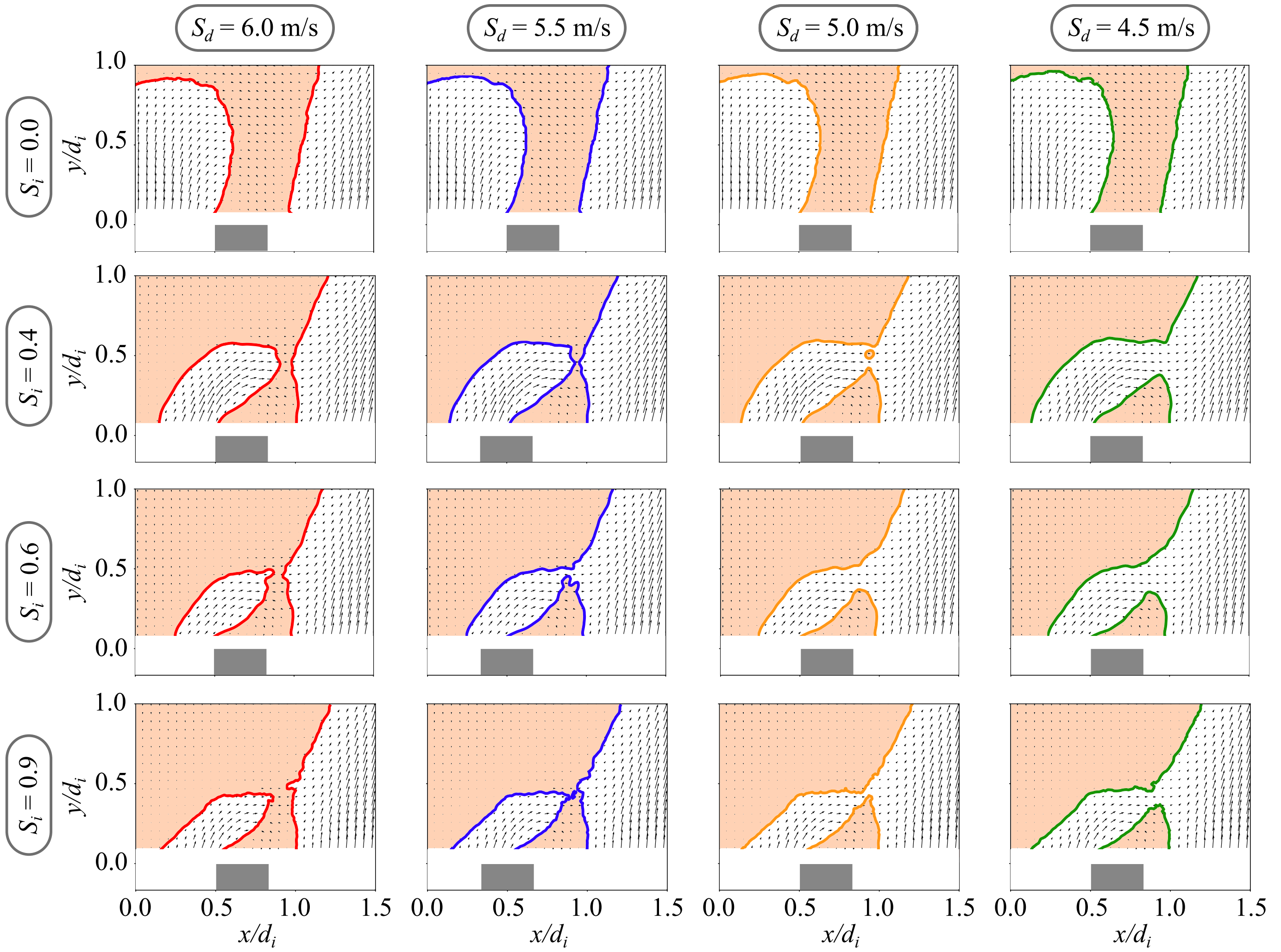

Figure 7.10 – Evolution of the TFUP zone with the triple flame displacement speed S_d for different inner swirl numbers S_i for flame F_8 in Tab. 7.3. From the top to the bottom: S_i = 0.0 - 0.4 - 0.6 - 0.9.

Table 7.5 – Diluted F_8 flames (see Tab. 7.3) with inner swirl level S_i, central jet angle α_i, mass fraction of hydrogen in the central channel $Y_{H_2,i}$, and mass fraction of oxygen in the annular channel $Y_{O_2,e}$. Symbols appearing in Fig. 7.11 for the observed transitions are reported.

Flame	F_8													
S_i	0.0			0.2			0.4			0.6			0.9	
α_i [deg]	8			15			32			41			48	
Symbol	○	□	△	○	□	△	○	□	△	○	□	△	○	□
$Y_{H_2,i}$	0.08	0.28	0.15	0.54	0.43	0.31	1.00	0.87	0.77	1.00	0.87	0.77	1.00	0.77
$Y_{O_2,e}$	0.21	0.17	0.19	0.20	0.21	0.21	0.20	0.21	0.23	0.21	0.22	0.23	0.21	0.23

ifying the gas composition inside the injection channels in order to control the value of the triple flame speed S_d and vary the boundary of the TFUP zone without altering the structure of the velocity field at the burner outlet. Change of the air composition inside the external channel is made by dilution with N_2. Inside the central channel, hydrogen is mixed with CH_4 and He. To limit perturbations of the velocity field, the injection velocities u_i and u_e and the total thermal power P_{th} are kept constant in these experiments.

Experiments are first conducted with hydrogen inside the central channel and air diluted by nitrogen inside the external channel. The burner is always ignited with a high N_2 dilution rate in the external channel to

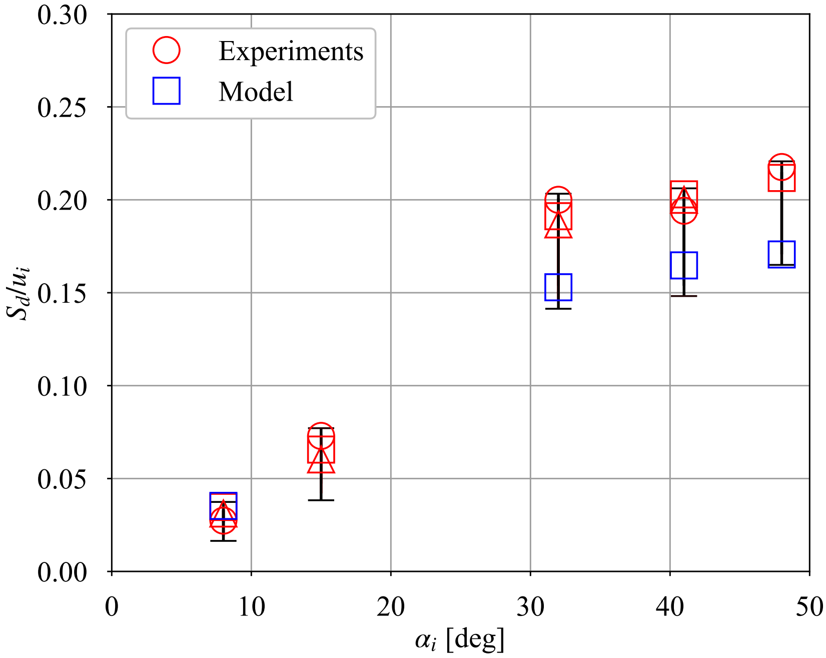

Figure 7.11 – Comparison of the predicted flame transitions with experiments for diluted H_2/CH_4/He-air/N_2 flames with $u_i = 34$ m/s. Values for S_d are calculated using Cantera. Flow conditions for each central jet angles α_i are reported in Tab. 7.5. Conditions for diluted flames F_8 are described in Tab. 7.3.

reduce the value of the triple flame speed and start with a lifted flame. The nitrogen flowrate is then decreased step by step, in order to increase progressively the triple flame speed S_d until the flame re-anchors to the hydrogen rim. Nitrogen, air, helium, methane and hydrogen flowrates at which this transition takes place are recorded and the corresponding value of the triple flame speed S_d is calculated with Cantera using Eq. (7.2) for a freely propagating flame. This operation is then repeated by increasing the mass fraction of methane and helium in the central hydrogen channel. Experiments start again with a lifted flame and the flowrate of nitrogen is reduced until the flame re-anchors to the hydrogen nozzle.

Figure 7.11 compares the predicted and observed transitions for flames F_8 in Tab. 7.3. The normalized triple flame displacement speed S_d/u_i at which flame re-attachment takes place is plotted as a function of the expansion angle α_i of central fuel jet. For fixed injection u_e and u_i velocities, α_i changes with the inner swirl number S_i as reported in Tab. 7.5. The square symbols in blue correspond to predictions of the TFUP model deduced with the same analysis as in Fig. 7.10. The red symbols denote the conditions leading to the observed transition when the gas composition inside the internal and external channels are varied. The dilution levels in each channel for the different transitions observed are reported in Tab. 7.5. The corresponding error bars are drawn for the observed transition points. They mainly result from the propagated uncertainties on the flowrates on the estimation of the triple flame speed S_d and the step width between dilution points in both channels. The error bars are asymmetric. They are wider in the direction of lower values for S_d/u_i due to the experimental methodology.

Two important conclusions can be drawn from Fig. 7.11. For a fixed aerodynamic flow field, independently on the way the gas composition is changed inside the external channel by nitrogen dilution or inside the internal channel of the burner by mixing hydrogen with different concentrations of helium and methane, the transition at which re-anchoring takes place is always found for the same value of the triple flame speed S_d. This proves that the edge flame speed is the correct physical parameter triggering these transitions for the range of operating conditions explored. Secondly, Fig. 7.11 also shows good agreement between predicted and observed transitions, with a small under estimation of the triple flame speed at which re-attachment takes place for the swirled cases when $S_i > 0$. Nevertheless, these differences remain small and within the error bars. These results nicely validate the TFUP model.

From a technological standpoint, it is more interesting to over predict the range where the flames are anchored than the opposite, because the lifted flames are the targeted ones in technical applications powered by hydrogen [95]. Figure 7.11 also highlights the benefits of swirling the hydrogen stream to enlarge the range of operating conditions with lifted flames [95]. Moreover, it can also be concluded that a moderate swirl number $S_i = 0.4$ already leads to a large widening of the regime with lifted flames. Increasing further the inner swirl number only produces a small improvement compared to operation with $S_i = 0.4$. The case for $S_i = 0.2$ ($\alpha_i = 15°$) is also reported, but data for the velocity field are not available for this case and as a consequence the TFUP zone could not be delimited.

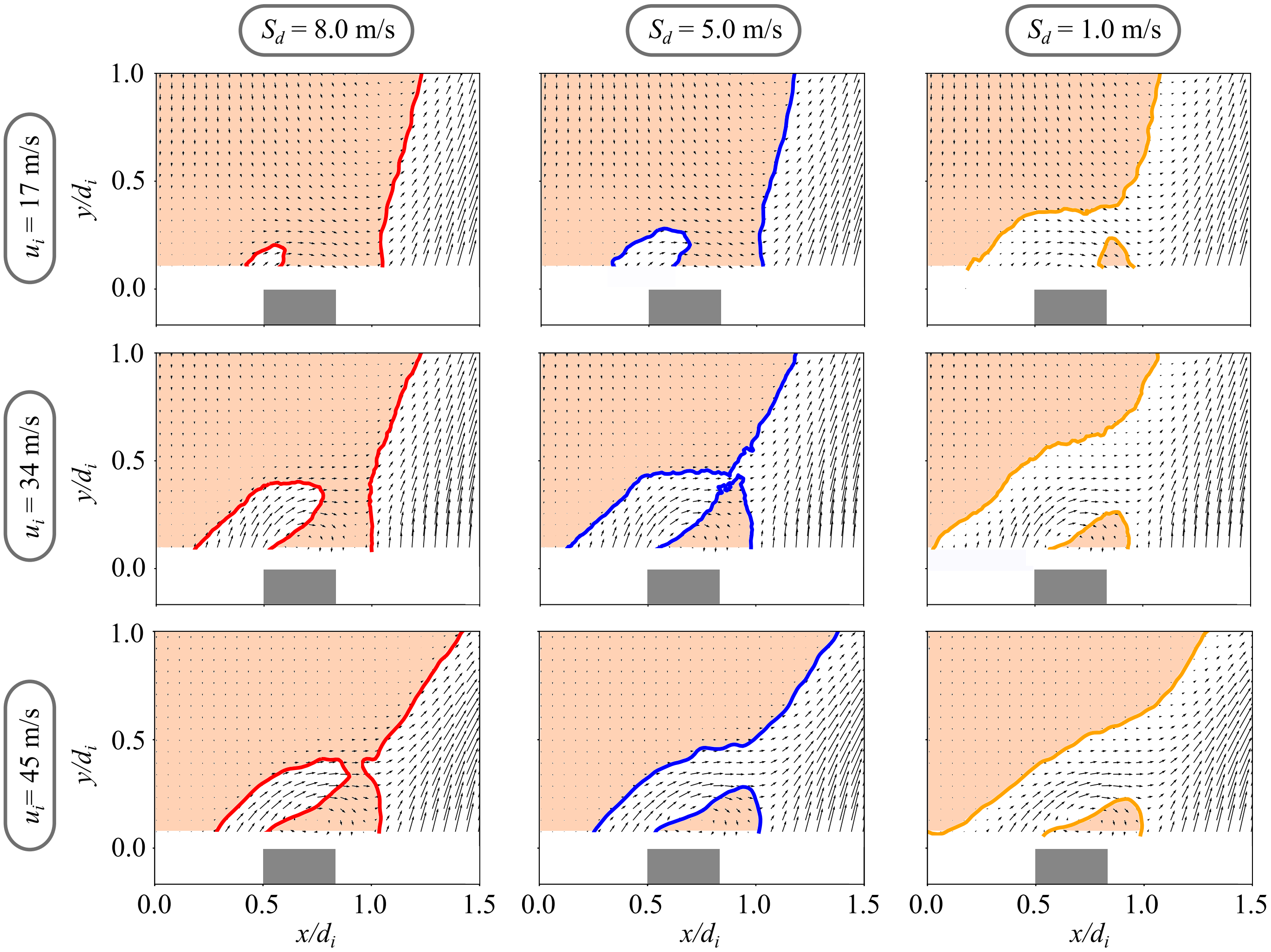

Figure 7.12 – Evolution of the TFUP zone with the triple flame displacement speed S_d for different central injection velocities u_i and a fixed inner swirl number $S_i = 0.6$. From the top to the bottom: u_i = 17 - 34 - 45 m/s corresponding to flames F_7 to F_9 in Tab. 7.3.

The same experiments are now repeated for a fixed inner swirl level $S_i = 0.6$ varying the central injection velocity from $u_i = 17$ m/s to $u_i = 45$ m/s. This new set of experiments covers flames F_7 to F_9 in Tab. 7.3 for the same air injection velocity $u_e = 28.5$ m/s. The velocity fields in the wake of the central injector with the TFUP boundaries superimposed are presented in Fig. 7.12 for different values of the triple flame speed S_d. In the top row in Fig. 7.12 obtained for the lowest central injection velocity $u_i = 17$ m/s corresponding to flame F_7 in Tab. 7.3 with $\alpha_i = 64°$ (Tab. 7.6), the velocity in the wake of the hydrogen injector lips remains low because of the low impulsion of the central jet. This leads to a very small velocity projected in the reference frame of the edge flame and to a small value of the predicted triple flame speed $S_d = 1.8$ m/s leading to flame re-attachment. This threshold level is indeed comparable to the one $S_d = 1.2$ m/s obtained for the non-swirling central jet case shown in Fig. 7.10. Results in the second row in Fig. 7.12 coincide with the third row in Fig. 7.10 obtained for $S_i = 0.6$, $u_i = 34$ m/s (flame F_8 in Tab. 7.3) and $\alpha_i = 41°$

(Tab. 7.6) and were already commented leading to a predicted minimum triple flame speed $S_d = 5.6$ m/s for flame re-attachment. Finally, the bottom row shows the case with the highest central injection velocity $u_i = 45$ m/s corresponding to flame F_9 in Tab. 7.3 with $\alpha_i = 50^\circ$ (Tab. 7.6). For this last case, the central jet expands radially and as consequence, the radial velocity above the central injector lips takes high values. Flame re-anchoring is hindered. Transition to anchored flame would require values of the triple flame speed higher than $S_d = 7$ m/s. These results confirm previous observations made in [95, 144]. For a fixed dual swirl injector geometry and a fixed gas composition, i.e. a fixed value of S_d, the injection velocity u_i of the fuel in the central tube is the main parameter determining the flame stabilization regime for the range of operating conditions explored.

Table 7.6 – Diluted flames F_7, F_8 and F_9 (see Tab. 7.3) with central injection velocity u_i, central jet angle α_i, mass fraction of hydrogen in the central channel $Y_{H_2,i}$, and mass fraction of oxygen in the annular channel $Y_{O_2,e}$. Symbols appearing in Fig. 7.13 for the observed transitions are reported.

Flame	F_7					F_8			F_9		
u_i [m/s]	17					34			45		
α_i [deg]	64					41			50		
Symbol	○	□	△	○	□	△	○	□	△	▷	◁
$Y_{H_2,i}$	1.00	0.77	0.60	0.48	0.39	1.00	0.87	0.77	1.00	0.87	0.77
$Y_{O_2,e}$	0.18	0.19	0.20	0.21	0.22	0.21	0.22	0.23	0.22	0.23	0.23

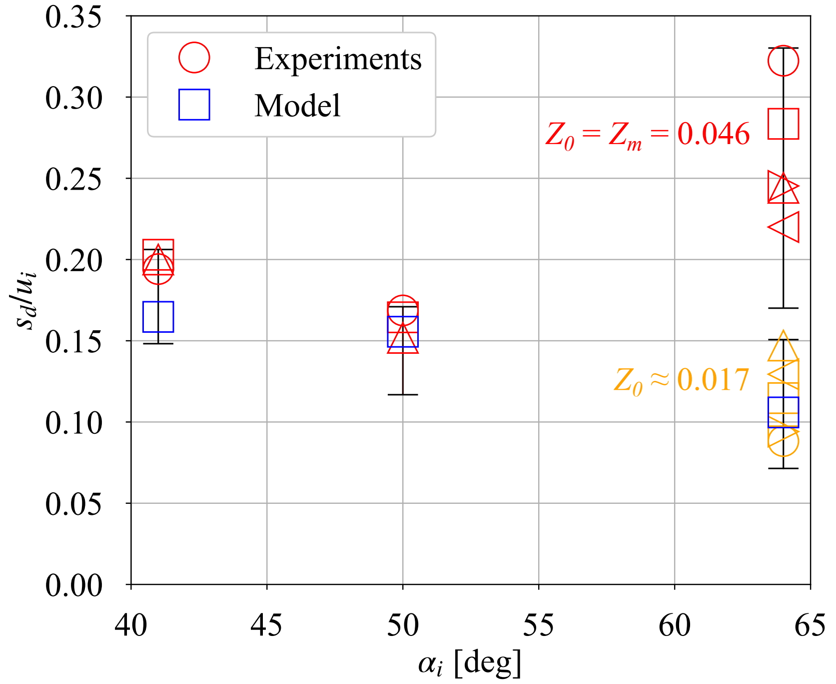

Figure 7.13 – Comparison of the predicted flame transitions with observations made for diluted $H_2/CH_4/He$-air/N_2 flames with $S_i = 0.6$. Yellow symbols correspond to S_d values calculated at the highest equivalence ratio measured in the TFUP zone. Red symbols correspond to S_d values calculated for the maximum laminar burning velocity. The injection velocity changes from $u_i = 17$ m/s to $u_i = 45$ m/s inside the central channel and is fixed to $u_e = 28.5$ m/s inside the air channel. Flow conditions for diluted flames F_7 to F_9 are described in Tab. 7.3.

Predictions deduced from Fig. 7.12 in cold flow conditions are compared in Fig. 7.13 to the observations made for the flame stabilization regime. As in Fig. 7.11, results are presented for the ratio S_d/u_i as a function of the expansion angle α_i of the central jet. Values for α_i, $Y_{H_2,i}$ and $Y_{O_2,e}$ are reported in Tab. 7.6. In these cases, the value of the triple flame speed S_d is deduced from the combustible mixture featuring the highest laminar burning velocity with Eq. (7.2) and it has been checked with Raman scattering that this mixture fraction is indeed reached by the flow within the TFUP zone for flames F_8 and F_9.

However for flame F_7, corresponding to $\alpha_i = 64^o$ obtained for the lowest injection velocity $u_i = 17$ m/s, the equivalence ratio in the TFUP zone measured by Raman scattering does not exceed $\phi \sim 0.6$. In this latter case, the mixture fraction $Z_m = 0.046$ leading to the highest laminar burning velocity does not belong to the TFUP zone (see Fig. 7.5). As a consequence, the edge flame can only propagate along the highest mixture fraction $Z_0 < Z_m$ which is available in the TFUP zone. This mixture fraction needs to be determined to apply the TFUP model. For this last operating condition, predictions are presented in Fig. 7.13 in red for S_d calculated with $Z_m = 0.046$ corresponding to the highest laminar burning velocity of the combustible mixture and for $Z_0 = 0.017$ corresponding to the maximum mixture fraction measured inside the TFUP zone at $y = 4$ mm by Raman scattering. The TFUP model over-estimates the threshold ratio S_d/u_i below which the flame re-anchors whith $Z_m = 0.046$. A similar atypical behavior has already been observed in a previous study carried out for non-swirling jet flames with a small co-flow. This last regime was designated in [90] as a premixed propagation regime. In this regime, the edge flame velocity cannot be estimated with the triple flame speed calculated at the equivalence ratio corresponding to the maximum laminar burning velocity. A good estimation can be made by determining the laminar burning velocity used in Eq. (7.2) at the highest equivalence ratio available for the edge flame in the TFUP zone. Here, the maximum mixture fraction available for the edge flame is $Z_0 = 0.017$ corresponding to an equivalence ratio equal to $\phi \simeq 0.6$ and a triple flame speed equal to $S_d \approx 2.4$ m/s.

7.4 Conclusion

One must keep in mind, that all the results that were presented were obtained in cold flow conditions with two-dimensional PIV data and one dimensional Raman scattering measurements. The three dimensional structure of the flow was not considered and rough approximations were made to deduce the edge flame propagation line. These approximations were however shown to give satisfactory predictions of the transitions from lifted to re-anchored flame regimes when the inner swirl level, the central injection velocity and the composition of the gases in the external and internal channels were modified.

It is also worth mentioning that the companion problem of the transition from anchored to lifted flames was not addressed in this work. Initial experiments indicate that the physical mechanisms leading to flame detachment are more complicated than for flame re-anchoring.

These validations are also limited to a fixed geometry of the burner with a fixed injector recess distance y_i, fixed inner d_i and outer d_e channel diameters, a fixed outer swirl level S_e, a fixed injector lip thickness $1/2\,(d_{ie} - d_i)$ and a given size of the combustion chamber. The effect of these parameters remains to be investigated.

Finally these experiments were carried out at atmospheric conditions with gases injected at $T_0 = 20°\mathrm{C}$ and $p_0 = 1$ bar. Investigation at higher inlet temperatures and higher pressures need to be carried out to further validate the TFUP model.

The stabilization of partially premixed H_2/air flames above a dual-swirl co-axial injector has been investigated. A model called TFUP for Triple Flame Upstream Propagation has been presented and validated with detailed flow characterizations. It has been shown that:

- Mixing between the inner swirled hydrogen jet and outer swirled air jet in a dual swirl co-axial injector can be investigated by substituting helium instead of hydrogen in cold flow conditions to determine the mixture fraction.
- The TFUP model based on PIV data and mixture fraction measurements made in cold flow conditions yields satisfactory predictions of the transition from lifted to re-anchored flames when the inner swirl, the central injection velocity and the gas composition in the internal and external injection channels are varied.
- In a dual co-axial swirl hydrogen injector, the mechanisms by which the operability range with lifted flames widens when swirl is conferred to the central hydrogen stream have been elucidated. They are

due to the fast expansion of the central jet cutting the low velocity zone above the hydrogen injector lips.

- In most cases, the TFUP model can be applied without knowledge of the exact mixture composition inside the TFUP zone by considering that an edge flame will propagate at the triple flame speed of a combustible mixture formed by the fuel and oxidizer featuring the maximum laminar burning velocity. When the combustible mixture does not reach this mixture fraction in the TFUP zone, the edge flame propagate along the line with the highest equivalence ratio available in the zone with a triple flame speed determined for this equivalence ratio. In all cases, the predicted transition from lifted to anchored flame is in good agreement with experimental observations.

Future experiments will aim at further analysis of the impact of the outer swirl level, the inner and outer diameters of the dual swirl coaxial injector and the thickness of the injector lips. The TFUP model needs also to be validated for increased pressure and temperature of inlet gases, which is not possible with the current test bench. The TFUP model however paves the way to develop tools for the design of industrial combustors powered by hydrogen with lifted flames.

Conclusion and perspectives

The structure of the flow, mixing between fuel and oxidizer, flame stabilization and pollutant emissions from a coaxial dual swirl CH_4/H_2/air injector have been investigated. The annular channel can be supplied with air or with a CH_4/air mixture and the central channel with pure hydrogen. The annular swirl level, the dimension of the injector and the dimensions of the combustion chamber have been kept fixed. Two flame stabilization regimes have been observed. Flames can be anchored to the hydrogen injector lips or lifted above the injector. A large experimental analysis combined to theoretical low order modeling has been carried out to unveil the physical mechanisms leading to the observations made.

The main contributions of this work are listed below:

- A wide parametric analysis has been carried out to explore the influence of the inner swirl level, the central injector recess, the injection velocities and the content of hydrogen in the global fuel mixture on the flame stabilization regimes once the setup has reached thermal equilibrium.

- The inner swirl level has been identified as a necessary condition to lift the flame above the hydrogen injector lips. PIV measurements in cold flow conditions revealed that the central jet penetrates inside the CRZ and a low velocity zone is present in the wake of the injector lips between the shear layers of the central and the annular flows. This zone is identified as the cause of flame anchoring for all operating conditions explored without swirl conferred to the central hydrogen flow.

- When a swirl is imparted to the central hydrogen flow, the jet expands radially right out at the central tube outlet, cutting the low velocity zone above the injector lips. This is the main cause of the flame lift-off identified in this work. Moreover, it has been shown that the stability of the CRZ is substantially enhanced with an inner swirl motion. In this case, the CRZ penetrates inside the central channel and creates a flow blockage at the outlet of the central injector and consequently accelerates the flow close to the hydrogen injector lips.

- When the burner is operated with a CH_4/air mixture in the annular channel and hydrogen in the central tube, the flame is lifted for relatively moderate hybridization rate with hydrogen in the global fuel mixture. Increasing the hydrogen content, the probability to stabilize a lifted flame decreases.

- Applying a recess distance to the central injector with respect to the combustion chamber backplane widely enlarges the operating range at which the flame is lifted. In cold flow experiments, it has been shown that the CRZ diameter and the angle of the expanding swirled flow in the combustion chamber decrease when the injector recess distance increases. Moreover, the recirculation velocities along the centerline increase. For each inner swirl level investigated, an optimum recess distance has been found for which the range of operating conditions with lifted flames is maximum.

- The hydrogen injection velocity has been identified as the main parameter driving the flame stabilization regime for a fixed injector geometry. Above a threshold hydrogen injection velocity, the flame is always lifted. A weak linear dependence of the threshold hydrogen injection velocity with the bulk velocity in the annular channel has also found and has been characterized.

- A strong PVC instability has been found in the cold air jet without central injection. The linear dependence of the PVC frequency with the air flowrate has been verified. When a swirled flow is injected through the central channel, the intensity of the PVC instability in terms of velocity fluctuations considerably drops. This has been verified for two selected operating conditions.

- For three reference H_2/air flames, PIV measurements have been repeated in reactive conditions. The angle of the annular jet increases and the magnitude of the recirculation velocities along the centerline drop compared to cold flow experiments. The measured flow velocity fields for lifted and anchored flames featuring the same operating conditions confirm this effect implying a decrease of the CRZ diameter at the outlet of the annular channel, and consequently a reduction of the flow blockage at the outlet of the injector.

- A 1D1S Raman scattering system has been used to infer the mixing between the two jets in cold flow conditions. A parametric analysis reveals the large enhancement of mixing in the first millimeters above the injector outlet when a swirl motion is imparted to the central flow. The premixing degree before the outlet of the annular air channel increases with the injector recess distance applied to the central fuel channel. It has been shown that the mixing rate is slightly lower in the annular channel than in the combustion chamber.

- In the case of the central flow without swirl motion, a competition between the central jet and the counter-flow created by the CRZ determines the structure of the flow field near the burner outlet. When the axial impulsion ratio between the flow in the CRZ and the central jet is significantly above unity, mixing is not influenced by the CRZ. An increase of this ratio leads to a destabilization of the central jet by the recirculating flow.

- A mixing progress variable has been introduced to quantify the influence of each parameter on mixing. For a central injector flush mounted with the combustion chamber backplane, the injection velocity ratio and the angle of the central jet have been identified as the main parameters driving the mixing progress along the vertical axis. The mixing progress has been shown to be independent of the density ratio between the couple of gas injected in each channel, except for unswirled cases with a low impulsion of the central jet.

- A model for mixing has been proposed considering that the central jet is diluted by the external flow through a surface exchange that takes the shape of an inverted truncated cone corresponding to the interface between the two jets. A mixing progress parameter has been derived from this modeling approach that enables to scale all the measured mixing progress variables. For a wide range of inner swirl levels, velocity ratios, density ratios and total flowrates, the data reasonably collapse on a single line when they are plotted against the mixing progress parameter.

- CO emissions from CH_4/H_2/air flames have been measured at the outlet of the combustion chamber. They decrease with the hydrogen content in the fuel mixture due to the decrease of the carbon content of the fuel blend. They increase with the thermal power due to the increase of strain rate, but are only slightly sensitive to the inner swirl level and the central injector recess.

- NOx emissions have been shown to be particularly high for anchored flames without inner swirl. They are lowered by a factor two for anchored flames when an inner swirl is imparted to the central hydrogen jet, and are further lowered for lifted flames when the central injector is set with a recess with respect to the annular channel outlet. In all cases, NOx emissions increase monotonically with the hydrogen content in the global fuel mixture. This is attributed to the increase of NOx formation through the Zeldovich pathway due to the increase of the flame temperature with the hydrogen content.

- For H_2/air flames, NOx emissions increase with the global equivalence ratio due again to the increase of adiabatic flame temperature that promotes thermal NOx formation. They drop monotonically with the thermal power for a fixed global equivalence ratio. The emissions seem to reach an asymptotic value in the limit of high thermal powers. This value depends on the global equivalence ratio. Moreover, a dependence with the flame stabilization regime has been highlighted and attributed to the different combustion modes, diffusion for anchored flames and partially premixed for lifted flames. A scaling law based on the adiabatic flame temperature and the residence time of burnt gases in the combustion chamber has been defined. The adiabatic flame temperature multiplied by the residence time at the power 1/3 enables to scale NOx emissions of lifted flames on a single line for the full range of inner swirl levels, injector recess distances and injection velocities investigated.

- The thermal boundary conditions have been measured for three selected flames at several locations to validate companion numerical flow simulations. These data were completed by the gas temperature profiles at the outlet of the combustion chamber and inside the outer recirculation zones of the flow.

- A model based on the edge flame displacement speed, called TFUP for Triple Flame Upstream Propagation, has been proposed to predict flame reanchoring. It models flame reanchoring as an edge flame traveling from the lifted flame to the injector lips along the iso-mixture fraction line available in the flow for which the flame laminar burning velocity is maximum. This leading edge flame can propagate from the flame to the hydrogen injector lips only if the edge flame speed, idealized to the triple flame speed, is lower than the local flow velocity tangent to the propagation line.

- Qualitative predictions of the model have been coroborated with experiments by diluting the flows with nitrogen in the annular air channel and argon in the central hydrogen tube. This strategy allows to control independently the values of the stoichiometric mixture fraction and of the theoretical triple flame speed. It has been demonstrated that the increase of the triple flame speed leads as predicted by the model to flame reanchoring. Moving the stoichiometric mixture fraction line towards the symmetry axis of the burner, i.e. towards lower velocities, the flame reanchors despite an increase of the stoichiometric mixture fraction.

- Using a limited amount of experimental data measured mostly in cold flow conditions, the TFUP zone has been determined and a value of the triple flame speed for which the flame should reanchor to the injector lips has been predicted. The predictions have been shown to be in good agreements with the observed transitions for $CH_4/H_2/He$/-air/N_2 flames for a wide range of inner swirl levels, injection velocities and dilution schemes.

This work opens perspectives for future experimental and numerical studies in order to improve the development of a H_2/air injector technology for hydrogen fueled gas turbines. They can be expressed as follow:

- Experiments in cold flow conditions have extensively been used in this work. The observations made need to be further consolidated in reactive conditions. In particular, mixing should be better characterized in hot flow conditions.

- Measurements for the velocity fields are limited in this work to mean and RMS values. Further experiments with time resolved diagnostics are needed to better understand the unsteady mechanisms leading to the observed flame transitions.

- All experiments presented in this work have been carried out at atmospheric conditions with gas injected at ambient conditions. The influence of air pre-heating temperature is currently investigated at IMFT by Hervé Magnes. Investigation on the influence of the overall pressure in the combustion chamber is also planned in 2024. Controlling both air inlet temperature and overall pressure in the combustion chamber will allow to reproduce closer thermodynamic conditions inside the combustion chamber of gas turbines. These experiments will allow to test the low order model proposed in this work for the prediction of flame reanchoring and the injector technology. Tests in an annular combustion chamber are also envisaged at EM2C laboratory and will constitute an important step to validate the technology in geometries similar to those of gas turbines.

- Only flame reanchoring has been investigated but the lift-off of an attached flame to a lifted flame remains to be elucidated. The initial experiments made in this thesis then deepened in the work of Hervé Magnes. Rapid flame visualization with intensified cameras and OH-PLIF measurements are planned in the future to better understand the flame lifting mechanisms.

- A wide experimental campaign at high pressure with advanced laser diagnostics is planned with colleagues from KAUST university on selected operating conditions to create a complete database for the validation of numerical flow simulations. This database will be proposed for a test case in the TNF database (tnfworkshop.org/data-archives). The dual swirl injector HYLON has the advantage to provide both diffusion and partially premixed combustion modes for H_2/air flames. This constitutes a good test case to validate hydrogen combustion models. The validation of these models is a preliminary step for the design of new hydrogen-fuelled systems assisted by numerical flow simulations.

- The HYLON concept has been patented jointly by Safran Helicopter Engines and Institut National Polytechnique de Toulouse in 2022 [99]. The next step is to rise the concept to TRL 5 with a laboratory scale prototype tested under engine relevant conditions. The DFDS variant of the injector is envisaged as an alternative for fuel-flex power generation and for industrial furnace burners.

Bibliography

[1] P. Malanima. Energy in History, pages 1–29. Springer International Publishing, Cham, Switzerland, 2014.

[2] J. B. J. Fourier. Mémoire sur les températures du globe terrestre et des espaces planétaires. Mémoires de l'Académie Royale des Sciences de l'Institut de France, Paris, France, 1827.

[3] J. Tyndall. On the transmission of heat of different qualities through gases of different kinds. Proceedings of the Royal Institution, 3:155–158, 1859.

[4] P. C. Jain. Greenhouse effect and climate change: scientific basis and overview. Renewable Energy, 3(4-5):403–420, 1993.

[5] IEA. World Energy Outlook 2019. IEA Reports, 2019.

[6] United Nations / Framework Convention on Climate Change. Adoption of the Paris agreement. 21st Conference of the Parties, 2015.

[7] P. Chiesa, G. Lozza, and L. Mazzocchi. Using hydrogen as gas turbine fuel. Journal of Engineering for Gas Turbines and Power, 127(1):73–80, 2005.

[8] G. Kakoulaki, I. Kougias, N. Taylor, F. Dolci, J. Moya, and A. Jäger-Waldau. Green hydrogen in europe – A regional assessment: Substituting existing production with electrolysis powered by renewables. Energy Conversion and Management, 228:113649, 2021.

[9] C. B. Meher-Homji. The historical evolution of turbomachinery. pages 281–322, 2000.

[10] A. H. Lefebvre. Gas turbine combustion. Hemisphere Pub. Corp Washington, 1983.

[11] L. Opfer, I. V. Roisman, and C. Tropea. Primary atomization in an airblast gas turbine atomizer, pages 3–27. Springer Netherlands, Dordrecht, Netherlands, 2013.

[12] S. Kumar, D. D. Rathod, and S. Basu. Experimental investigation of performance of high-shear atomizer with discrete radial-jet fuel nozzle: mean and dynamic characteristics. Flow, 2:E31, 2022.

[13] Rolls Royce plc. The jet engine. John Wiley and Sons, Chichester, United Kingdom, 5th edition, 2015.

[14] M. A. Nemitallah, A. A. Abdelhafez, and M. A. Habib. Premixed combustion for gas-turbine applications, pages 13–97. Springer International Publishing, Cham, 2020.

[15] R. K. Bhargava, M. Bianchi, A. De Pascale, G. Negri di Montenegro, and A. Peretto. Gas turbine based power cycles - A state-of-the-art review, pages 309–319. Springer Berlin Heidelberg, Berlin, Heidelberg, 2007.

[16] A. Valera-Medina, H. Xiao, M. Owen-Jones, W. I. F. David, and P. J. Bowen. Ammonia for power. Progress in Energy and Combustion Science, 69:63–102, 2018.

[17] M. Alhuy Nazari, M. Fahim Alavi, M. Salem, and M. E. H. Assad. Utilization of hydrogen in gas turbines: A comprehensive review. International Journal of Low-Carbon Technologies, 17:513–519, 2022.

[18] A. Valera-Medina, F Amer-Hatem, A. K. Azad, I. C. Dedoussi, M. de Joannon, R. X. Fernandes, P. Glarborg, H. Hashemi, X. He, S. Mashruk, J. McGowan, C. Mounaim-Rouselle, A. Ortiz-Prado, A. Ortiz-Valera, I. Rossetti, B. Shu, M. Yehia, H. Xiao, and M. Costa. Ammonia for power. Energy Fuels, 35(9):6964–7029, 2021.

[19] ETN Global. The path towards a zero-carbon gas turbine. 2020.

[20] A. Haj Ayed, K. Kusterer, H. H. W. Funke, J. Keinz, and D. Bohn. CFD based exploration of the dry-low-NOx hydrogen micromix combustion technology at increased energy densities. Propulsion and Power Research, 6(1):15–24, 2017.

[21] H. H. W. Funke, N. Beckmann, J. Keinz, and A. Horikawa. 30 Years of dry-low-NOx Micromix combustor research for hydrogen-rich fuels—An overview of past and present activities. Journal of Engineering for Gas Turbines and Power, 143(7), 2021.

[22] R. H. Chen and J. F. Driscoll. The role of the recirculation vortex in improving fuel-air mixing within swirling flames. Symposium (International) on Combustion, 22(1):531–540, 1989.

[23] A. K. Gupta, D. G. Lilley, and N. Syred. Swirl flows. Tunbridge Wells, Kent, England, Abacus Press, 488 p., 1984.

[24] D. Durox, J. P. Moeck, J. F. Bourgouin, P. Morenton, M. Viallon, T. Schuller, and S. Candel. Flame dynamics of a variable swirl number system and instability control. Combustion and Flame, 160(9):1729–1742, 2013.

[25] N. Syred and J. M. Beér. Combustion in swirling flows: A review. Combustion and Flame, 23(2):143–201, 1974.

[26] D. E. Cavaliere, J. Kariuki, and E. Mastorakos. A comparison of the blow-off behaviour of swirl-stabilized premixed, non-premixed and spray flames. Flow, Turbulence and Combustion, 91:347–372, 2013.

[27] S. A. Schumaker and J. F. Driscoll. Coaxial turbulent jet flames: Scaling relations for measured stoichiometric mixing lengths. Proceedings of the Combustion Institute, 32(2):1655–1662, 2009.

[28] S. A. Filatyev, J. F. Driscoll, C. D. Carter, and J. M. Donbar. Measured properties of turbulent premixed flames for model assessment, including burning velocities, stretch rates, and surface densities. Combustion and Flame, 141(1-2):1–21, 2005.

[29] J. I. Ramos and H. T. Somer. Swirling flow in a research combustor. AIAA Journal, 23(2):241–248, 1985.

[30] N. A. Chigier and J. M. Beér. Velocity and static-pressure distributions in swirling air jets issuing from annular and divergent nozzles. Journal of Basic Engineering, 86:788–796, 1964.

[31] O Lucca-Negro and T O'Doherty. Vortex breakdown: A review. Progress in Energy and Combustion Science, 27(4):431–481, 2001.

[32] M. O. Vigueras-Zuñiga, A. Valera-Medina, and N. Syred. Studies of the precessing vortex core in swirling flows. Journal of Applied Research and Technology, 10:755–765, 2012.

[33] N. Syred. A review of oscillation mechanisms and the role of the precessing vortex core (PVC) in swirl combustion systems. Progress in Energy and Combustion Science, 32(2):93–161, 2006.

[34] S. Candel, D. Durox, T. Schuller, J. F. Bourgouin, and J. P. Moeck. Dynamics of swirling flames. Annual Review of Fluid Mechanics, 46:147–173, 2014.

[35] F. Martinelli, A. Olivani, and A. Coghe. Experimental analysis of the precessing vortex core in a free swirling jet. Experiments in Fluids, 42:827–839, 2007.

[36] S. Terhaar, K. Oberleithner, and C. O. Paschereit. Key parameters governing the precessing vortex core in reacting flows: An experimental and analytical study. Proceedings of the Combustion Institute, 35(3):3347–3354, 2015.

[37] S. Wang, J. Zheng, L. Xu, Q. An, X. Han, C. Zhang, L. Li, X. Xia, and F. Qi. Experimental investigation of the helical mode in a stratified swirling flame. Combustion and Flame, 244:112268, 2022.

[38] K. Oberleithner, M. Stöhr, S. H. Im, C. M. Arndt, and A. M. Steinberg. Formation and flame-induced suppression of the precessing vortex core in a swirl combustor: Experiments and linear stability analysis. Combustion and Flame, 162(8):3100–3114, 2015.

[39] P. Jochmann, A. Sinigersky, M. Hehle, O. Schäfer, R. Koch, and H. J. Bauer. Numerical simulation of a precessing vortex breakdown. International Journal of Heat and Fluid Flow, 27(2):192–203, 2006.

[40] Z. Wang, X. Li, Z. Feng, and Z. Yang. The role of precessing vortex core in two combustion regimes: Numerical simulation studies. Journal of Mechanical Science and Technology, 33(1):433–446, 2019.

[41] Y. Zhang and M. Vanierschot. Determination of single and double helical structures in a swirling jet by spectral proper orthogonal decomposition. Physics of Fluids, 33(1):015115, 2021.

[42] I. V. Litvinov, S. I. Shtork, P. A. Kuibin, S. V. Alekseenko, and K. Hanjalic. Experimental study and analytical reconstruction of precessing vortex in a tangential swirler. International Journal of Heat and Fluid Flow, 42:251–264, 2013.

[43] D. Galley, S. Ducruix, F. Lacas, and D. Veynante. Mixing and stabilization study of a partially premixed swirling flame using laser induced fluorescence. Combustion and Flame, 158(1):155–171, 2011.

[44] I. Boxx, C. D. Carter, M. Stöhr, and W. Meier. Study of the mechanisms for flame stabilization in gas turbine model combustors using kHz laser diagnostics. Experiments in Fluids, 54:1532, 2013.

[45] Q. An, W. Y. Kwong, B. D. Geraedts, and A. M. Steinberg. Coupled dynamics of lift-off and precessing vortex core formation in swirl flames. Combustion and Flame, 168:228–239, 2016.

[46] A. Schönborn, P. Sayad, and J. Klingmann. Influence of precessing vortex core on flame flashback in swirling hydrogen flames. International Journal of Hydrogen Energy, 39(35):20233–20241, 2014.

[47] M. M. A. Ahmed and M. Birouk. Effect of fuel nozzle geometry and airflow swirl on the coherent structures of partially premixed methane flame under flashback conditions. Experimental Thermal and Fluid Science, 99:304–314, 2018.

[48] R. Zhang, I. Boxx, W. Meier, and C. D. Slabaugh. Coupled interactions of a helical precessing vortex core and the central recirculation bubble in a swirl flame at elevated power density. Combustion and Flame, 202:119–131, 2019.

[49] A. N. Belousov and A. K. Gupta. PVC and instability in swirl combustors. Chemical Engineering Communications, 47(4-6):363–380, 1986.

[50] M. Fairweather, M. P. Ormsby, C. G. W. Sheppard, and R. Woolley. Turbulent burning rates of methane and methane–hydrogen mixtures. Combustion and Flame, 156(4):780–790, 2009.

[51] Mechanical and UCSD Aerospace Engineering (Combustion Research). Chemical-Kinetic mechanisms for combustion applications, 2012. http://combustion.ucsd/edu.

[52] O. Tuncer, S. Acharya, and J. H. Uhm. Dynamics, NOx and flashback characteristics of confined premixed hydrogen-enriched methane flames. International Journal of Hydrogen Energy, 34(1):496–506, 2009.

[53] C. Eichler, G. Baumgartner, and T. Sattelmayer. Experimental investigation of turbulent boundary layer flashback limits for premixed hydrogen-air flames confined in ducts. Journal of Engineering for Gas Turbines and Power, 134(1):011502, 2012.

[54] Impact of chamber back pressure on the ignition dynamics of hydrogen enriched premixed flames. Proceedings of the Combustion Institute, 2022. 10.1016/j.proci.2022.07.236.

[55] K. T. Kim, J. G. Lee, H. J. Lee, B. D. Quay, and D. A. Santavicca. Characterization of forced flame response of swirl-stabilized turbulent lean-premixed flames in a gas turbine combustor. Journal of Engineering for Gas Turbines and Power, 132(4):041502, 2010.

[56] W. Zhang, J. Wang, W. Lin, R. Mao, H. Xia, M. Zhang, and Z. Huang. Effect of differential diffusion on turbulent lean premixed hydrogen enriched flames through structure analysis. International Journal of Hydrogen Energy, 45(18):10920–10931, 2020.

[57] C. K. Law, G. Jomaas, and J. K. Bechtold. Cellular instabilities of expanding hydrogen/propane spherical flames at elevated pressures: Theory and experiment. Proceedings of the Combustion Institute, 30(1):159–167, 2005.

[58] Y. Sheng, S. Abhishek, L. Wenkai, W. Fujia, and C. K. Law. Extreme role of preferential diffusion in turbulent flame propagation. Combustion and Flame, 188:498–504, 2018.

[59] Q. Cazères. Analysis and reduction of chemical kinetics for combustion applications. PhD thesis, Université de Toulouse, France, 2021.

[60] L. Berger, K. Kleinheinz, A. Attili, and H. Pitsch. Characteristic patterns of thermodiffusively unstable premixed lean hydrogen flames. Proceedings of the Combustion Institute, 37(2):1879–1886, 2019.

[61] H. Guo, G. J. Smallwood, F. Liu, Y. Ju, and Ö. L. Gülder. The effect of hydrogen addition on flammability limit and NOx emission in ultra-lean counterflow CH4/air premixed flames. Proceedings of the Combustion Institute, 30(1):303–311, 2005.

[62] G. J. Rørtveit, J. E. Hustad, S. C. Li, and F. A. Williams. Effects of diluents on NOx formation in hydrogen counterflow flames. Combustion and Flame, 130(1-2):48–61, 2002.

[63] J. Warnatz, U. Maas, and R. W. Dibble. Combustion: Physical and chemical fundamentals, modeling and simulation, experiments, pollutant formation. Springer Berlin, Heidelberg, Germany, 1996.

[64] S. R. Turns. Understanding NOx formation in nonpremixed flames: Experiments and modeling. Progress in Energy and Combustion Science, 21(5):361–385, 1995.

[65] S. C. Li and F. A. Williams. NOx formation in two-stage methane–air flames. Combustion and Flame, 118(3):399–414, 1999.

[66] D Charlston–Goch, B.L Chadwick, R.J.S Morrison, A Campisi, D.D Thomsen, and N.M Laurendeau. Laser-Induced fluorescence measurements and modeling of nitric oxide in premixed flames of CO+H2+CH4 and air at high pressures: I. Nitrogen fixation. Combustion and Flame, 125(1):729–743, 2001.

[67] M. K. El Hossaini. Review of the new combustion technologies in modern gas turbines. Rijeka, Croatia, 2013. IntechOpen.

[68] M. J. Moore. NOx emission control in gas turbines for combined cycle gas turbine plant. Proceedings of the Institution of Mechanical Engineers, Part A: Journal of Power and Energy, 211(1):43–52, 1997.

[69] A. F. Sarofim and J. H. Pohl. Kinetics of nitric oxide formation in premixed laminar flames. Symposium (International) on Combustion, 14(1):739–754, 1973.

[70] J. W. Bozzelli and A. M. Dean. O + NNH: A possible new route for NOx formation in flames. International Journal of Chemical Kinetics, 27(11):1097–1109, 1995.

[71] J. E. Harrington, G. P. Smith, P. A. Berg, A. R. Noble, J. B. Jeffries, and D. R. Crosley. Evidence for a new NO production mechanism in flames. Symposium (International) on Combustion, 26(2):2133–2138, 1996.

[72] A. N. Hayhurst and E. M. Hutchinson. Evidence for a new way of producing NO via NNH in fuel-rich flames at atmospheric pressure. Combustion and Flame, 114(1-2):274–279, 1998.

[73] J. Hwang, K. Sohn, N. Bouvet, and Y. Yoon. NOx scaling of syngas H2/CO turbulent non-premixed jet flames. Combustion Science and Technology, 185(12):1715–1734, 2013.

[74] S. R. Turns, F. H. Myhr, R. V. Bandaru, and E. R. Maund. Oxides of nitrogen emissions from turbulent jet flames: Part II—Fuel dilution and partial premixing effects. Combustion and Flame, 93(3):255–269, 1993.

[75] M. Leroy, C. Mirat, A. Renaud, and R. Vicquelin. Stabilization of low-NOx hydrogen flames on a dual-swirl coaxial injector. Journal of Engineering for Gas Turbines and Power, 145:021021, 2022.

[76] J. Oh, J. Hwang, and Y. Yoon. EINOx scaling in a non-premixed turbulent hydrogen jet with swirled coaxial air. International Journal of Hydrogen Energy, 35(16):8715–8722, 2010.

[77] W. M. Pitts. Assessment of theories for the behavior and blowout of lifted turbulent jet diffusion flames. Symposium (International) on Combustion, 22(1):809–816, 1989.

[78] L. Vanquickenborne and A. van Tiggelen. The stabilization mechanism of lifted diffusion flames. Combustion and Flame, 10(1):59–69, 1966.

[79] N. Peters and F. A. Williams. Liftoff characteristics of turbulent jet diffusion flames. AIAA Journal, 21(3):423–429, 1983.

[80] S. Byggstøyl and B. F. Magnussen. A model for flame extinction in turbulent flow. Turbulent Shear Flow, 4:381–395, 1985.

[81] H. G. Im and J. H. Chen. Structure and propagation of triple flames in partially premixed hydrogen–air mixtures. Combustion and Flame, 119(4):436–454, 1999.

[82] R. W. Schefer, M. Namazian, and J. Kelly. Stabilization of lifted turbulent-jet flames. Combustion and Flame, 99(1):75–86, 1994.

[83] M. S. Cha and P. D. Ronney. Propagation rates of nonpremixed edge flames. Combustion and Flame, 146(1-2):312–328, 2006.

[84] J. Buckmaster. Edge-flames. Progress in Energy and Combustion Science, 28(5):435–475, 2002.

[85] D. B. Clayton, M. S. Cha, and P. D. Ronney. Propagation and extinction of premixed edge-flames. Proceedings of the Combustion Institute, 37(2):1823–1830, 2019.

[86] L. Muñiz and M. G. Mungal. Instantaneous flame-stabilization velocities in lifted-jet diffusion flames. Combustion and Flame, 111(1-2):16–31, 1997.

[87] C. D. Brown, K. A. Watson, and K. M. Lyons. Studies on lifted jet flames in coflow: the stabilization mechanisms in the near- and far-fields. Flow, Turbulence and Combustion, 62:249–273, 1999.

[88] G. R. Ruetsch, L. Vervisch, and A. Liñán. Effects of heat release on triple flames. Physics of Fluids, 7(6):1447–1454, 1995.

[89] A. Joedicke, N. Peters, and M. Mansour. The stabilization mechanism and structure of turbulent hydrocarbon lifted flames. Proceedings of the Combustion Institute, 30(1):901–909, 2005.

[90] T. F. Guiberti, W. R. Boyette, Y. Krishna, W. L. Roberts, A. R. Masri, and G. Magnotti. Assessment of the stabilization mechanisms of turbulent lifted jet flames at elevated pressure using combined 2-D diagnostics. Combustion and Flame, 214:323–335, 2020.

[91] E. Villermaux and H. Rehab. Mixing in coaxial jets. Journal of Fluid Mechanics, 425:161–185, 2000.

[92] A. Aniello, D. Laera, S. Marragou, H. Magnes, L. Selle, T. Schuller, and T. Poinsot. Experimental and numerical investigation of two flame stabilization regimes observed in a dual swirl H2-air coaxial injector. Combustion and flame, 249:112595, 2023.

[93] G. Oztarlik, L. Selle, T. Poinsot, and T. Schuller. Suppression of instabilities of swirled premixed flames with minimal secondary hydrogen injection. Combustion and Flame, 214:266–276, 2020.

[94] T. Schuller, S. Marragou, G. Oztarlik, T. Poinsot, and L. Selle. Influence of hydrogen content and injection scheme on the describing function of swirled flames. Combustion and Flame, 240:111974, 2022.

[95] S. Marragou, H. Magnes, T. Poinsot, L. Selle, and T. Schuller. Stabilization regimes and pollutant emissions from a dual fuel CH4/H2 and dual swirl low NOx burner. International Journal of Hydrogen Energy, 47(44):19275–19288, 2022.

[96] S. Ducruix, D. Durox, and S. Candel. Theoretical and experimental determinations of the transfer function of a laminar premixed flame. Proceedings of the Combustion Institute, 28(1):765–773, 2000.

[97] T. Schuller, S. Ducruix, D. Durox, and S. Candel. Modeling tools for the prediction of premixed flame transfer functions. Proceedings of the Combustion Institute, 29(1):107–113, 2002.

[98] D. Durox, T. Schuller, N. Noiray, and S. Candel. Experimental analysis of nonlinear flame transfer functions for different flame geometries. Proceedings of the Combustion Institute, 32(1):1391–1398, 2009.

[99] S. Richard, C. Viguier, S. Marragou, and T. Schuller. Dispositif d’injection de dihydrogène et d’air (FR Patent No FR2111267). Institut National de la Propriété Industrielle, 2021.

[100] N. A. Chigier and A. Chervinsky. Experimental investigation of swirling vortex motion in jets. Journal of Applied Mechanics, 34(2):443–451, 1967.

[101] V. A. G. Gaydon and H. G. Wolfhard. Flames – Their structure, radiation and temperature. The Macmillan Company, New York, United States, 1960.

[102] R. B. Price, I. R. Hurle, and T. M. Sugden. Optical studies of the generation of noise in turbulent flames. Symposium (International) on Combustion, 12(1):1093–1102, 1969.

[103] M. Gatti, R. Gaudron, C. Mirat, L. Zimmer, and T. Schuller. Impact of swirl and bluff-body on the transfer function of premixed flames. Proceedings of the Combustion Institute, 37(4):5197–5204, 2019.

[104] S. Brohez, C. Delvosalle, and G. Marlair. A two-thermocouples probe for radiation corrections of measured temperatures in compartment fires. Fire Safety Journal, 39(5):399–411, 2004.

[105] A. Degeneve. Stabilization, structure and thermal behavior of oxy-flames with a variable swirl level. PhD thesis, Université Paris-Saclay, France, 2020.

[106] C. R. Shaddix. Correcting thermocouple measurements for radiation loss: A critical review. Albuquerque, United States, 1999.

[107] F. P. Incropera and D. P. Dewitt. Fundamentals of heat and mass transfer. John Wiley Sons, Chichester, United Kingdom, 1996.

[108] K. D. Jensen. Flow measurements. Journal of the Brazilian Society of Mechanical Sciences and Engineering, 26(4):400–419, 2004.

[109] D. Durox, S. Ducruix, and F. Lacas. Flow seeding with an air nebulizer. Experiments in Fluids, 27:408–413, 1999.

[110] D. V. Petrov. Raman spectrum of methane in nitrogen, carbon dioxide, hydrogen, ethane, and propane environments. Spectrochimica Acta Part A: Molecular and Biomolecular Spectroscopy, 191:573–578, 2018.

[111] A. H. Chen, J. F. Driscoll, J. Kelly, M. Namazian, and R. W. Schefer. A comparison of bluff-body and swirl stabilized flames. Combustion Science and Technology, 71(4-6):197–217, 1990.

[112] A. Degeneve, C. Mirat, J. Caudal, R. Vicquelin, and T. Schuller. Effects of swirl on the stabilization of non-premixed oxygen-enriched flames above coaxial injectors. Journal of Engineering for Gas Turbines and Power, 141(12):121018, 2019.

[113] T. F. Dixon, J. S. Truelove, and T. F. Wall. Aerodynamic studies on swirled coaxial jets from nozzles with divergent quarls. Journal of Fluids Engineering, 105(2):197–203, 1983.

[114] T. Mahmud, J. S. Truelove, and T. F. Wall. Flow characteristics of swirling coaxial jets from divergent nozzles. Journal of Fluids Engineering, 109(3):275–282, 1987.

[115] S. Yuasa. Effects of swirl on the stability of jet diffusion flames. Combustion and Flame, 66(2):181–192, 1986.

[116] A. Degeneve, R. Vicquelin, C. Mirat, J. Caudal, and T. Schuller. Impact of co- and counter-swirl on flow recirculation and liftoff of non-premixed oxy-flames above coaxial injectors. Proceedings of the Combustion Institute, 38(4):5501–5508, 2021.

[117] M. D. Durbin, M. D. Vangsness, D. R. Ballal, and V. R. Katta. Study of flame stability in a step swirl combustor. Journal of Engineering for Gas Turbines and Power, 118(2):308–315, 1996.

[118] S. Chouaieb, W. Kriaa, H. Mhiri, and P. Bournot. Swirl generator effect on a confined coaxial jet characteristics. International Journal of Hydrogen Energy, 42(48):29014–29025, 2017.

[119] T. Fiala and T. Sattelmayer. Heat release and UV-Vis radiation in non-premixed hydrogen-oxygen flames. Experiments in Fluids, 56:1–15, 2015.

[120] R. W. Schefer, W. D. Kulatilaka, B. D. Patterson, and T. B. Settersten. Visible emission of hydrogen flames. Combustion and Flame, 156(6):1234–1241, 2009.

[121] F. J. Cloos, D. Stapp, and P. F. Pelz. Swirl boundary layer and flow separation at the inlet of a rotating pipe. Journal of Fluid Mechanics, 811:350–371, 2017.

[122] M. García-Villalba and J. Fröhlich. LES of a free annular swirling jet – Dependence of coherent structures on a pilot jet and the level of swirl. International Journal of Heat and Fluid Flow, 27(5):911–923, 2006.

[123] L. Selle, G. Lartigue, T. Poinsot, R. Koch, K.-U. Schildmacher, W. Krebs, B. Prade, P. Kaufmann, and D. Veynante. Compressible large eddy simulation of turbulent combustion in complex geometry on unstructured meshes. Combustion and Flame, 137(4):489–505, 2004.

[124] S.H. Park and H.D. Shin. Measurements of entrainment characteristics of swirling jets. International Journal of Heat and Mass Transfer, 36(16):4009–4018, 1993.

[125] M. M. Ribeiro and J. H. Whitelaw. Coaxial jets with and without swirl. Journal of Fluid Mechanics, (96):769–795, 1980.

[126] J. Fröhlich, M. García-Villalba, and W. Rodi. Scalar mixing and large-scale coherent structures in a turbulent swirling jet. Flow, Turbulence and Combustion, 80:47–59, 2008.

[127] A. Katoch, T. F. Guiberti, D. V. de Campos, and D. A. Lacoste. Dual-fuel, dual-swirl burner for the mitigation of thermoacoustic instabilities in turbulent ammonia-hydrogen flames. Combustion and Flame, 246:112392, 2022.

[128] B. J. Hill. Measurement of local entrainment rate in the initial region of axisymmetric turbulent air jets. Journal of Fluid Mechanics, 51(4):773–779, 1972.

[129] H. Rehab, E. Villermaux, and E. J. Hopfinger. Flow regimes of large-velocity-ratio coaxial jets. Journal of Fluid Mechanics, 345:357–381, 1997.

[130] S. A. Schumaker and J. F. Driscoll. Mixing properties of coaxial jets with large velocity ratios and large inverse density ratios. Physics of Fluids, 24(5):055101–055101–21, 2012.

[131] S. R. Lee, S. S. Park, and S. H. Chung. Flame structure and thermal NOx formation in hydrogen diffusion flames with reduced kinetic mechanisms. KSME Journal, 9(3):377–384, 1995.

[132] G. Ribert, N. Zong, V. Yang, L. Pons, N. Darabiha, and S. Candel. Counterflow diffusion flames of general fluids: Oxygen/hydrogen mixtures. Combustion and Flame, 154(3):319–330, 2008.

[133] C. T. Chong, S. S. Lam, and S. Hochgreb. Effect of mixture flow stratification on premixed flame structure and emissions under counter-rotating swirl burner configuration. Applied Thermal Engineering, 105:905–912, 2016.

[134] S. R. Turns and F. H. Myhr. Oxides of nitrogen emissions from turbulent jet flames: Part I—Fuel effects and flame radiation. Combustion and Flame, 87(3-4):319–335, 1991.

[135] G. J. R. Newbold, G. J. Nathan, D. S. Nobes, and S. R. Turns. Measurement and prediction of NOx emissions from unconfined propane flames from turbulent-jet, bluff-body, swirl, and precessing jet burners. Proceedings of the Combustion Institute, 28(1):481–487, 2000.

[136] H. S. Kim, V. K. Arghode, M. B. Linck, and A. K. Gupta. Hydrogen addition effects in a confined swirl-stabilized methane-air flame. International Journal of Hydrogen Energy, 34(2):1054–1062, 2009.

[137] R. H. Chen and J. F. Driscoll. Nitric oxide levels of jet diffusion flames: Effects of coaxial air and other mixing parameters. Symposium (International) on Combustion, 23(1):281–288, 1991.

[138] F. Cozzi and A. Coghe. Behavior of hydrogen-enriched non-premixed swirled natural gas flames. International Journal of Hydrogen Energy, 31(6):669–677, 2006.

[139] F. Ommi and M. Azimi. Most effective combustion technologies for reducing NOx emissions in aero gas turbines. The International Journal of Multiphysics, 6(4):417–424, 2012.

[140] M. Skottene and K. E. Rian. A study of NOx formation in hydrogen flames. International Journal of Hydrogen Energy, 32(15):3572–3585, 2007.

[141] P. N. Kioni, B. Rogg, K. N. C. Bray, and A. Liñán. Flame spread in laminar mixing layers: The triple flame. Combustion and Flame, 95(3):276–290, 1993.

[142] P. N. Kıoni, K. N. C. Bray, D. A. Greenhalgh, and B. Rogg. Experimental and numerical studies of a triple flame. Combustion and Flame, 116(1-2):192–206, 1999.

[143] T. Tahtouh, F. Halter, E. Samson, and C. Mounaïm-Rousselle. Effects of hydrogen addition and nitrogen dilution on the laminar flame characteristics of premixed methane–air flames. International Journal of Hydrogen Energy, 34(19):8329–8338, 2009.

[144] S. Marragou, H. Magnes, A. Aniello, L. Selle, T. Poinsot, and T. Schuller. Experimental analysis and theoretical lift-off criterion for H2/air flames stabilized on a dual swirl injector. Proceedings of the Combustion Institute, 39(4):4345–4354, 2023.